Can localized impurities exert global effects on lipid model membranes?

by

Sherry See Wai Leung

M.Sc., Simon Fraser University, 2007

B.Sc. (Hons.), University of British Columbia, 2004

Thesis Submitted in Partial Fulfillment
of the Requirements for the Degree of

Doctor of Philosophy

in the
Department of Physics
Faculty of Sciences

SIMON FRASER UNIVERSITY
Spring 2015

APPROVAL

Name: Sherry See Wai Leung

Degree: Doctor of Philosophy

Title: Can localized impurities exert global effects on lipid model membranes?

Examining Committee:

Chair: Dr. David Sivak
Assistant Professor

Dr. Jenifer Thewalt
Senior Supervisor
Professor

Dr. John Bechhoefer
Supervisor
Professor

Dr. Nancy Forde
Supervisor
Associate Professor

Dr. Eldon Emberly
Internal Examiner
Associate Professor
Department of Physics

Dr. Raghu Parthasarathy
External Examiner
Associate Professor
Department of Physics
University of Oregon

Date Defended/Approved: Apr 23, 3015

Partial Copyright Licence

The author, whose copyright is declared on the title page of this work, has granted to Simon Fraser University the non-exclusive, royalty-free right to include a digital copy of this thesis, project or extended essay[s] and associated supplemental files ("Work") (title[s] below) in Summit, the Institutional Research Repository at SFU. SFU may also make copies of the Work for purposes of a scholarly or research nature; for users of the SFU Library; or in response to a request from another library, or educational institution, on SFU's own behalf or for one of its users. Distribution may be in any form.

The author has further agreed that SFU may keep more than one copy of the Work for purposes of back-up and security; and that SFU may, without changing the content, translate, if technically possible, the Work to any medium or format for the purpose of preserving the Work and facilitating the exercise of SFU's rights under this licence.

It is understood that copying, publication, or public performance of the Work for commercial purposes shall not be allowed without the author's written permission.

While granting the above uses to SFU, the author retains copyright ownership and moral rights in the Work, and may deal with the copyright in the Work in any way consistent with the terms of this licence, including the right to change the Work for subsequent purposes, including editing and publishing the Work in whole or in part, and licensing the content to other parties as the author may desire.

The author represents and warrants that he/she has the right to grant the rights contained in this licence and that the Work does not, to the best of the author's knowledge, infringe upon anyone's copyright. The author has obtained written copyright permission, where required, for the use of any third-party copyrighted material contained in the Work. The author represents and warrants that the Work is his/her own original work and that he/she has not previously assigned or relinquished the rights conferred in this licence.

Simon Fraser University Library
Burnaby, British Columbia, Canada

revised Fall 2013

Abstract

The currently accepted model for cell membrane organization involves "lipid rafts", which differ in composition from the surrounding lipid sea. The existence of these nano-scale heterogeneities is supported by observation of coexisting ordered and disordered lipid phases in lipid model membranes. Fluorescence is a popular family of techniques that can provide dynamic and structural information about membranes. With any probe method, characterization of the effects of fluorescent probe addition on the systems they are used to study is important for the interpretation of experimental data. Comparison can be made between labelled and unlabelled samples using a non-perturbing method, such as deuterium nuclear magnetic resonance spectroscopy (^{2}H NMR).

This thesis used ^{2}H NMR to study the effects of an equipartitioning probe, Laurdan, and a non-equipartitioning probe, naphthopyrene, on a well-studied three-component lipid membrane system (35:35:30 dioleoyl-*sn*-glycero-3-phosphocholine (DOPC)/dipalmitoyl-*sn*-glycero-3-phosphocholine-D62 (DPPC-D62)/cholesterol) with a miscibility phase transition. In phase-separated membranes, 0.03-0.6% naphthopyrene disordered lipid chains of DPPC-D62 in the liquid-disordered phase, but not of those in the liquid-ordered phase. 0.1-2% Laurdan did not affect the DPPC-D62 in either phase in these membranes. Above the miscibility transition temperature ($\sim$ 22°C), there is a single homogeneous liquid phase that is not perturbed by the addition of either probe. Laurdan is particularly well suited to the study of phase separation in lipid membranes. It partitions equally well into ordered and disordered lipid phases and displays a polarity-dependent emission spectral shift. Laurdan general polarization (GP) parameter, which characterizes said spectral shift, has been used to characterize membrane fluidity. Two-photon excitation microscopy Laurdan GP images were acquired for membranes with 0.2-2% Laurdan, and Laurdan GP values were found to be strongly correlated with ^{2}H NMR methylene order parameters of DPPC-D62 in the liquid-ordered phase. Finally, photo-induced phase separation is known to occur in fluorescence microscopy experiments; however, our ^{2}H NMR experiments showed that naphthopyrene can alter membrane properties in the absence of light.

The fact that trace amounts of probe (e.g., 0.03-0.6% naphthopyrene) affect lipid molecular order has biological implications: biomolecules present in very small amounts are known to have important functions in cells.

Keywords: Laurdan; naphthopyrene; impurity; lipid model membrane; deuterium nuclear magnetic resonance spectroscopy (^{2}H NMR); liquid disordered-liquid ordered coexistence ($\mathbf{l_d}$+$\mathbf{l_o}$)

To my family

Acknowledgements

My supervisor, Dr. Jenifer Thewalt, was instrumental to the successful completion of this work. I thank her for providing a nurturing learning environment and for being a wonderful supervisor. Past members of the Thewalt lab, Drs. Elana Brief, Xin Chen, John Cheng, Christian Code, Yawei Hsueh, Laila Singh, Mehran Shaghaghi and Amir Keyvanloo taught me everything I needed to know about our beloved spectrometer, deuterium NMR, and lipids. I am greatly indebted to our collaborators at the University of Southern Denmark, Drs. Luis Bagatolli, Jonathan Brewer, and Ole Mouritsen, and other members of the Danish Centre of Excellence for Biomembrane physics, MEMPHYS, for their multiple contributions to this project: materials, training in fluorescence techniques, fruitful discussions, valuable mentoring, and hospitality. I would like to specifically thank the following members of MEMPHYS for the practical advice they gave: Kirstin Wagner, Lucas Solenko, Anders Hansen, Morten Christensen, Bastien Loubet, Tripta Bhatia, and Lars Duelund. I thank Dr. Sarah Veatch for doing the preliminary work that led to this project; my supervisory committee, Drs. Nancy Forde and John Bechhoefer, and Dr. Martin Zuckermann for their helpful suggestions and critiques; and lab volunteers Mike Kirkness, Jason Wang, and Bashe Bashe for providing technical and data analysis support. I also acknowledge Jean-François Caron for his editing contributions, useful discussions, and ongoing grammar lessons; and Joyce Leung for editing contributions. This thesis would not have been possible without the support from a very understanding partner and the best sister in the world. Finally, I thank my parents for their patience, love, and support.

Funding has been provided by NSERC Alexander Graham Bell Canada Graduate Scholarship, Michael Smith Foundation Foreign Travel Supplement, Simon Fraser University Graduate Fellowship, and MEMPHYS at Syddansk Universititet. Conference travel funding has been provided by the Biophysical Society, the Biophysical Society of Canada, and Simon Fraser University.

Contents

List of Tables

List of Figures

List of Acronyms

^{2}H NMR deuterium nuclear magnetic resonance spectroscopy

A488-CTB recombinant CTB conjugated with Alexa Fluor 488

AFM atomic force microscopy

Biotin-DPPE biotinylated-DPPE

Bodipy-DPPC 2-(4,4-difluoro-5,7-dimethyl-4-bora-3a,4a- diaza-s-indacene-3-pentanoyl)-1-hexadecanoyl-sn-glycero-3-phosphocholine

bSm bovine brain sphingomyelin

CCT Cytidine 5'-triphosphate:choline-phosphate cytidylyltransferase

CFM confocal fluorescence microscopy

chol cholesterol

CTB cholera toxin B

DDW deuterium-depleted water

DHE dehydroergosterol

DiI dialkylindocarbocyanine

DiIC12 1,1- didodecyl-3,3,3,3-tetramethylindocarbocyanine perchlorate

DLPC 1,2-dilauroyl-*sn*-glycero-3-phosphocholine (12:0-12:0)

DMPC 1,2-dimyristoyl-*sn*-glycero-3-phosphocholine (14:0-14:0)

DMSO dimethyl sulfoxide

DOPC 1,2-dioleoyl-*sn*-glycero-3-phosphocholine (18:1-18:1)

DPH diphenylhexatriene

DPPC 1,2-dipalmitoyl-*sn*-glycero-3-phosphocholine (16:0-16:0)

DSC differential scanning calorimetry

DSPC 1,2-distearoyl-*sn*-glycero-3-phosphocholine (18:0-18:0)

eSm chicken egg sphingomyelin

ESR electron spin resonance spectroscopy

FCS fluorescence correlation spectroscopy

FID free induction decay

FLIM fluorescence lifetime imaging microscopy

FRAP fluorescence recovery after photo-bleaching

FT-IR Fourier transform infrared spectroscopy

$\mathbf{G_{M1}}$ ganglioside

GP general polarization

GPMV giant plasma membrane vesicle

GUV giant unilamellar vesicle

$\mathbf{k_p}$ partition coefficient

$\mathbf{L}_\beta$ gel phase

ld liquid-disordered

lo liquid-ordered

LUV large unilamellar vesicle

$\mathbf{M_1}$ average spectral width

MLV multilamellar vesicle

MVV multivesicular vesicle

NMR nuclear magnetic resonance

NSOM near-field scanning optical microscope

N-WASP neural Wiscott-Aldrich syndrome protein

NSAID non-steroidal anti-inflammatory drugs

PAH polycyclic aromatic hydrocarbons

PC phosphatidylcholine

PIP2 phosphatidylinositol 4,5 bisphosphate

POPC 1-palmitoyl-2-oleoyl-*sn*-glycero-3-phosphocholine (16:0-18:1)

pSm palmitoyl sphingomyelin

RET Förster resonance energy transfer

Rh-DPPE 1,2-dihexadecanoyl-*sn*-glycero-3-phosphoethanolamine-N-(Lissamine rhodamine B sulfonyl)(ammonium salt)

Rh-DOPE 1,2-dioleoyl-*sn*-glycero-3-phosphatidylethanolamine-N-(Lissamine rhodamine B sulfonyl)(ammonium salt)

SAXS small angle X-ray diffraction

Sm sphingomyelin

SNR signal-to-noise ratio

so sold-ordered

sSm steroyl sphingomyelin

SUV small unilamellar vesicle

$\mathbf{T_m}$ melting transition temperature

$\mathbf{T_{mix}}$ miscibility transition temperature

TLC thin layer chromatography

t-PnA trans-parinaric acid

TMA-DPH trimethylammonium-diphenylhexatriene

TR-DPPE Texas Red 1,2-dihexadecanoyl-sn-glycero-3-phosphoethanolamine, triethylammonium salt

WAXS wide angle X-ray diffraction

Chapter 1

Introduction

1.1 What do lipids do in cells?

The four major molecules of life are carbohydrates, nucleic acids, proteins, and lipids. Carbohydrates provide energy to cells. Nucleic acids carry genetic information that is passed from generation to generation. Proteins carry out functions and catalyze reactions. Historically, lipids were only the backdrop on which all the above take place. It is now known that lipids are more than mere structural components that hold life together; they too play important roles in biological processes. A number of examples are given below.

The conversion of sphingomyelin, a sphingolipid, to ceramide signals the apoptotic cascade in aging cells. Sphingosine-1-phosphate, a lysophospholipid, directs the movements of lymphocytes (e.g., B and T cells) within and from Lymphoid tissues (e.g., lymph nodes) [1]. Phosphatidylinositols are membrane phospholipids with an inositol headgroup and a sugar ring. They reside in the inner leaflet of the plasma membrane and perform numerous functions: examples include propagating signals from antigen-engaged B and T cell antigen receptors, and promoting lymphocyte activation, proliferation, and differentiation [1]. Phosphatidylinositol 4,5 bisphosphate (PIP2), in particular, is involved in exocytosis, endocytosis, membrane trafficking, and the activation of multiple enzymes [2].

The cell plasma membrane is a bilayer composed of lipids and proteins. Lipids and proteins can interact directly or indirectly. Enzymes such as protein kinase C and protein kinase B bind lipids via their headgroups and convert them into messenger molecules [3]. Proteins, such as Src kinase, and K-Ras, have poly-basic motifs that interact with lipids via weak electrostatic interactions. Many other proteins have amphipathic helices that embed them into the membrane (e.g., pyruvate oxidase, MirD, DnaA, Cytidine 5'-triphosphate:choline-phosphate cytidylyltransferase (CCT)) [see review 4]. Embedded amphiphiles can affect membrane properties such as bending stiffness, lateral packing density, intramembrane dipole potential, and interfacial surface charge density; many of these, in turn, can affect membrane protein aggregation, distribution, and function [5].

The lipid raft hypothesis postulates that lateral membrane heterogeneities in cell membranes act as concentration platforms for other molecules in biological processes [see reviews 6, 7]. It is thought that "raft components" aggregate to form more ordered lipid rafts surrounded by a disordered lipid "sea" and that these physical arrangements facilitate functional organization of other biomolecules. Lipid rafts are purported to be 10-100 nm sized regions enriched in cholesterol, sphingomyelin, glycosphingolipids, and GPI-anchored proteins. Putative roles include signal transduction, protein and lipid sorting, cholesterol transportation, and endocytosis [8]. Rafts can also be hijacked and used by pathogens [7, 9]. For example, the purported raft component ganglioside (G_{M1}) is the receptor for cholera toxin [9]. Also, the expression of FimH by *Escherichia coli* allows them to escape detection by their target host. The presence of FimH allows E.coli to be internalized by macrophages via cholesterol-rich microdomains instead of lysosomes, thereby allowing them to escape digestion by the host cell [9]. Lastly, DNA virus SV 40 enters cells via caveolae (i.e., non-clathrin coated pits) [9]. The existence of lipid rafts in biological systems is still controversial because of their small size and dynamic nature [10, 11].

1.2 How is studying lipids profitable?

In addition to increasing fundamental understanding of biology, the study of lipids has direct applications in pharmaceutical, agricultural, and food industries. Aspirin, ibuprofen, and naproxen are common non-steroidal anti-inflammatory drugs (NSAID) that are widely used for their analgesic (pain-killing) and antipyretic (fever-reducing) effects, in addition to their anti-inflammatory effects. Their analgesic effects partially derive from their non-selective inhibition of cyclooxygenase, but it is unclear how they can interact with multiple other protein targets. Non-specific interactions with the membrane may explain how these drugs can have broad effects on cell function [5]. NSAIDs are amphiphilic, and there is evidence that their association with cell membranes alters membrane properties. Similar arguments have also been proposed for interactions between hydrophobic insecticides and multiple membrane-bound proteins [12].

Pharmaceutical companies are currently researching ways to use liposomes and lipid nanoparticles as drug carriers and immunological adjuvants. Most free drugs[1] are removed from our bodies by our immune system before performing their designed therapeutic function. Lipid encapsulation can help the active drug evade detection by the immune system, ensuring that they reach their target organ and cells. Since many drugs are harmful, it is also necessary to prevent them from acting on healthy cells. Ideally, they should be designed for selective uptake by the target cell. There have been many successes in liposomal drug development thus far. Liposomes have been shown to increase transdermal drug adsorption of topically applied drugs [13]. Liposomes show enhanced accumulation in tumour tissues, and liposomal cancer treatment has been vastly successful [14]. Liposomal drugs AmBisome and Doxil are currently used clinically, with sales in the hundreds of millions of dollars per year [14]. The ability to release the drugs at the right place and time requires careful tuning of the physical properties of these systems. Since lipids are one of the main building blocks of these systems; full characterization of lipid physical properties allows us to engineer better drug delivery systems.

1.3 How are lipids studied?

Biophysicists are interested in physical properties such as membrane elasticity, hydration, thickness, and fluidity. The latter, membrane fluidity, encompasses a number of observables: rotational diffusion, translational order (lateral diffusion), and conformational order (trans/gauche ratio in acyl chains) [7].

Biological membranes are complex mixtures of proteins, carbohydrates, lipids, and hybrid molecules such as gangliosides (glycosphingolipid with sugar modifications). It is difficult to pinpoint the key role of each individual component in such a complex system. To complicate matters, the compositions of natural membranes are very dynamic and always changing. Luckily, some of the physical properties biophysicists are interested in can be

---

[1] Free drugs are drugs that have not been encapsulated by a liposome.

accurately measured in model membranes made with only a few components [7]. The approach taken in this thesis is to begin understanding complex membranes using a bottom up approach.

1.3.1 Model lipid membranes

The basic building block of a membrane is the lipid bilayer. Lipid bilayers are typically found in one of three phases: liquid disordered phase ($\mathbf{l_d}$), liquid ordered phase ($\mathbf{l_o}$), and gel phase – or solid ordered ($\mathbf{s_o}$) – phase [15, 16]. Lipids in the liquid phases can diffuse laterally within the plane of the bilayer more rapidly than those in the gel phase. Typical diffusion coefficient is $D \approx 10^{-12}$ m^2/s in the liquid phases and 10^3 times smaller in the gel phase [17–19]. The lipid chains of the gel phase are in the all-trans configuration, allowing close lipid packing, and resulting in a more rigid membrane. The $\mathbf{l_o}$ phase has only been observed in membranes containing cholesterol (or similar sterols), whose rigid ring structure imposes more restricted conformations on the lipid chains and reduces the number of gauche rotamers in the chains. The gauche configuration causes kinks in the lipid chain that prevents them from packing tightly in the $\mathbf{l_d}$ phase. The lipid chains in the $\mathbf{l_o}$ phase are more extended [20]. The $\mathbf{l_o}$ phase also differs from the $\mathbf{l_d}$ phase in that (1) translational diffusion is approximately two-fold slower [21, 22], (2) the lipid chains have less rotational freedom [23], and (3) trans-gauche isomerization is slower than in the $\mathbf{l_d}$ phase. Multiple phases can coexist, in accordance with the Gibbs phase rule (Appendix A). For example, below the $\mathbf{l_d}+\mathbf{l_o}$ miscibility transition temperature (T_{mix}), both $\mathbf{l_d}$ and $\mathbf{l_o}$ phases can be found in the same membrane. This thesis will look at T_{mix} extensively.

To study the simplest model of the outer leaflet of the plasma membrane bilayer, three lipid components are required: cholesterol (chol), sphingomyelin (Sm), and an unsaturated phosphatidylcholine (PC). In practice, even a binary mixture can exhibit complex phase behaviour [24]. Typical model membranes are ternary mixtures made with cholesterol, a lipid with a high melting temperature, and a lipid with a low melting temperature. This is the simplest mixture capable of producing the micron-scale $\mathbf{l_o}$ phase domains that are central to the lipid raft hypothesis, but it is known that ternary mixtures are difficult to study and model [19, 25–28].

Biological membranes tend to be unilamellar. Methods exist for making unilamellar vesicles of various sizes (Fig. 1.1). The vesicles are aptly named giant unilamellar vesicles

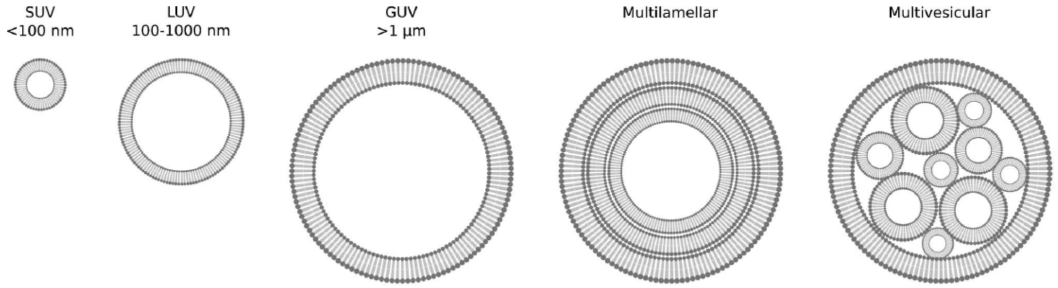

Figure 1.1: Vesicle types: small unilamellar vesicle (SUV), large unilamellar vesicle (LUV), giant unilamellar vesicle (GUV), multilamellar vesicle (MLV), and multivesicular vesicle (MVV). Reproduced from [29] with permission from The Royal Society of Chemistry.

(GUVs) (10-100 μm diameter), large unilamellar vesicles (LUVs) (100 nm diameter), and small unilamellar vesicles (SUVs) (30-50 nm diameter) [30, 31]. Of these, GUVs most closely resemble biological plasma membranes in size [30, 32, 33]. Another type of vesicle, multilamellar vesicles (MLVs), forms spontaneously when lipids are placed into an aqueous solution. The sizes of MLVs are reported to vary greatly (0.5-10 μm [34–37]). MLVs have an onion-like structure: typically hundreds of 5 nm thick bilayers, separated by water layers, and enclosing a small internal volume [38, 39].

Another type of model membrane system is "cell blebs" or giant plasma membrane vesicle (GPMV). GPMVs are cell membranes removed from live cells. In terms of complexity, GPMVs are intermediate between cell membranes and model lipid membranes. In the presence of 1-5% (v/v) ethanol, acetone, or DMSO, the cell membrane of rat basophil leukemia cells pulls away from the cytoskeleton and buds off as vesicles [40]. GPMVs contain a variety of plasma membrane protein and lipid species, but do not include membrane proteins attached to cytoskeletal components. For eukaryotic cells, the lipid species residing in the two leaflets of the bilayer are different [41]. GPMVs do not have the same degree of asymmetry as cell membranes, and the membrane is no longer connected to active cellular processes.

The observation of phase separation in a variety of model membranes supports the lipid raft hypothesis. Macroscopic phase separation in ternary – composed of three lipid components – GUVs [42], quaternary GUVs, supported bilayers, and monolayers [43] has been directly observed by fluorescence microscopy and atomic force microscopy (AFM).

Deuterium nuclear magnetic resonance spectroscopy (^{2}H NMR) and other techniques corroborate these observations by providing evidence for the presence of multiple distinct populations of lipids in a vesicle. Such phases have been observed in GPMVs too, usually at temperatures somewhat below physiological [44].

1.3.2 Biophysical techniques

Many experimental techniques are used for studying lipid phase states and phase transitions. Some are bulk techniques reporting on thermodynamic and macroscopic properties of a collection of lipids or vesicles, while others allow characterization of individual vesicles or atoms. Some of these techniques are listed below. The techniques provide complementary information on different length and time scales. They also each have their own advantages and shortcomings. For these reasons, it is important to employ a variety of techniques when studying complex ternary and quaternary mixtures. The techniques used in this thesis are ^{2}H NMR and fluorescence microscopy.

- Differential scanning calorimetry (DSC) measures the heat required for a sample to undergo a physical phase transition [45].
- In Fourier transform infrared spectroscopy (FT-IR), the frequency of CH_2 stretching vibrations is used to estimate the number of gauche-rotamers [46].
- Small angle X-ray diffraction (SAXS) is used to monitor monolayer and bilayer repeat spacing, and hydrophobic thickness [46, 47].
- Wide angle X-ray diffraction (WAXS) is used to determine chain packing, and extent of lipid motion [46, 47].
- ^{2}H NMR monitors the nuclear spin of deuterated lipids to give information on segmental order parameters. Spin relaxation measurements can divulge information about lipid motions [48].
- Electron spin resonance spectroscopy (ESR) monitors the electron spin of excited unpaired electrons [49]. Since there are no unpaired electrons in lipids, spin probes are added to membranes and the orientation of the nitroxide (N-O) bond of the probe with respect to the applied magnetic field is observed. ESR can also be used to measure order parameters.

- AFM measures membrane thickness in supported monolayers and bilayers [50].

- Mechanical techniques, such as micro-pipette aspiration, measure tension [51].

- Fluorescence microscopy relies on partitioning properties of fluorescent probes to allow visualization of micron sized macroscopic phase separation [50].

- Fluorescence lifetime imaging microscopy (FLIM) can show phase separation since the fluorescence lifetimes of some probes are phase state dependent [52, 53].

- In fluorescence anisotropy/polarization experiments, fluorescent probes are excited with polarized light. The excitation light polarization dictates the polarization of the emitted light. Thus, the polarization of the emitted light contains information about the rotational dynamics of the probe, which indirectly reports on membrane fluidity [27, 54].

- With an appropriate pair of fluorescent probes, Förster resonance energy transfer (RET) experiments are used to monitor phase separation [55].

- Fluorescence recovery after photo-bleaching (FRAP) can measure lipid diffusion in membranes [18].

- Fluorescence correlation spectroscopy (FCS) measures dye mobility and characterize lipid dynamics via auto-correlations of a fluorophore's temporal fluctuations [19, 50].

1.4 Motivation for this project

The existence of lipid rafts in living systems remains contentious [56]. The earliest method of detection by the isolation of a detergent-resistant membrane fraction has been called into question because of the highly artificial conditions involved. Microscopists have yet to directly see lipid rafts in biological systems [57, 58]. The presumed small size and dynamic nature of rafts are the causes for their elusiveness.

A great deal of lipid research is done using fluorescence. Figures 1.2-1.3 show the structures of some lipid probes. Fluorophores are typically polycyclic aromatic hydrocarbons (PAH) or heterocycles[2]. Previously, it was commonly assumed that the minuscule amount

---

[2] Heterocycles are cyclic compound with at least two types of elements in the ring structure.

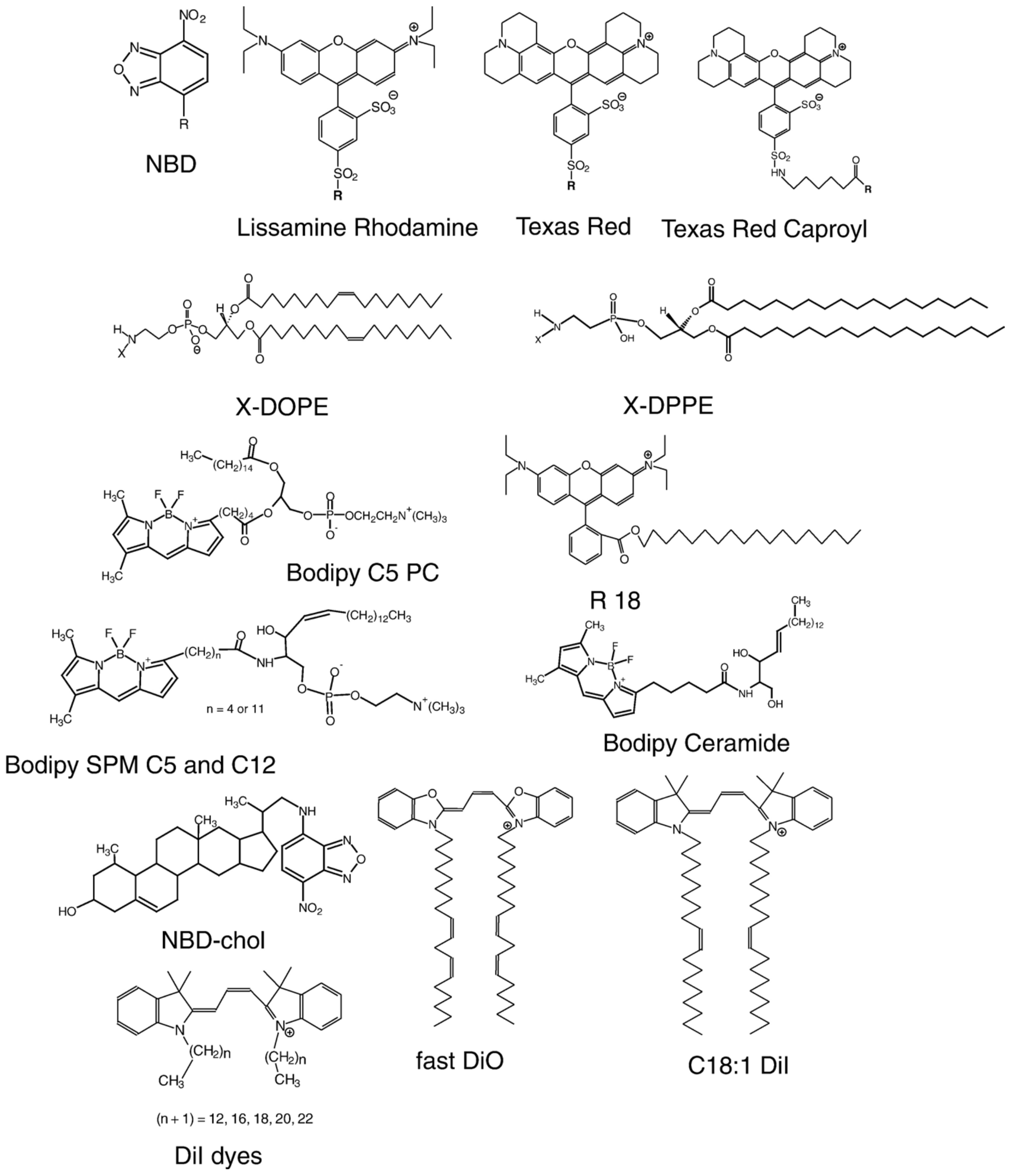

Figure 1.2: Compendium of Lipid Probe Structures: lipid analog dyes. Reproduced from [59] with permission from Elsevier.

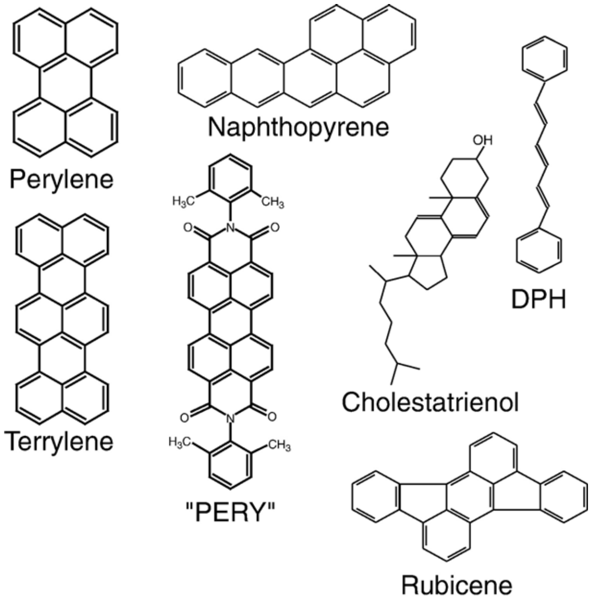

Figure 1.3: Compendium of Lipid Probe Structures: polycyclic aromatic hydrocarbons and DPH. Reproduced from [59] with permission from Elsevier.

(e.g., 0.1-0.5 mol% for fluorescence microscopy) of probe used did not perturb the lipid membrane system they were used to study. In thermodynamic terms, the probe may be seen as an ideally dilute solute [27]. Only a very small amount of probe (e.g., 0.1 mol% for fluorescence microscopy) is required. McConnell [60], Veatch and Keller [61] showed that 0.2-2.0% probe in mixed component lipid membranes had little to no effect on the observed phase behaviour of monolayers. In the early 2000's, researchers began to question this assumption [62, 63].

Studies involving impurities in binary liquid systems date back to the 1970's [64–66]. In 2004, Veatch et al. [67] reported that 0.2-2% TR-DPPE had no effect on T_{mix} of 35:35:30 DOPC/DPPC/chol, but later research showed that the samples with 0.2-2% TR-DPPE behaved differently than membranes completely devoid of probe [68, 69]. In 2007, using ^{2}H NMR, our lab showed that trace amounts of the carbocyanine fluorescent probe DiIC12 altered the physical properties of ternary membranes in a way similiar to TR-DPPE. Incorporation of 0.5% DiIC12 increased T_{mix} by a dramatic 6°C [70].[3] Also in 2007, Baumgart et al. [59] published a study of 26 different fluorescent probes using a typical model raft mixture (DOPC/Sm/chol) that demonstrated the need for better understanding of fluorescent

---

[3] There has been a decrease in the amount of probe used in the field since publication of our 2007 paper [70]. Newer papers typically use less than 0.5 mol%.

probes. Some of these intricacies are discussed below. Not surprisingly, Juhasz et al. [28] found inconsistent T_{mix} when using different probes. Using atomistic molecular dynamics, Skaug et al. [71] were able to reproduce results that showed TR-DPPE increasing T_{mix} of a generic ternary mixture. One of the outstanding questions left from these studies is whether the partitioning of probes alters T_{mix}. Before exploring this question any further, we will consider some interesting observations on probe behaviour in the literature.

1.4.1 Fluorescent probe-lipid membrane interactions

Small changes in lipid composition of the membrane can cause some lipid probes to show altered behaviour. This suggests that minor components can have large effects on membranes [40, 61]. We and others have provided evidence of fluorescent probes affecting membrane properties [70, 72]. This section presents these and many other examples of trace impurities altering membrane properties. It is surprising that these trace components can have such profound effects. These examples remind us that it is not safe to underestimate the contributions from minor components.

Fluorescent probes do not partition into particular membrane phases

Membrane composition can alter probe partitioning preference [73]. Popular dialkylindocarbocyanine (DiI) family of dyes will partition into the $\mathbf{l_d}$, $\mathbf{l_o}$, or $\mathbf{s_o}$ phase depending on the host membrane system. For example, DiIC18 prefers the $\mathbf{l_d}$ phase in bovine brain sphingomyelin (bSm)/bPC/chol, 27:50:23 bSm/DOPC/chol and Sm/DOPC/chol [19]; the $\mathbf{l_o}$ phase in Sm/DLPC/chol, 27:50:23 DSPC/DOPC/chol [19]; and the gel phase in DLPC/DPPC; and it shows very weak preference between coexisting fluid phases in 35:35:30 DOPC/DPPC/chol [19, 59]. DiIC20, which goes into the $\mathbf{l_d}$ phase in Sm/POPC + 10% chol membranes, but prefers the $\mathbf{l_o}$ phase in DSPC/DOPC + 40% chol membranes [68]. DiIC22 prefers the $\mathbf{l_d}$ phase in 27:50:23 bSm/DOPC/chol, but it associates with the $\mathbf{l_o}$ phase if the bSm is replaced with DSPC.

Both short and long chain (12-22 carbon chain) DiI partitioned into the $\mathbf{l_d}$ phase in bSm:DOPC:chol; but in DSPC:DOPC:chol, long chain DiI (C18:0-C22:0) preferred the $\mathbf{l_o}$ phase, and short chain DiI (C12:0-C16:0) preferred the $\mathbf{l_d}$ phase. There are two points to note. One, these ternary mixtures are very similar. Two of the three components are the same. 50% of the third component, bSm is 18:0 Sm; DSPC also has 18:0 lipid chains. Two, DiI probes' partitioning behaviour are dependent on the probe's chain length. This is not true for all probes: in some cases, partitioning preference is dictated by the fluorescent moiety.

Other types of probes also show membrane composition dependent partitioning behaviour. Trans-parinaric acid (t-PnA) prefers the gel phase induced by indomethacin in dual labelled 33:33:33 DOPC/DPPC/chol, but if no gel phase is present it will partition equally into both the $\mathbf{l_d}$ and $\mathbf{l_o}$ phases [74].

It can be seen from these examples that in general probes do not partition into particular membrane phase states. Rather, partitioning is dependent on the local chemical environment of the lipid domains [30]. Thus, the terms '$\mathbf{l_d}$ probe' and '$\mathbf{l_o}$ probe' should only be used in conjunction with specific lipid compositions and conditions, and probes should only be used to identify membrane phases after careful characterization in the membrane system of interest. Furthermore, it is important to keep in mind that the partitioning can be characterized by a partition coefficient, and the probe is only *preferentially* partitioning into one phase over another.

Dual labelling alters probe partition coefficient

Dual labelling is one of the common methods used to verify membrane domain identity in microscopy experiments [e.g., 33, 68]. Membrane phase states are assigned by using multiple fluorophores with different partitioning properties. Dual labelling is also necessary in FRET experiments [e.g., 75]. Juhasz et al. [28] reported that the addition of a second or a third probe can alter a probe's partitioning preference. For example, DiIC18 does not show strong preferential partitioning when used on its own in the 35:35:30 DOPC/DPPC/chol membranes in the temperature range of 15-43°C [25]. When the membrane is dual labelled, Bodipy-PC caused DiIC18 to partition into the $\mathbf{l_d}$ phase in the temperature range of 26 to 30°C. These results suggest that dual labelling cannot guarantee the identity of a membrane phase state.

To complicate matters further, complementary dye pair partitioning can show membrane composition dependence [59, 76, 77]. For example, (16:0,Bodipy)-PC and C20:0-DiI showed complementary partitioning in DSPC/DOPC/chol, but both partitioned into the $\mathbf{l_d}$ phase of Sm/DOPC/chol [59]. This of course is simply an extension of the observations described in the previous section. Perylene partitioned indiscriminately into

$\mathbf{l_d}$ and $\mathbf{l_o}$ phase in 27:50:23 *bovine brain* Sm:DOPC:chol membranes dual labelled with perylene and 1,2-dioleoyl-*sn*-glycero-3-phosphatidylethanolamine-N-(Lissamine rhodamine B sulfonyl)(ammonium salt) (Rh-DOPE) [59], but it partitioned only into the $\mathbf{l_o}$ phase in 25:50:25 *chicken egg* Sm:DOPC:chol membranes dual labelled with the same probes [78]. Natural Sm from different sources differs in composition (see Sec. 1.4.2).

Fluorescence intensity is not always directly related to probe concentration

Using fluorescence microscopy to observe phase coexistence relies on the contrast provided by fluorescent dyes. The underlying assumptions are that the differences between the two environments cause the probe to prefer one environment over another and that the intensity of light emitted is directly correlated with the amount of probe present. There are multiple scenarios where the latter assumption fails. For instance, probes can exhibit concentration-dependent self-quenching, as is the case with the fluorescent probe C12NBD-PC. Fluorescence intensity of C12NBD-PC was found to decrease with increasing probe concentration in 2:1 PC:Sm LUV [79]. Fluorescence emission intensity can be membrane phase dependent [73]. DiI probes are brighter in $\mathbf{l_o}$ than in $\mathbf{l_d}$ or gel phase. Quantum yield of NBD increases with decreasing polarity of its environment [80]. Nile Red derivative, NR12S, has higher quantum yield in the $\mathbf{l_d}$ phase than the $\mathbf{s_o}$ phase [81].

Photoselection can also diminish emission. The emission intensity from fluorophores affected by photoselection is dependent on the excitation light polarization direction. Examples of probes affected by photoselection include terrylene, perylene, and naphthopyrene. These are all PAH. The absorption and emission dipole moments of all three of these probes point roughly along the longest axis of the dye molecule [59]. They emit at the highest intensities in the direction of the excitation light polarization. In equatorial plane images of homogeneous $\mathbf{l_o}$ GUVs with these probes, intensity was high in the direction of the excitation light, and weak in the orthogonal direction [59, fig. 7]. In contrast, in $\mathbf{l_d}$ GUV, emission from these probes is homogeneous and independent of the excitation light polarization. This is because in the $\mathbf{l_d}$ phase, the probes have more freedom to wobble, i.e., they are not confined to a particular orientation in space.

Fluorescent probes alter membrane structure

G_{M1} has been used as a $\mathbf{l_o}$ phase marker. G_{M1} specifically binds to cholera toxin B (CTB). G_{M1} is usually visualized by fluorescence techniques by using a fluorescent labelled CTB. Using AFM and near-field scanning optical microscope (NSOM), Coban et al. [82] found unlabeled G_{M1} localized in Sm-chol domains of 1:1:1 DOPC/Sm/chol monolayers whereas chain-labelled Bodipy-G_{M1} was located predominantly in the fluid DOPC phase. Coban et al. demonstrated that small amounts of both native and labeled G_{M1} (0.4 and 4%) dramatically changed domain morphology and size in DOPC/DPPC and DPPC/DOPC/-chol monolayers.

Bouvrais et al. [72] found that the membrane bending elasticity of pure POPC membranes was affected by the inclusion of fluorescent probes. In particular, the addition of 2% Bodipy-PC increased the bending modulus[4] k_c of pure POPC membranes by 15%, and 2% Rh-DPPE and NBD-PC had similar effects. In comparison, 2% Laurdan led to an 8% decrease in k_c. They attributed all the probe-induced changes to photo-induced peroxide formation resulting from the light of their microscope (more details in Ch. 5).

A number of probes have been shown to alter membrane structure. Work in the Thewalt lab showed that 0.1-0.5% DiIC12 modified the molecular order of the DPPC lipid chains in 35:35:30 DOPC/DPPC-D62/chol membranes: the $\mathbf{l_d}$ phase was more disordered and the $\mathbf{l_o}$ phase was more ordered [70].

Photoperoxidation

Photoperoxidation refers to the oxidative degradation of lipids in the presence of molecular oxygen, light, and a sensitizing agent. Photoperoxidation is known to alter the structures of cell and artificial membranes [83]. Ayuyan and Cohen [84] proved that photoperoxidation promotes membrane phase separation. They showed that excitation by a regular fluorescence lamp during microscopy of a Rh-DOPE labelled GUV resulted in lipid peroxide formation and that the formation of these peroxides promoted formation and enlargement of optically visible domains. Based on these experiments, we can conclude that fluorescent probes may act as sensitizing agents. Zhao et al. [68] also showed that Bodipy, DiO, DiI, Texas Red 1,2-dihexadecanoyl-sn-glycero-3-phosphoethanolamine, triethylammonium

---

[4] The bending modulus measures how easily a membrane may deform at constant surface area.

salt (TR-DPPE), and naphthopyrene are all capable of supporting the production of light-induced domain separation.[5] Also, the findings of Bouvrais et al. [72] may be interpreted in the context of photoperoxidation induced changes in the membrane.

The evidence these groups used to support their claim that the phase separation was light-induced are as follows. Both Ayuyan and Cohen [84] and Zhao et al. [68] found that the addition of free radical scavenger NPG delayed light-induced domain formation.[6] Zhao et al. [68] and Bouvrais et al. [72] both found that reducing the illumination time, and reducing the amount of dye used was sufficient to reduce the effects of photoperoxidation. Interestingly, Zhao et al. [68] observed that light-induced domains formed 50 times faster in 33/34/33 pSm/POPC/chol doped with 0.8% TR-DPPE than with 0.15% probe; this is inconsistent with the findings of Veatch et al. [67] that suggested 0.2 and 2% TR-DPPE had similar effects on membranes. Zhao et al. [68] reported that after the initial induction of phase separation, the fractional area of the two phases does not change with time. This is consistent with the saturation effect noted by our lab [70], and is also consistent with Veatch et al. [67]: T_{mix} of 35:35:30 DOPC/DPPC-D62/chol membrane was increased substantially by addition of DiIC12, but a higher concentration of DiIC12 (2%) had similar effects as a lower concentration (0.2%) [61, 70].

1.4.2 Trace molecules with important biological functions

My project will not only further our understanding of how fluorescent probes interact with membranes, but also shed light on how minor biological components could affect lipid organization in model and cell membranes. The cell is a crowded place stuffed with thousands of biomolecules [30]. Many of these molecules are only present in minuscule amounts, yet they have important biological functions. Even small changes in lipid compositions or lipid structures can modify model membrane physical properties. Small amounts of biomolecules, such as PIP2, Caveolin-1, and CTB, have been shown to perturb model membranes [85–87].

---

[5] Their studies were conducted on DSPC/DOPC/chol, DSPC/POPC,chol, and Sm/POPC/chol made with Sm of various types.

[6] Zhao et al. [68] found that the amount of NPG needed would perturb the phase behaviour, however. This is why the addition of free radical scavenger is not the best way to prevent photoperoxidation in membrane studies.

Actin formation increases T_{mix}

Phosphatidylinositol 4,5 bisphosphate (PIP2) is an important lipid second messenger with many different functions such as attaching the cytoskeleton to the plasma membrane, exocytosis, endocytosis, membrane trafficking, and the activation of various enzymes even though it accounts for less than 1% of phospholipids in cell membranes [2]. The formation of dendritic actin networks is controlled through a complex cascade of chemical interactions. The branching complex Arp2/3 is responsible for formation of dendritic actin networks. The transient binding of actin nucleation promoting factor neural Wiscott-Aldrich syndrome protein (N-WASP) by PIP2 and GTP-bound Cdc42 controls activation of Arp2/3. Liu and Fletcher [85] found that actin network formation can induce de novo membrane domain formation, and can spatially bias the development of liquid disordered domains in model membranes. The formation of such a network with as little as 0.6% PIP2 can increase T_{mix} by 4°C, stabilizing existing membrane domains. Replacing PIP2 with 0.6% fluorescent labelled tetramethyl rhodamine PIP2 (TMR-PIP2) increased T_{mix} by 7°C.

Insoluble caveolin-1 fragments decrease T_{mix}

The caveolin-1 protein plays a structural role in caveolae formation. It is enriched in caveolae, a special type of lipid raft involved in cell signalling and lipid metabolism. In cells, caveolin-1 binds cholesterol and associates with sphingomyelin. Horton et al. [86] studied the caveolin scaffolding domain (CAV-CSD) by truncating it and attaching a fluorescent probe that either makes the peptide fragment water-soluble (CAV-SOL) or water-insoluble (CAV-INSOL). One percent of a fluorescent water insoluble caveolin-1 fragment is found to depress T_{mix} of membranes composed of equimolar DOPC and bSm, and 20 to 35% chol [86].

Cholera toxin B-G_{M1} binding induces phase separation

Cholera patients suffer from diarrhea. They can excrete a liter or more of fluid every hour [88]. The bacteria *Vibrio cholerae* responsible for the illness adhere tightly to the gut epithelium, and secrete cholera enterotoxin or cholera toxin, which is a lipopolysaccharide [89, chapter 2]. The A subunit of cholera toxin is responsible for the diarrhea. The B subunit of cholera toxin (CTB) aids the A subunit's infiltration of the cell by binding to G_{M1}, which is present throughout the host cell surface and concentrated into raft-like domains. One CTB can bind 5 G_{M1} molecules.[7] Binding of CTB and G_{M1} induced phase separation in DOPC:Sm:chol:G_{M1} membranes even when there was only 0.2% G_{M1} present. Phase separation was observed regardless of the initial phase state of the membrane prior to binding [87]. Phase separation was observed with dual labelled GUV dyed with two of perylene, recombinant CTB conjugated with Alexa Fluor 488 (A488-CTB), and DiIC12.

Natural sphingomyelin does not behave as its major constituent

Sphingomyelin (Sm) is one of the major class of lipids in cellular plasma membrane, and is one of the major components of lipid rafts. Natural Sm have complex compositions. The chain length and degree of saturation of the contents depend on the source of the Sm. For example, chicken egg sphingomyelin (eSm) is highly enriched in long-chain saturated fatty acids (80% palmitoyl (16:0)[8]). The main component of bovine brain sphingomyelin (bSm) is C18 Sm (about 50%), and bovine milk Sm are almost an even mix of chain lengths (16, 22, 23, and 24 carbons) [91]. T_{mix} in vesicles containing natural Sm extracts are different than would be predicted based on either chain melting temperature of its major constituent or bulk transition temperature of lipid extract. For example, 50% of bSm is 18:0 Sm. The melting temperature of bSm is 35°C [92], 18:0 Sm is 45°C [93], and DSPC, a PC with two 18:0 chains, is 55°C [94]. Slight changes in Sm composition resulting in large changes in melting temperature may indicate significant contributions from the minor components on overall membrane phase behaviour [61].

Membrane softness altered by small amount of cholesterol

Cholesterol is ubiquitous in eukaryotes and is a major player in the lipid raft hypothesis. Lemmich et al. [95] observed systematic freezing-point depression of DMPC-D54 melting transition temperature (T_m) and broadening of the specific-heat peak with the addition of 0.5-4% chol using DSC. Small-angle neutron scattering experiments also showed the addition of up to 3% cholesterol softened bilayers [95].

---

[7] In Hammond et al. [87] and Putzel and Schick [90], CTB-G_{M1} binding is referred to as “cross-linking”. This binding or “cross-linking” is more accurately described as clustering since no covalent bonds are formed between the molecules.

[8] A palmitoyl chain (16:0) has 16 carbons and no double bonds.

Small variations in chain length change membrane bending elasticity and main transition temperature

The T_m of homologous saturated phosphatidylcholines with similar chain lengths are quite different (Table 1.1) [96]. The bending moduli of bilayers of these lipids are also quite different [96]. Small variations in chain length can induce larger effects on bending elasticity than the addition of 2% probe discussed earlier in Sec. 1.4.1 [72].

Table 1.1: Main transition temperature (T_m) and bending moduli (k_c) of homologous saturated phosphatidylcholines at $T \geq T_m + 16°C$ for DLPC and DMPC, and at $T \geq T_m + 6°C$ for DPPC. For all three lipids, k_c is almost constant above $T \geq T_m + 6°C$. Data from [96].

Lipid	Chain Lengths	T_m (°C)	Bending Modulus ($\times 10^{-19}$J)
DLPC	(12:0, 12:0)	2.1	0.92 ± 0.05
DMPC	(14:0, 14:0)	23.9	1.27 ± 0.09
DPPC	(16:0, 16:0)	41.4	1.50 ± 0.09

1.5 Why study Laurdan and naphthopyrene?

Some probes preferentially incorporate into one lipid phase over another. This property has been employed to visualize phase separation in GUVs by confocal and epi- fluorescence microscopy. Most of these probes prefer[9] the $\mathbf{l_d}$ phase of most lipid membranes, and very few prefer the $\mathbf{l_o}$ phase because more disordered environments can more easily accommodate probes of various chemical structures.

Our previous work [70] showed that adding minuscule amounts of the probe DiIC12, but not DiOC18, significantly affected membrane physical properties. Both of these are carbocyanine probes and are similar in structure. DiIC12 partitioned favourably into the $\mathbf{l_d}$ phase, but not the $\mathbf{l_o}$ phase in 35:35:30 DOPC/DPPC-D62/chol GUV. In comparison, DiOC18 showed a very weak preference for the $\mathbf{l_o}$ phase. Uneven partitioning leads to increased local probe concentration. Even though bulk probe concentration is low, local probe density can be high, and this can perturb the membrane [70]. We hypothesized that the partitioning properties of probes determined their effect on membranes. In particular, non-equal partitioning probes alter membrane phase behaviour, and equipartitioning ones

---

[9] Note that "prefer" here is used in the sense explained earlier in Sec. 1.4.1.

do not. This thesis sets out to test this hypothesis by testing an equipartitioning probe, Laurdan, and a $\mathbf{l_o}$-preferring probe, naphthopyrene.

Chapter 2

Fluorescence and ^{2}H NMR: theoretical background and materials

The addition of a fluorescent molecule or moiety allows us to use a number of fluorescence techniques to study biomolecules. The rotational correlation times of biomolecules are comparable to typical fluorescence lifetimes (1-10 ns). This project examines what happens to ternary model membranes exhibiting $\mathbf{l_d{+}l_o}$ phase coexistence when fluorescent probes are added. This chapter describes the fundamental principles behind fluorescence and deuterium nuclear magnetic resonance spectroscopy (^{2}H NMR), and their uses in lipid studies. After a brief introduction to fluorescence and two-photon excitation microscopy (Sec. 2.1), the two probes of interest, Laurdan and naphthopyrene, will be introduced (Secs. 2.2-2.3). ^{2}H NMR was chosen for this study because it does not require the use of fluorescent probes. ^{2}H NMR will follow in Sec. 2.4. In order to do ^{2}H NMR, we must deuterate at least one of the lipids. We chose to use the relatively well-studied 35:35:30 DOPC/DPPC-D62/chol membrane system in our study (Sec. 2.5).

2.1 Fluorescence

This section presents the general principle of fluorescence and its relevance in lipid studies. Pedagogic coverage of fluorescence can be found in a comprehensive textbook by Lakowicz [97]. This thesis deals in particular with Laurdan, two-photon excitation microscopy, and their use in lipid research. Enrico Gratton, Tiziana Parasassi, and Luis Bagatolli have written many review and pedagogic articles about these topics [30, 98, 99]. The results of fluorescence steady-state spectroscopy and microscopy experiments performed are presented in Ch. 4, and discussion of the experimental details and data analysis techniques are deferred until Sec. 4.1 and Appendices B and C.

2.1.1 Why use fluorescence in lipid membrane phase studies?

There are many reasons why fluorescence is widely used in molecular biology and biophysics: (1) It is a very sensitive technique. Only a few fluorophore molecules are needed for detection because the fluorescence process has a very short turnover time, and each fluorophore is capable of fluorescing numerous times. (2) Fluorescence is a mature technique with numerous probes available commercially. (3) Fluorescence spectra are sensitive to the environment of the probe. Fluorescence can be used to measure properties such as solvent polarity, pH, viscosity, ion concentrations, and temperature. This information can be used to differentiate various lipid membrane phases. (4) Fluorescence can be used in both simple and complex mixtures, including biological membranes. (5) Fluorescence can be combined with microscopy to provide spatial information that bulk techniques, such as ^{2}H NMR and differential scanning calorimetry (DSC), cannot.

While many proteins are auto-fluorescent to some extent because of the presence of amino acids such as tryptophan, lipids are not naturally fluorescent. Extrinsic fluorophores are needed for membrane studies. They are available commercially and are an active area of research and development. An ideal lipid probe should be stable under continuous illumination, has high quantum yield, and does not perturb the system it is used to study. It should also have low solubility and low emission intensity in water. Low solubility and low emission intensity in water ensures that all fluorescent signal coming from the probe is coming from the fraction of probe embedded in the membrane.

Figure 1.2 shows the structures of some lipid probes. Some of them are lipid analogues: fluorescent moieties (e.g., NBD, Lissamine Rhodamine, Texas Red, Texas Red caproyl) are attached to either the headgroups of lipids such as DOPE or DPPE, or to the hydrocarbon chains (e.g., Bodipy ceramide and Bodipy Sm). Others are fluorescent cholesterol derivatives (e.g., NBD-chol). Carbocyanine dyes (e.g., DiI and DiO), and fluorescent polycyclic aromatic hydrocarbons (PAH) (e.g., perylene, terrylene, naphthopyrene, DPH, rubicene) are also suitable for use in lipid studies because the hydrophobic hydrocarbon regions of these dyes embed them into the interior of the membrane. In fact, probes are sensitive to the subtle differences between membrane phases: some probes will choose one micro-environment over another in a heterogeneous membrane. This can be used to provide contrast between different membrane phases in microscopy experiments.

Probes that do not partition differently into different membrane phases can still be used to probe membrane phase states if their fluorescence properties are sensitive to the environment they are in. Probe properties such as fluorescence lifetime, steady-state anisotropy, and rotational diffusion time can be altered by the probe's environment, and can be used to semi-quantitatively determine the relative amounts of various membrane phases present [100]. Polarization of the probe gives rise to fluorescence anisotropy that can be a measure of viscosity of the probe's environment. The emission spectra of Dansyl, Prodan and Laurdan are shifted to longer wavelengths (red-shifted) when they are in more polar environments. The emission spectra of fluorescein and coumarin derivatized analogues are highly pH sensitive [101]. Concentration-dependent self-quenching properties of a probe can be used to infer the presence of coexisting phases [79]. Probes are sensitive to properties that differ between the various membrane phases and can help identify the role of membrane heterogeneity in biological processes.

2.1.2 Principles of fluorescence

A fluorophore has multiple electronic states, each of which is split into a number of vibrational and rotational energy levels. Fluorescence involves transitions between the electronic states. Figure 2.1 shows, in a very simplified form, the three main steps of fluorescence:

1. **Excitation** – A fluorophore absorbs a photon and is excited from the ground state (S_0) to one of the vibrational modes of a higher electronic state (S_1'). In a bulk sample, all energetically accessible vibrational modes of the electronic state can be populated. The photon is supplied by an external source, such as a laser. The time scale for light absorption is on the order of 10^{-15} s.

2. **Relaxation** – The fluorophore typically remains in the excited electronic state for 10^{-9}-10^{-8} s. The fluorophore can transition between vibrational modes of the same electronic state by undergoing conformational changes and/or interacting with the

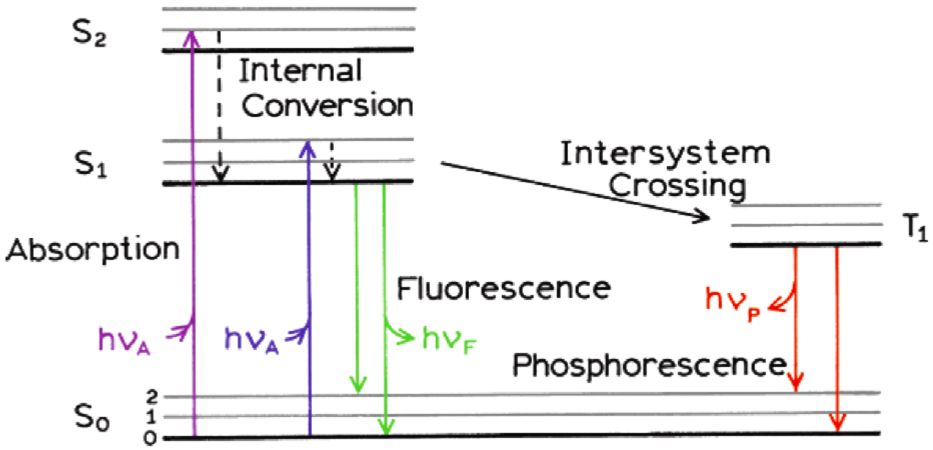

Figure 2.1: The three stages of fluorescence: (1) excitation, (2) relaxation, and (3) emission. The molecule absorbs a photon of energy $h\nu_A$ from an external source, such as a laser. It later emits a photon of energy $h\nu_F$. Principles of fluorescence spectroscopy by Lakowicz, Joseph R. [97]. Reproduced with permission of Springer-Verlag New York Inc in the format Thesis/Dissertation via Copyright Clearance Center.

environment. These transitions occur in about 10^{-12} s and tend to leave the fluorophore in the lowest energy vibrational mode (S_1).

3. **Emission** – The fluorophore returns from S_1 to S_0 by emitting a photon of energy $h\nu_F$. The fluorescence emission spectrum is generally independent of the excitation wavelength. This is known as Kasha's rule [97].

Fluorescence measurements involve exciting fluorescent molecules or moieties with light of an appropriate energy and measuring the light emitted by the fluorophore thereafter. Absorption of a photon and excitation take place effectively instantaneously on the molecular time scales. In comparison, the time between excitation and emission is very long. During this time, the fluorophore can interact with neighbouring molecules, and these interactions can alter the energy state of the fluorophore.

Collisions with other molecules (collisional quenching) and formation of non-fluorescent complexes with quencher molecules (static quenching[1]) can decrease the fluorescence intensity. Quantum yield is the ratio of the number of photons emitted to those absorbed.

---

[1] Mechanisms of static quenching include electron transfer, spin-orbit coupling, and inter-system crossing to the triplet state. In the triplet state, the excited electron has the same spin as the ground state electron since it is not paired to the ground state electron.

Quantum yield is close to unity if the non-radiative decay rate is much smaller than the radiative decay rate. Non-radiative decay occurs when the excess electronic energy is converted to excess vibrational or rotational energy, which is then transferred to the surrounding medium (internal conversion), or transferred to a quencher molecule that transiently collides with or forms a complex with the excited-state molecule. Non-radiative decay also occurs if the fluorophore goes from the singlet state to the triplet state (inter-system crossing) although this mechanism is relatively rare. Fluorescence emission is a random process; the time each molecule spends in the excited state can vary. Fluorescence lifetime is defined as the average time the fluorophore spends in the excited state before returning to the ground state. Intrinsic or natural lifetime refers to the lifetime of the fluorophore in the absence of non-radiative processes.

In general, solvent polarity and local environment affect the emission spectral properties. Fluorescence spectra are shifted to longer wavelengths (red shifted) with increasing solvent polarity. In membranes, the higher density of lipid packing in more ordered phases causes greater exclusion of polar molecules from the membrane interior than in more disordered phases. Polarity sensitive probes can be used to determine membrane phases.

Transition dipole moment

The transition dipole moment

$$\vec{\mu}_{ij} = \langle i | e\hat{r} | j \rangle \tag{2.1}$$

describes a transition between energy states $|i\rangle$ and $|j\rangle$ of a molecule. If $|i\rangle$ and $|j\rangle$ are the same state, then Eq. 2.1 represents the permanent dipole moment. The Stark effect is observed if the permanent dipole moment is non-zero, as well as being different between the ground and excited states: a dipole moment is induced by and is proportional to an applied electric field. This occurs in Laurdan.

Anisotropy

Fluorophores absorb photons whose electric field vectors are parallel to their absorption transition dipole. Similarly, photons are preferentially emitted according to the fluorophore's emission transition dipole.[2] Consequently, the emitted light is polarized along

---

[2] The absorption and emission transition moments typically lie in different directions.

a fixed axis in the fluorophore. The extent of the emission polarization is described by anisotropy

$$r = \frac{I_{\|} - I_{\perp}}{I_{\|} + 2I_{\perp}} \tag{2.2}$$

where $I_{\|}$ and $I_{\perp}$ are the emission intensities if emission polarizers were applied parallel and perpendicular to the direction of polarization of the excitation light. Anisotropy arises because all fluorophores have transition moments for absorption and emission that lie along a specific direction within the fluorophore.

While the fluorophore is in the excited state, rotational diffusion can displace the emission dipole of the fluorophore, thus reducing the anisotropy. Anisotropies are related to the angular displacement of a fluorophore between the time of absorption and emission and are decreased with higher rotational rates. Rotational diffusion is affected by viscosity of the solvent, and the size and shape of the fluorophore. The rotational rates of fluorophores in cell and model membranes are such that the anisotropy values are sensitive to membrane composition. Rotational correlation times for most proteins are also comparable to typical fluorescence lifetimes. This is why fluorescence anisotropy measurements are widely used in biochemistry and biophysics.

Photoselection

The probability of absorption is proportional to $\cos^2\theta$, where θ is the angle between the absorption transition moment of the probe and the polarization of the excitation light. Excitation with polarized light results in a population of excited fluorophores that are preferentially oriented along the direction of polarization. This is the photoselection effect. In the case of two-photon excitation, since there are two photons involved, the excitation efficiency is proportional to $\cos^4\theta$ [99]. Emission is strongly dependent on the alignment of the absorption transition moment and light polarization [102].

Resonance energy transfer

Förster resonance energy transfer (RET) can occur if the emission spectrum of a fluorophore (donor) overlaps the absorption spectrum of another molecule (acceptor). This process is caused by the coupling of the donor and acceptor via a dipole-dipole interaction.[3]

---

[3] This is not the same as the acceptor absorbing the donor's emission.

The extent of energy transfer is determined by the spectral overlap (which determines the Förster distance) and the physical distance between donor and acceptor. Förster distances are typically 1.5 to 6 nm, comparable to membrane thicknesses.

2.1.3 Two-photon excitation microscopy

Two-photon excitation microscopy is used for imaging Laurdan-doped giant unilamellar vesicles (GUVs) in this thesis. In two-photon excitation microscopy, two photons are absorbed simultaneously by the fluorophore. The sum of the photon energies must be the same as the energy required for one-photon excitation. Each of the photons must have roughly half the energy required for one-photon excitation, i.e., in the near-IR range (wavelength of 700-1,100 nm). In comparison, lasers for confocal microscopy are typically in the UV-Vis range.

With two-photon excitation, the excitation is restricted to the focal volume (1 μm^3). The two photons have to be localized to the same space at the same time (within 10^{-18} s) in order for absorption to occur. Two-photon excitation requires very high photon flux (10^{20}-10^{30} photons/cm^2/s). Excitation does not occur outside the focal volume since the photon flux is too low to cause two-photon excitation, and the photons do not have enough energy individually for excitation. Since the photons have to be absorbed simultaneously, the process depends quadratically on laser light intensity (see Sec. 2.1.4).

Photodamage of the sample and photobleaching of probes outside the focal volume is minimized compared to confocal microscopy since the photons outside the focal volume have very low energy. The longer wavelength used in two-photon excitation is scattered less strongly by most materials. Two-photon excitation, with the advantage of reduced scatter and reduced exposure of laser light to out-of-focus regions can help minimize imaging artifacts resulting from photoperoxidation [33].

The disadvantages of two-photon microscopy include the high cost of ultrafast lasers, and increased photobleaching rate in the focal volume. Femtosecond (10^{-15} s) lasers capable of generating ultra short light pulses ($\sim$ 100 fs) with a repetition rate of $\sim$ 100 MHz (i.e., 1 pulse/10 ns) are required for two-photon excitation since the two-photon excitation process is inherently less efficient than one-photon excitation. Patterson and Piston [103] found photobleaching rates between one- and two-photon excitation are comparable at low excitation laser power levels, since the laser is mostly off during two-photon excitation. Even though photon flux is high during the pulses, the average power is low [104].

2.1.4 Two-photon absorption

Consider the interaction of light and atoms. In two-photon absorption, an atom of the medium makes a transition from its ground state to an excited state by the simultaneous absorption of two photons. Two-photon absorption was first suggested by Göppert-Mayer [105], and is described in various physics textbooks. I will follow the treatment by Laud [106].

Light-matter interaction

The magnitude of the polarization of the material can be expressed as a power series of the applied electric field ($\vec{E}$) strength

$$P(t) = \epsilon_0 \left[\chi^{(1)} E(t) + \chi^{(2)} E^2(t) + \chi^{(3)} E^3(t) + \cdots \right] \tag{2.3}$$

where ϵ_0 is the permittivity of free space, $\chi^{(1)}$ is the linear susceptibility, $\chi^{(2)}$ is the second-order nonlinear optical susceptibility tensor, and $\chi^{(3)}$ is the third-order non-linear optical susceptibility tensor. The linear and nonlinear susceptibility coefficients are determined by the optical properties of the medium.

In linear optics, when the light intensity is low and the oscillations are small enough, the higher-order terms can be ignored. The induced polarization depends linearly on the electric field strength. The refractive index and the absorptivity of the material are independent of the light passing through the medium.

When the excitation source is a laser – a source of intense, coherent light, the applied electric fields are comparable to the interatomic electric fields (10^8 V/m). The dipoles in the medium no longer respond linearly to the alternating electric field of the light beam. Atomic nuclei are too massive and inner electrons are too tightly bound to respond to the excitation, i.e. they are not polarizable. The outer electrons become the only ones responsible for the polarization of the medium caused by the light beam. This is the regime of nonlinear optics where the higher-order terms must be considered. Two-photon absorption is a non-linear optical effect.

The physics of two-photon absorption

This section is a derivation of two-photon absorption using time-dependent perturbation theory. Consider the Hamiltonian

$$\hat{H} = \hat{H}_0 + \hat{H}'(t), \tag{2.4}$$

where $\hat{H}_0$ is the unperturbed time-independent Hamiltonian, and $\hat{H}'(t)$ is a small time-dependent perturbation that is non-zero for between $0 \leq t \leq \tau$. The time-dependent Schrödinger equation,

$$(\hat{H}_0 + \hat{H}'(t))|\psi, t\rangle = i\hbar\frac{\partial}{\partial t}|\psi, t\rangle, \tag{2.5}$$

can be solved using perturbation theory by assuming the solution can be written as a linear combination of the eigenstates $|u_n\rangle$:

$$|\psi, t\rangle = \sum_n C_n(t)\exp(-iE_nt/\hbar)|u_n\rangle \tag{2.6}$$

$$\frac{dC_m(t)}{dt} = \frac{1}{i\hbar}\sum_{n=0}^{\infty} C_n(t)\langle u_m|\hat{H}'(t)|u_n\rangle \exp((-i/\hbar)(E_n - E_m)t). \tag{2.7}$$

Suppose the fluorophore starts in $|u_0\rangle$ at $t = 0$, and

$$C_0(0) = 1 \tag{2.8}$$

$$C_m(0) = 0 \quad \text{for all } m, m > 0. \tag{2.9}$$

Plugging this into Eq. 2.7 and letting $\omega_{mn} = (E_m - E_n)/\hbar$ gives the first-order approximation,

$$\frac{dC_m^{(1)}(t)}{dt} = \frac{1}{i\hbar}\langle u_m|\hat{H}'(t)|u_n\rangle \exp(i\omega_{mn}t) \tag{2.10}$$

and

$$C_m^{(1)}(t) = \frac{1}{i\hbar}\int_0^t \langle u_m|\hat{H}'(t)|u_n\rangle \exp(i\omega_{mn}t')dt' \ , \tag{2.11}$$

which can be used to find the second-order approximation, etc.

In the case of high-intensity light interacting with a fluorophore, the main contribution comes from the dipole interaction. The specific perturbation to the Hamiltonian is

$$\hat{H}'(t) = \sum_j e\vec{r}_j \cdot \ \vec{E}_o \cos(\omega t) \tag{2.12}$$

where e is the charge of the electron, and the first-order terms (Eq. 2.11) become

$$C_m^{(1)}(t) = \frac{eE_o\langle u_m|X|u_n\rangle}{2\hbar} \times \left\{ \frac{1-\exp(i(\omega_{mn}+\omega)t)}{\omega_{mn}+\omega} + \frac{1-\exp(i(\omega_{mn}-\omega)t)}{\omega_{mn}-\omega} \right\} \tag{2.13}$$

where X is the position operator. Extending to second-order,

$$\frac{dC_l^{(2)}(t)}{dt} = \frac{1}{i\hbar}\sum_m C_m^{(1)}(t)\langle u_l|\hat{H}'(t)|u_m\rangle \exp(-i\omega_{lm}t) \tag{2.14}$$

$$\begin{aligned} &= \frac{1}{i\hbar}\sum_m \frac{eE_o\langle u_m|X|u_n\rangle}{2\hbar} \times \left\{ \frac{1-\exp(i(\omega_{mn}+\omega)t)}{\omega_{mn}+\omega} + \frac{1-\exp(i(\omega_{mn}-\omega)t)}{\omega_{mn}-\omega} \right\} \\ &\times \langle u_l|\hat{H}'(t)|u_m\rangle \exp(i\omega_{lm}t)\ . \end{aligned} \tag{2.15}$$

Since

$$\langle u_l|\hat{H}'(t)|u_m\rangle = \langle u_l|\sum_j e\vec{r}_j \cdot \ \vec{E}_o \cos(\omega t)|u_m\rangle \tag{2.16}$$

$$= eE_o\langle u_l|X|u_m\rangle \left\{ \frac{e^{i\omega t}+e^{-i\omega t}}{2} \right\}\ , \tag{2.17}$$

Eq. 2.15 becomes

$$\begin{aligned} \frac{dC_l^{(2)}(t)}{dt} = \frac{1}{i\hbar}\sum_m & \frac{e^2E_o^2\langle u_l|X|u_m\rangle\langle u_m|X|u_n\rangle}{4\hbar} \\ & \times \left\{ \frac{1-\exp(i(\omega_{mn}+\omega)t)}{\omega_{mn}+\omega} + \frac{1-\exp(i(\omega_{mn}-\omega)t)}{\omega_{mn}-\omega} \right\} \\ & \times \{\exp(i(\omega_{lm}+\omega)t) + \exp(i(\omega_{lm}-\omega)t)\}\ . \end{aligned} \tag{2.18}$$

Assume $E_l > E_m > E_n$, then ω_{lm} and ω_{mn} are positive. Keeping only the terms where the driving frequency (ω) is close to the transition frequencies (i.e., ($\omega_{mn} \approx \omega$) and ($\omega_{lm} \approx \omega$)), and ignoring smaller terms, the second-order solution becomes

$$\begin{aligned}
C_l^{(2)}(t) &= \frac{1}{i\hbar}\sum_m \frac{e^2E_o^2\langle u_l|X|u_m\rangle\langle u_m|X|u_n\rangle}{4\hbar} \\
&\times \int_0^t \frac{1-\exp(i(\omega_{mn}-\omega)t')}{\omega_{mn}-\omega}\exp(i(\omega_{lm}-\omega)t')dt' \\
&= \frac{1}{4\hbar^2}\sum_m e^2E_o^2\langle u_l|X|u_m\rangle\langle u_m|X|u_n\rangle \\
&\times \left[\frac{1-\exp(i(\omega_{lm}-\omega)t)}{(\omega_{mn}-\omega)(\omega_{lm}-\omega)} - \frac{1-\exp(i(\omega_{ln}-2\omega)t)}{(\omega_{mn}-\omega)(\omega_{ln}-2\omega)}\right]
\end{aligned} \tag{2.19}$$

where $\omega_{ln} = \omega_{lm} + \omega_{mn}$. The resonance at $\omega_{ln} = 2\omega$ corresponds to the two-photon absorption process. The transition probability between the states n and l

$$|C_l^{(2)}(t)|^2 = \sum_m \frac{e^4E_0^4|\langle u_l|X|u_m\rangle\langle u_m|X|u_n\rangle|^2}{16\hbar^4(\omega_{mn}-\omega)^2} \times \frac{4\sin^2[(\omega_{ln}-2\omega)t/2]}{(\omega_{ln}-2\omega)^2} \tag{2.20}$$

is the probability of the two-photon process occurring. The transition probability is proportional to the square of the intensity.[4]

The rate of two-photon absorption is

$$R = \sum_m \frac{\pi e^4E_0^4|\langle u_l|X|u_m\rangle\langle u_m|X|u_n\rangle|^2}{8\hbar^4(\omega_{mn}-\omega)^2}\delta(\omega_{ln}-2\omega) \tag{2.21}$$

where

$$\delta(\omega_{ln}-2\omega) = \frac{2}{\pi}\lim_{t\to\infty}\frac{\sin^2[(\omega_{ln}-2\omega)t/2]}{(\omega_{ln}-2\omega)^2 t} \tag{2.22}$$

is the Dirac delta function.

Detection

This section follows the derivation by Xu and Webb [107]. The number of photons absorbed per fluorophore per unit time

$$N_a(t) = \int_V dV\sigma_2 C(\vec{r},t)I^2(\vec{r},t) \tag{2.23}$$

---

[4] The intensity is the energy a wave transports per unit time per unit area. The intensity of an electromagnetic wave is $I = \epsilon_0 cE^2$, and the average intensity over an extended period of time is $\langle I\rangle = \epsilon_0 cE_0^2/2$ in vacuum.

where V is the illuminated sample volume, σ_2 is the two-photon absorption cross section, and C is the dye concentration. In the absence of saturation, photobleaching, stimulated emission, and self-quenching, the number of emitted photons collected by the measurement system per unit time is

$$F(t) = \frac{\phi \eta_2 N_a}{2}, \tag{2.24}$$

where ϕ is the fluorescence collection efficiency of the measurement system, and η_2 is the fluorescence quantum efficiency of the dye. The factor of 1/2 comes from the fact that two photons are absorbed in each excitation. In practice, only time-averaged photon flux is measured. By separating out the spatial $S(\vec{r})$ and temporal distribution $I_0(t)$ of the incident light,

$$I(\vec{r}, t) = S(\vec{r}) I_0(t), \tag{2.25}$$

the time-averaged photon flux can be written as

$$\langle F(t) \rangle = \frac{\phi \eta_2 C \sigma_2 \langle I_0^2(t) \rangle \int_V dV S^2(\vec{r})}{2}. \tag{2.26}$$

Most detectors can only give a signal that is proportional to $\langle I_0(t) \rangle$, so we can rewrite the last equation as

$$\langle F(t) \rangle = \frac{g \phi \eta_2 C \sigma_2 \langle I_0(t) \rangle^2 \int_V dV S^2(\vec{r})}{2}, \tag{2.27}$$

where $g = \langle I_0^2(t) \rangle / \langle I_0(t) \rangle^2$ is a measure of the second-order temporal coherence of the excitation source.

Now, consider the spatial part. Numerical aperture is defined as

$$\mathrm{NA} = n \sin \theta, \tag{2.28}$$

where n is the index of refraction of the medium and θ is the half-angle of collection of the lens. The relationship between the instantaneous incident power P and I_0 follows from energy conservation:

$$I_0(t) = \frac{\pi (\mathrm{NA})^2}{\lambda^2} P(t) \ . \tag{2.29}$$

In samples whose thickness is much greater than the focal depth,

$$\int_{V \to \infty} S^2(\vec{r}) dV \approx \frac{8 n \lambda^3}{\pi^3 (\mathrm{NA})^4}. \tag{2.30}$$

In principle, using longer-wavelength light broadens the point-spread function.[5] The intrinsic resolution of two-photon excitation is lower, but in practice two-photon microscopy and one-photon microscopy provide the same spatial resolution [104]. In two-photon excitation microscope, a high numerical aperture objective is used to concentrate light into a diffraction limited focal volume of $1\mu\text{m}^3$.

Next, we consider the temporal part. For a mode-locked laser, the focused intensity is

$$I_0(t) = I_0\left(t + \frac{m}{f}\right) \quad m = 1, 2, 3, ..., \tag{2.31}$$

where f is the pulse repetition rate. The duty cycle is $f\tau$, where τ is the excitation pulse width (FWHM). Define $g_p = gf\tau$ which depends on the shape of the laser pulse and the duty cycle.

With appropriate considerations for the spatial and time dependence of a mode-locked pulse laser,

$$\langle F(t)\rangle \approx \frac{1}{2}\phi\eta_2 C\sigma_2 \frac{g_p}{f\tau}\frac{8n\langle P(t)\rangle^2}{\pi\lambda}. \tag{2.32}$$

Numerical value of g for mode-locked Ti:sapphire laser is approximately 10^5 ($f \approx 100$ MHz and $\tau \approx 100$ fs), which means dyes can be excited with very low average laser power with mode-locked lasers.

Two-photon excitation of an atom depends on the incident radiation frequency, electric field strength, and the binding energy of the atomic electrons. This is true for multi-photon excitation in general. Molecules with high two-photon absorption cross-sections are usually large, highly conjugated hydrophobic compounds, such as Laurdan [108].

---

[5] The point-spread function of an optical device is the image of a single point object.

2.2 Laurdan (6-lauroyl-2-(N,N-dimethylamino)naphthalene)

Laurdan belongs to a family of 2-(dimethylamino)-6-acylnaphthalene dyes first synthesized by Gregorio Weber in 1979. Other members of this family include Acdan (6-acetyl) and Prodan (6-propionyl). Figure 2.2 shows the structure of some of these dyes and their positions when embedded in a lipid membrane. Laurdan's lauric acid tail (12-carbon tail) anchors it into the membrane [ref 19-20 of 109], with the fluorescent naphthalene moiety near phospholipid's glycerol backbone, i.e., near the lipid-water interface. The fluorescent group is about 1 nm from the centre of the bilayer [110]. Laurdan partitions completely out of the aqueous phase in the presence of lipid membranes [111]. Probes in this dye family exhibit high sensitivity to the polarity of their environment. Laurdan is currently the most used 2-(dimethylamino)-6-acylnaphthalene derivative for membrane studies because it satisfies many of the desirable qualities of lipid probes: stability under continued illumination, high quantum yield, low solubility [111] and low emission intensity in water [112]. It is thought that Laurdan minimally perturbs the system being studied. This will be verified in this thesis.

Laurdan's sensitivity to polarity has been used to distinguish between different membrane phase states. In all cases studied in the literature up to now, it partitions almost equally into all membrane phases, so different regions of the membrane can be probed simultaneously. Laurdan's $\mathbf{l_d}$-$\mathbf{l_o}$ partition coefficient (K_p) of 1.24 ± 0.47 [113] makes it particularly useful for observing $\mathbf{l_d}+\mathbf{l_o}$ phase coexistence.[6] Laurdan goes into both the $\mathbf{l_d}$ and the $\mathbf{l_o}$ phase, but the emission properties are different in the two different environments. The steady state and time-resolved emission spectra of Laurdan in $\mathbf{l_d}$ membrane are red shifted approximately 50 nm from that of Laurdan in the $\mathbf{s_o}$ phase (Fig. 2.3).

Laurdan's emission spectra are independent of phospholipid headgroups and linkage types [112], because rotational diffusion of water molecules around the excited state dipole of Laurdan is the main factor in determining Laurdan's spectroscopic properties [109, 114]. Part of Laurdan's excited state energy is used to reorient water dipoles into an energetically favorable orientation. The amount of water penetration is a measure of lipid packing [112].

---

[6] The partition coefficients of Laurdan between coexisting $\mathbf{l_d}$ and $\mathbf{l_o}$ phase was calculated from the partition coefficients between lipid phase and aqueous phase as determined by equilibrium titration. Composition of the $\mathbf{l_o}$ and $\mathbf{l_d}$ large unilamellar vesicles (LUVs) tested were 25:35:40 and 70:25:05 POPC:chicken egg sphingomyelin (eSm):cholesterol (chol), respectively [113].

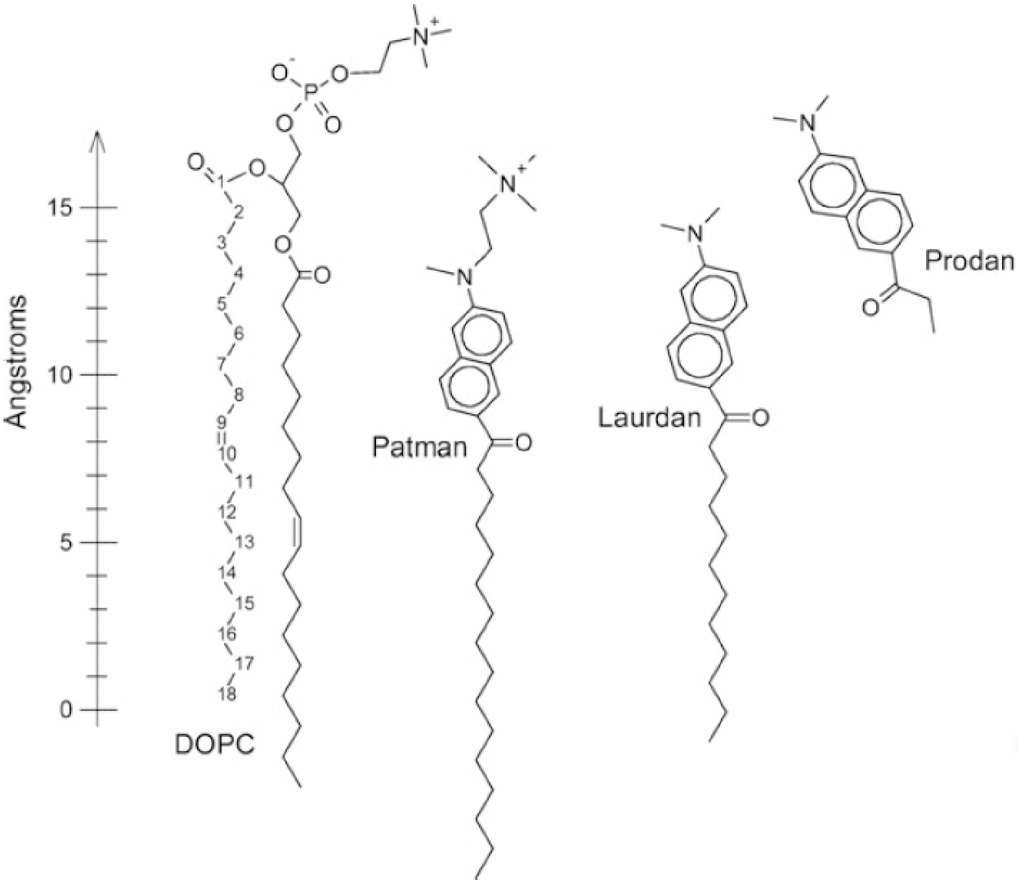

Figure 2.2: Location of naphthalene probes Patman, Laurdan, and Prodan with respect to DOPC in a membrane. The naphthalene moiety is the fused pair of benzene ring. The scale shows approximate distance from the bilayer centre. Reproduced from [99] with kind permission from Springer Science and Business Media.

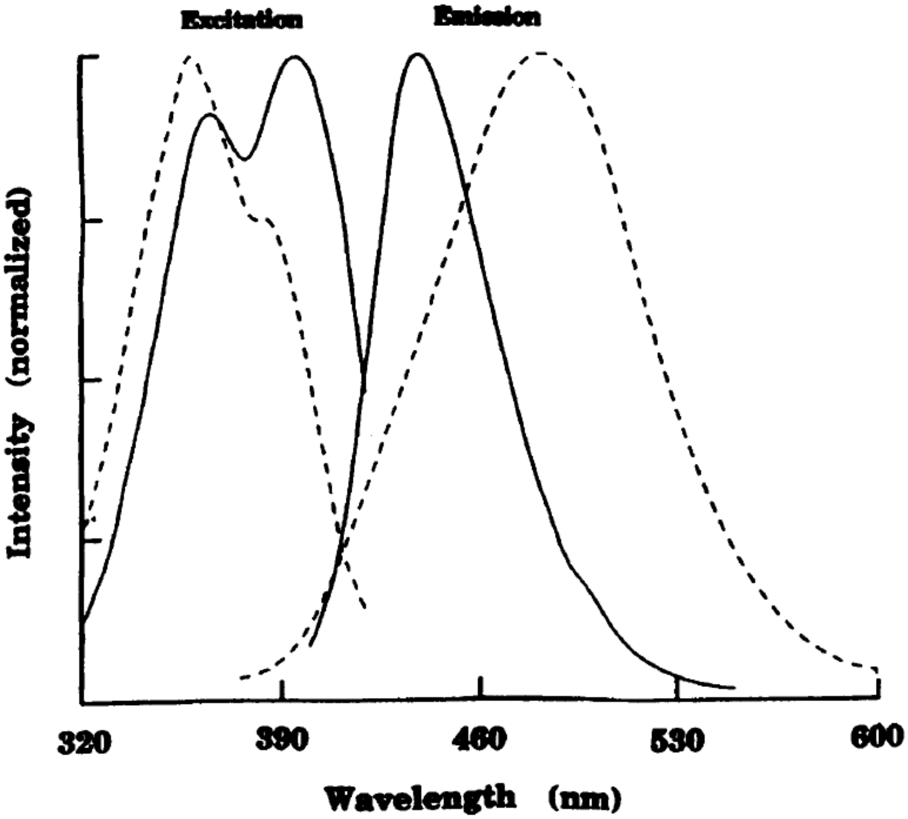

Figure 2.3: Normalized excitation and emission spectra of Laurdan in DPPC MLV at 20°C (solid line) and 60°C (dashed line). Excitation spectra were measured at emission wavelength of 440 nm, and emission spectra were measured at excitation wavelength of 340 nm. Reproduced from [109] with permission from Elsevier.

Water reorientation occurs on the same time scale as Laurdan's fluorescence lifetime in the liquid-crystalline phase (4.3 ns [109]) [115].

2.2.1 Effects of photoselection

Laurdan is susceptible to photoselection effects (Sec. 2.1.2). This effect is not unique to Laurdan (Sec. 1.4.1). Figure 2.4 shows the effects of photoselection on micrographs of gel (20°C) and liquid-crystalline phase (50°C) DPPC membranes. The excitation light used for these micrographs is linearly polarized. Although the membrane is homogeneous at both temperatures, there are regions of higher and lower intensity in the 20°C image.

Consider a gel phase spherical vesicle doped with Laurdan. In gel phase membranes, the high chain order of the lipid membrane restrict Laurdan's orientation, and Laurdan's electronic transition moment is always parallel to the bilayer normal. In the polar regions of the vesicle, Laurdan's electronic transition moment is orthogonal to the polarization of the excitation light, and no excitation occurs [77]. In the equatorial region, Laurdan excitation is maximal along one direction, and minimal along the other direction, as can be seen in the micrograph.

Now consider the liquid-crystalline case. In a fluid phase, Laurdan can wobble around, while keeping its electronic transition moment roughly parallel with the bilayer normal. Excitation in the polar regions is possible in the liquid-crystalline case because Laurdan is free to wobble. For the same reason, the excitation in the equatorial region is less anisotropic than in the gel case.

Linearly polarized light caused optically homogeneous gel phase vesicles to show varying intensity at the equatorial plane [102, fig. 6], but circularly polarized excitation light can circumvent this problem. If the vesicle is excited with circularly polarized light, all molecules in the equatorial region would be excited with the same efficiency.

2.2.2 General polarization (GP)

Figure 2.3 showed the excitation and emission spectra of Laurdan in gel and liquid-crystalline DPPC MLV. The emission spectrum in the gel phase (20°C) is centered around 440 nm and that of the liquid-crystalline phase (60°C) is centered around 490 nm. The emission spectrum of Laurdan in the liquid-crystalline is red-shifted as compared to that of the gel phase. The opposite is true for the excitation spectrum. It is generally the case

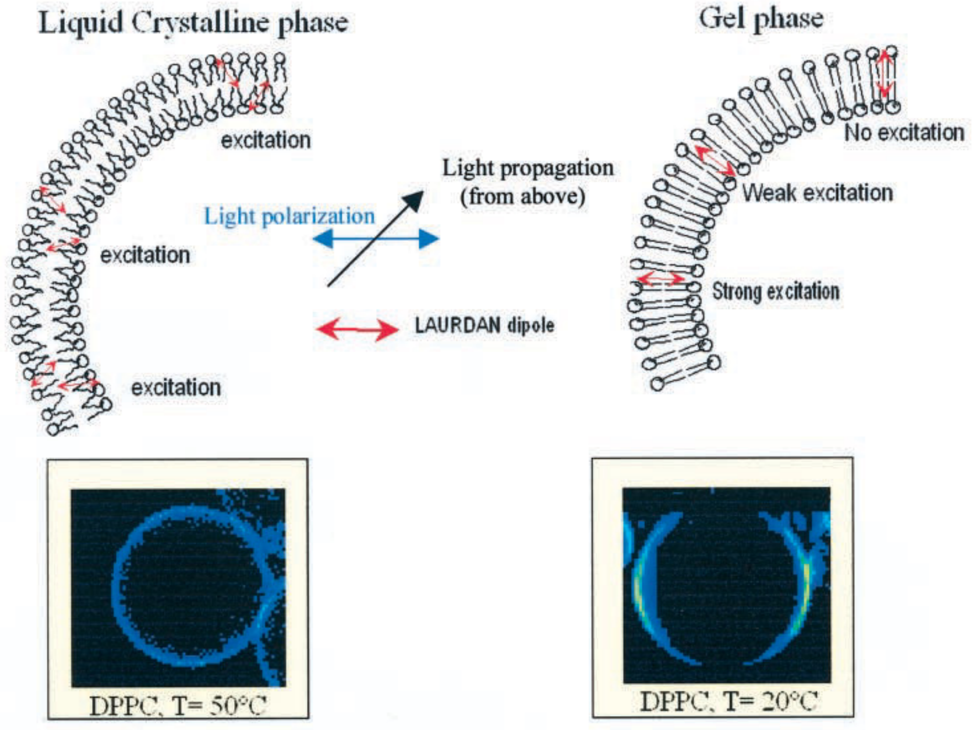

Figure 2.4: Photoselection of Laurdan in the liquid-crystalline and gel phases. Micrographs show gel (20°C) and liquid-crystalline phase (50°C) DPPC. Both vesicles shown are homogeneous, yet there are regions of higher and lower intensity in the 20°C image attributable to the photoselection effect. In the gel phase, the Laurdan dipole is strictly parallel to the bilayer surface normal. Excitation is strongest when these dipoles are parallel to the direction of light polarization (blue arrow). The direction of light propagation is into the page. In the liquid-crystalline phase, Laurdan can wobble, averaging out the photoselection effect observed in gel phase. Adapted from [102] with permission from Elsevier.

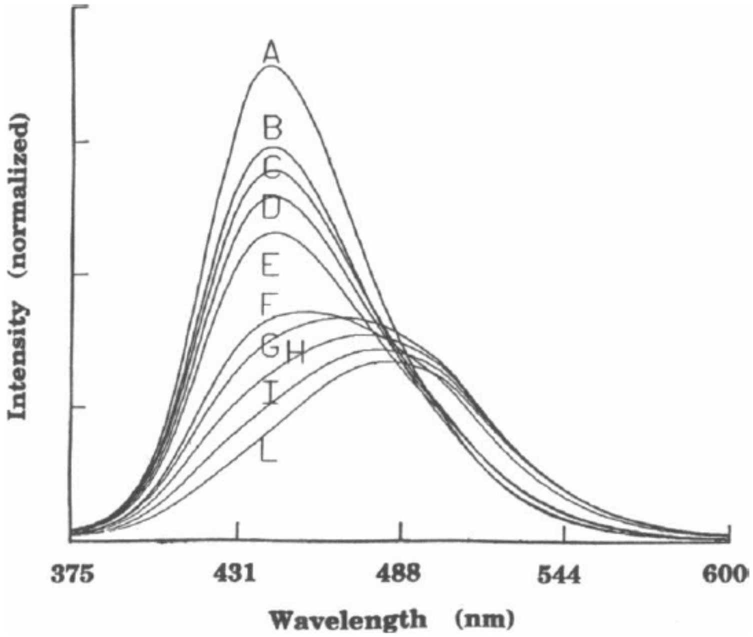

Figure 2.5: Emission spectra of Laurdan in DPPC MLV measured at excitation wavelength of 350 nm at A 30, B 35, C 37, D 38, E 39, F 41, G 42, H 45, I 50, L 60°C. Reproduced from [109] with permission from Elsevier.

that the emission spectrum is a mirror image of the absorption spectrum. The similarity in shapes of the two spectra occurs because the vibrational energy levels of the excited states are similar to those of the ground states [97]. Figure 2.5 shows the emission spectra at intermediate temperatures, illustrating that this shift is gradual and continuous as the membrane becomes increasingly fluid because of increased thermal energy.

Laurdan general polarization (GP) was proposed by Parasassi et al. [116] as an analytical method to quantify the amount of $\mathbf{s_o}$ and $\mathbf{l_d}$ phase in coexistence in model membranes. GP is calculated from measured fluorescence intensities at 440 and 490 nm,

$$\mathrm{GP} = \frac{I_{440} - I_{490}}{I_{440} + I_{490}} \tag{2.33}$$

using a single excitation wavelength. The name comes from the analogy with the definition of fluorescence polarization used in earlier literature:

$$P = \frac{I_{\parallel} - I_{\perp}}{I_{\parallel} + I_{\perp}} \ . \tag{2.34}$$

Polarization and anisotropy measure the same thing, and use of the latter is now more common. Polarization, anisotropy, and GP are all independent of local probe concentration or surface area since they are all intensity ratiometric measurements [112, 115].

The red shift in emission spectrum is caused by dipolar relaxation of Laurdan after excitation. Laurdan GP is influenced by the motion of polar molecules near Laurdan, which is dependent on the viscosity. Recall that anisotropy values depend on the viscosity in the vicinity of the fluorophore. When Laurdan is embedded in the membrane, the polar molecules in question are the few water molecules that have infiltrated the membrane. Water penetration is very dependent on phospholipid packing, and less dependent on lipid lateral motion [117]. Hence, GP is sensitive to phospholipid packing, and lipid chain order [118]. Harris et al. [118] found that the Laurdan spectrum is more sensitive to lipid order than membrane fluidity. Membrane fluidity here refers to the ability of Laurdan sized molecules to diffuse within the membrane. In comparison, Laurdan anisotropy is sensitive to both [118].

Dual-channel microscopy allows GP images to be obtained. Fluorescence intensity images at 440 nm and 490 nm are collected simultaneously, and combined to form a GP image. Interestingly, information from GP images at the equatorial region obtained with linearly polarized light can be used to deduce the size of coexisting lipid domains, even if they are smaller than the resolution of the microscope [119, 120].

2.3 Naphthopyrene

A literature search was done to find a suitable representative $\mathbf{l_o}$ preferring probe. The following is a list of candidate probes that were considered: NBD-DPPE [59, 121], cholesterol derivatives (dehydroergosterol (DHE) [122, 123], Bodipy-chol), carbocyanine (DiIC18, DiIC20, DiIC22) [59], N-Bodipy-ganglioside (G_{M1}) [124], recombinant CTB conjugated with Alexa Fluor 488 (A488-CTB) [87], A488-AA4-GD1b, YFP-GL-GPI, trans-parinaric acid (t-PnA) [5], LcTMADPH [125], and PAH (perylene [78, 87], perylene monoimide [126], terrylene [59], naphthopyrene [59], LcTMADPH). These probes have been reported to partition into the $\mathbf{l_o}$ phase.

The search for an appropriate representative $\mathbf{l_o}$ preferring probe for use in this thesis was particularly challenging. Most commonly used probes prefer partitioning into a more disordered environment, such as the $\mathbf{l_d}$ phase. A more disordered environment can

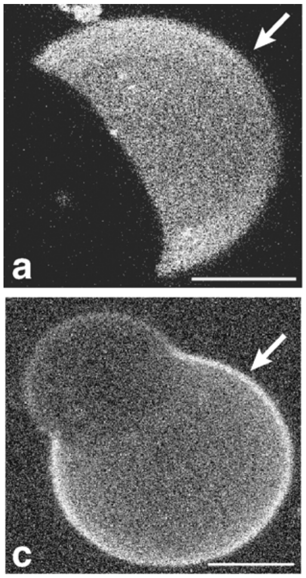

Figure 2.6: Hemispherical projections of confocal images of 50:27:23 DOPC/DSPC/chol GUVs labelled with (a) Rh-DOPE and (c) NBD-DPPE. Scale bar is 5 μm. Adapted from [59] with permission from Elsevier.

more easily accommodate probes of various chemical structures. Many $\mathbf{l_d}$-preferring probes partition almost completely into the $\mathbf{l_d}$ phase. In contrast, most $\mathbf{l_o}$ phase markers only show weak to modest preference for the $\mathbf{l_o}$ phase. For example, Fig. 2.6 shows a vesicle dyed with NBD-DPPE and one with 1,2-dioleoyl-*sn*-glycero-3-phosphatidylethanolamine-N-(Lissamine rhodamine B sulfonyl)(ammonium salt) (Rh-DOPE). The contrast provided by the latter is much greater. NBD-DPPE is a headgroup labelled lipid analogue with saturated acyl chains. It is frequently used as an $\mathbf{l_o}$ phase marker, yet it shows only modest preference for the $\mathbf{l_o}$ phase [28, 59]. Since we were interested in seeing if partitioning of a probe can explain probe-induced changes, it is desirable that the probe partitions strongly into the $\mathbf{l_o}$ phase.

As mentioned in Sec. 1.4.1, some probes show membrane-composition-dependent partitioning behaviour. It is important to choose a probe that shows preference for the $\mathbf{l_o}$ phase in the chosen membranes specifically. Perylene did not show partitioning preference in 27/50/23 bovine brain sphingomyelin (bSm)/DOPC/chol [59].

A number of fluorescent cholesterol derivatives exist; examples include DHE, cholestratienol, and Bodipy-chol. They are often used to replace all or a significant portion of the cholesterol content because they are used as a membrane component and as a probe simultaneously [127, 128]. These cholesterol derivatives would be nearly fully embedded into the hydrophobic region of the membrane. Even small changes in a sterol's tail structure can alter sterol/POPC ordering [129]. The structures of fluorescent cholesterol analogues tend to be quite different from cholesterol. In fact, the properties of DHE are more like ergosterol and desmosterol [127]. These probes would likely completely change the membrane system. Cholesterol derivatives were rejected since one of our goals was to conduct this study in a well-characterized ternary mixture.

A number of labelled-protein raft markers are available, e.g., N-Bodipy-G_{M1} and A488-CTB, but specific protein-lipid interactions can obscure the non-specific probe-lipid interactions of interest to us. Some of these markers requires the use of additional membrane components; e.g., G_{M1} is required for using A488-CTB as a probe. Our aim is to identify non-specific interactions that causes changes to the membrane physical properties. The use of protein-based raft markers would make our results more difficult to interpret.

We decided to use only probes that were commercially available to ensure quality of the fluorescent probes and reproducibility of the experiments. Perylene monoimide and LcTMADPH were eliminated as suitable candidate probes because they were synthesized in individual laboratories. Fluorescence is a burgeoning field, and new probes are being designed and synthesized every day. Given the unique and complex characteristics of each probe (Sec. 1.4.1),we wanted to study well-established probes that have been fully characterized. Another factor that was considered was the availability of probe. Off-the-shelf probes are more readily available.

In the end, naphthopyrene was chosen as the representative $\mathbf{l_o}$ preferring probe for this study. One of the main reasons for choosing naphthopyrene is its robust partitioning preference. Naphthopyrene shows preference for the $\mathbf{l_o}$ phase in a wide variety of model membrane systems, including bSm [59], 1:1 sphingomyelin (Sm)/chol [59], Sm/POPC/chol [68] (a variety of Sm was used), bSm/DOPC/chol [68], eSm/DOPC/chol [59], and GPMV [40, 130]. While change in Sm source – and thus a change in the ratio of long-to-short chain Sm – can alter the partitioning preference of some probes, naphthopyrene partitioning is not affected by Sm composition [68].

Most importantly, naphthopyrene has been shown to prefer the $\mathbf{l_o}$ phase in a ternary membrane very similar to the one in this study: naphthopyrene and Rh-DOPE showed complementary partitioning in 40:40:20 DOPC/DPPC/chol [38]. Rh-DOPE prefers the $\mathbf{l_d}$

phase in a number of lipid mixtures and is typically considered a $\mathbf{l_d}$ probe. The complimentary partitioning would imply that naphthopyrene partitioned into the $\mathbf{l_o}$ phase in these membranes. Juhasz et al. [28] also showed naphthopyrene partitioned into the $\mathbf{l_o}$ phase in 32:48:20 DOPC/DPPC/chol. In this study, the identity of the naphthopyrene-enriched phase was confirmed by dual labelling the membrane with naphthopyrene and TR-DPPE, and by confirming that TR-DPPE was a robust $\mathbf{l_d}$ preferring probe in an earlier paper [131].

The excitation and emission spectra of naphthopyrene are shown in Fig. 2.7. The disadvantages of using naphthopyrene in fluorescence studies are that it is a weak probe, requiring higher concentration, and it photo-bleaches quickly [133]. These disadvantages do not affect results presented in this thesis since only ^{2}H NMR is used to determine whether the presence of naphthopyrene into the $\mathbf{l_o}$ phase alters ternary membrane miscibility. It is important to note that naphthopyrene, like most other $\mathbf{l_o}$ phase makers, shows only a moderate preference for the $\mathbf{l_o}$ phase: e.g., compare the distribution of fluorescence from naphthopyrene with that of Rh-DOPE in Fig. 2.8.

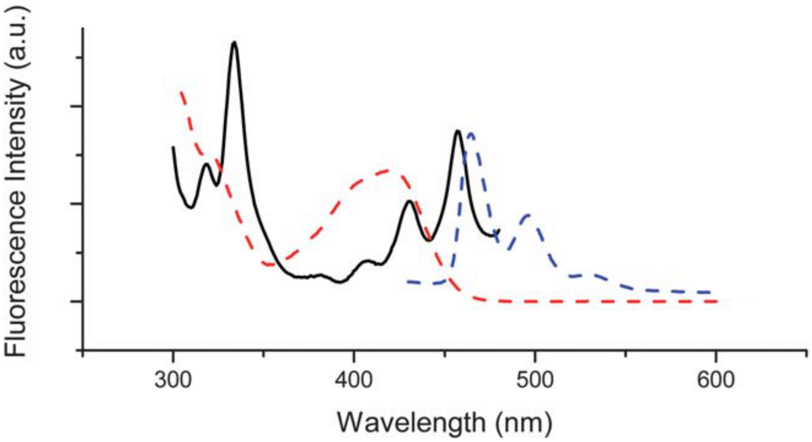

Figure 2.7: Excitation (black, 510 nm emission) and emission (blue, 410 nm excitation) spectra of naphthopyrene solubilized in decanoic acid vesicles with encapsulated $Fe(CN)_6{}^{3-}$. The absorbance spectrum of $Fe(CN)_6{}^{3-}$ is in red [132] - Adapted by permission of The Royal Society of Chemistry.

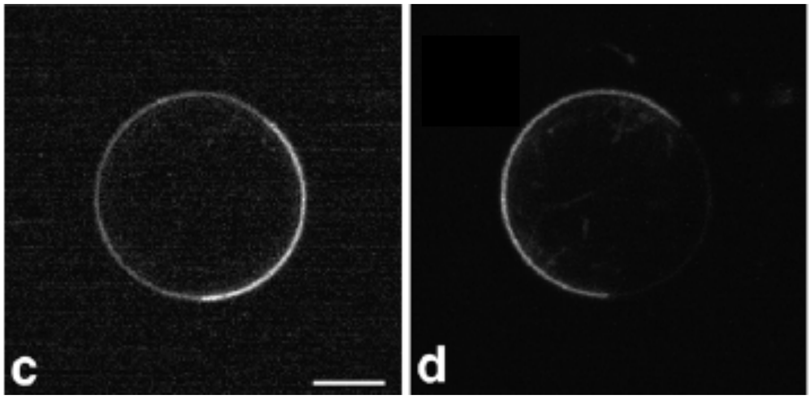

Figure 2.8: Equatorial images of 50:27:23 DOPC/bSm/chol GUVs dual labelled with naphthopyrene (c) and Rh-DOPE (d) obtained by two-photon laser scanning microscopy at an excitation wavelength of $\lambda = 750$ nm. Scale bar is 5 μm. Adapted from [59] with permission from Elsevier.

2.4 Deuterium nuclear magnetic resonance (^{2}H NMR)

Substitution of protons on a lipid with deuterons allows us to use ^{2}H NMR to study lipid membrane phase behaviour because the molecular rotations in the different phases are either slower than, similar to, or faster than the NMR time-scale. More specifically, rotations in liquid-crystalline are faster than, in gel are similar to, and in crystalline are slower than the NMR time-scale. ^{2}H NMR data reflect the environment of the individual molecules averaged over the data collection time.

^{2}H NMR was chosen for this study of probe effects because it requires no extrinsic fluorescent probes. The following treatment of ^{2}H NMR is modified from my masters thesis [134, chapters 3 and 4]. An overview of the advantages of using ^{2}H NMR for studying lipids was given in Sec. 1.1. In Sec. 2.4.1, the specific reasons for its use in lipid phase studies is outlined. The rest of the chapter describes the fundamental principles of ^{2}H NMR. A detailed treatment can be found in a review article by Seelig [48]. Experimental details and the analytical tools used will be deferred until Sec. 3.1 since the results of ^{2}H NMR experiments are presented in Ch. 3.

2.4.1 Why use ^{2}H NMR in lipid membrane phase studies?

^{2}H NMR can be used to identify a variety of lipid membrane phases because the spectral characteristics of the various phases are different (Fig. 2.9). Lipids in the $\mathbf{s_o}$ phase are tightly packed and do not rotate freely. Each deuteron is in a slightly different local environment and the associated spectrum does not have any sharp features. In comparison, liquid crystalline phases' spectra are full of sharp peaks. Lipids in these liquid phases undergo rapid axially symmetric rotations about the director axis on the NMR time scale and diffuse laterally freely. Chains in the $\mathbf{l_d}$ phase are more flexible than those in the $\mathbf{l_o}$ phase. The two phases share similar spectral shapes, but $\mathbf{l_d}$ spectra are approximately half as wide as $\mathbf{l_o}$ spectra. Rotations about the director axis of liquid phase lipids lead to a spectrum that is composed of superimposed Pake doublets – a distinct spectral feature in ^{2}H NMR (see Sec. 2.4.4) – with each pair of equivalent deuterons contributing to one Pake doublet. The frequency separation between the highest points of the Pake doublet is the quadrupolar splitting. Quantitative analysis can be performed on motionally averaged quadrupolar splittings. Only liquid phases are observed in this thesis.

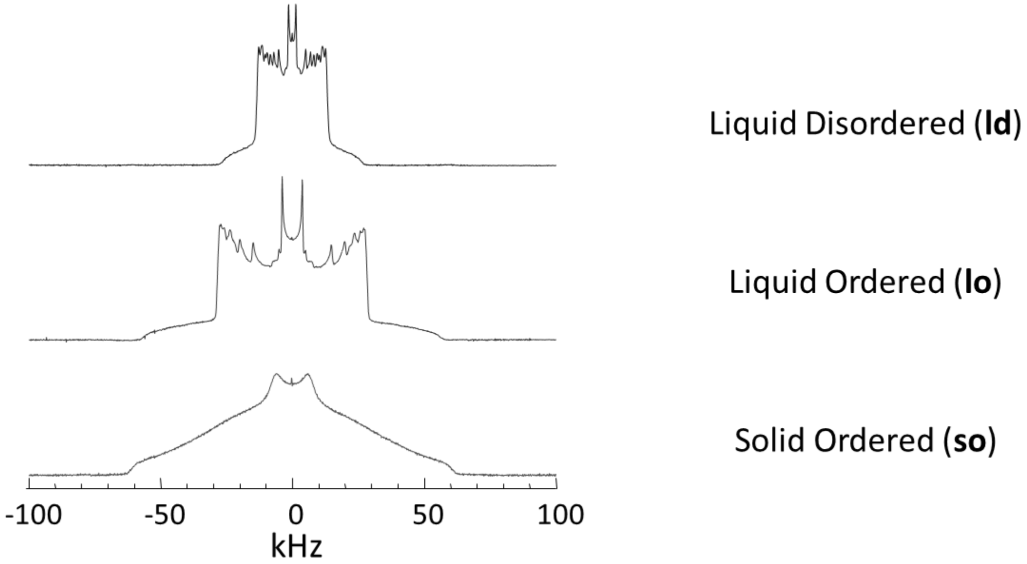

Figure 2.9: ^{2}H NMR spectra of liquid disordered ($\mathbf{l_d}$), liquid ordered ($\mathbf{l_o}$), and solid ordered ($\mathbf{s_o}$ or gel) phases. The $\mathbf{l_d}$ and $\mathbf{l_o}$ spectra are similar in shape, but the $\mathbf{l_o}$ spectrum is wider.

A spectrum is composed of superpositioned Pake doublets with contributions from all deuterons on the lipid. ^{2}H NMR is sensitive to the motion of individual lipid molecules, and the spectrum is a superposition of the signal from all deuterium in the system. The spectrum of a phase-separated membrane is a proportional superposition of the spectra of the individual phases. Such a spectrum can be analyzed quantitatively to give information about the proportion of the phases present.

^{2}H NMR is an established technique for determining lipid membrane phases [48, 135–140]. ^{2}H NMR is well suited to the study of lipid chain behaviour because the observed quadrupolar splitting in the spectrum is directly proportional to the average order parameter, which measures the order of C–D bonds in hydrocarbon chains (see Sec. 2.4.4). An advantage of ^{2}H NMR over some of the other techniques mentioned in Sec. 1.3.2 is that it is non-invasive: no extrinsic probe is required. Fluorescent probes used in fluorescence microscopy and bulky nitroxide spin label groups used in electron spin resonance spectroscopy (ESR) have been shown to cause perturbations in lipid systems and distort phase boundaries [48, 70]. While the deuterons themselves can be viewed as probes, their small size and the fact that they are chemically equivalent to the hydrogen atoms they replace make them a good choice for studying hydrocarbon chains. Moreover, the gyromagnetic ratio of deuterium ($\gamma = 4.11 \times 10^7$ rad/T/s) is much smaller than that of protons ($\gamma = 2.68 \times 10^8$

rad/T/s). In proton NMR, line broadening from dipolar interactions is on the same order of magnitude as the line splitting caused by nearest-neighbour dipolar interaction. In contrast, line-widths resulting from dipolar interactions between deuterons are much smaller than the splitting caused by quadrupolar interactions, allowing individual lines to be resolved in ^{2}H NMR .

^{2}H NMR also has some disadvantages. NMR at temperatures relevant to biology is an insensitive technique because it relies on the population differences between the various spin states (see Sec. 2.4.2). In addition, the natural abundance of deuterium is low (0.015%). Thus, lipid components must be deuterated synthetically. Deuteration at specific positions or on an entire lipid chain are both possible, with the latter being easier to perform chemically. Deuterated lipids are available commercially, but they are costly (e.g., \$742 for 200 mg DPPC-D62 vs. \$50 for 200 mg DPPC), attesting to the difficulty of synthesizing these molecules.[7] Since ^{2}H NMR is a relatively insensitive technique, large quantities of deuterated lipids are required. Furthermore, the assignment of peaks in ^{2}H NMR spectra to the deuterons at a particular carbon position on perdeuterated lipids can be ambiguous if the peaks are not well separated. Selectively deuterated lipids can be used to unambiguously assign peaks, but they are even more difficult to synthesize and their use can significantly increase data acquisition time.

2.4.2 Principles of NMR

A nucleus with spin quantum number I can occupy one of $m = -I, -I+1, ..., I-1, I$ degenerate states, where m is the quantum number for the z-component of the angular momentum I_z. In an external magnetic field $\vec{B_o} = B_o\hat{z}$, the states are no longer degenerate and the energy of a spin in state m is

$$E_m = -\gamma\hbar m B_o \tag{2.35}$$

where γ is the gyromagnetic ratio of the nucleus and $\hbar$ is Planck's constant divided by 2π. The Larmor frequency is defined as $\omega_o = \gamma B_o$. For a collection of such spins, the equilibrium population of state m, N_m, is dictated by Boltzmann statistics and the ratio of population

---

[7] PC can be extracted from natural sources, such as chicken egg yolk [141]. Palacios and Wang [141] reported yields of 10-20% for phospholipid production. Natural PC is about 30% DPPC. Cost of an organic egg is \$0.60 CDN in 2014.

for two states m and m' ($m > m'$) is

$$\frac{N_m}{N_{m'}} = e^{-\Delta E/kT} \tag{2.36}$$

where ΔE is the difference in energy between the two states[8], k is Boltzmann's constant and T is temperature that gives rise to a net macroscopic magnetization along the direction of the external magnetic field. Typically, this population difference is very small, but this small population difference is the basis of NMR.

A radio-frequency pulse at the Larmor frequency applied orthogonal to the external magnetic field (i.e., in the $\hat{z}$ direction) will cause the spins to undergo transitions between the two energy levels separated by an energy of ΔE, thus changing the number of spins in the two states, and resulting in a magnetization orthogonal to the external magnetic field. When the radio-frequency pulse is switched off, the spins will relax back to the equilibrium state, resulting in a time-dependent transverse magnetization orthogonal to the external magnetic field that is detectable by the coil of a NMR spectrometer.[9] This is the basis of NMR signal detection.

2.4.3 Deuterium

Deuterium (D or ^{2}H) is a stable isotope of hydrogen. The nucleus of deuterium contains a proton and a neutron and is known as a deuteron. In contrast, the hydrogen nucleus contains no neutrons. The similarities in size and local chemical environment between a deuteron and a proton make deuterons ideal probes in the study of hydrocarbon chains. Isotope effects are minor and chemical shifts are similar to those obtained using proton NMR (^{1}H NMR). Note that deuterium-depleted water (DDW) has been used as a solvent in this project to ensure that no deuterium signal comes from the water.

^{2}H NMR involves observing interactions between deuterons and their environment. In the experiments described in this thesis, both DPPC chains are perdeuterated – the hydrogen nuclei on the acyl chain are replaced with deuterons. As such, ^{2}H NMR experiments report on the molecular motion of DPPC acyl chains.

---

[8] See Eq. (2.56)-(2.57) for ΔE for ^{2}H NMR.

[9] This results from Faraday's law which states that changing magnetic flux induces a current.

Quadrupolar interactions

There are two parts to the Hamiltonian of the deuteron:

$$\mathcal{H} = \mathcal{H}_M + \mathcal{H}_Q \tag{2.37}$$

where $\mathcal{H}_M$ is the Hamiltonian of the Zeeman interaction and $\mathcal{H}_Q$ is the Hamiltonian of the quadrupolar interaction. The Zeeman interaction is between the nuclear magnetic dipole moment $\vec{\mu} = \gamma\hbar\vec{I}$ and the external magnetic field $\vec{B_o} = B_o\hat{z}$:

$$\mathcal{H}_M = -\vec{\mu}\cdot\vec{B_o} = -\gamma\hbar I_z B_o. \tag{2.38}$$

Deuterons have nuclear spin 1 ($I = 1$) and therefore their quantum number m or I_z can take on values of -1,0, or 1. In an external magnetic field, there are therefore three energy levels attributable to Zeeman interactions. This Hamiltonian gives rise to the energies described by (2.35).

Charge distributions outside the nucleus can cause an electric field gradient at the deuterium nucleus. The nuclear charge distribution of the deuteron is non-spherically symmetric; this gives rise to an electric quadrupole moment. The quadrupolar interactions are between the electric quadrupole moment and the electric field gradient. Dipolar interactions are negligible in this case. Quadrupolar interactions cause the three Zeeman energy levels to be shifted.

The quadrupolar interaction is between the nuclear quadrupolar moment and the electric field gradient at the nucleus generated by nearby charges. The quadrupole tensor is defined as

$$Q_{\alpha\beta} = \int (3x'_\alpha x'_\beta - \delta_{\alpha\beta}r'^2)\rho(\vec{x'})d\tau' \tag{2.39}$$

where $\rho(\vec{x'})$ is the charge density, τ' is the volume of the nucleus, and $\alpha, \beta = x, y, z$. The quadrupolar moment Q is equal to Q_{zz}. For deuterons, $Q = 2.875 \times 10^{-31}$ m^2 [48]. The quadrupolar Hamiltonian in its full form is

$$\mathcal{H}_Q = \frac{eQ}{4I(2I-1)}[V_0(3I_z^2 - I^2) + V_{\pm1}(I_\mp I_z + I_z I_\mp) + V_{\pm2}I_\mp^2] \tag{2.40}$$

where e is the elementary charge, $I_{\pm} = I_x \pm iI_y$ are the usual spin raising and lowering operators, and

$$
\begin{aligned}
V_0 &= V_{zz} && (2.41)\\
V_{\pm1} &= V_{xz} \pm iV_{yz} && (2.42)\\
V_{\pm2} &= \frac{1}{2}(V_{xx} - V_{yy} \pm 2iV_{xy}) && (2.43)
\end{aligned}
$$

where $V_{\alpha\beta}$ are the second derivatives of the electrostatic potential V with respect to the appropriate molecular x, y, z axes. The electric field gradient can be expressed in terms of its irreducible tensor components:

$$
\begin{aligned}
V^{(2,0)} &= V_{zz} && (2.44)\\
V^{(2,\pm1)} &= \pm\sqrt{\frac{2}{3}}(V_{xz} \pm iV_{yz}) && (2.45)\\
V^{(2,\pm2)} &= \sqrt{\frac{1}{6}}(V_{xx} - V_{yy} \pm 2iV_{xy}). && (2.46)
\end{aligned}
$$

The electrostatic field gradient is a symmetric and traceless tensor and can be transformed into the principal coordinate system in which it takes the form

$$
V_p = \begin{pmatrix} V_{xx} & 0 & 0 \\ 0 & V_{yy} & 0 \\ 0 & 0 & V_{zz} \end{pmatrix} \tag{2.47}
$$

and

$$
V_{xx} + V_{yy} + V_{zz} = 0. \tag{2.48}
$$

Choosing x, y, z such that $|V_{zz}| \geq |V_{xx}| \geq |V_{yy}|$, the largest field gradient and the asymmetry parameter are defined as

$$
\begin{aligned}
eq &= V_{zz} && (2.49)\\
\eta &= \frac{V_{xx} - V_{yy}}{V_{zz}} && (2.50)
\end{aligned}
$$

respectively, and it follows that $0 \leq \eta \leq 1$.

For deuterium, the quadrupolar interaction is much smaller than the Zeeman interaction and the problem can be treated with perturbation theory where $\mathcal{H}_Q$ is considered a small perturbation to $\mathcal{H}_M$. In the high field approximation, $V_0 >> V_{\pm 1}$ and $V_0 >> V_{\pm 2}$. Eq. (2.40) simplifies to

$$\mathcal{H}_Q = \frac{eQ}{4I(2I-1)}[V_0(3I_z^2 - I^2)] \tag{2.51}$$

To first order, the energy levels of the Hamiltonian in Eq. (2.37) are

$$E_m = -\gamma\hbar m B_o + \frac{eQ}{4I(2I-1)} V^{(2,0)}[3m^2 - I(I+1)] \tag{2.52}$$

where $V^{(2,0)}$ is the transformed element of the electric field gradient. Explicit form of $V^{(2,0)}$ is given in Sec. 2.4.4. Explicitly, the three energy levels for deuterium ($I = 1$) are

$$\begin{aligned} E_{+1} &= -\gamma\hbar B_o + \frac{1}{4}eQV^{(2,0)} && (2.53)\\ E_0 &= -\frac{1}{2}eQV^{(2,0)} && (2.54)\\ E_{-1} &= \gamma\hbar B_o + \frac{1}{4}eQV^{(2,0)} && (2.55) \end{aligned}$$

These energies dictate the spin population of each state and the net macroscopic magnetization (Eq. (2.36)).

2.4.4 The physics of solid state ^{2}H NMR spectroscopy

Excitation by RF pulses at appropriate frequencies induces energy transitions between $m = 0$ and $+1$, and -1 and 0.[10] The resonance energies are

$$\begin{aligned} h\nu_+ &= E_{-1} - E_0 = \gamma\hbar B_o + \frac{3}{4}eQV^{(2,0)} && (2.56)\\ h\nu_- &= E_0 - E_{+1} = \gamma\hbar B_o - \frac{3}{4}eQV^{(2,0)} && (2.57) \end{aligned}$$

where $\nu_\pm$ are the frequencies of the lines arising from the quadrupolar interaction in a ^{2}H NMR spectrum. The ^{2}H NMR spectrum is typically plotted as an offset from the deuterium Larmor frequency. The two lines resulting from the two transitions thus appears

---

[10] Certain conditions may lead to transitions between $m = +1$ and -1.

symmetric on either side of zero with a separation frequency of

$$\Delta\nu_Q = \nu_+ - \nu_- = \frac{3}{2}\frac{eQ}{h}V^{(2,0)} \tag{2.58}$$

Since the electric field gradient is defined in terms of the molecular axes and the angular momentum operators are in the laboratory frame, the electric field gradient must be rotated into the laboratory frame by applying the Wigner rotation matrix. It can be found using irreducible tensors that

$$\Delta\nu_Q(\theta, \phi) = \frac{3}{2}\frac{e^2qQ}{h}\left(\frac{3\cos^2\theta - 1}{2} + \frac{1}{2}\eta sin^2\theta \cos 2\phi\right) \tag{2.59}$$

where θ is the azimuthal angle and ϕ is the polar angle. More explicitly, θ is the angle between the external magnetic field and the C–D bond for an oriented sample composed of C–D bonds in a single direction (Fig. 2.10). The term e^2qQ/h is known as the static quadrupolar coupling constant and is 126 kHz for C–D bonds of methylene (CD_2) groups. For C–D bonds, V_{zz} is roughly parallel with the bond direction and $\eta \sim 0$, which makes the second term in Eq. (2.59) negligible.

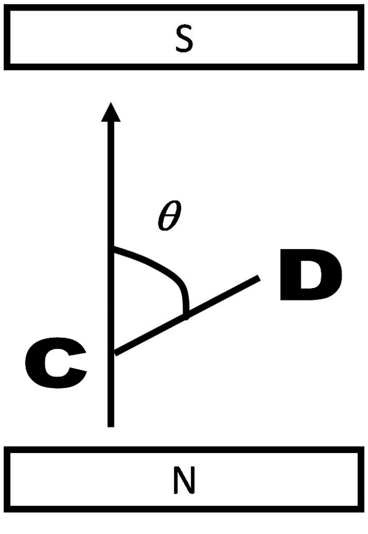

Figure 2.10: Orientational dependence. The angle between the external magnetic field and the C–D bond for an oriented sample is denoted θ in (2.59).

In multilamellar vesicle (MLV), there are random distributions of deuterium nuclear spin orientations. Assuming a uniform distribution of N nuclei over the surface of a sphere of radius r, the surface area density of nuclei is $N/4\pi r^2$. The number of nuclei oriented between θ and $\theta + d\theta$ with respect to $\vec{B_o}$ is

$$dN = \frac{N}{4\pi r^2} 2\pi r^2 \sin\theta d\theta = \frac{N}{2}\sin\theta d\theta \tag{2.60}$$

The probability density is thus

$$p(\theta) = \frac{\sin\theta}{2}. \tag{2.61}$$

It follows that there are more spins oriented at 90° than at any other angle.

A random distribution of spin orientations in a sample will give rise to a "powder spectrum" given by

$$S(\xi_\pm) \propto \frac{1}{\sqrt{2\xi_+ + 1}} + \frac{1}{\sqrt{-2\xi_- + 1}} \tag{2.62}$$

where

$$\xi_\pm = \frac{\nu_\pm - (\gamma\hbar B_o)}{(3/4)(e^2qQ/h)} = \pm\frac{3\cos^2\theta - 1}{2} \tag{2.63}$$

The most intense peaks on the spectrum, known as the Pake doublets, correspond to the singularity at 90° in Eq. (2.62). The separation frequency between the Pake doublet corresponding to this angle is called the quadrupolar splitting and is equal to

$$\Delta\nu_Q = \frac{3}{4}\frac{e^2qQ}{h}. \tag{2.64}$$

In the liquid-crystalline phase, rotations about the director axis of lipids have a period of about 10^{-9} s. Since the NMR time-scale (1/quadrupolar splitting) is on the order of 10^{-6} s, only an average orientation of the C–D bond is detected, narrowing the powder splitting by a factor of S_{CD}. S_{CD} is known as the order parameter and is defined as

$$S_{CD} = \frac{< 3\cos^2\theta_i - 1 >}{2}. \tag{2.65}$$

where θ_i is the angle between the C–D bond on the i-th carbon and the director axis of the lipid and the angular brackets denote time-averaging (Fig. 2.11). It is a measure of the angular excursion of the C–D bond around the director axis. Rotation of an all-trans chain will narrow the spectrum by a factor of 2. Rewriting the separation frequency for lipids in the liquid-crystalline phase, Eq. (2.59) becomes

$$\Delta\nu_Q(\theta, \theta_i) = \frac{3}{2}\frac{e^2qQ}{h}\left(\frac{3\cos^2\theta - 1}{2}\right)\frac{< 3\cos^2\theta_i - 1 >}{2} \tag{2.66}$$

where θ is the angle between the external magnetic field and the director axis of the lipid.

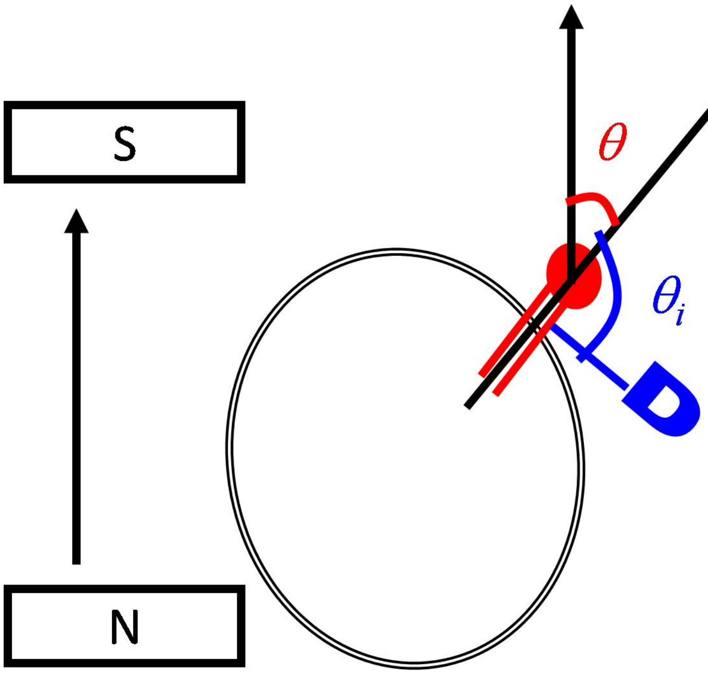

Figure 2.11: Orientational dependence – rapid rotation. The angle between the external magnetic field and the director axis of the lipid is denoted θ and the angle between the C–D bond on the i-th carbon and the director axis of the lipid is denoted θ_i in Eq. (2.66).

2.4.5 Quadrupolar echo

Data acquisition cannot immediately proceed after sending out the radio-frequency pulses since the same coil is used for pulsing and for detection. The ^{2}H NMR spectra of lipid membranes can extend out to ±126 kHz with respect to the Larmor frequency. In the time domain, this means that the free induction decay (FID) decays rapidly during receiver dead-time. The first few points of the FID are lost and the resulting spectrum is distorted. The quadrupolar echo is used to refocus the spins such that the full FID, neglecting relaxation effects, is reproduced as an "echo" long after the receiver dead-time. Fourier transformation of the last half of this echo yields an undistorted spectrum. The two pulse sequence of the quadrupolar echo is 90y-τ-90x-τ-echo. The physics of the quadrupolar echo sequence is presented here following the treatment given by Solomon [142, 143].

The useful part of the density matrix before the application of any pulses is proportional to I_z.

$$\rho_{eq} \propto I_z \tag{2.67}$$

where the notation eq signify that the system is in equilibrium with the external magnetic field at the sample temperature.

Define the time of the application of the 90y pulse as $t = 0$. The application of a 90° pulse is equivalent to a rotation such that

$$\rho(t=0) = R_y \rho_{eq} R_y^{-1} \tag{2.68}$$

$$R_y = e^{-i\varphi I_y} \tag{2.69}$$

$$(\varphi = \pi/2 \text{ for a } 90^\circ\text{pulse}). \tag{2.70}$$

Thus, immediately following the 90y pulse, the density matrix at t=0 is

$$\rho(0) = I_x. \tag{2.71}$$

After evolving in the external magnetic field during the time interval $0 < t < \tau$, the density matrix becomes

$$\rho(\tau) = e^{-iaI_z^2\tau}\rho(0)e^{iaI_z^2\tau} \tag{2.72}$$

where $a = 3e^2qQ/4\hbar$ is the value of the quadrupole perturbation. The application of the second pulse at time τ once again rotates the density matrix and so, similar to Eq. (2.68), $\rho(\tau)$ becomes

$$\rho'(\tau) = R_x \rho(\tau) R_x^{-1} \tag{2.73}$$

where

$$R_x = e^{-i\varphi I_x} \tag{2.74}$$

after the pulse.

The signal induced in the sample coil is proportional to

$$S(t) = Tr[\rho(t)I_+] \tag{2.75}$$

and therefore, the signal detected after the 90x pulse at time t is

$$S(t) = Tr[e^{-iaI_z^2(t-\tau)}\rho'(\tau)e^{iaI_z^2(t-\tau)}I_+]\ , \tag{2.76}$$

which can be expanded to

$$S(t) = \sum_{m,m',m''} < m|R_x|m'' >< m''|\rho(0)|m' >< m'|R_x^{-1}|m+1 > \\ \times [I(I+1) - m(m+1)]^{1/2} e^{ia[(2m+1)(t-\tau)-(m''^2-m'^2)\tau]}. \tag{2.77}$$

An echo occurs when $S(t)$ is independent of a and all the nuclei are in phase. This occurs when

$$\frac{t-\tau}{\tau} = \frac{m''^2 - m'^2}{2m+1} > 1. \tag{2.78}$$

For $I = 1$, Eq. (2.77) becomes zero and there is no signal when $m = I = 1$. The value $m''^2 - m'^2 = 0$ gives a time-independent signal. The desired echo occurs when $m'' - m' = \pm 1$. The allowed values of (m, m', m'') are $(0, 0, \pm 1)$ and $(-1, \pm 1, 0)$ and thus the echo occurs at $t = 2\tau$.

2.5 DOPC/DPPC/chol membranes

Why study DOPC/DPPC/chol (Fig. 2.12) membranes? In order to isolate the effects of fluorescent probes, all experiments were done on a single membrane system (35:35:30 DOPC/DPPC-D62/chol). This mixture was chosen for a number of reasons:

1. The ternary mixture DOPC/DPPC/chol is a model for the outer leaflet of animal cell plasma membranes [47].
2. The two phospholipids, DPPC and DOPC, have the same phosphatidylcholine headgroup, simplifying the interactions between the head groups.
3. The low-melting temperature lipid, DOPC, is chosen over the more biologically relevant POPC because its ternary mixture with DOPC shows immiscible liquid phases over a wide compositional range.
4. The ternary mixture DOPC/DPPC/chol [19, 23, 25, 47, 52, 67, 131, 144–146] and the binary mixtures DOPC/DPPC [119, 121, 147–149], DPPC/chol [5, 20, 45, 49, 102, 150–156], and DOPC/chol [5] have been studied extensively both experimentally and theoretically.

5. Other works examining probe effects have also been done on DOPC/DPPC/chol [28, 70].

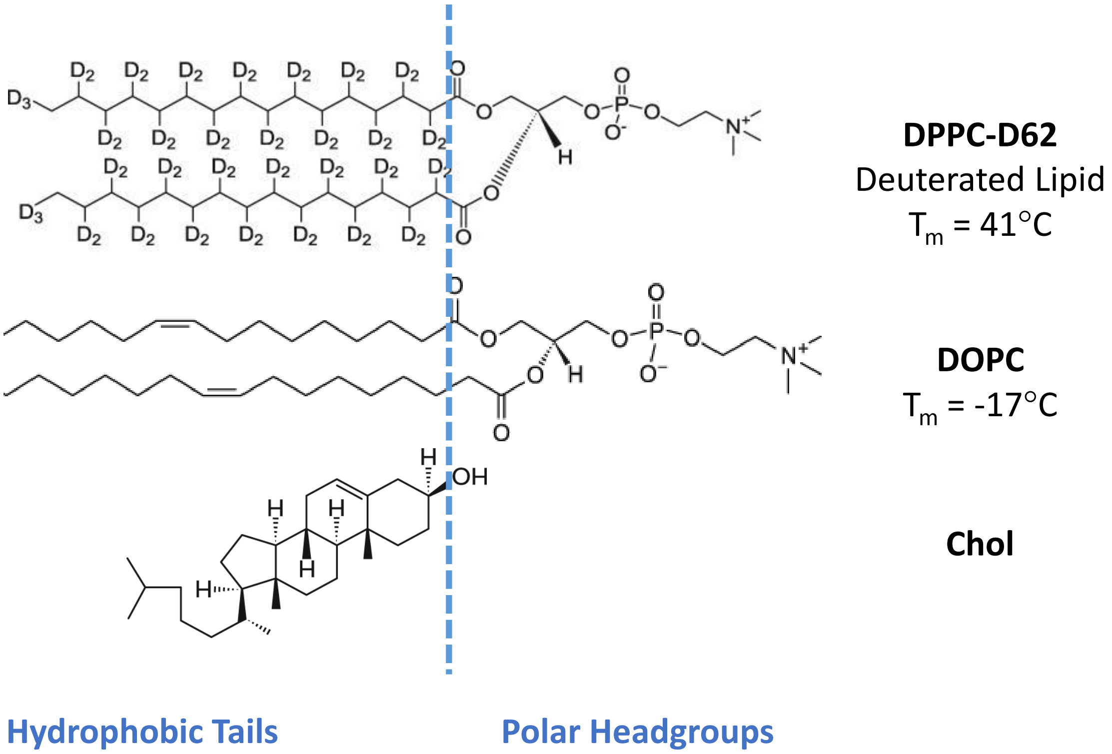

Figure 2.12: Lipid structures for DPPC-D62, DOPC and cholesterol.

Chapter 3

^{2}H NMR spectroscopy investigation of probe effects on MLV

Deuterium nuclear magnetic resonance spectroscopy (^{2}H NMR) is an established technique in lipid membrane studies. It is suitable for studying the effect of fluorescent probes on the membranes because it does not require the use of extrinsic probes. In ^{2}H NMR, the protons in the lipids are replaced with deuterons. Deuteration minimally alters membrane (Sec. 3.1.2).

The inherent low sensitivity of NMR experiments requires that multilamellar vesicle (MLV) be used. The increased amount of lipid per vesicle increases the amount of signal from each vesicle. Details on MLV preparation, deuterium NMR spectroscopy and analysis are adapted from my masters thesis [134], and presented in Sec. 3.1. Sections 3.2-3.6 are devoted to the results from ^{2}H NMR experiments on 35:35:30 DOPC/DPPC-D62/chol membranes with and without fluorescent probes. The membranes are heated through the $\mathbf{l_d}$-$\mathbf{l_o}$ miscibility transition, and the effects of probes are characterized.

3.1 Methods

3.1.1 Preparing multilamellar vesicles

MLV were made with 35:35:30 DOPC/DPPC-D62/chol + ϵ% fluorescent probe. Probe concentrations used in this thesis were between 0.1 and 2% for Laurdan and between 0.03 and 0.6% for naphthopyrene. Typical probe concentrations used in fluorescence microscopy and spectroscopy are between 0.1 and 0.5% for bilayer and multilamellar work. The highest concentration of 2% was chosen for Laurdan experiments to explore the effect of probe contents beyond trace amounts.

A large lipid stock solution is made, and then divided into multiple samples with varying probe concentration. For a batch with 5 different Laurdan concentrations, 200 mg DOPC, 200 mg DPPC-D62 and 84 mg chol were mixed to achieve the desired 35:35:30 DOPC/DPPC-D62/chol molar composition. After mixing, this mixture is divided into five portions, and the probe is added. The probe is added to the various samples at the same time so that only the probe concentration changes between samples. A sample without probe (referred to as 0% sample in this thesis) was made with every batch as control. The probe, dissolved in methanol, was added and the standard protocol (see below) was followed from step 2 onwards. Sinha et al. [100] showed that probe can be added to either dried lipids or lipids in solvent.

The standard protocol in the Thewalt lab for making MLV is as follows:

1. **Combine appropriate quantities of lipids.** 200 mg DOPC, 200 mg DPPC-D62, 84 mg chol were mixed. DPPC-D62 was used because at least one of the lipids must be deuterated. Lipids were purchased from Avanti Polar Lipids Inc. (Alabaster, AL), either in powder form or in chloroform ($CHCl_3$). Powder form lipids are dissolved in $CHCl_3$ to facilitate transfer between vials. After transfer, N_2 gas is used to dry off most of the solvent. Complete removal of residue $CHCl_3$ is carried out in the next step.

2. **Dissolve lipids in 80:20 benzene:MeOH (v/v) and lyophilize until dry.** Dissolving the lipids in this solvent ensures thorough mixing of the lipids. Lyophilization (freeze-drying) removes the solvent by sublimation to prevent de-mixing, which can occur during evaporation. Lyophilization will not work if the benzene:methanol ratio is lower than 80:20 (v/v). Removing the last solvent molecules requires 12-24 hours of lyophilization.

3. **Hydrate lipids in deuterium-depleted water (DDW).** 700 μL of DDW is used since that is the maximum capacity of the NMR tube, and it is more than enough water to fully hydrate the lipids. Hydration is known to affect membrane phase state [54, 157, 158]. Excess water ensures that there are no undissolved lipids; all lipids in the sample are in the same chemical environment, and the behaviour of the

system is independent of the amount of water. DDW was purchased from Sigma Aldrich Co. (St. Louis, MO).

4. **Freeze, thaw, and mix. Repeat four more times.** Samples were held in glass scintillation vials and dipped in liquid nitrogen (-210°C) until completely frozen. Samples were then held, by latex gloved hands, until they have been thawed to room temperature. The sample was then heated by a sub-boiling water bath (~ 60°C). The water bath temperature has to be above the gel-to-liquid crystalline temperature of the high melting lipid, DPPC-D62, and below the boiling point of DDW to prevent water loss. The temperature should be as low as possible to prevent lipid degradation. Temperatures were kept 20°C above the melting temperature of the high-melting lipid (DPPC $\mathrm{T_m}$ is 41°C). After several minutes, the sample was mixed with a bench-top vortex mixer. The freeze-thaw-mix process promotes homogeneous MLV formation.

3.1.2 ^{2}H NMR spectroscopy

^{2}H NMR allows the environment of the deuterons to be observed. ^{2}H NMR is an excellent technique for studying phases in lipid membranes because the spectra of $\mathbf{l_d}$, $\mathbf{l_o}$, and gel phases are distinct from one another. In regions of large-scale phase coexistence, the ^{2}H NMR signal is directly proportional to the content of deuterated lipid in each phase. Distinguishing features from the spectra of $\mathbf{l_d}$, $\mathbf{l_o}$, and gel phases are identifiable even when more than one phase is present. The ^{2}H NMR experiments of this thesis report on the DPPC-D62 palmitoyl chains' motional behaviour.

^{2}H NMR was performed using a 7.0 T Oxford Magnet with a locally built spectrometer operating at 46.8 MHz using the quadrupolar echo technique, which involved two 90° pulses of 3.95 μs duration, 90° out of phase, 40 μs apart, and repeated every 300 ms [138]. Data were collected with quadrature detection and 8-CYCLOPS phase cycling (see below).

The vesicles were placed into the spectrometer immediately after they were made. This helps minimize light and oxygen exposure, which can promote lipid degradation. They were allowed to equilibrate at each temperature for at least 20 minutes before data collection. Experiments proceeded from low to high temperatures with one degree increments. Lipid integrity was checked at the end by repeating measurements at 27°C, and by thin layer chromatography (Appendix D).

Quadrature detection

The receiver electronics of the spectrometer cannot handle the large frequencies ($\sim 10^6$ Hz) associated with solid state NMR. During data acquisition, the signal is down-shifted by subtracting off a reference frequency ($\sim 10^6$ Hz), and it is the offset from this reference frequency that is detected. The reference used is typically the Larmor frequency (46.8 MHz). Quadrature detection is used to distinguish between a positive and a negative offset: the signal is detected in two 90° out-of-phase channels.

Phase cycling

Phase-insensitive noise can be averaged out over the course of a set of experiments by varying the phases systematically, and adding the signals from desired pathways coherently. Eight permutations of two 90° out-of-phase pulses are possible. 8-CYCLOPS (CYCLically Ordered Phase Sequence) phase cycling involves alternating the pulse used for the first and second pulse between (x,y), (y,-x), (-x,-y), (-y,x), (x,-y), (-y,-x), (-x,y), (y,x). 8-CYCLOPS phase cycling dictates that data acquisition must involve only multiples of 8 scans.

Average spectral width

The first moment of a spectrum can be used to characterize the width of a spectrum. Since the first moment of a symmetric spectrum is zero, and ^{2}H NMR spectra are symmetric about the Larmor frequency ($\omega = 0$ kHz), the average spectral width (M_1) is defined as

$$\mathrm{M}_1 = \frac{\sum\limits_{\omega=-x}^{x} |\omega| I(\omega)}{\sum\limits_{\omega=-x}^{x} I(\omega)} \tag{3.1}$$

where ω is the offset frequency from the Larmor frequency, $I(\omega)$ is the intensity at ω, and $\mathrm{x}=2\pi\cdot 50$ kHz for spectra taken above 32°C (i.e., homogeneous liquid crystalline spectra) and $2\pi \cdot 65$ kHz for spectra taken at and below 32°C. The second moment can also characterize the width of a spectrum, but it gives more weight to the larger frequencies. Since the higher frequencies have more noise, Eq. (3.1) is a better measure of spectral width.

A perdeuterated lipid has all the hydrogens on one or both of its chains substituted with deuterons. In the $\mathbf{l_o}$ or $\mathbf{l_d}$ phase, lipids undergo rapid axially symmetric motion about their long axes. As a result, each deuteron along a perdeuterated lipid chain contributes a Pake doublet to the spectrum, with an associated quadrupolar splitting

$$\Delta\nu_Q = \frac{3}{4}\frac{e^2qQ}{h}|S_{\mathrm{CD}}| \tag{3.2}$$

where e^2qQ/h is the static quadrupolar coupling constant and S_{CD} is a measure of the angular excursions of the C–D bond with respect to the lipid long axis. For $\mathbf{l_d}$+$\mathbf{l_o}$ phase separated membranes, ^{2}H NMR spectra are superpositions of the weighted $\mathbf{l_d}$ and $\mathbf{l_o}$ "end-point" spectra (Appendix F).

Scans

There was 30 mg of DPPC-D62 in each sample in batch L2 and 40 mg of DPPC-D62 in each sample of batch L3 and batch N1.[1] The signal-to-noise ratio (SNR) is proportional to the amount of deuterated lipid. Increasing the number of scans can compensate for insensitivity of NMR experiments (Sec. 2.4.2) since SNR $\propto \sqrt{\text{Number of Scans}}$. 10,000 scans were averaged.

Repetition time (TR)

Repetition time (TR) is the time between the start of successive scans. Experimentally, shorter TR is more desirable because faster data acquisition means more data can be collected within a given amount of time, improving the SNR. Motionally restricted spins, such as those in crystalline solids, have longer spin lattice relaxation times (T_1); their signal can be lost in successive scans as a result of incomplete relaxation if TR is too short. Gel and liquid crystalline phases lipids have relatively short T_1. For example, T_1 for the methyls of liquid crystalline DPPC-D62 at 45°C is 275 ms and 100 ms for gel phase DPPC-D62 at 20°C [159]. Methylenes have considerably shorter T_1, $\sim$ 50 ms, than methyls. TR of 300 ms was used in this thesis, unless otherwise noted, since that should give most spins, except the methyl groups, enough time to return to the equilibrium state.

For 35:35:30 DOPC/DPPC-D62/chol membranes, 2 s TR data shows that 300 ms was not enough for the methyl groups to fully relax between successive scans (data not shown).

---

[1] The quantities used (200 mg DPPC-D62) in Sec. 3.1.1 were for the entire batch of L3 and N1. In each of these two batches, there were five samples made.

Although some signal intensity in the methyl peaks was lost, SNR was improved because of the higher number of scans (in the same amount of data collection time) achievable.

Methyl peak intensity ratio

Lipids in spherical MLV are randomly oriented in space. The lipid chains are thus also oriented in all directions. For lipids undergoing fast axial rotations, e.g., in the $\mathbf{l_d}$ or $\mathbf{l_o}$ phase, the spectra are superposition of Pake doublets. Deconvolution of such spectra into corresponding spectra for perfectly aligned bilayers using Lorentzian line shapes is known as dePaking in ^{2}H NMR [160].

The methyl peaks from the dePaked spectrum fitting well to Lorentzian line shapes indicates that the methyls are given enough time between scans to fully relax. The methyl peak areas are directly proportional to the number of spins.

Let N_{Ao}, N_{Ap}, N_{Ac} be the number of DOPC, DPPC-D62, and cholesterol molecules in the A phase, and N_{Bo}, N_{Bp}, N_{Bc} be the corresponding number in the B phase. In the presence of excess water, the membrane phases are not sensitive to the amount of water present, and the membrane can be treated as a lipids-only system. The concentrations of DOPC, DPPC-D62, and cholesterol in the A phase are

$$C_{Ao} = \frac{N_{Ao}}{N_{Ao} + N_{Ap} + N_{Ac}} \tag{3.3}$$

$$C_{Ap} = \frac{N_{Ap}}{N_{Ao} + N_{Ap} + N_{Ac}} \tag{3.4}$$

$$C_{Ac} = \frac{N_{Ac}}{N_{Ao} + N_{Ap} + N_{Ac}} \tag{3.5}$$

and analogous expressions can be written for concentrations of these lipids in the B phase. Let the total number of lipid molecules in the membrane be

$$N_T = (N_{Ao} + N_{Ap} + N_{Ac}) + (N_{Bo} + N_{Bp} + N_{Bc}) \ , \tag{3.6}$$

and the fraction of the total lipids in the A phase and B phase be

$$f_A = \frac{N_{Ao} + N_{Ap} + N_{Ac}}{N_T} \tag{3.7}$$

and

$$f_B = \frac{N_{Bo} + N_{Bp} + N_{Bc}}{N_T} \ , \tag{3.8}$$

respectively, then

$$\frac{f_A C_{Ap}}{f_B C_{Bp}} = \frac{N_{Ap}}{N_{Bp}} \ . \tag{3.9}$$

The right hand side (N_{Ap}/N_{Bp}) can be calculated from ^{2}H NMR by measuring the intensity of the methyl peaks in the two phases.

If the methyl groups of the $\mathbf{l_d}$ and $\mathbf{l_o}$ lipids have different T_1s, and if the methyls did not fully relax (see Sec. 3.1.2), the ratios of $\mathbf{l_d}/\mathbf{l_o}$ methyl signal intensity would not accurately reflect the $\mathbf{l_d}$ to $\mathbf{l_o}$ DPPC-d62 ratio. For accurate measurements, TR of 2 s was used in Sec. 3.6.

Effects of deuteration on lipid phase transitions

Perdeuteration of lipid chains is known to decrease the main transition temperatures ($\mathrm{T_m}$) of pure lipids. $\mathrm{T_m}$ is a measure of the stability of the gel phase relative to the fluid phase [62]. For example, increasing chain length of saturated lipids increases $\mathrm{T_m}$ because the increased hydrophobic interactions stabilize the gel phase. Deuteration, on the other hand, decreases the van der Waals forces between the lipids, and decreases $\mathrm{T_m}$. Aussenac et al. [62] showed that the $\mathrm{T_m}$ of pure DMPC decreased with increasing deuterium content of the lipid chain. $\mathrm{T_m}$ is 37.75°C for DPPC-D62, and 41.2°C for unlabelled DPPC [20, 159]. $\mathrm{T_m}$ is expected to be about 2°C lower per deuterated chain [67].

Thus, a binary mixture of 75:25 lipid A: lipid B, where lipid A is perdeuterated is intrinsically different from one where lipid B is perdeuterated. Strictly speaking, to make a valid comparison, one should only compare mixtures with the same level of deuteration. Namely, where both lipids have the same level of deuteration, or the mixture must be a 50:50 mixture [161]. The former is usually not done since peak resolution and identification is difficult if the two lipid chains experience similar environments. Lu et al. [161] compared singly deuterated and doubly deuterated 50:50 DMPC/DSPC at 60°C and found that a weighted sum of the two singly deuterated spectra yielded a spectrum similar to that of the doubly deuterated membrane.

Our lab also found that percent differences in C4-C6 order parameters between alternately perdeuterated $\mathbf{l_d}$ binary membranes are the same for 50:50 mixtures and for other lipid ratios for DMPC/DSPC [161], DPPC/POPC [162, and J. Thewalt unpublished data] and POPC/PSm [162–164] [165]. This suggests that despite differences in T_m of individual lipids resulting from deuteration, the information reported on molecular order is robust. In this thesis, only 35% of the total lipids are deuterated; deuteration is not expected to alter lipid membrane molecular order significantly.

Juhasz et al. [131] performed confocal fluorescence microscopy (CFM) experiments using chain-perdeuterated and non-deuterated DPPC, and 0.1% TR-DPPE. Deuterated and non-deuterated DOPC/DPPC/chol GUVs were prepared at two compositions (32:48:20 and 35:35:30). DPPC-D62 was used in the deuterated mixtures. The one with the higher deuterated DPPC content (32:48:20) was expected to be more affected by the deuterium label. Domain fluctuations were stronger in non-deuterated samples for both compositions. Phase transitions in the non-deuterated samples were at higher temperatures:$\sim$ 1-2°C higher in the 32:48:20 membranes, and $\sim$ 3-7°C higher in the 35:35:30 membranes. This is surprising given that one would expect the one with the higher deuterated DPPC content to be more affected by the deuterium label. Given that (1) their samples were continuously illuminated, (2) they were using TR-DPPE, which is known to be photo-sensitive (see Sec. 5.8), and that (3) the differences were greatest as their experiment proceeded, some of these differences may not be related to deuterium labelling.

3.2 ^{2}H NMR spectra of MLV with high Laurdan content

Figure 3.1 shows selected ^{2}H NMR spectra for 35:35:30 DOPC/DPPC-D62/chol multilamellar vesicles (MLV) with and without 2% fluorescent probe Laurdan between 10 and 60°C. Even though 2% probe is higher than typical values used in fluorescence experiments, membranes with and without Laurdan produce similar spectra. It is known from the literature that the $\mathbf{l_d}+\mathbf{l_o}$ miscibility transition is within the temperature range chosen [23, 25]. The horizontal axis of a ^{2}H NMR spectrum is the offset from the deuterium Larmor frequency. The spectra are symmetric about the Larmor frequency, and the separation frequency between a pair of corresponding peaks – i.e., a Pake doublet – is the quadrupolar splitting. The quadrupolar splitting is proportional to the order parameter, a measure of chain rigidity (Eq. (3.2)). The peaks near 0 kHz belong to the terminal methyls, and the other peaks are from the methylene groups on the deuterated lipid chains (i.e., DPPC-D62); the methyl peaks' intensities are higher than those of the methylene peaks (Fig. 3.2).

The spectra above 25°C in Fig. 3.1 are typical of liquid crystalline membranes: the methylene signals are the dominant spectral feature between 4 and 20 kHz. The peaks near ±20 kHz are slightly higher since several methylenes have similar quadrupolar splittings. The spectra below 25°C are typical of $\mathbf{l_d}+\mathbf{l_o}$ membranes. These spectra are weighted sums of the $\mathbf{l_d}$ and $\mathbf{l_o}$ spectra. The $\mathbf{l_o}$ spectra are similar in shape to the $\mathbf{l_d}$ spectra, but they are about 50% wider. Lipid chains in the $\mathbf{l_d}$ phase are more flexible than those in the $\mathbf{l_o}$ phase. The more flexible the chains, the smaller the associated quadrupolar splittings of the Pake doublet. The bumps near ±20 kHz in the low temperature spectra are evidence of $\mathbf{l_d}+\mathbf{l_o}$ phase coexistence: the bump is the $\mathbf{l_d}$ plateau edge peeking out from the $\mathbf{l_o}$ spectrum (Fig. 3.2). No sign of a gel phase is present in these spectra: a gel phase would increase the shoulder region (20-60 kHz) intensity and distort the superpositioned Pake doublets.

Figure 3.3 shows the same spectra using a narrower range of frequencies to highlight the methyl peaks. The spectra above 25°C have one set of methyl peaks and are typical of homogeneous fluid phases where all lipids in the membrane are in the same liquid ($\mathbf{l_d}$ or $\mathbf{l_o}$) phase. The spectra below 25°C are typical of $\mathbf{l_d}+\mathbf{l_o}$ coexistence: they are superpositions of $\mathbf{l_d}$ and $\mathbf{l_o}$ spectra and have three sets of methyl peaks. The narrowest pair, with a quadrupolar splitting of 3-4 kHz, belongs to the $\mathbf{l_d}$ methyls, and the other two, with quadrupolar splittings of 8-10 kHz, belong to the $\mathbf{l_o}$ methyls. Of the $\mathbf{l_o}$ methyl peaks, the narrower pair belongs to the *sn*-1 chain methyls, and the wider pair belongs to the *sn*-2 chain methyls of the $\mathbf{l_o}$ phase. In the $\mathbf{l_o}$ phase, the methyl groups on the two chains experience slightly different environments, and as a result produce two doublets having slightly different separation frequencies. In the $\mathbf{l_d}$ phase, however, these differences are averaged out by rapid molecular motions, and the signals from the two groups overlap.

As temperature increases, the lipid chain becomes more flexible, and the quadrupolar splittings decrease. This is most evident for spectra at temperatures above miscibility transition temperature (T_{mix}). Below T_{mix}, the temperature-dependent changes in quadrupolar splitting are complicated by the temperature-dependent changes in $\mathbf{l_d}$ and $\mathbf{l_o}$ compositions. The $\mathbf{l_o}$ methyl quadrupolar splitting decreases more than the $\mathbf{l_d}$ methyl splitting with temperature. The T_{mix} reported in the ^{2}H NMR experiments of this thesis was the lowest temperature at which the $\mathbf{l_d}$ and $\mathbf{l_o}$ methyls peaks were not resolvable by eye. In particular,

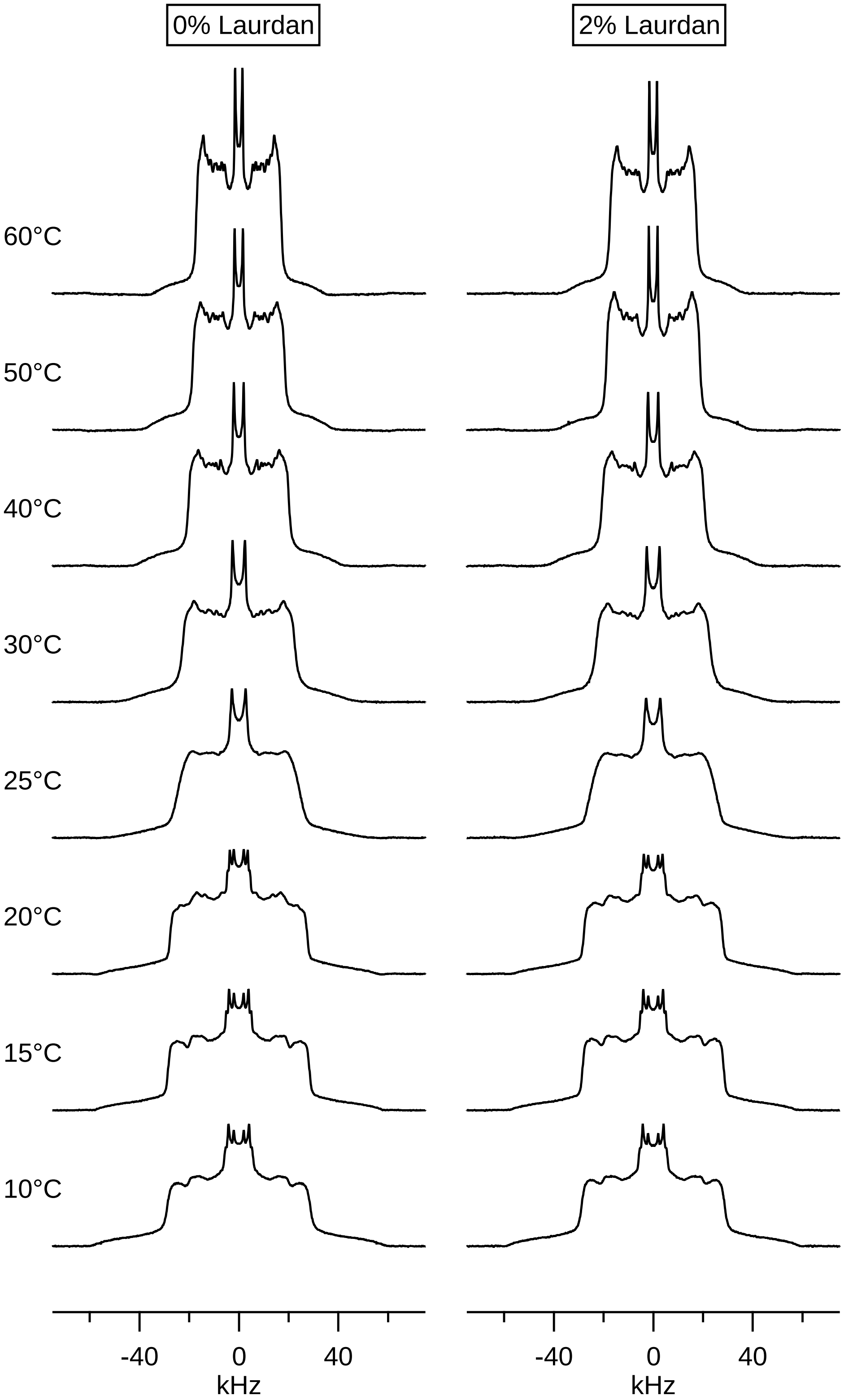

Figure 3.1: ^{2}H NMR spectra between 10 and 60°C for 35:35:30 DOPC:DPPC-D62:chol membranes with 0% (left) and 2% (right) Laurdan. Data from batch L2.

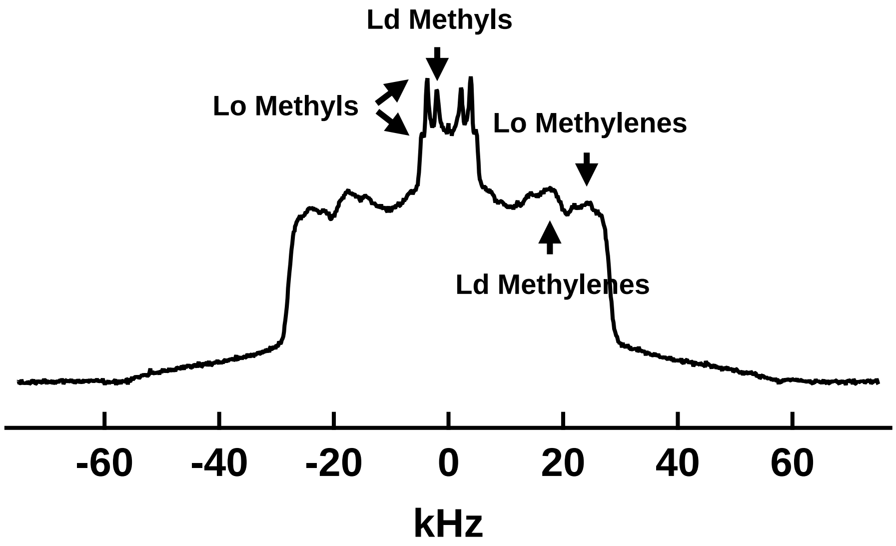

Figure 3.2: ^{2}H NMR spectra exhibiting $\mathbf{l_d}$+$\mathbf{l_o}$ phase coexistence.

the edge of the single methyl peak should be smooth if the membrane is in a single phase. The quadrupolar splitting of the wider $\mathbf{l_o}$ methyl peak creating a bump in the edge is an indication that there is more than one type of membrane environment. Visual inspection of the spectra in Fig. 3.3 shows that T_{mix} is between 20 and 25°C.[2] The 0 and 2% Laurdan spectra look almost identical, suggesting that up to 2% Laurdan does not dramatically alter membrane phase behaviour.

3.3 ^{2}H NMR spectra of MLV with trace Laurdan content

A follow-up experiment was performed using a smaller range of temperatures near T_{mix} (15-40°C) and a lower range of probe concentrations (0-0.5%). This concentration range is typical of fluorescence experiments. This set of experiments will be referred to as batch L3, and the previous set will be referred to as batch L2. A probe-free sample (0%) was made for each batch separately as a control. The temperature range was chosen using the data from batch L2 that showed that T_{mix} is between 20 and 25°C. The maximum temperature was kept low in order to minimize sample degradation and to eliminate water evaporation. Data collection was also expedited by this strategy.

---

[2] In Sec. 3.3, spectra with smaller temperature increments will be shown, and the reader will be able to determine T_{mix} by spectral inspection with greater precision.

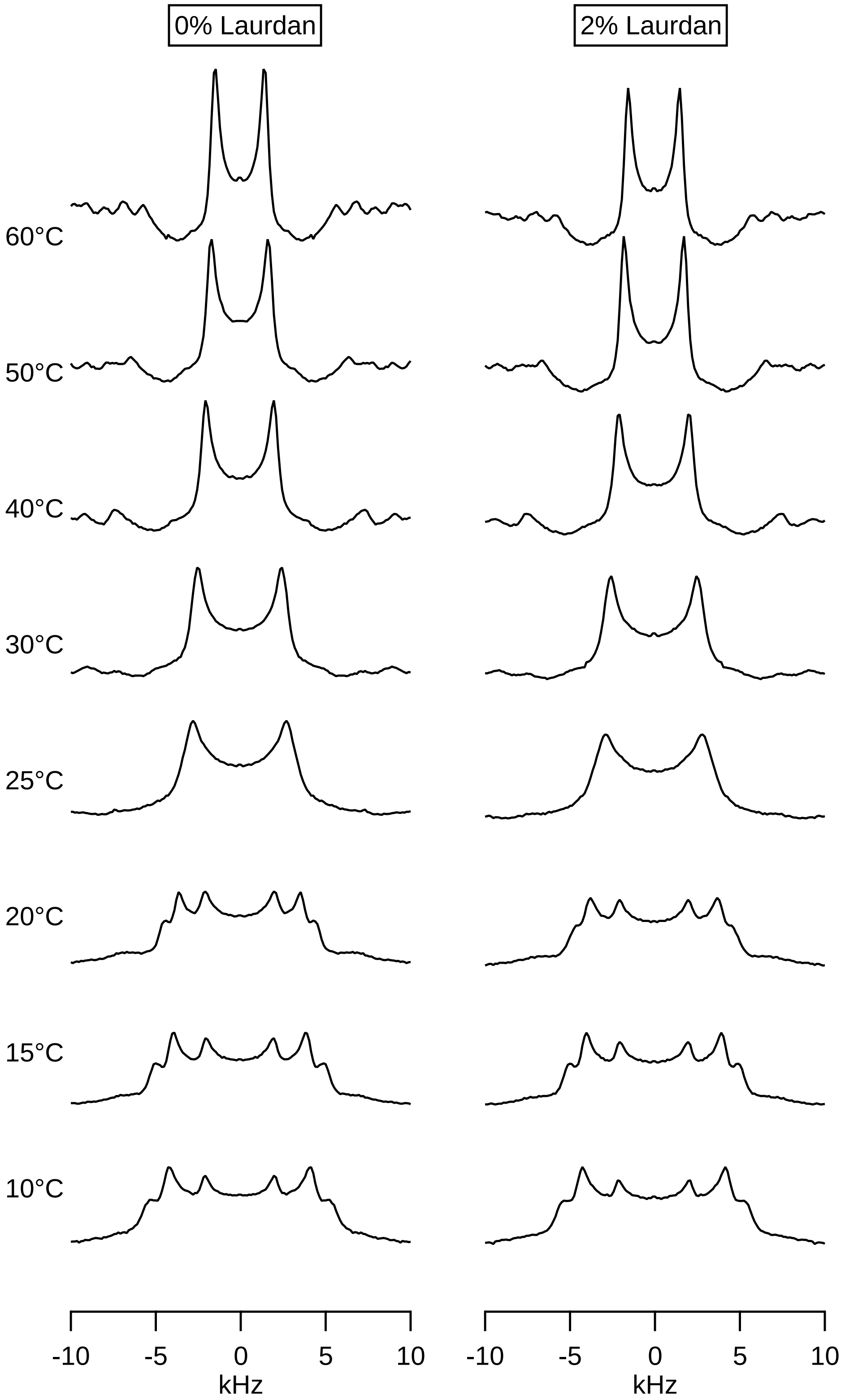

Figure 3.3: ^{2}H NMR spectra, focusing on the methyl peaks, between 10 and 60°C for 35:35:30 DOPC:DPPC-D62:chol MLV with 0 (left) and 2% (right) Laurdan. The 0 kHz spikes are an artifact from the data-analysis protocol. Data from batch L2.

Spectra for batch L3 are shown in Figs. 3.4-3.6 and the methyl regions are highlighted in Figs. 3.7-3.9. The probe-free sample in batch L3 and the probe-free sample in batch L2 have slightly different T_{mix} (21°C versus 24°C for batch L2). Differences between batches will be examined later in Sec. 3.5. All samples from batch L3 have the same T_{mix} (see Fig. 3.20); the addition of 0.1-0.5% Laurdan did not alter spectra significantly. Additional analysis is deferred to Secs. 3.5-3.7.

3.4 ^{2}H NMR spectra of MLV with naphthopyrene

In this thesis, naphthopyrene is the representative $\mathbf{l_o}$-preferring probe. These experiments set out to test whether a $\mathbf{l_o}$-preferring probe would alter membrane phase properties the way DiIC12, a non-equipartitioning probe, did in our previous work. The previously described experiments with Laurdan were repeated with naphthopyrene. Figures 3.10-3.12 show ^{2}H NMR spectra of 35:35:30 DOPC/DPPC-D62/chol MLV with 0-0.6% naphthopyrene, and Figs. 3.13-3.15 focus on the methyl peaks. As with Laurdan, the addition of naphthopyrene does not change the overall spectral shape, or the methyl peaks' appearance. In contrast to Laurdan, though, naphthopyrene did cause a measurable increase in T_{mix}. Additional analysis follows in the next three sections (Secs. 3.5-3.7).

3.5 Batch-to-batch variation

A probe-free sample was made with each batch, so that probe effects can be assigned unambiguously. Batch-to-batch variation could be identified by looking at the probe-free sample in all three batches. Figure 3.16 shows the methyl quadrupolar splittings for the control sample in each batch. Recall that there are three sets of methyl splittings below T_{mix}: one from the $\mathbf{l_d}$ methyls, and two from the $\mathbf{l_o}$ methyls (Sec. 3.2). Only one of the two $\mathbf{l_o}$ methyl splittings is plotted since the splitting of the *sn*-2 peak is hard to measure near T_{mix}. Above T_{mix}, only one methyl splitting is measured. As noted in Sec. 3.3, the T_{mix} of batches L2 (24°C) and L3 (21°C) are different. Batches L3 and N1 have the same T_{mix}. Methyl splittings from all three samples overlap above T_{mix}. Below T_{mix}, the batch L2 $\mathbf{l_d}$ methyls are more ordered, and the $\mathbf{l_o}$ methyls are more disordered than the other two samples. It is interesting that the batch-to-batch variations disappear above T_{mix}.

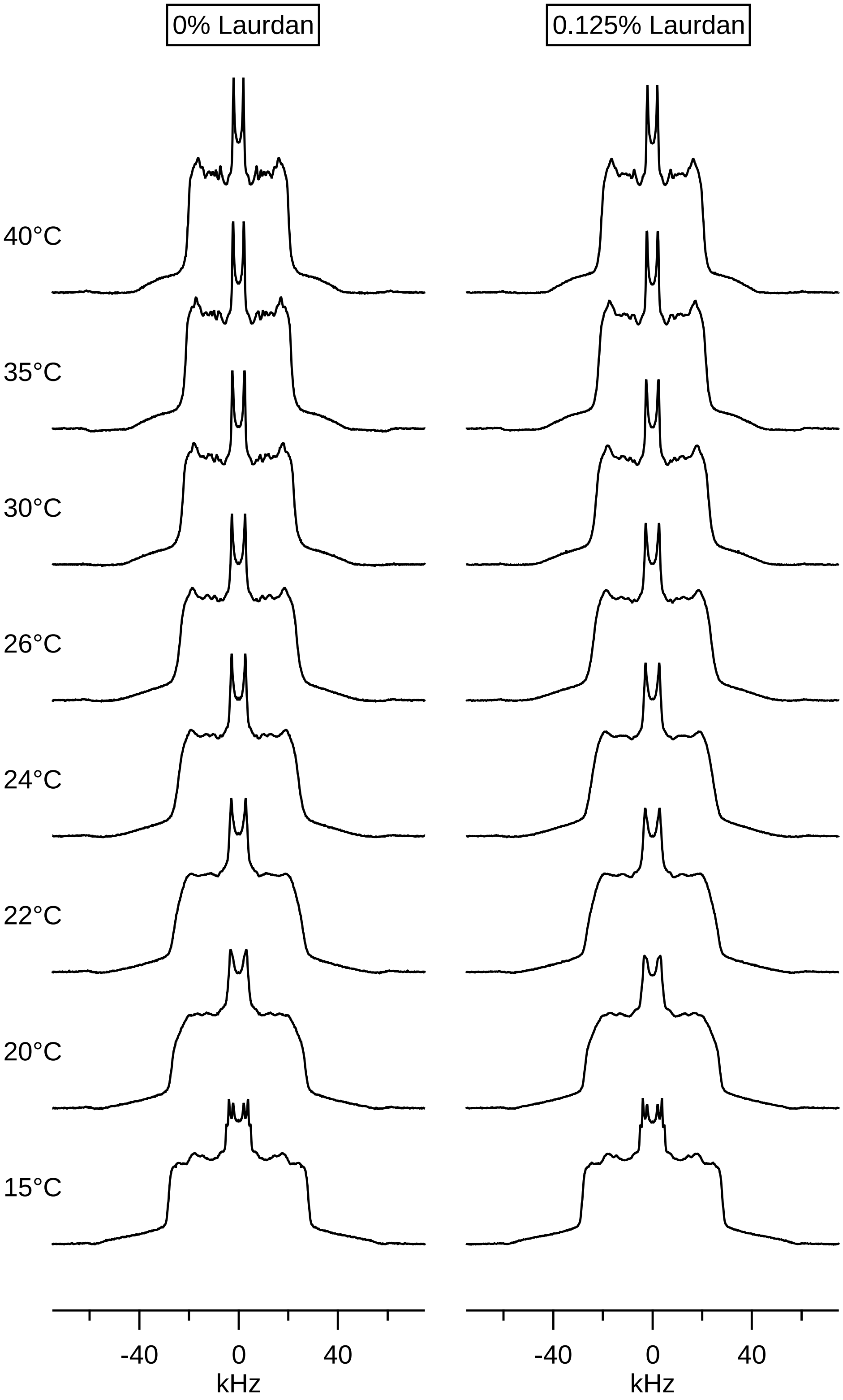

Figure 3.4: ^{2}H NMR spectra between 15 and 40°C for 35:35:30 DOPC:DPPC-D62:chol MLV with 0% (left) and 0.1% (right) Laurdan. Data from batch L3.

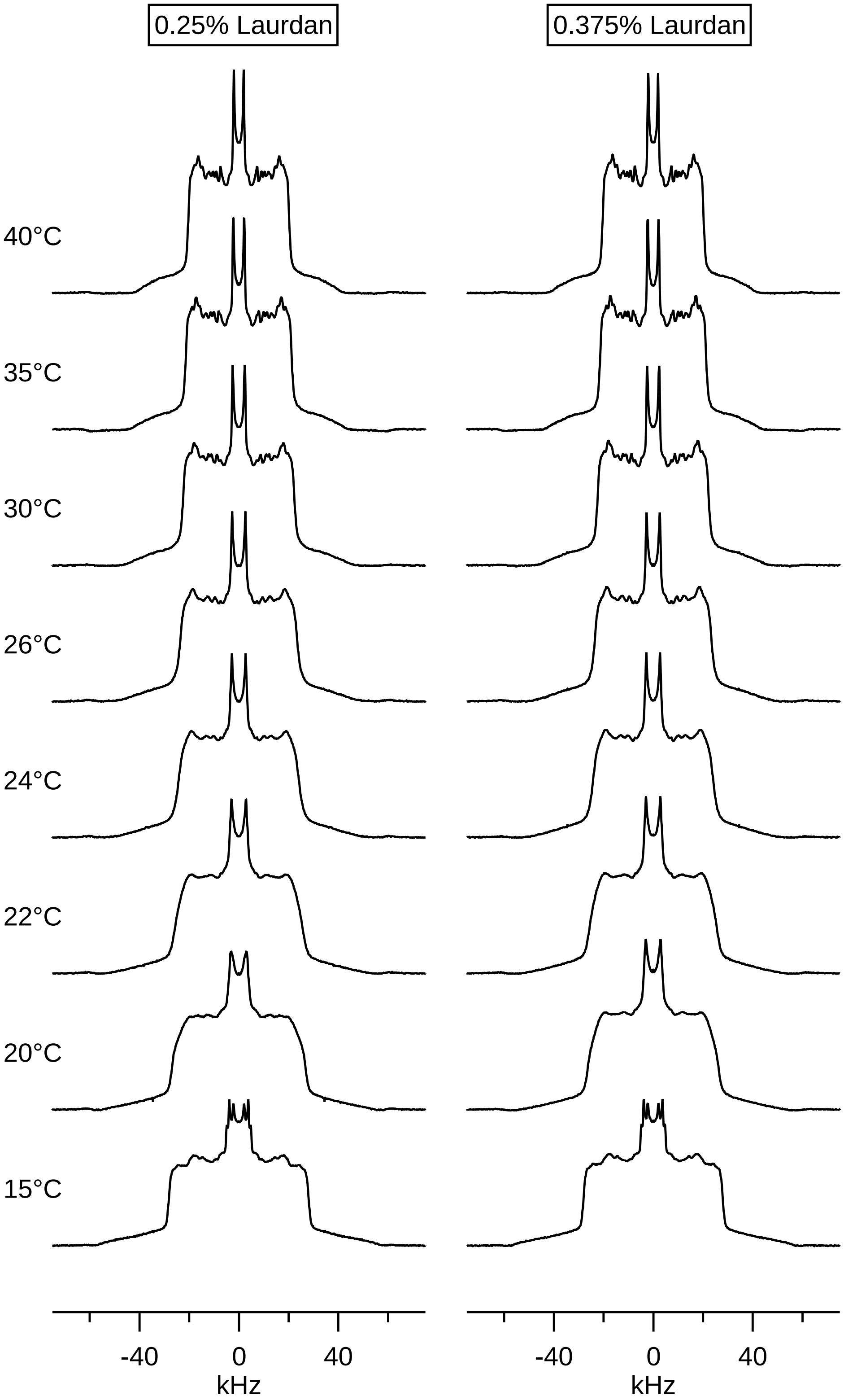

Figure 3.5: ^{2}H NMR spectra between 15 and 40°C for 35:35:30 DOPC:DPPC-D62:chol MLV with 0.3% (left) and 0.4% (right) Laurdan. Data from batch L3.

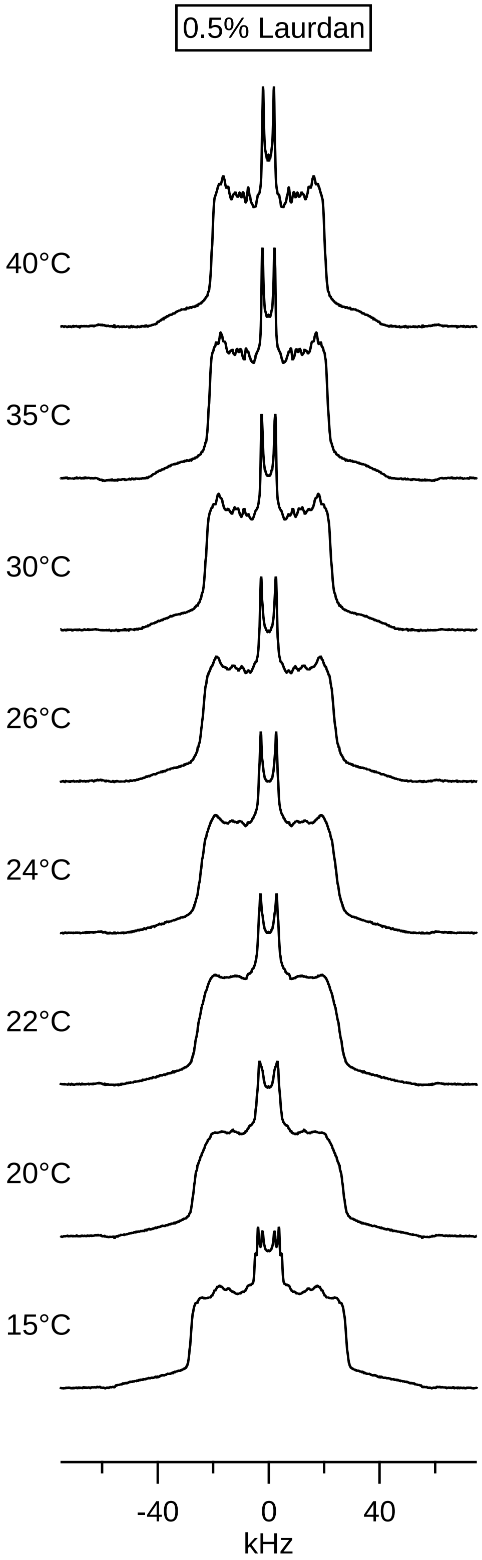

Figure 3.6: ^{2}H NMR spectra between 15 and 40°C for 35:35:30 DOPC:DPPC-D62:chol MLV with 0.5% Laurdan. Data from batch L3.

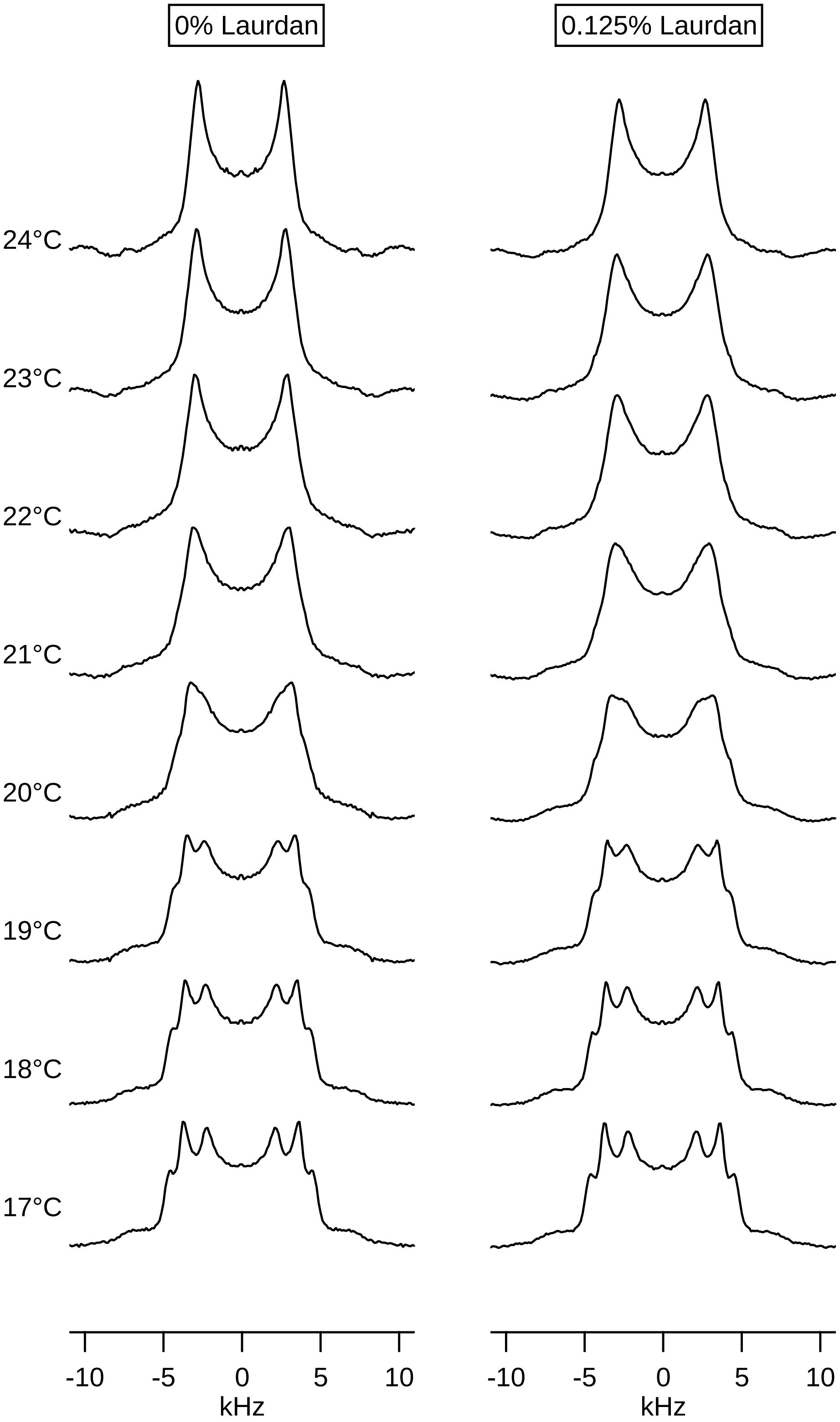

Figure 3.7: ^{2}H NMR spectra, focusing on the methyl peaks, between 17 and 24°C for 35:35:30 DOPC:DPPC-D62:chol MLV with 0% (left) and 0.1% (right) Laurdan. Data from batch L3.

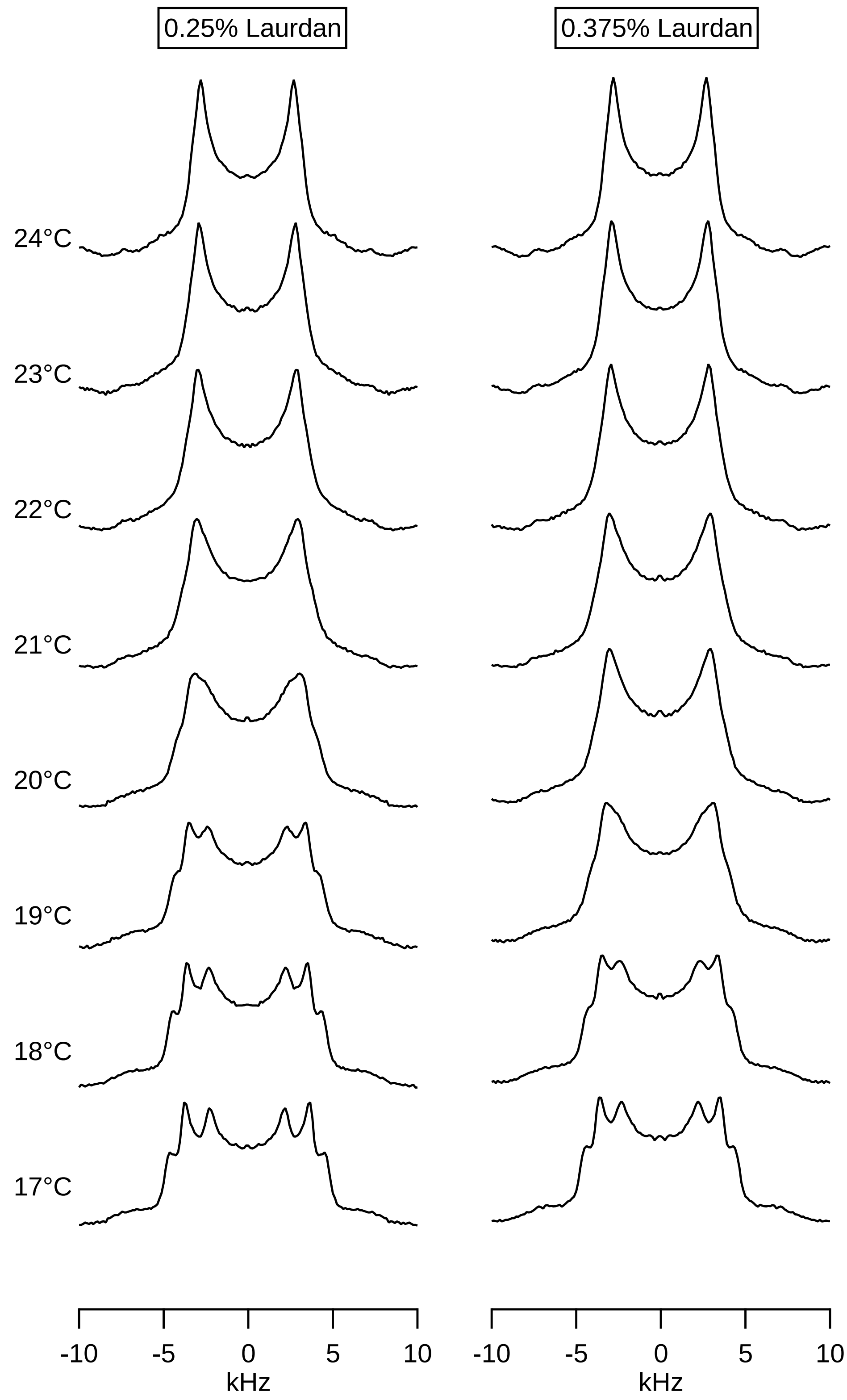

Figure 3.8: ^{2}H NMR spectra, focusing on the methyl peaks, between 17 and 24°C for 35:35:30 DOPC:DPPC-D62:chol MLV with 0.3% (left) and 0.4% (right) Laurdan. Data from batch L3.

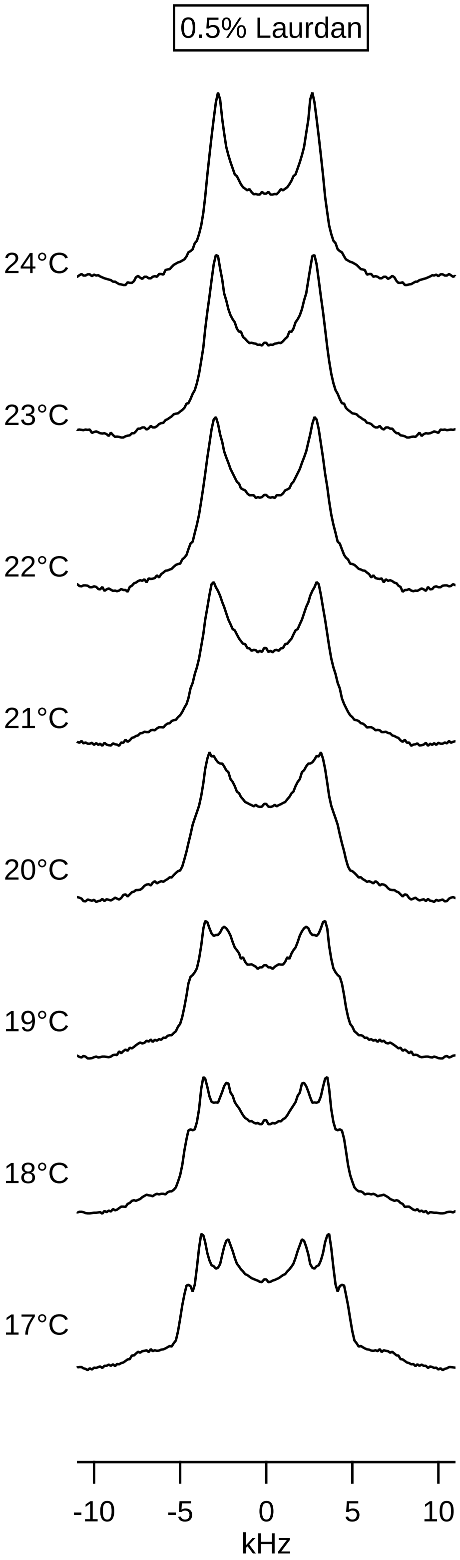

Figure 3.9: ^{2}H NMR spectra, focusing on the methyl peaks, between 17 and 24°C for 35:35:30 DOPC:DPPC-D62:chol MLV with 0.5% Laurdan. Data from batch L3.

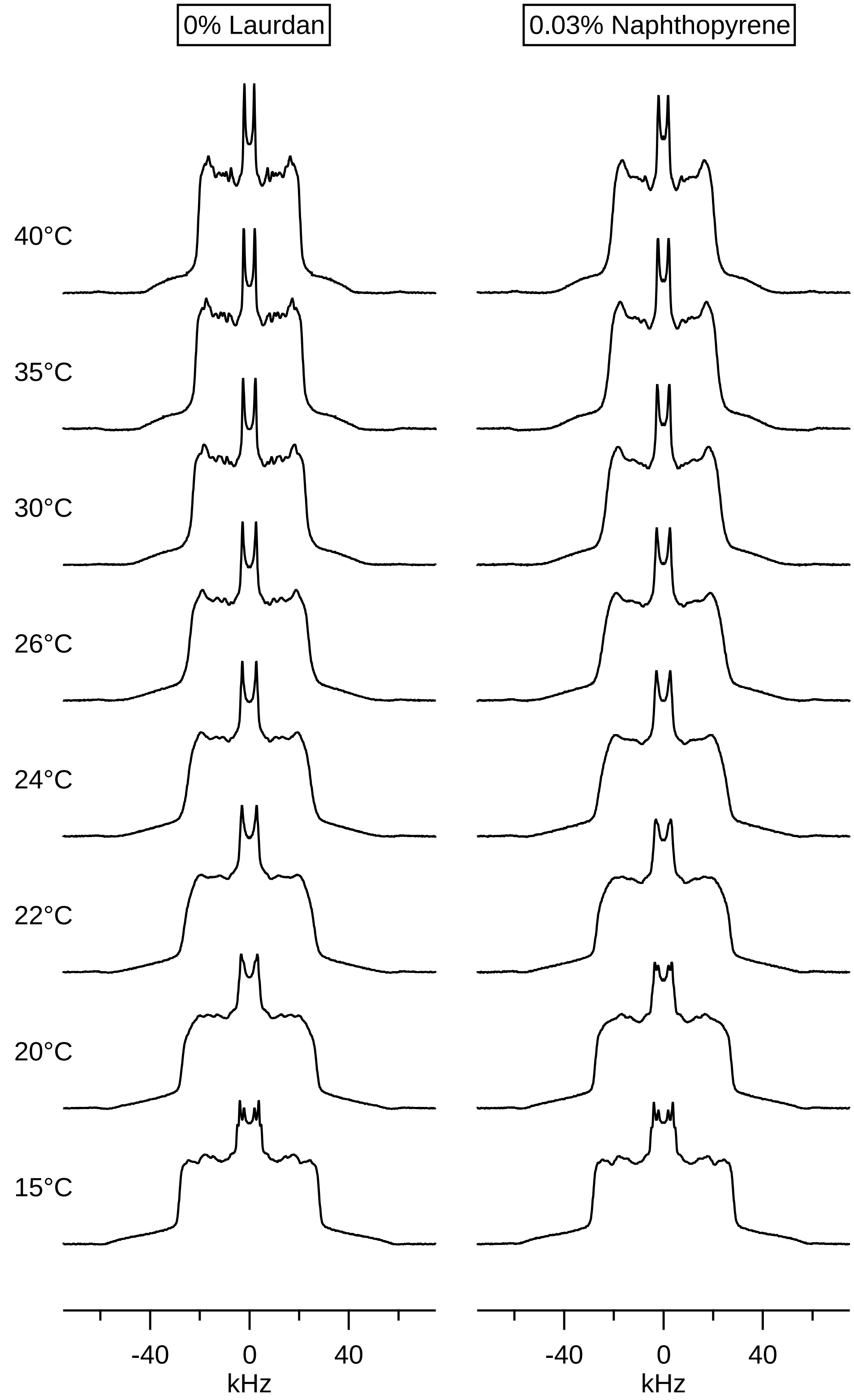

Figure 3.10: ^{2}H NMR spectra between 15 and 40°C for 35:35:30 DOPC:DPPC-D62:chol MLV with 0 (left) and 0.03% (right) naphthopyrene.

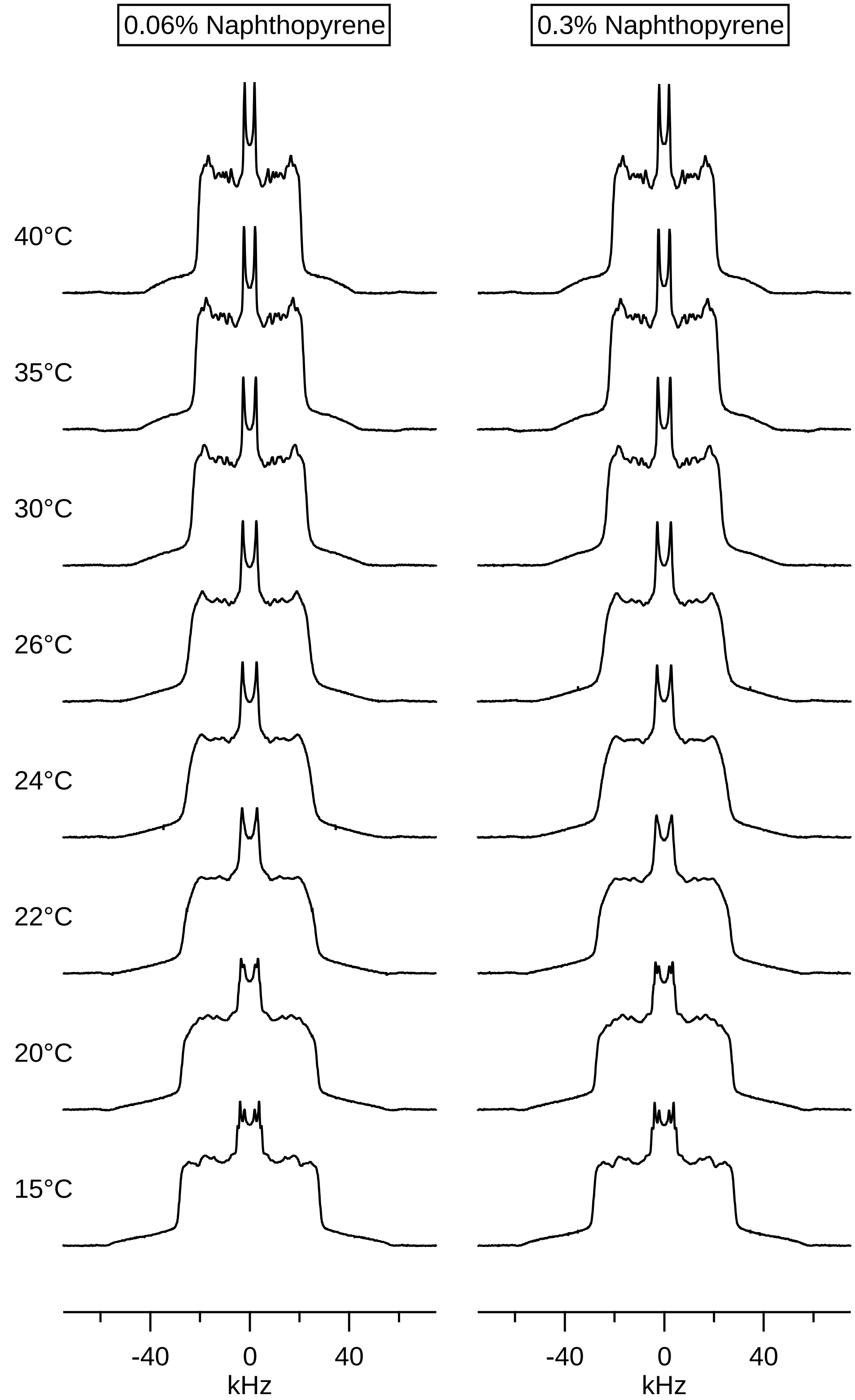

Figure 3.11: ^{2}H NMR spectra between 15 and 40°C for 35:35:30 DOPC:DPPC-D62:chol MLV with 0.06 (left) and 0.3% (right) naphthopyrene.

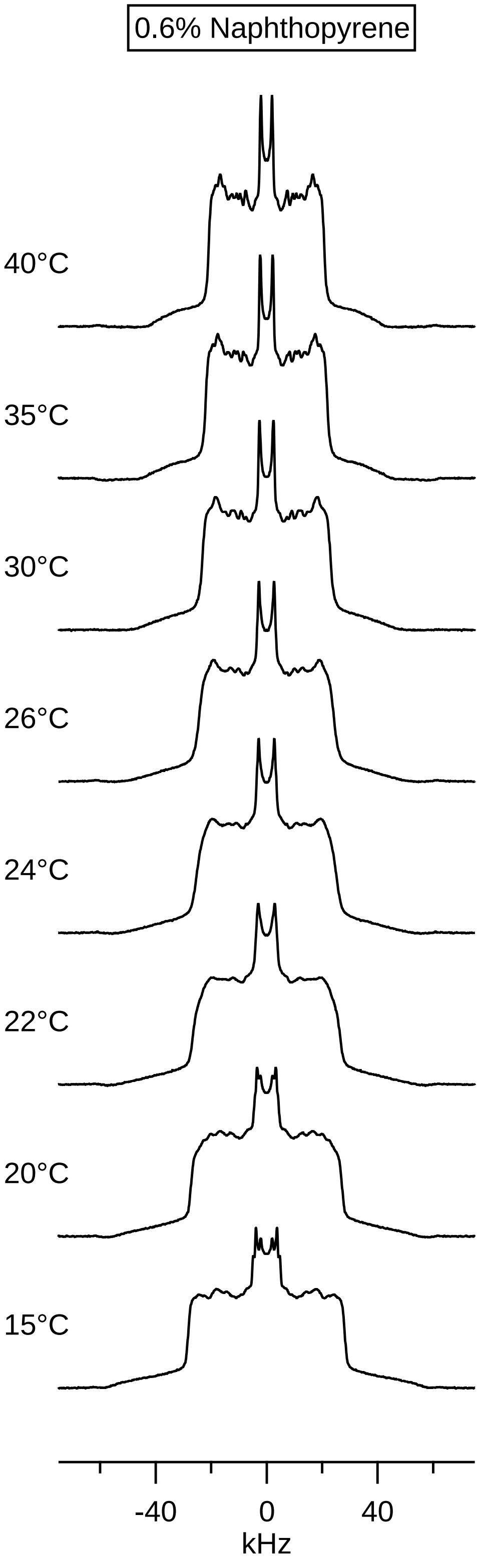

Figure 3.12: ^{2}H NMR spectra between 15 and 40°C for 35:35:30 DOPC:DPPC-D62:chol MLV with 0.6% naphthopyrene.

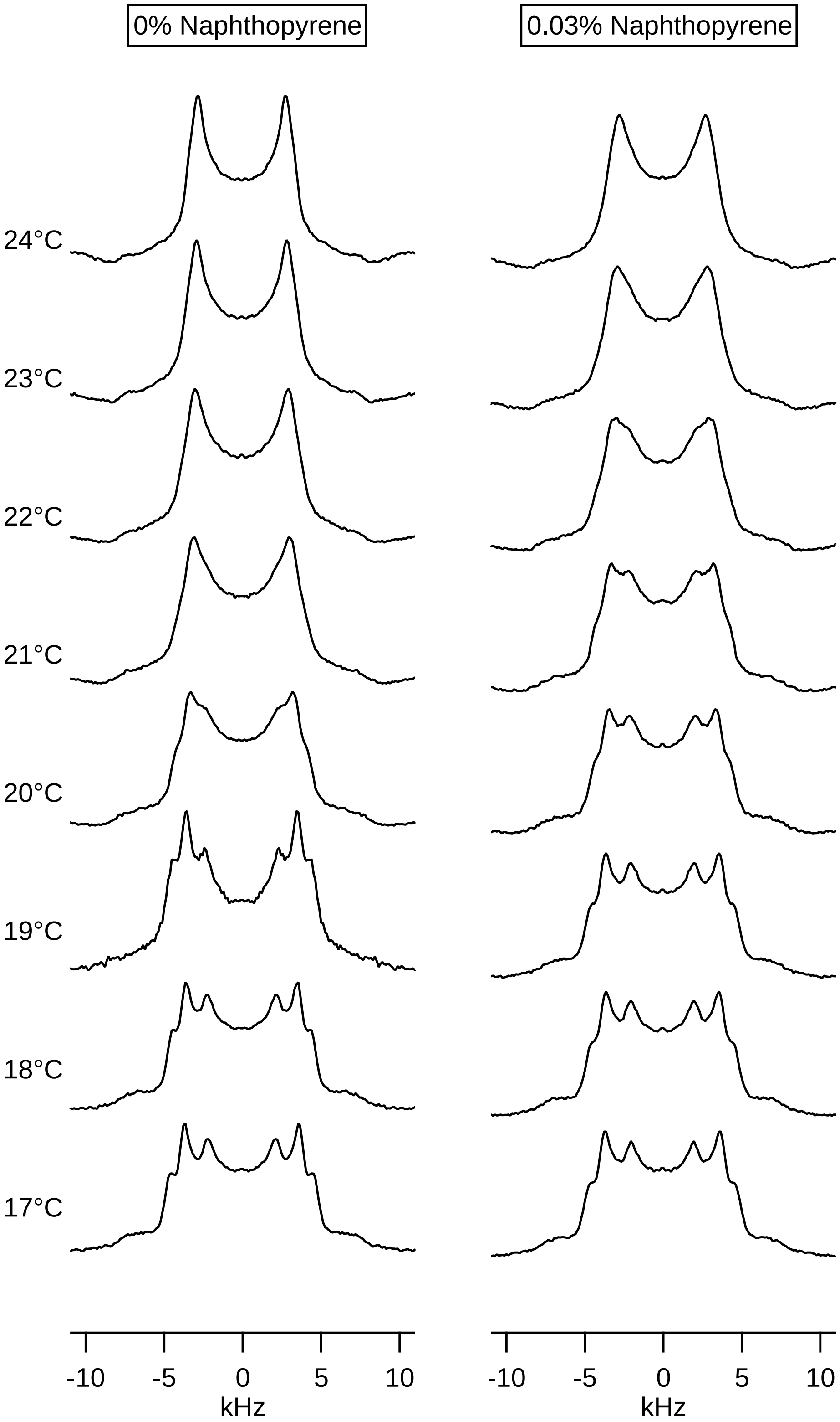

Figure 3.13: ^{2}H NMR spectra, focusing on the methyl peaks, between 17 and 24°C for 35:35:30 DOPC:DPPC-D62:chol MLV with 0 (left) and 0.03% (right) naphthopyrene.

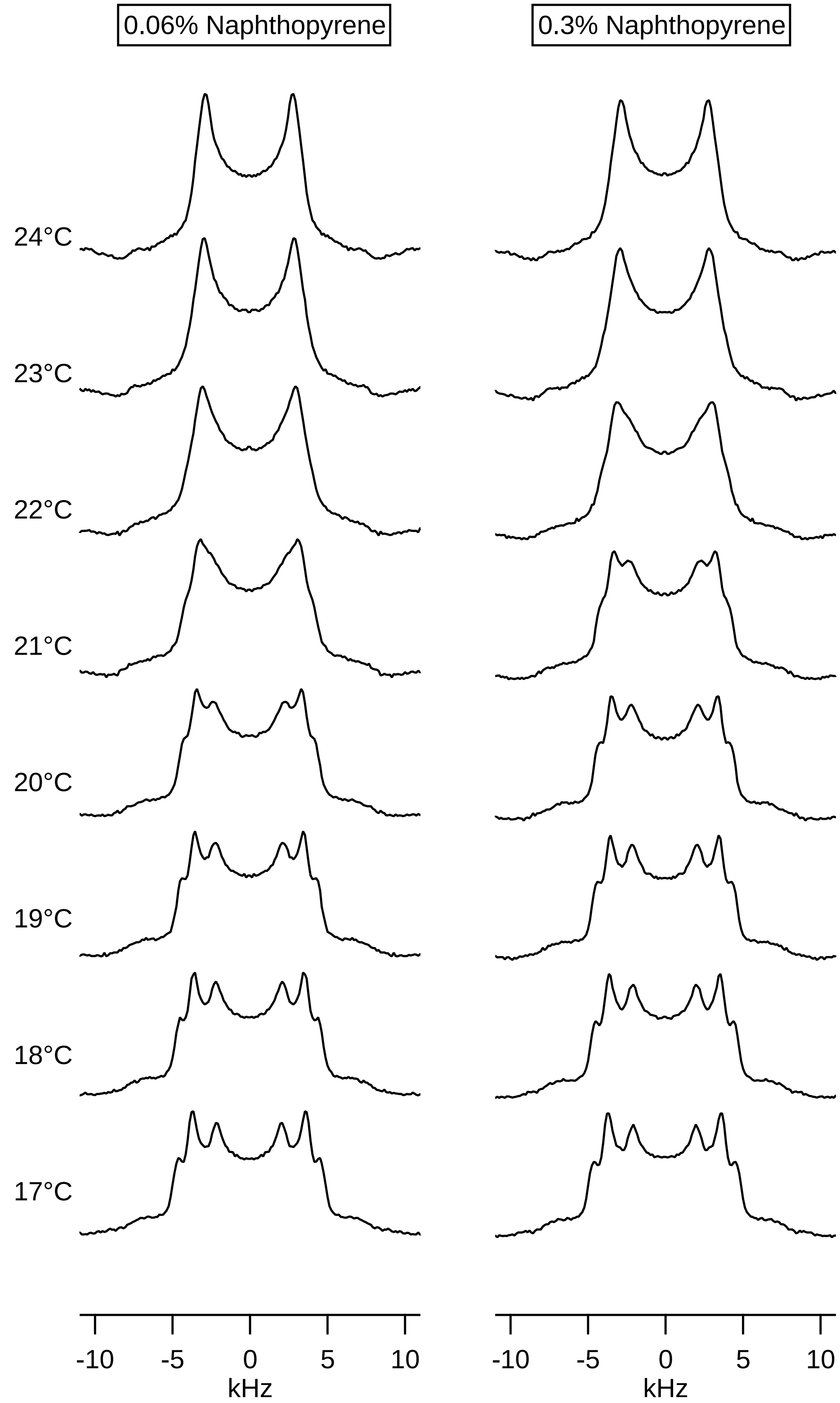

Figure 3.14: ^{2}H NMR spectra, focusing on the methyl peaks, between 17 and 24°C for 35:35:30 DOPC:DPPC-D62:chol MLV with 0.06 (left) and 0.3% (right) naphthopyrene.

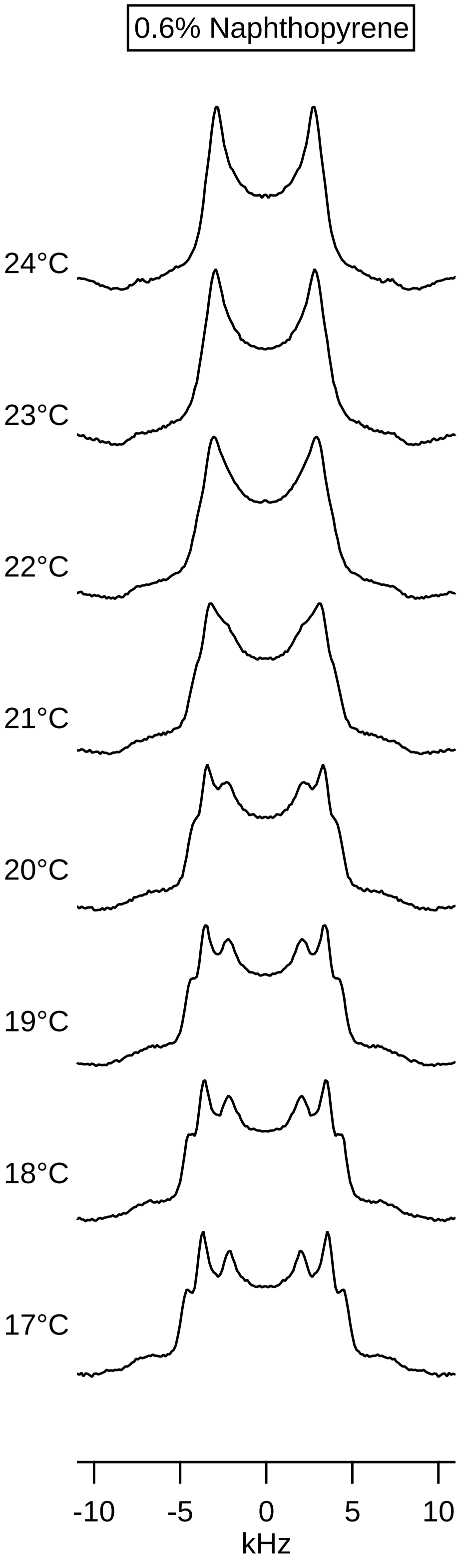

Figure 3.15: ^{2}H NMR spectra, focusing on the methyl peaks, between 17 and 24°C for 35:35:30 DOPC:DPPC-D62:chol MLV with 0.6% naphthopyrene.

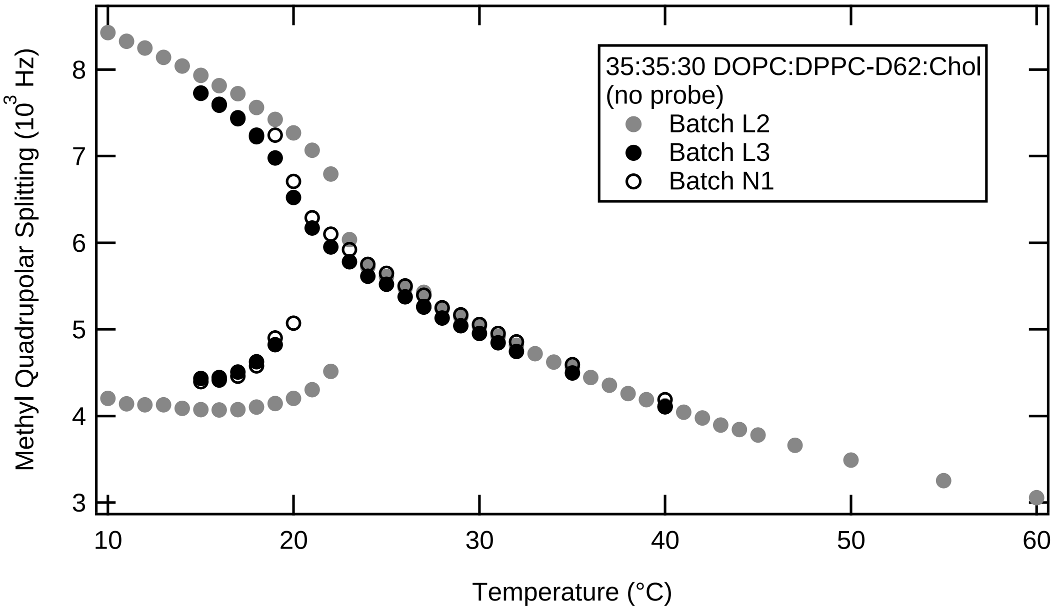

Figure 3.16: ^{2}H NMR methyl splitting for probe-free 35:35:30 DOPC/DPPC-D62/chol MLV. Errors are smaller than the symbols.

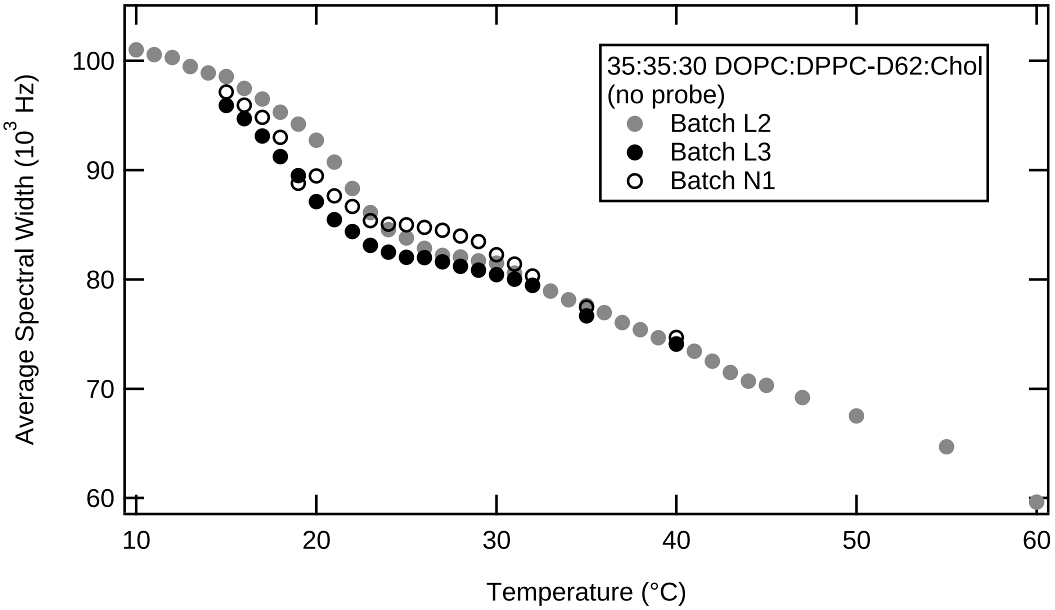

Figure 3.17: ^{2}H NMR M_1 for probe-free 35:35:30 DOPC/DPPC-D62/chol MLV. Measurement of M_1 for batch L3 at 35°C and for batch N1 at 19°C was affected by a known artifact in some of our spectra at ±60 kHz, caused by sporadic acoustic ringing of the coil [134, appendix A].

Figure 3.17 shows the temperature dependence of M_1. Changes in M_1 reflect changes in spectral shape resulting from phase transitions (Sec. 3.1.2). Since M_1 sums over the spectra of all methylene and methyl groups on the deuterated lipid chain, differences in M_1 reflect overall changes to the deuterated lipid chain. The $\mathbf{l_d}$, $\mathbf{l_o}$, and $\mathbf{s_o}$ phases all have different M_1 ranges because of their unique spectral shapes. The M_1 can also be used to quantify the differences between $\mathbf{l_d}+\mathbf{l_o}$ and $\mathbf{l_d}$ spectra: The more ordered spectra have larger M_1 values attributable to the spread of the spectra to frequencies of larger magnitude. As temperature increases, average spectral width decreases as the acyl chains gain more conformational freedom. Phase transitions are marked by sudden changes in the slope of a graph of M_1 versus temperature. In Fig. 3.17 this sudden change is completed by 24.5±0.5°C for batch L2, and at 22.5±0.5°C for batches L3 and N1. These temperatures are 0.5-1.5°C higher than T_{mix} determined from visual inspection of the spectra. Above these temperatures, M_1 is only decreasing because the lipid chains are becoming more flexible. Below these temperatures, the rate of change in M_1 is higher since M_1 decreases for two reasons: increase in lipid chain mobility and decrease in number of lipids in the $\mathbf{l_o}$ phase. Near 10°C, the changes become more gradual again.

Batch-to-batch variation arises because lipid weight determination is difficult with small quantities of lipid. Lipids are hygroscopic: they pick up water from the atmosphere easily, and it is difficult to fully remove water from the lipids. When small quantities of lipid are used, the amount of absorbed water can contribute greatly to the weight. When they are dry, static can make them stick to the spatula and fly away from their container. Thus, stock solution compositions may vary. Note that T_{mix} is exquisitely sensitive to composition. While in the homogeneous phase (above 23°C in Fig. 3.16), it is evident that all three "control" samples are very similar.

3.6 Proportion of DPPC-D62 in the two phases

Additional experiments were performed on batch 2 at TR of 2 s. Figure 3.18 shows an example dePaked spectrum at 18°C for 35:35:30 DOPC/DPPC-D62/chol MLV. Lorentzian line shapes fitted well to the methyl peaks of dePaked spectrum. This indicates that the terminal methyls are fully relaxed after 2 s and that the methyl peak areas in the spectrum are directly proportional to the number of spins in each phase. Spectra obtained with TR

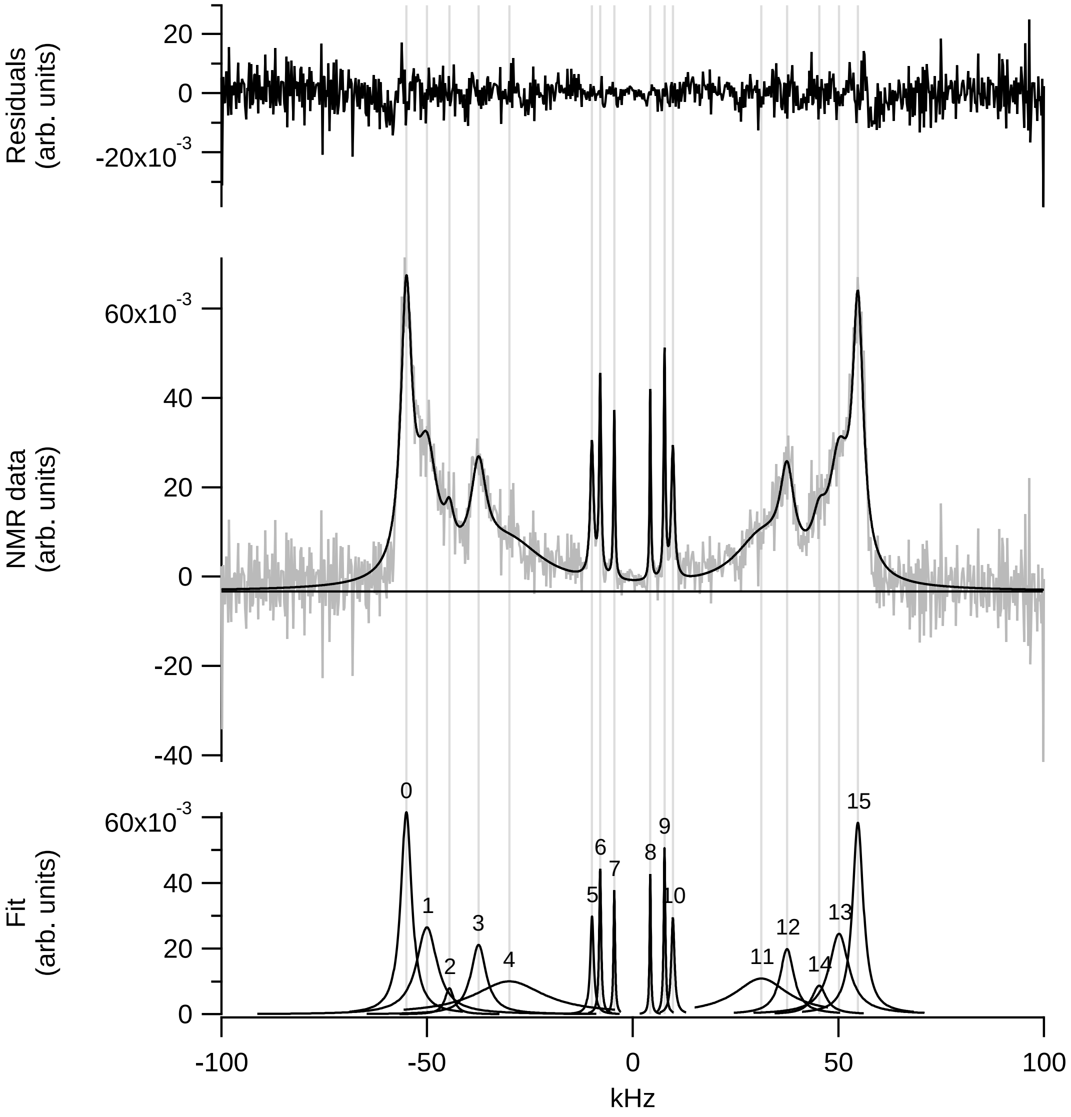

Figure 3.18: DePaked spectra with fit and residuals for probe free 35:35:30 DOPC/DPPC-D62/chol MLV from batch L2 at 18°C. (Top) Residuals from the fit. (Middle) The dePaked spectrum is shown in gray, the sum of the fitted Lorentzian peaks is shown in black, and the fitted baseline is the flat line just below 0 arb.units. (Bottom) 15 individual Lorentzian peaks that were fitted to the dePaked spectrum using the MultipeakFit package in Igor Pro. Peaks 5 and 10 are assigned to the *sn*-2 $\mathbf{l_o}$ methyls. Peaks 6 and 9 are assigned to the *sn*-1 $\mathbf{l_o}$ methyls. Peaks 7 and 8 are assigned to the $\mathbf{l_d}$ methyls.

= 2 s differs from 300 ms TR spectra in that the methyl groups had time to equilibrate in between scans; their signal intensity is higher in the 2 s TR spectra. The fraction of DPPC-D62 that is in the **l$_\mathbf{d}$** phase is thus given by the ratio of the methyl peak areas of the **l$_\mathbf{d}$** phase to the sum of the **l$_\mathbf{d}$** and **l$_\mathbf{o}$** phase (right hand side of Eq. (3.9)). In the example shown, the **l$_\mathbf{d}$**-to-**l$_\mathbf{o}$** methyl peak area ratio was 3.25. This means that 23.5% of DPPC-D62 are in the **l$_\mathbf{d}$** phase and 76.5% are in the **l$_\mathbf{o}$** phase. Figure 3.19 shows the temperature dependence of percent DPPC-D62 in the **l$_\mathbf{d}$** phase in 35:35:30 DOPC/DPPC-D62/chol membranes devoid of probe. Although the tight packing of chol and saturated lipids are typically associated with the more ordered phase, Fig. 3.19 shows that there is a moderate amount of DPPC-D62 in the **l$_\mathbf{d}$** phase as well. As temperature approaches T$_{\mathrm{mix}}$, the fraction of DPPC-D62 in the **l$_\mathbf{d}$** phase increases, but only slightly.

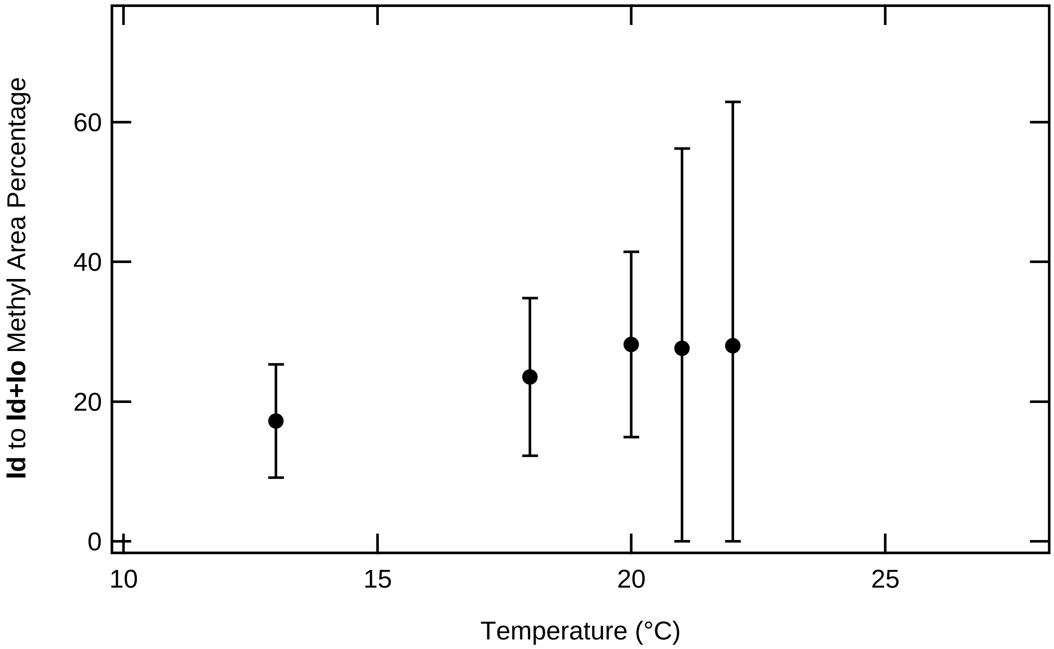

Figure 3.19: Percent of DPPC-D62 methyl signal from the **l$_\mathbf{d}$** phase in 35:35:30 DOPC/DPPC-D62/chol MLV below T$_{\mathrm{mix}}$. The **l$_\mathbf{d}$** methyl peak area was divided by the sum of the **l$_\mathbf{d}$** and **l$_\mathbf{o}$** methyl peak areas.

3.7 Effect of fluorescent probes on membranes

Figure 3.20 (top) shows the lowest temperature where a single methyl quadrupolar splitting is visible during visual inspection of the spectrum for 35:35:30 DOPC/DPPC-D62/chol membranes containing either Laurdan or naphthopyrene at various probe concentrations.

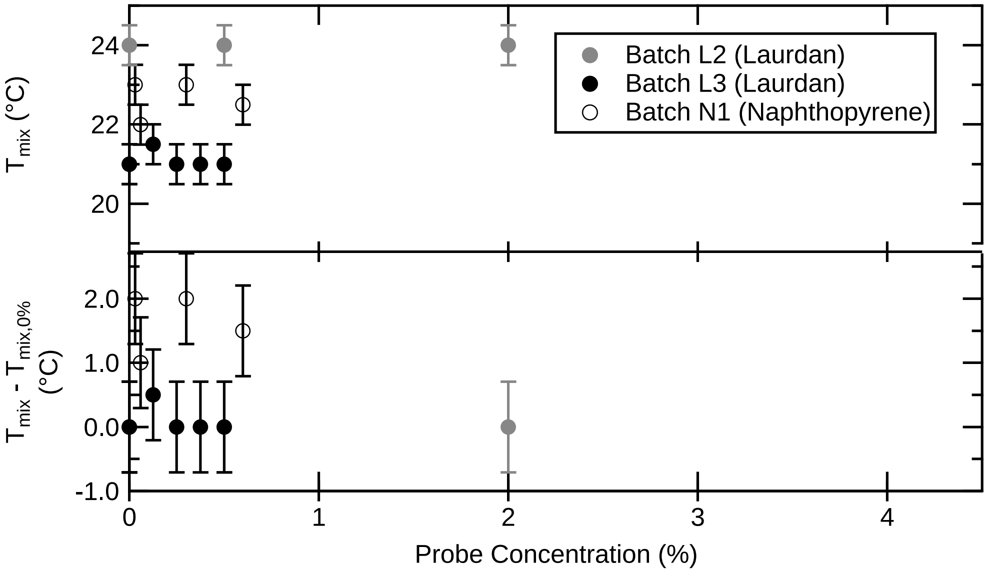

Figure 3.20: Miscibility transition temperature (T_{mix}) measured using ^{2}H NMR for 35:35:30 DOPC/DPPC-D62/chol MLV with both fluorescent probes. A number of points overlap: 0% batch L3 and 0% batch N1 have the same T_{mix}; T_{mix} at 0.5% Laurdan for both batch L2 and L3 are the same as 0%.

A probe-free sample is made with each batch, and the difference between T_{mix} and the T_{mix} measured for the probe-free sample from the same batch is shown in Fig. 3.20 (bottom). Both batch L2 and batch L3 data shows that adding 0.1-2% Laurdan does not change T_{mix}. Adding 0.03-0.6% naphthopyrene, however, raised T_{mix} by 1-2°C.

3.7.1 Laurdan

Figures 3.21 and 3.22 show the temperature dependence of methyl quadrupolar splittings for membranes with various Laurdan concentrations. The fork in the graph indicates T_{mix}. Below T_{mix}, two splittings are shown: the larger splitting comes from the $\mathbf{l_o}$ *sn*-1 methyls and the smaller one is from the $\mathbf{l_d}$ methyls. Our ability to measure both splittings indicate $\mathbf{l_d}+\mathbf{l_o}$ phase coexistence. Above T_{mix}, a single methyl splitting is measured for the homogeneous fluid phase. Some T_{mix} in Figs. 3.21-3.22 may be 1-2°C lower than shown in Fig. 3.20 since visual inspection can pick up on barely resolvable peaks, but the peak picking algorithm used in determining methyl quadrupolar splitting cannot measure the splitting if the two peaks are insufficiently resolved. Regardless of absolute temperature of T_{mix}, the addition of 0.1-2% Laurdan alters T_{mix} by less than 1°C, which is within batch-to-batch variation

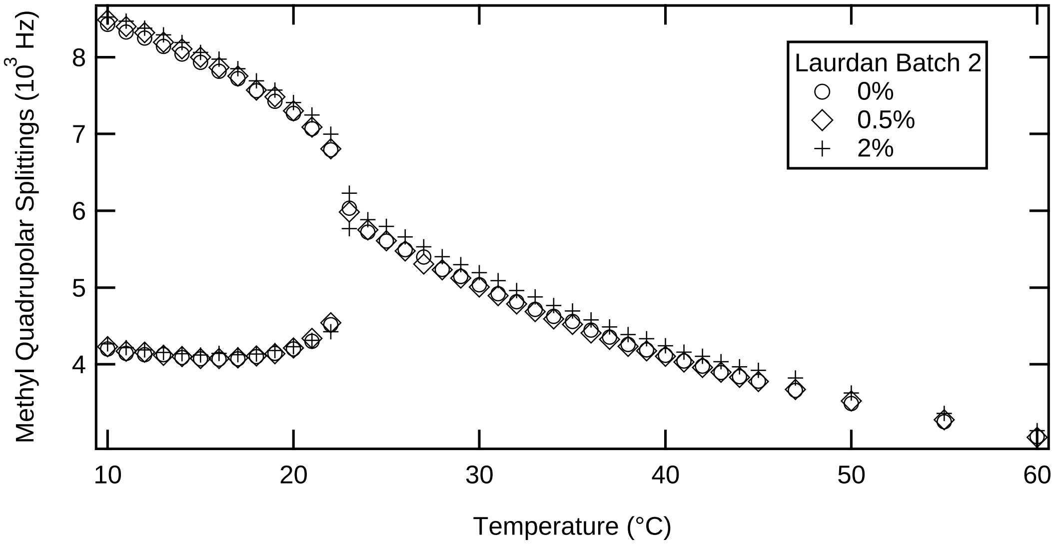

Figure 3.21: Temperature dependence of ^{2}H NMR methyl quadrupolar splittings of 35:35:30 DOPC/DPPC-D62/chol MLV with 0-2% Laurdan. Data from batch L2. There are more data points at 27°C because 27°C is repeated at the end of the temperature run to check for sample degradation.

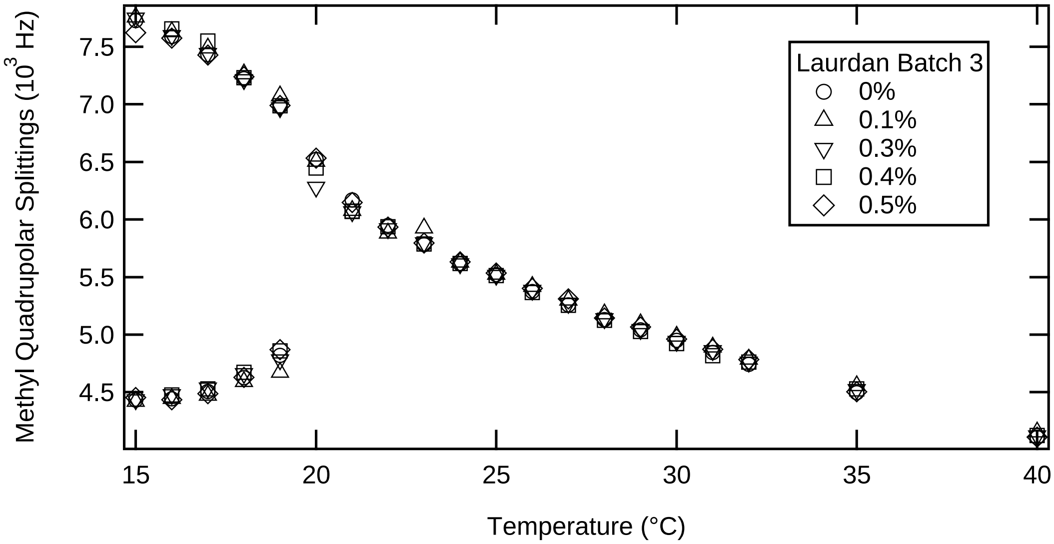

Figure 3.22: Temperature dependence of ^{2}H NMR methyl quadrupolar splittings of 35:35:30 DOPC/DPPC-D62/chol MLV with 0-0.5% Laurdan. Data from batch L3. There are more data points at 27°C because 27°C is repeated at the end of the temperature run to check for sample degradation. 0.4% M_1 from 15 to 20°C appears to be lower because of thermocouple misplacement (see Fig. 3.24).

(Sec. 3.5). Figures 3.23 and 3.24 show M_1 temperature dependence for membranes with 0.1-2% Laurdan. The data for all concentrations nearly coincide, indicating that the rest of the DPPC-D62 chains were also not affected by Laurdan.

Addition of 0.1-2% Laurdan did not alter conformational order of the methyl or the methylene groups on the two lipid chains of DPPC-D62 and had negligible effect on T_{mix} of 35:35:30 DOPC/DPPC-D62/chol MLV.

3.7.2 Naphthopyrene

Figure 3.25 shows the temperature dependence of the methyl quadrupolar splittings for membranes containing 0.03-0.6% naphthopyrene. 0.03-0.6% naphthopyrene increases T_{mix} by 1-2°C. Below T_{mix}, $\mathbf{l_o}$ methyl group conformational order is mostly insensitive to naphthopyrene concentration, but the $\mathbf{l_d}$ methyl quadrupolar splittings decrease (at a given temperature) in the presence of naphthopyrene.

Below T_{mix}, the $\mathbf{l_o}$ methyl splittings remained unchanged far away from T_{mix} and increased by 5% near T_{mix} (at $T = T_{mix} - 2°C$) in the presence of naphthopyrene. It is unclear why the $\mathbf{l_o}$ splittings remain unchanged far from (and below) T_{mix} since more naphthopyrene is expected in the $\mathbf{l_o}$ phase than the $\mathbf{l_d}$ phase. It is surprising that the $\mathbf{l_d}$ methyls were more affected by the addition of naphthopyrene than the $\mathbf{l_o}$ methyls, given the scarcity of DPPC-D62 in the $\mathbf{l_d}$ phase (Fig. 3.19). Fluorescence microscopy experiments (see Fig. 4.14) also show that the $\mathbf{l_o}$ domain areas are bigger than the $\mathbf{l_d}$ domain areas in 35:35:30 DOPC/DPPC-D62/chol GUVs. The $\mathbf{l_d}$ methyl splittings decreased 2-15% in the presence of naphthopyrene. The greatest changes in $\mathbf{l_d}$ methyl splittings were also observed near T_{mix}. Unexpectedly, the decrease is not proportional to the concentration of naphthopyrene. Naphthopyrene interacting with the $\mathbf{l_d}$ phase DPPC-D62 could be an indication that naphthopyrene is present in the $\mathbf{l_d}$ phase, which would be consistent with naphthopyrene showing only a modest preference for the $\mathbf{l_o}$ phase over the $\mathbf{l_d}$ phase (Fig. 2.8). It might also be that naphthopyrene is changing the composition of the $\mathbf{l_d}$ and $\mathbf{l_o}$ phases. The chemical structure of naphthopyrene is reminiscent of the fused ring structure of chol. It may be that naphthopyrene pushes DOPC out from the $\mathbf{l_o}$ phase.

Figure 3.26 shows M_1 temperature dependence for membranes containing 0.03-0.6% naphthopyrene. The curves overlap above T_{mix}, indicating that the methylenes are unaffected by incorporation of naphthopyrene. Below T_{mix}, M_1 was 2-4% higher in samples with

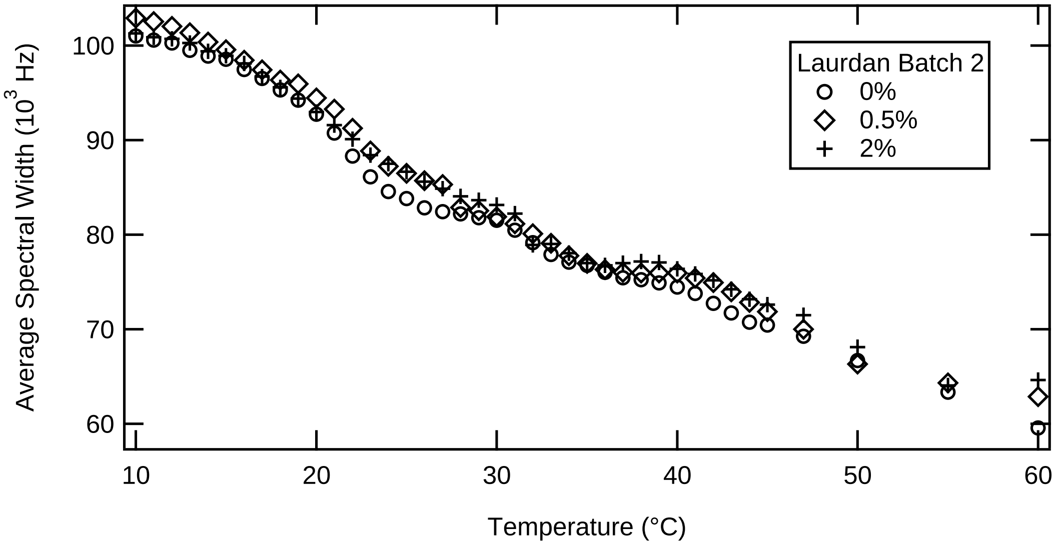

Figure 3.23: ^{2}H NMR average spectral width temperature dependence for 35:35:30 DOPC/DPPC-D62/chol MLV with 0-2% Laurdan. Data from batch L2.

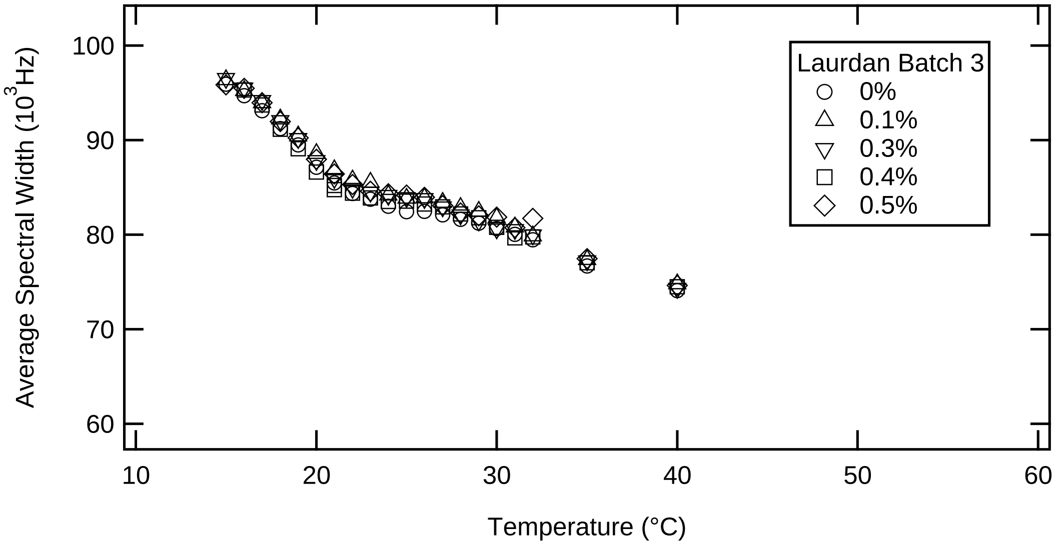

Figure 3.24: ^{2}H NMR average spectral width temperature dependence for 35:35:30 DOPC/DPPC-D62/chol MLV with 0-0.5% Laurdan. Data from batch L3. 0.4% M_1 from 15 to 20°C appears to be lower because of thermocouple misplacement. When shifted 2 degrees over, then those points do overlap with the other probe concentrations.

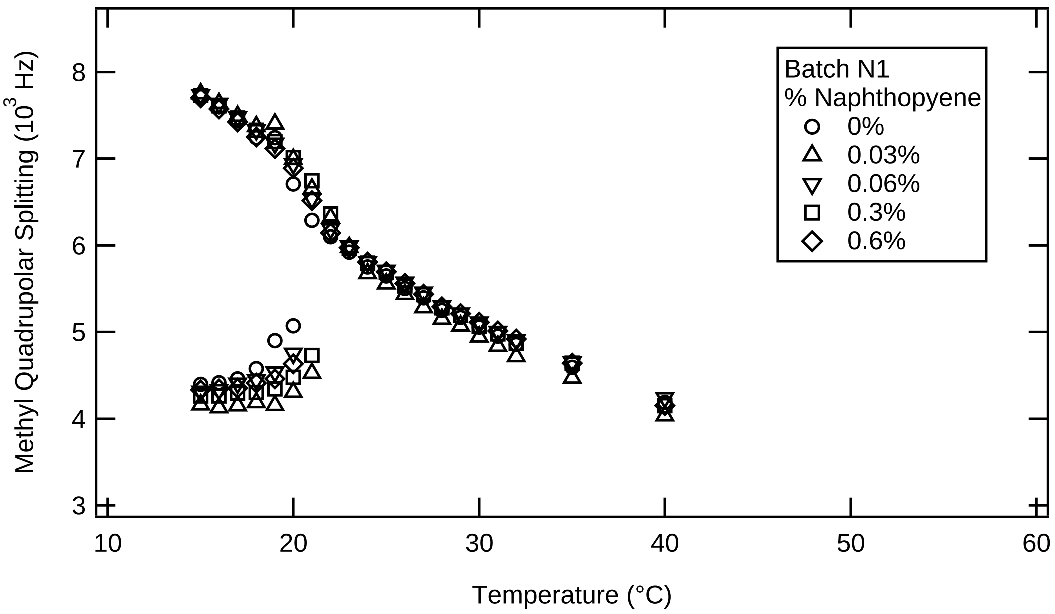

Figure 3.25: ^{2}H NMR methyl quadrupolar splittings temperature dependence for 35:35:30 DOPC/DPPC-D62/chol + 0-0.6% naphthopyrene MLV.

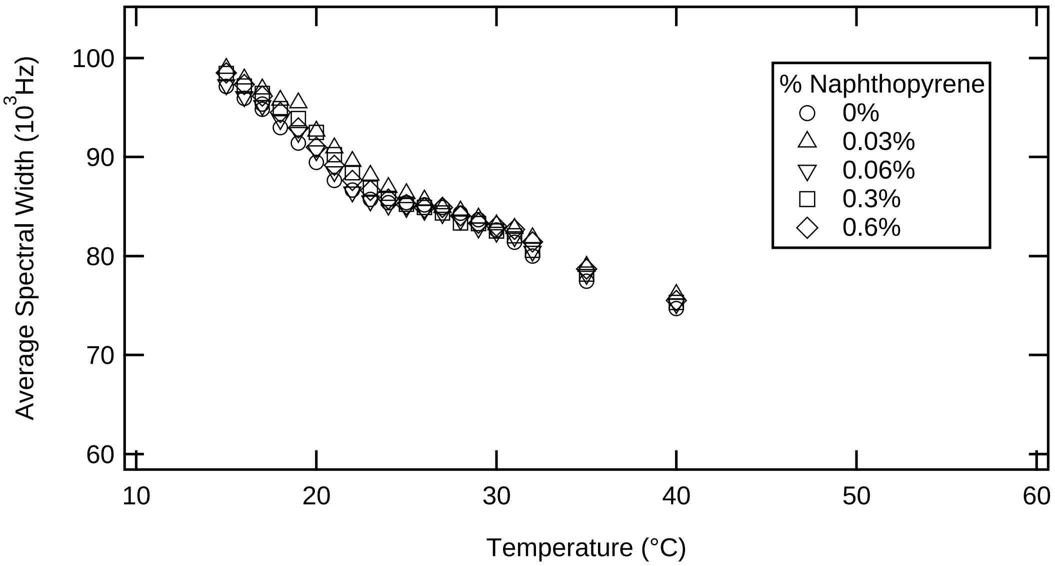

Figure 3.26: ^{2}H NMR average spectral width temperature dependence for 35:35:30 DOPC/DPPC-D62/chol + 0-0.6% naphthopyrene MLV.

naphthopyrene incorporated, indicating that naphthopyrene increased DPPC-D62 chain order. These changes are on the same order of magnitude as those caused by a 1°C temperature difference.

In summary, naphthopyrene decreases the **l_d** and has little effect on the **l_o** methyl group order. Probe-induced increases in M_1 suggests that overall membrane stiffness is increased below T_{mix} because of naphthopyrene.

3.8 Chapter summary

The **l_d** and the **l_o** phase both have signature ^2H NMR spectra that are easy to identify, even when they coexist. Phase assignment can be done in the presence or absence of probe; ^2H NMR is well suited to the task of determining the effect of fluorescent probes on the phase states of MLVs.

This chapter presented data from membranes with either Laurdan or naphthopyrene incorporated. Laurdan is a probe that partitions nearly equally between the **l_d** and the **l_o** phases. Membranes made with 35:35:30 DOPC/DPPC-D62/chol are not altered significantly by the addition of 0.1-2% Laurdan. Some batch-to-batch variations are noted in probe-free membranes; they are most obvious in the methyl splittings below T_{mix}. Comparison of the samples here with mixtures with the same nominal compositions in the literature will be made in the Discussion (Ch. 5). Spectral shape, average spectral width, methyl quadrupolar splittings, and T_{mix} are similar for samples with and without Laurdan. Their similarity is amazing given the batch-to-batch variations found in probe-free samples.

Naphthopyrene has a modest preference for the **l_o** phase. The addition of naphthopyrene increased T_{mix} by 1-2°C. Below T_{mix}, it also decreased the order in the DPPC-D62 **l_d** methyls, but the order of the **l_o** methyls remained unaffected far from T_{mix}. Above T_{mix}, the methyl groups were also unaffected by the presence of naphthopyrene.

Chapter 4

Fluorescence microscopy investigation of Laurdan's effects on GUV

When vesicles are doped with fluorescent probes, the individual vesicles can be directly observed with microscopy. Giant unilamellar vesicle (GUV), because of their large size, are the model system of choice for microscopy because of the optical resolution of the microscope (~200-300 nm). Not only do the vesicles have to be big enough, the domains also have to be big enough in order for them to be resolvable under the microscope. Unilamellar membranes are required for phase determination using fluorescence since intralamellar spacing is smaller than the resolution of the microscope. Typical microscopy experiments rely on probes that partition preferentially into a particular phase. In contrast, Laurdan is an environment-sensitive membrane probe that partitions equally throughout fluid membrane phases. However, Laudan general polarization (GP) (Eq. 2.33) images obtained with two-photon excitation microscopy can divulge phase state information about different parts of a vesicle.

This chapter focuses on the use of Laurdan in membrane studies. The experiments of this chapter were performed at Centre for Membrane Biophysics at the University of Southern Denmark under the supervision of Luis Bagatolli and Jonathan Brewer. Fluorescence spectroscopy experiments illustrate the power of microscopy (Sec. 4.2). Details on the protocols used in giant unilamellar vesicle preparation, two-photon excitation microscopy, and image analysis are presented in Sec. 4.1. The experimental protocol was chosen to parallel deuterium nuclear magnetic resonance spectroscopy (^{2}H NMR) experiments as much as possible so that the results can be compared directly with ^{2}H NMR. A discussion of the differences between the two protocols, namely the use of GUV instead of MLV, will be deferred to Sec. 5.6. Secs. 4.3-4.5 are devoted to micrographs and GP temperature dependence from microscopy experiments.

4.1 Methods

4.1.1 Fluorescence spectrometry

Bulk Laurdan GP in 35:35:30 DOPC/DPPC-D62/chol multilamellar vesicles (MLVs) was measured with an ISS Chronos Fluorimeter. The method used for making MLVs was the same as the one (freeze-thaw-mix) used in ^{2}H NMR experiments (Sec. 3.1). 5 mm cuvettes were used to hold the MLVs for fluorimeter measurements. GPs were averaged over 50 scans at each temperature. The 0.05% Laurdan sample was taken with 200 scans; the higher scan number was used to compensate for the lower probe content. In order to match equilibration times between temperatures in ^{2}H NMR experiments, the following protocol involving three water baths was implemented:

1. Six samples with various probe concentrations were placed into six cuvettes and placed into water bath #1, and equilibrated to a particular temperature.
2. Three cuvettes were placed into the fluorimeter, which was already heated/cooled to the same temperature as water bath #1 using water bath #2. A thermocouple was inserted into the probe-free sample and the measured temperature was recorded.
3. After measurements were taken, the three cuvettes were moved into water bath #3, which was set to the next temperature up.
4. The other three cuvettes were taken from water bath #1, and steps 2 and 3 were repeated.
5. When all six samples were done, water bath #2 was set to the next temperature, and the fluorimeter was given at least 10 min to equilibrate. When the thermocouple indicated that the fluorimeter has reached the next temperature, measurements at the next temperature were taken. Water bath #1 was prepared for other experiments down the line.

4.1.2 Preparing giant unilamellar vesicles

Electroformation is a common method for making GUV with high phosphatidylcholine (PC) and low charged lipid content [166]. It produces a relatively monodisperse population of vesicles, with higher yield and less multivesicular vesicle (MVV)[1] formation than the more traditional gentle hydration method [77]. Vesicles formed by electroformation are unilamellar [43, 102, 167, 168]. GUV and LUV have no significant curvature stress and it is thus expected that the lipid distribution between the two leaflets is the same [27]. Lamellarity can be checked in fluorescence experiments: multilamellar membranes show higher fluorescence intensity. Details on GUV formation and electroformation chamber fabrication can be found in [33, 166, 169]. GUV preparation, as performed in this thesis, is described below.

DOPC, DPPC-D62, and cholesterol were purchased from Avanti Polar Lipids. Concentrations of DOPC and DPPC-D62 were checked using phosphorous assay (Appendix E), and were consistent with those reported by Avanti Polar Lipids (10 mg/ml ± 10%). Lipids were used without further purification. Cholesterol was purchased in powder form, and dissolved in $CHCl_3$ to make a 10 mg/ml solution.

35:35:30 DOPC/DPPC-D62/chol lipid stock solution, with lipids dissolved in chloroform ($CHCl_3$), and appropriate amount of probe were prepared at 1mg/mL, and kept in amber vials filled with nitrogen gas. The vial caps have a silicon and a Teflon side. To prevent chemical reactions with $CHCl_3$, the chemically inert Teflon side faced the inside of the vial, and the threads of the vials were wrapped with Teflon tape to ensure a tight seal. The vials were wrapped in foil for added protection from light exposure, and kept in the freezer. This stock was diluted to 2 mg/mL with $CHCl_3$ prior to deposition on electroformation wires.

2 μL of the 2 mg/mL lipid solution was deposited on the electroformation platinum (Pt) wires. There were two wires per electroformation cell. 300 μL of 200 mM sucrose (0.070 Osm/Kg (measured)) was added to each electroformation chamber. At MEMPHYS, there were two different types of electroformation apparatus: closed- and open-bottom chambers (Fig. 4.1). Both types were made from Teflon. A cover slip was glued to the bottom of the open-bottom ones to hold liquid and to allow for imaging using an inverted microscope. Imaging cannot be done directly with the closed-bottom ones. A function

---

[1] Multivesicular vesicles are those enclosing other vesicles.

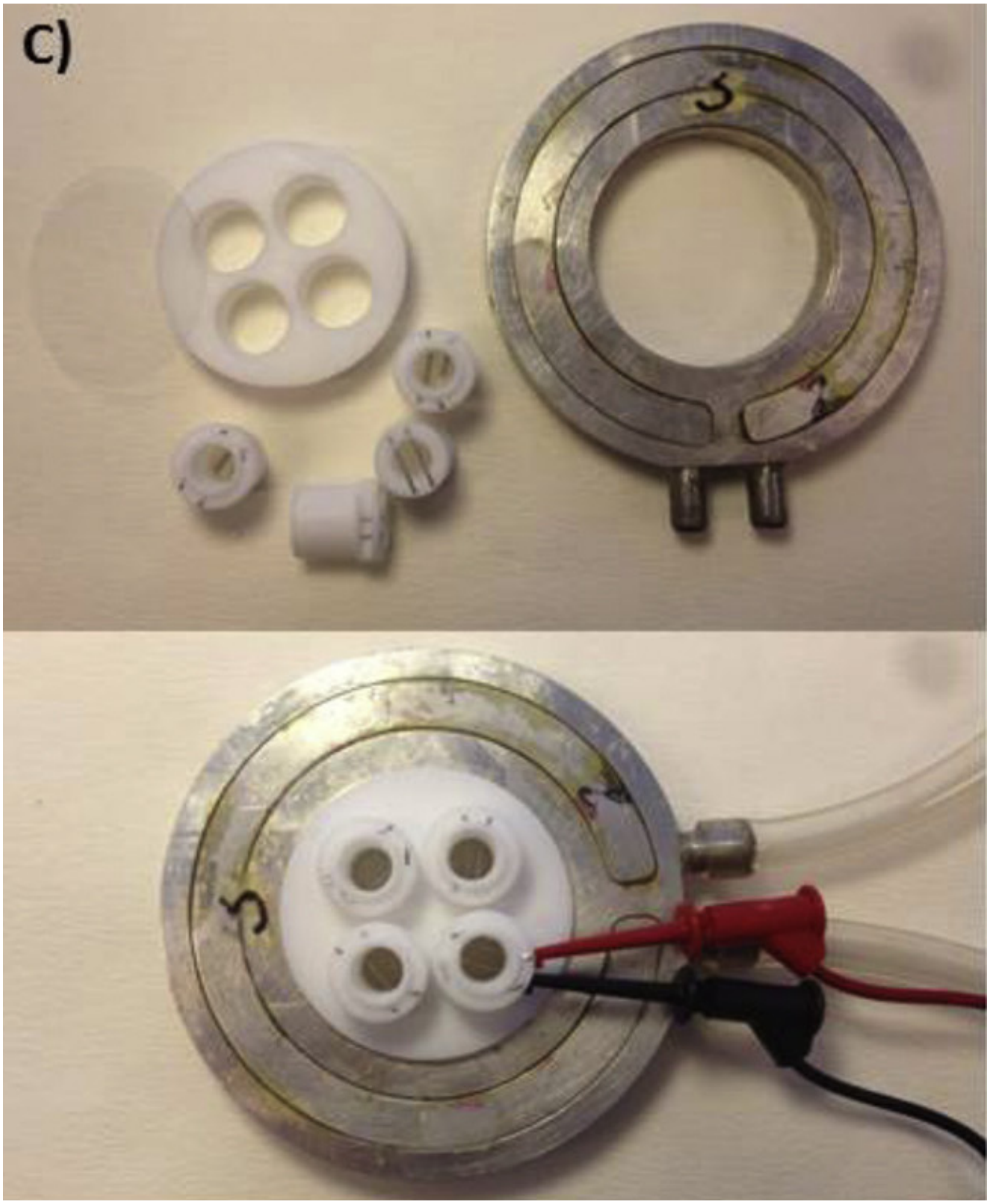

Figure 4.1: Temperature-controlled electroformation chamber. Lipids are applied to the Pt wires prior to assembly (top). Water is added to the chamber after assembly (bottom). A circulating water bath is connected to the metal ring by tygon tubing to heat or cool the electroformation chamber. Alligator clips connect the Pt wires to the function generator. Adapted from [170] with permission.

generator was attached to the Pt wires and set to generate a 2 V, 10 Hz, sine wave at ~55°C for 1h 50 min for vesicle formation. This temperature is above the main phase transition temperature of the highest melting point lipid (36°C for DPPC-D62[2]). The vesicle growth apparatus was insulated with a piece of Styrofoam placed on top of the electroformation chamber. Attempts at insulating the bottom with Styrofoam overheated the electroformation chamber and led to disassembly: the epoxy used to glue the cover slip glass to the Teflon over-heated. Standard epoxy from the hardware store was used. Optical grade epoxy can also be used, but hardware store epoxy was more viscous and easier to work with when applying to Teflon. Electroformation was performed at 55°C because of these technical constraints, even though Veatch [169] found 60°C to be optimal for GUV formation of 35:35:30 DOPC/DPPC-D62/chol GUV (see Sec.4.1.3). Following vesicle formation, the function generator was set to generate a 1 V, 2.5 Hz, sine wave for 10 min to detach the vesicles from the electroformation wires.

After GUV formation and detachment, the function generator was turned off, and the sample was allowed to equilibrate to room temperature for an hour. Cold water was added to the water bath reservoir at regular intervals to ensure a slow cooling rate since there was no cooling function on the water bath used. Allowing the sample to equilibrate to room temperature without a water bath would have resulted in a faster cooling rate.[3] The sample was then moved to the microscopy room water bath for further cooling below room temperature. The microscopy room water bath is capable of heating and cooling. The sample was cooled to the lowest desired imaging temperature and allowed to equilibrate for another 1.5 hr. Fast cooling rate of 10°C/s can cause internal vesicles of MVV to be expelled [173], but slower cooling rates and long equilibration times were chosen to ensure large domain formation for imaging purposes. Morales-Penningston et al. [33] describe additional consequences of fast and slow cooling rates.

---

[2] The main phase transition temperature of non-deuterated DPPC is 41°C [171]. Deuteration is expected to lower T_m by 2.5°C [67]

[3] Dr. Jonathan Brewer at the Centre for Membrane Biophysics, University of Southern Denmark, said he would cool his supported bilayer samples quickly until it got near the transition temperature, and then slowly cool through the transition to obtain large domains by cooling at a rate of 2°C/min, or he would cool from 60°C to room temperature in an hour [172]. Slower cooling rate would result in larger domains [172]. Since the NMR data show that T_{mix} is around 21°C, the cooling rate used in this thesis should be acceptable.

4.1.3 Electroformation temperature

As with MLV formation for ^{2}H NMR (Sec. 3.1.1), it is important that electroformation take place above T_m of the highest melting lipid, here DPPC-D62. Electroformation temperatures between 40 and 60°C are expected to form vesicles with the same T_{mix} [169]. Electroformation below these temperatures is possible, but the yield tends to be low to none. In one case, where electroformation occured below this temperature range by accident, very homogeneous GP images were obtained at imaging temperatures around and below room temperature (data not shown). Veatch [169] reported recording lower T_{mix} for vesicles grown below 40°C.

4.1.4 Immobilizing vesicles for imaging

The goal of these experiments is to obtain static images of the vesicles. One way to immobilize vesicles is to image them while they are still attached to the Pt electroformation wire. Figure 4.2 is an image of a vesicle immediately after electroformation and prior to vesicle detachment. From the roundedness of the main vesicle and its proximity to other vesicles, it can be inferred that the main vesicle is indirectly attached to the Pt wire via contact with other vesicles. Images collected in this manner have been published by other research groups [28, 131, 168], but there is also evidence that the vesicles should be detached prior to imaging [169]. Vesicles typically stay attached for about a day. Vesicles attached to other vesicles or other surfaces (e.g., the wire, the side wall of the chamber), appear more ordered at the attachment interface. Sides attached to the wire or to other vesicles are flat. These flat sides have different GP than the rest of the vesicle. The geometrical constraints imposed by neighbouring structures induce a different curvature that promotes aggregation of different lipids.

Observation of free-standing vesicles avoids curvature-induced order. The vesicles can be detached from the Pt wires after electroformation, and pipetted from the electroformation chamber into an observation chamber using a 1 mL micropipette. The pipette tip is cut off ~ 1 cm from the end to create a bigger hole, so that the vesicles do not rupture during transfer. Eight-chamber observation slides that are typically used in cell imaging can be used as the observation chamber. Typically, 400 μL of fluids (vesicles and solvent) is put into

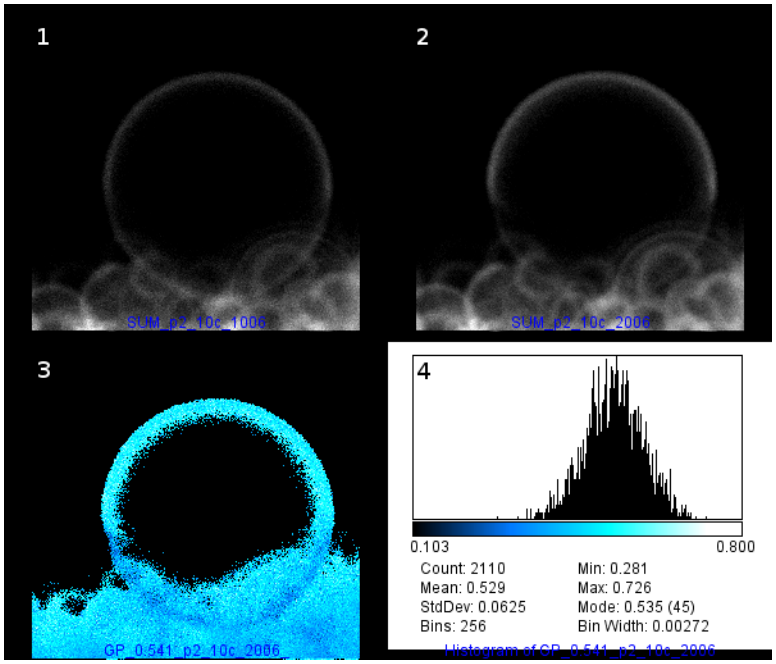

Figure 4.2: Micrographs of vesicles with 0.2% Laurdan at 10°C from the 121113 sample, attached to the electroformation wire. Intensity images at 490 nm (1) and 440 nm (2). (3) False colour GP image obtained via a pixel by pixel calculation of the GP using the intensity images, with the whole vesicle chosen as the ROI. (4) is the histogram corresponding to the ROI shown in (3). A higher GP means a more ordered membrane. The imaged area is a 80 μm×80 μm square.

each observation chamber. Temperature control is not possible with this type of observation chamber, and therefore this type of chamber was not used in this thesis.

Observing free-standing vesicles comes with its own challenges. The focusing ability of an inverted microscope requires the vesicles to be on the bottom of the slide in order for them to be within the working distance of the objective lens. The typical way to force vesicles to sink is by utilizing the density difference between sucrose and glucose: GUVs are electroformed in a sucrose solution, and then transferred to an observation chamber filled with glucose solution of the same osmolarity. Maintaining osmolarity ensures that there are no pressure differences that would cause the vesicles to burst. Sunken vesicles can move laterally.[4] ImageJ's `StackReg` function is used to correct for lateral and rotational vesicle movements that occur during imaging. This algorithm only accounts for translations and rotations within the focal plane. In the literature, sometimes GUVs are anchored using biotin-DPPE for imaging (see Appendix G). This introduces an extra component to the GUV composition. Experiments in this thesis do not contain biotin-DPPE. Avoiding additional components allows any effects to be unambiguously assigned to the probe.

Even vesicles that have been detached from the electroformation wire can be attached, or be in close proximity, to other vesicles, especially when there are many vesicles. There is a fine balance between having enough vesicles so that observations can be made on a reasonable number of vesicles in a given amount of time and having too many vesicles that they get too close to each other. When there are too many vesicles, it is difficult to find isolated free-standing ones for observation.

My experiments, unless stated otherwise, employ a hybrid approach where the electroformation chambers were used for observing sunken vesicles. Vesicles are encouraged to detach from the electroformation wire by applying a 1 V, 2.5 Hz sine wave for 10 min at the end of electroformation. Glucose is then directly added into the electroformation cells to sink the vesicles for observation with an inverted microscope.

4.1.5 Image collection

Two-photon excitation microscopy was performed with a custom-built inverted microscope. The excitation light was provided by a femtosecond Ti:Sa laser (Broadband Mai

---

[4] If air currents in the observation chamber are minimized, the vesicles will be still enough for imaging [174].

Tai XF-W2S with 10 W Millennia pump laser, and a tunable excitation range of 710-980 nm, Spectra Physics, Mountain View, CA). The excitation wavelength was tuned to 780 nm for Laurdan experiments. Circularly polarized light was used to avoid photoselection effects. Signal from the sample was split between two photomultiplier tubes (Hamamatsu H7422P-40) using a dichroic mirror splitting at 475 nm. Each channel contains a bandpass filter (438 ± 12 nm and 494 ± 10 nm). Nominally, these will be referred to as the 440 and 490 nm channels. The microscope was controlled by Globals for Images SimFCS software (Laboratory for Fluorescence Dynamics, University of California at Irvine, USA).

Laurdan GP images were constructed from fluorescence intensity images collected at two wavelengths, 440 nm and 490 nm. To minimize overall photo-damage to the vesicle and to avoid photoselection effects, images were only collected at the equatorial plane. The vesicle may look homogeneous at the equatorial plane if small or medium-sized domains were present at the poles. At temperatures below T_{mix}, given enough time, vesicles should completely phase separate into a single circular dark domain and a single circular bright domain [61].

Juhasz et al. [131] compared confocal fluorescence microscopy (CFM) with ^{2}H NMR using DOPC:DPPC:chol. They measured relative domain area using both techniques, and found them to be comparable. Thus, we will assume that MLV domains and GUV domains are comparable, and infer from the ^{2}H NMR data that the GUV domains were macroscopic (see Sec. 5.4), and were unlikely to be missed by equatorial plane images.

Laurdan GP values depend strongly on instrumental factors such as filter settings and photomultiplier tube gains. Thus, the relative sensitivity of the two microscopy channels have to be calibrated by using Laurdan with a known GP value. GP of Laurdan in DMSO at room temperature was measured with a fluorimeter (ISS Chronos, Champaign, IL, USA) using a 374 nm diode for excitation, and 440 nm and 490 nm as emission wavelengths. Laurdan GP is calculated from fluorimeter measurements using Vinci analysis software (ISS, Champaign, IL, USA) and compared with the literature GP value of 0.207 [112]. The GP factor used for this correction is

$$\mathrm{GP}_{\mathrm{corr}} = \frac{I_{(440)} - G \times I_{(490)}}{I_{(440)} + G \times I_{(490)}} \tag{4.1}$$

where

$$G = \frac{(GP_{\text{theo}} - 1)(GP_{\text{exp}} + 1)}{(GP_{\text{theo}} + 1)(GP_{\text{exp}} - 1)} \tag{4.2}$$

and where GP_{exp} is the experimentally determined GP value of the standard solution [112]. This correction is applied during data acquisition by entering GP_{exp} into the image acquisition software SimFCS (see Sec. 4.1.6). SimFCS is designed for use with Laurdan, and the correction factors are built-in.

It is known that the light used in microscopy experiments can induce phase separation [33, 84] and that fluorescently labelled vesicles are particularly susceptible to photodamage. To ensure enough unexposed vesicles remained for imaging at the higher temperatures, only 10-20 vesicles were imaged at each chosen temperature for each sample. This was a compromise between obtaining a statistically significant number of measurements and maintaining the integrity of the vesicles. To check that the phase separation observed was not photo-induced, experiments were performed at 19°C on a sample that has not been subjected to prior illumination (sample 16).

After changing the temperature, there is an equilibration period of 20 min, to parallel ^{2}H NMR experiment protocols. This combined with the constraint that vesicles begin to degrade after about a day restricted the number of temperatures that can be imaged to 5-7. At low temperatures, it is expected that the more fluid domains would be small and difficult to image, particularly with equatorial plane images. Thus, in order to find T_{mix}, imaging was done mostly near T_{mix}, as determined by ^{2}H NMR.

4.1.6 Image analysis

Image analysis has been done using Globals for Images SimFCS software (Laboratory for Fluorescence Dynamics, University of California at Irvine, USA) and Fiji (a variant of the open-source software ImageJ). SimFCS is proprietary software and not customizable. In comparison, ImageJ and Fiji are open-source and can be programmed using programming languages such as Python, Java, and their own macro language. Histograms can be exported from ImageJ as text files for further analysis in other data analysis software, such as Igor Pro. SimFCS was used for initial on-the-fly analysis and Fiji was used for more extensive analysis. They gave similar results.

A GP image was calculated from the images from two channels, one made from 440 nm light and one from 490 nm light. Each image is made up of multiple slices. The vesicle may move during the time of data collection. ImageJ's built-in `StackReg` function was used to align the slices within a given image compensating for such movement, and ImageJ's built-in `Z-project` was used to add up the intensity from each slice to ensure a sufficient signal-to-noise ratio. These images were binarized to an appropriate threshold level to help locate the region of interest (ROI). The threshold was chosen so that a reasonable amount of signal was counted in the channel, in the dimmer domain. Decreasing the threshold level increased the noise and may make the GP histogram asymmetric, but it did not affect peak position. The ROI was further tailored manually to exclude overlapping vesicles, neighbouring vesicles that were touching the vesicle of interest (VOI), and internal vesicles and other material that were inside the VOI. Rectangular and circular selection tools were used for the manual manipulations. The GP within a given VOI can take on a range of values and a histogram of pixel count versus GP can be constructed. For vesicles that were phase separated, two additional histograms were obtained: one for the high- and one for the low-GP domains. The interfaces between domains were excluded from analysis. A large region was excluded to minimize the signal from Laurdan that samples both domains in the scan time. The histogram for a phase separated VOI was almost a superposition of the high- and low-GP domain histograms and appeared bimodal. Analysis done on either the vesicle as a whole or on the individual domain histograms is equivalent. For this thesis it is done on the high- and low-GP domains' histograms (See Appendix C).

4.2 Steady-state fluorescence spectroscopy of Laurdan labelled MLV

Figure 4.3 shows the fluorescence emission spectra of 35:35:30 DOPC/DPPC-D62/chol + 5% Laurdan MLV between 16 and 43°C obtained using a fluorimeter. The MLVs used in these experiments were made using the same protocol as the ^{2}H NMR experiments. The temperature was controlled by a water bath connected to the fluorimeter and monitored by a thermocouple inserted into a blank sample in the fluorimeter. Both graphs in Fig. 4.3 show the same emission spectra: the top set of graphs has been normalized to the intensity at 490 nm; the bottom set has been normalized to the intensity at 440 nm. The graphs

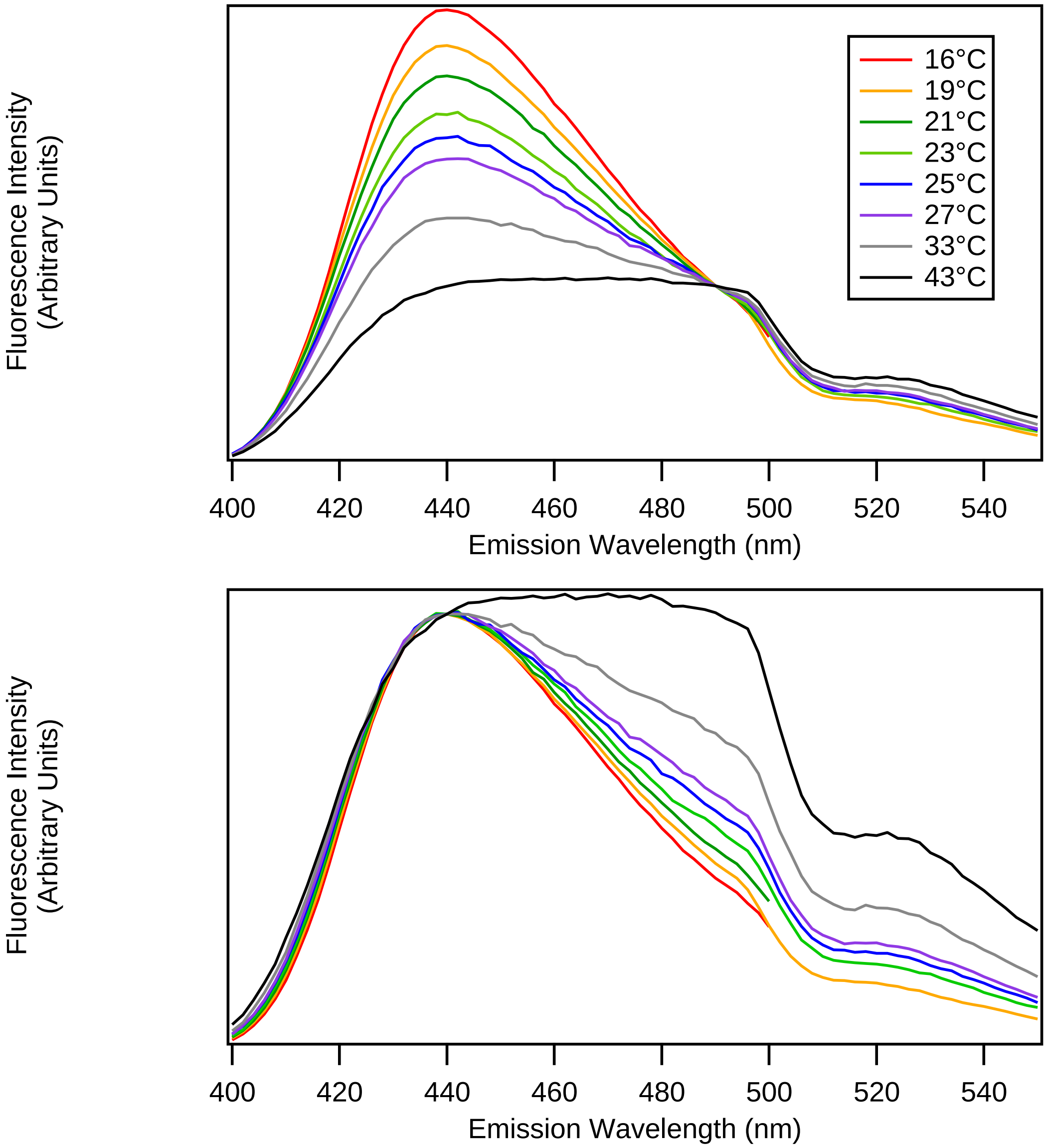

Figure 4.3: Fluorescence emission spectra of 35:35:30 DOPC/DPPC-D62/chol + 5% Laurdan MLV. The same spectra are shown in the top and the bottom. The top graph is scaled such that the intensity at 490 nm at all the different temperatures appear the same along the vertical axis. The bottom graph is scaled to the 440 nm intensity. A smaller range of wavelengths was used for 16 and 21°C.

are scaled differently to highlight the temperature induced changes at the two wavelengths relevant for GP calculations. The temperature range chosen includes temperatures close to and far away from the T_{mix} (21-22°C) measured using ^{2}H NMR. The spectra shift to longer wavelengths with increasing temperature: the intensity at 440 nm decreases, and the intensity at 490 nm increases with temperature. This is consistent with the spectra for DPPC MLV (Fig. 2.3). As temperature increases, Laurdan gains more access to water as the membrane gets more disordered.

The spectral differences in Fig. 4.3 can be summarized into the GP (Eq. 2.33). Laurdan GP is a ratio of fluorescence intensities. It is a number that can characterize the Laurdan emission spectrum and depends on the membrane phase state in Laurdan's vicinity. Figure 4.4 shows GP of 35:35:30 DOPC/DPPC-D62/chol + 0.05-5% Laurdan MLV measured directly by the fluorimeter. Laurdan GP can also be calculated from the emission spectra. The range of GP measured agrees with literature values for fluid phases [5, 98, 109, 175] (see Sec. 4.4). As expected, 5% Laurdan alters GP significantly. At high concentrations, Laurdan promotes water intercalating into the membrane. The data with 0.05 and 0.1% Laurdan was very noisy since these lower probe concentration resulted in lower signal. Noise level in the 0.05% sample was extremely high, even though 4 times as many scans were used as compared to the other probe concentrations. 0.1-2% Laurdan was innocuous to membrane GP.

Figure 4.4 shows that GP gradually decreases with increasing temperature. The data does not support the use of bulk GP measurements obtained using a single excitation wavelength for determination of T_{mix} in ternary membranes: there are no obvious changes at T_{mix}. Similar temperature-dependence of GP was also reported for $\mathbf{l_d}+\mathbf{l_o}$ to $\mathbf{l_d}$ transitions in other membrane systems (1:1:1 POPC:Sm:chol[5] [46]). The work of Parasassi and Gratton showed that using multiple excitation and emission wavelengths, the slope of the excitation and emission GP spectra (Fig. 4.5) can be used for determining membrane phase states and phase coexistence of liquid crystalline and $\mathbf{s_o}$ phases [109, 176]. We have not explored this option further with our liquid-liquid phase coexistence.

---

[5] There is controversy whether this mixture is $\mathbf{l_d}+\mathbf{l_o}$ or not.

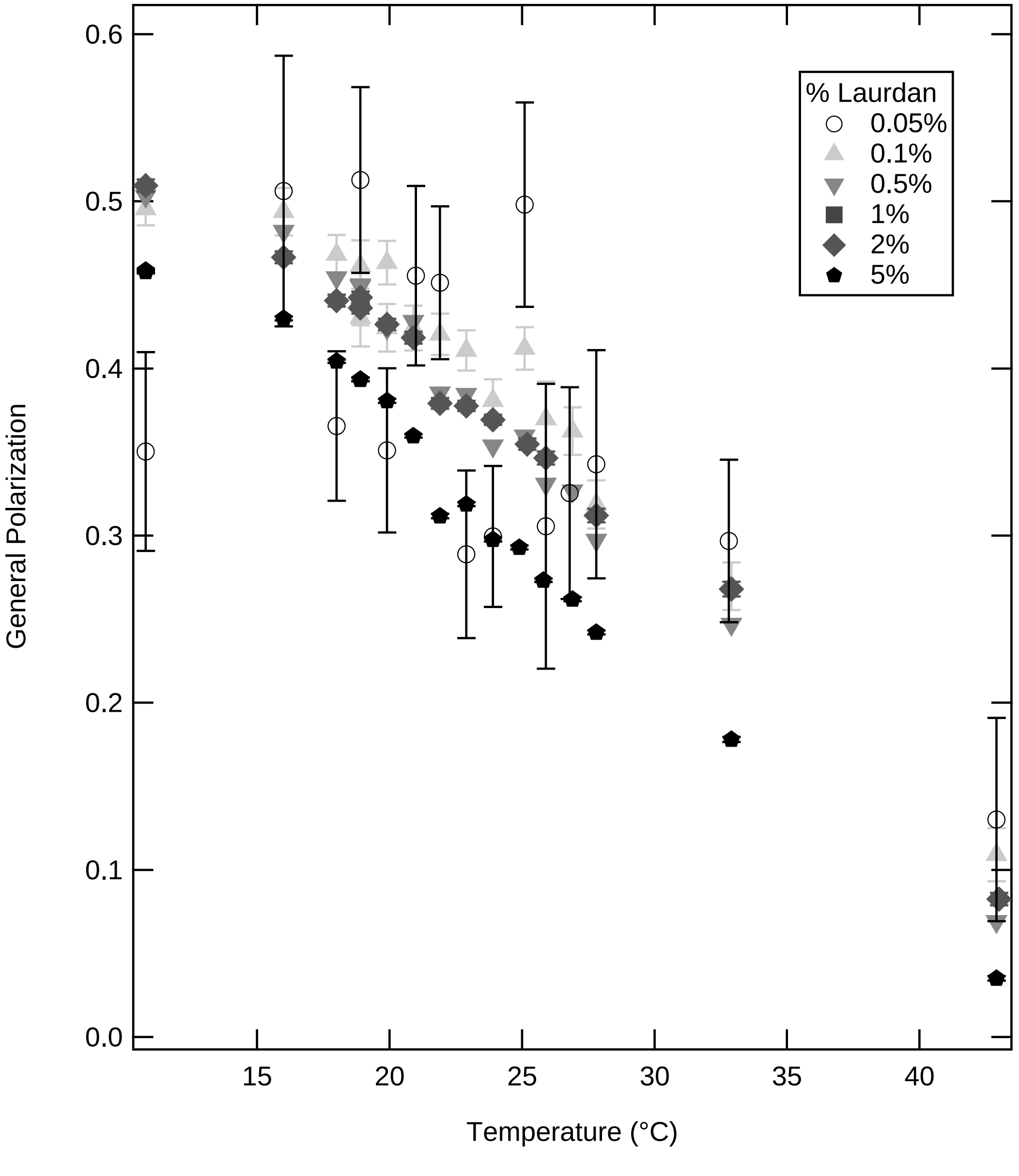

Figure 4.4: Bulk GP measured using fluorescence spectrometer for 35:35:30 DOPC/DPPC-D62/chol MLV with 0.05-5% Laurdan. Excitation wavelength 300 nm.

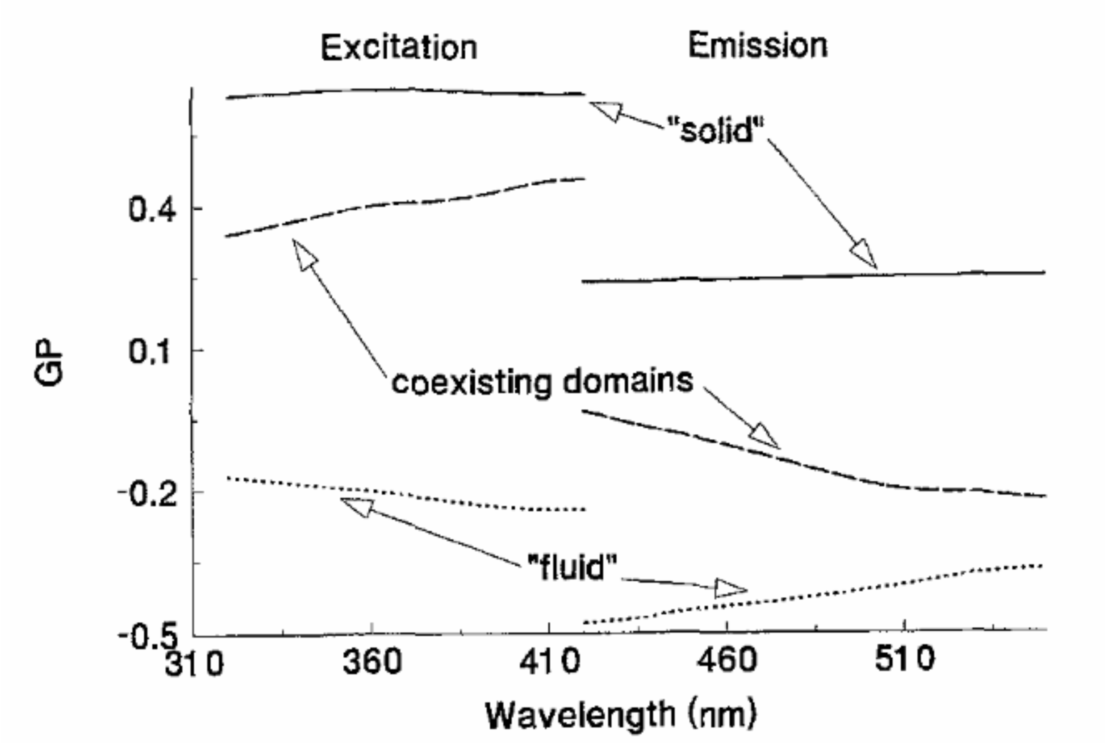

Figure 4.5: Excitation and emission Laurdan GP spectra can be used to determine membrane phase state. Excitation GP spectra were calculated by $GP = (I_{440} - I_{490})/(I_{440} + I_{490})$ using excitation wavelengths from 320 to 420 nm. Emission GP spectra were calculated by $GP = (I_{410} - I_{340})/(I_{410} + I_{340})$ using emission wavelengths from 420 to 550 nm. Reproduced from [176] with permission from Elsevier.

4.3 Two-photon excitation microscopy of GUV doped with Laurdan

In contrast to fluorescence spectroscopy, spatial information is available from fluorescence microscopy. Vesicles can be directly observed. Their shapes and sizes can be ascertained. The uniqueness of each vesicle can be appreciated. Most importantly macroscopic domains can be visualized and characterized. Microscopy in combination with Laurdan GP measurements is a powerful experimental approach for studying phase coexistence in model membranes. Sample micrographs and their associated GP histograms are shown in this section to give the reader an appreciation of the raw data and help the reader interpret the results presented in Sec. 4.5.

Figures 4.6 and 4.7 are examples of two-photon excitation micrographs taken at the equatorial plane of homogeneous and phase-separated GUV doped with Laurdan. The images encode spatial information about membrane phases not available from bulk GP measurements. The homogeneous vesicle (Fig. 4.6) is characterized by a single GP of 0.50 ± 0.04. Note that the vesicle membrane appears to be thicker in the GP image (Fig. 4.6 (3)) than in the intensity images (Fig. 4.6 (1) and (2)). The extra intensity on the inside of the vesicle comes from scattered light and has lower GP than the light from the vesicle itself. This scattered light does not meet the threshold intensity in the ROI selection algorithm (Sec. 4.1.6) and thus is excluded from the ROI.

In contrast, phase-separated vesicles have two well-separated domains. Phase separation is visually observable in both the fluorescence intensity and false colour GP images (Fig. 4.7): the images show disjoint regions within a vesicle. In the intensity images, it is clear that the low-GP domain has greater intensity at 490 nm (Fig. 4.7 (1)) compared to 440 nm (Fig. 4.7 (2)). Conversely, the high-GP domain has greater intensity at 440 nm than at 490 nm. The basis of the GP method is Laurdan's polarity-sensitive spectral red-shift. Membranes in different phase states have different GP. In the $\mathbf{l_d+l_o}$ case studied here, this difference for 35:35:30 DOPC/DPPC-D62/chol membranes is always at least 5%. The GP histogram for a phase-separated vesicle is bimodal. The histogram for each domain can be obtained by excluding only the other domain from the ROI. Figure 4.7 (5) shows a sample low-GP domain ROI, (6) is the associated histogram, and (7) and (8) are for the high-GP domain. The similarity between the histograms shown in (6) and (8), and that shown in (4)

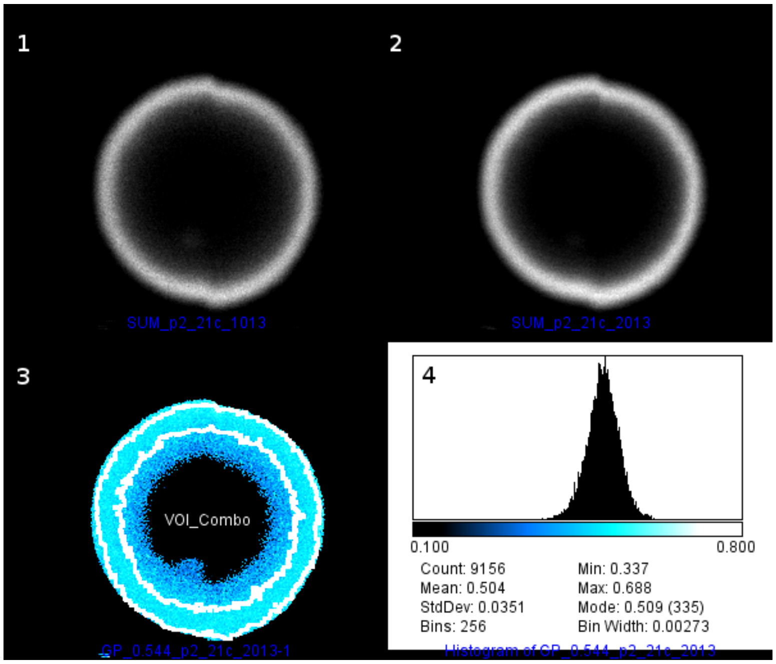

```
Count: 9156          Min: 0.337
Mean: 0.504          Max: 0.688
StdDev: 0.0351       Mode: 0.509 (335)
Bins: 256            Bin Width: 0.00273
```

Figure 4.6: Micrographs of a homogeneous 35:35:30 DOPC/DPPC-D62/chol vesicle with 0.2% Laurdan at 21°C from sample 10. Intensity images are shown in the top row at 490 nm (1) and 440 nm (2). False colour GP image (3) calculated pixel by pixel using the intensity images, with the whole vesicle chosen as the ROI (outlined in white). (4) is the corresponding histogram for the ROI shown in the GP image. Vertical axis on the histogram is pixel count. There was an issue with the microscope when this micrograph was taken: the misalignment of the left and right halves of the vesicle is an artifact. The GP was not affected by this. The imaged area is a 42.5 μm×42.5 μm square.

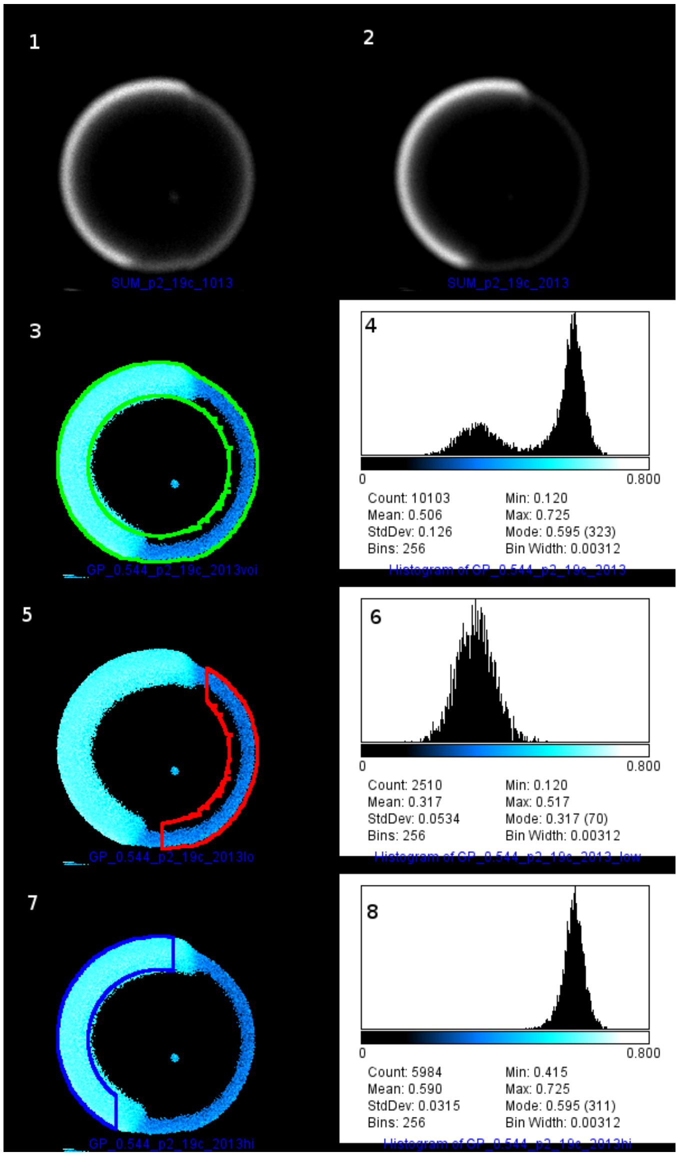

Figure 4.7: Micrographs of a phase-separated vesicle with 0.2% Laurdan at 18°C from sample 10. (1) Intensity images at 490 nm (1) and 440 nm (2). False-colour GP image calculated pixel by pixel using the intensity images, with the whole vesicle (3), low-GP domain (5), and high-GP domain (7) chosen as the ROI. The ROIs are outlined in green, red and blue, respectively. (4), (6), (8) are the corresponding histograms to the ROIs shown in the GP images on the left. Vertical axis on the histogram is pixel count. A higher GP means a more ordered membrane. The imaged area is a 59.5 μm×59.5 μm square.

shows that diffusional broadening of the GP is negligible. Signal intensity from the low-GP domain is lower than from the high-GP domain (Fig. 4.7 (1) and (2)). During ROI selection, a higher threshold is set to accommodate the channel with less signal. The higher threshold results in a ROI larger than the vesicle, and a noisier histogram. This noise typically does not affect peak position significantly.

For each sample, at each temperature, images were collected from 10 to 20 vesicles. Figures 4.8-4.10 are included to give an impression of the quality of the data used to examine the temperature- and probe concentration-dependent changes in GP. They are examples of GP measured from a collection of micrographs for GUV doped with 0.2, 0.4, and 2% Laurdan. Describing the trends and forming conclusions will be postponed until Sec. 4.5, however. The GP of individual vesicles is shown with unfilled symbols. For homogeneous vesicles, the GP shown is the mean from all pixels in the vesicle. For phase-separated vesicles, the mean GP of high- and low-GP regions are measured separately by isolating the ROI to the relevant region (e.g., Fig. 4.7 (5) and (7)). This is equivalent to finding the means of the two peaks in the bimodal distribution. Some of the homogeneous vesicles' histograms have asymmetric peaks. The mean of asymmetric peaks does not necessarily align with the position of the peak. It has been verified that the difference is typically less than 5% (see Appendix C).

The GPs from the individual vesicles are averaged and shown with filled symbols in Figs. 4.8-4.10. All micrographs for a given sample are collected within 25 hours of vesicle formation. Vesicles have a shelf life of about a day under the experimental conditions of this thesis. There is less data available for GP of the domains than for the homogeneous vesicles: the area of a vesicle is divided between the two domains, and hence the pixel count is lower.

Figure 4.11 shows the population-averaged GP of four different 0.2% Laurdan samples, illustrating batch-to-batch variation. The sample 10 data is the most complete set, with 7 temperatures sampled. All other samples will be compared to this set. Measurements for sample 06 are only available at 18°C. This data set agrees with data from sample 10: the high-GP domain and homogeneous GP points overlap; the low-GP domain data agrees within 13%. Sample 08 is an odd sample (see Fig. 4.13) because it is not phase separated at 14°C. Its GP behaves normally, however: the high-GP domain and homogeneous GPs of sample 08 are consistent with those of sample 10. The low-GP domain data is higher

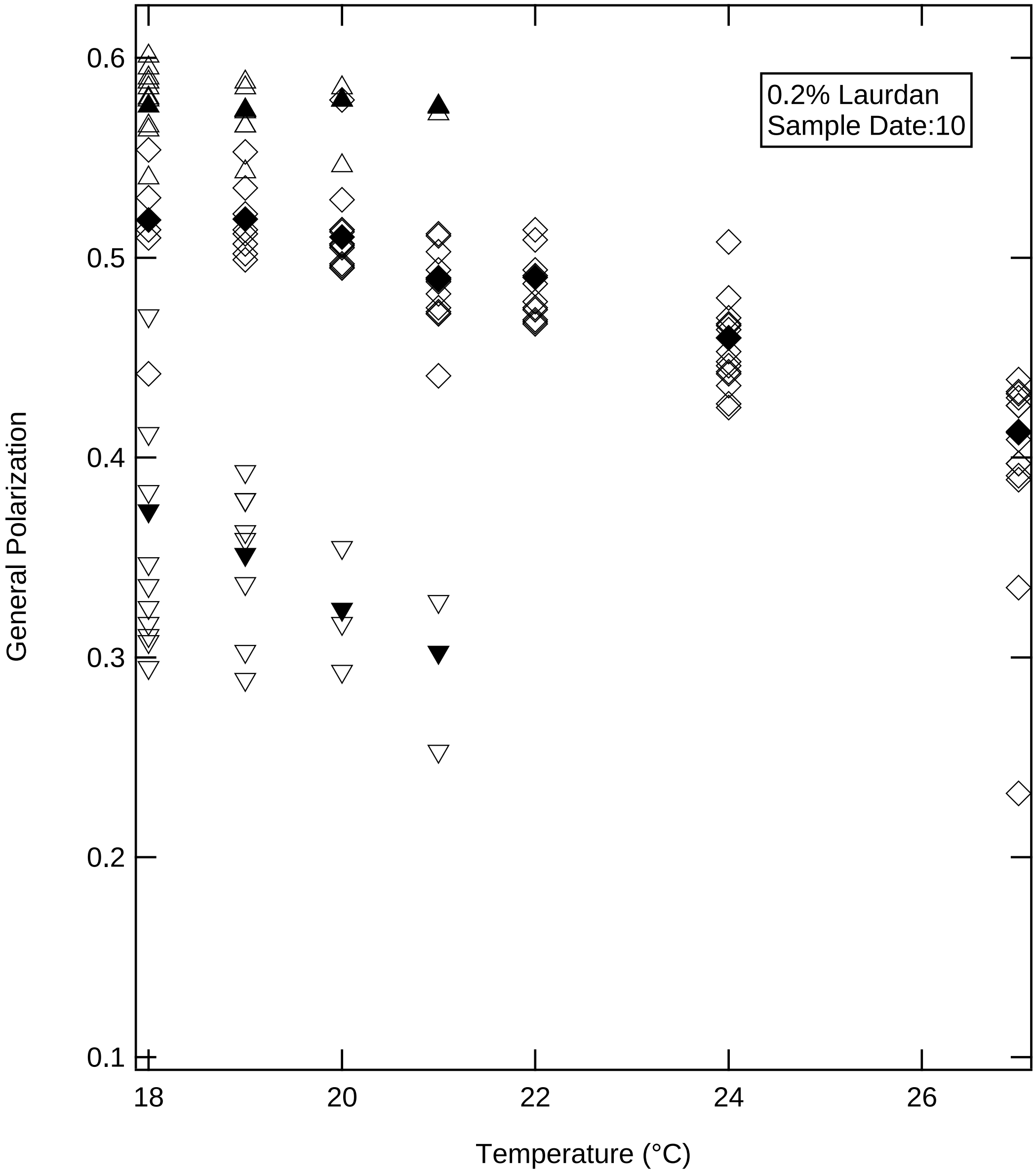

Figure 4.8: Temperature dependence of Laurdan GP at the equatorial plane of 35:35:30 DOPC/DPPC-D62/chol GUV doped with 0.2% Laurdan (sample 10). Each phase-separated vesicle is represented by two unfilled symbols: the GP value from the high-GP domain (△) and that from the low-GP domain (▽). Each homogeneous vesicle is represented by one unfilled symbol: the GP value from the whole vesicle(◇). The weighted mean GP are shown with filled symbols: high-GP domains (▲), low-GP domains (▼), and homogeneous vesicles (◆). Error bars have been left out for clarity.

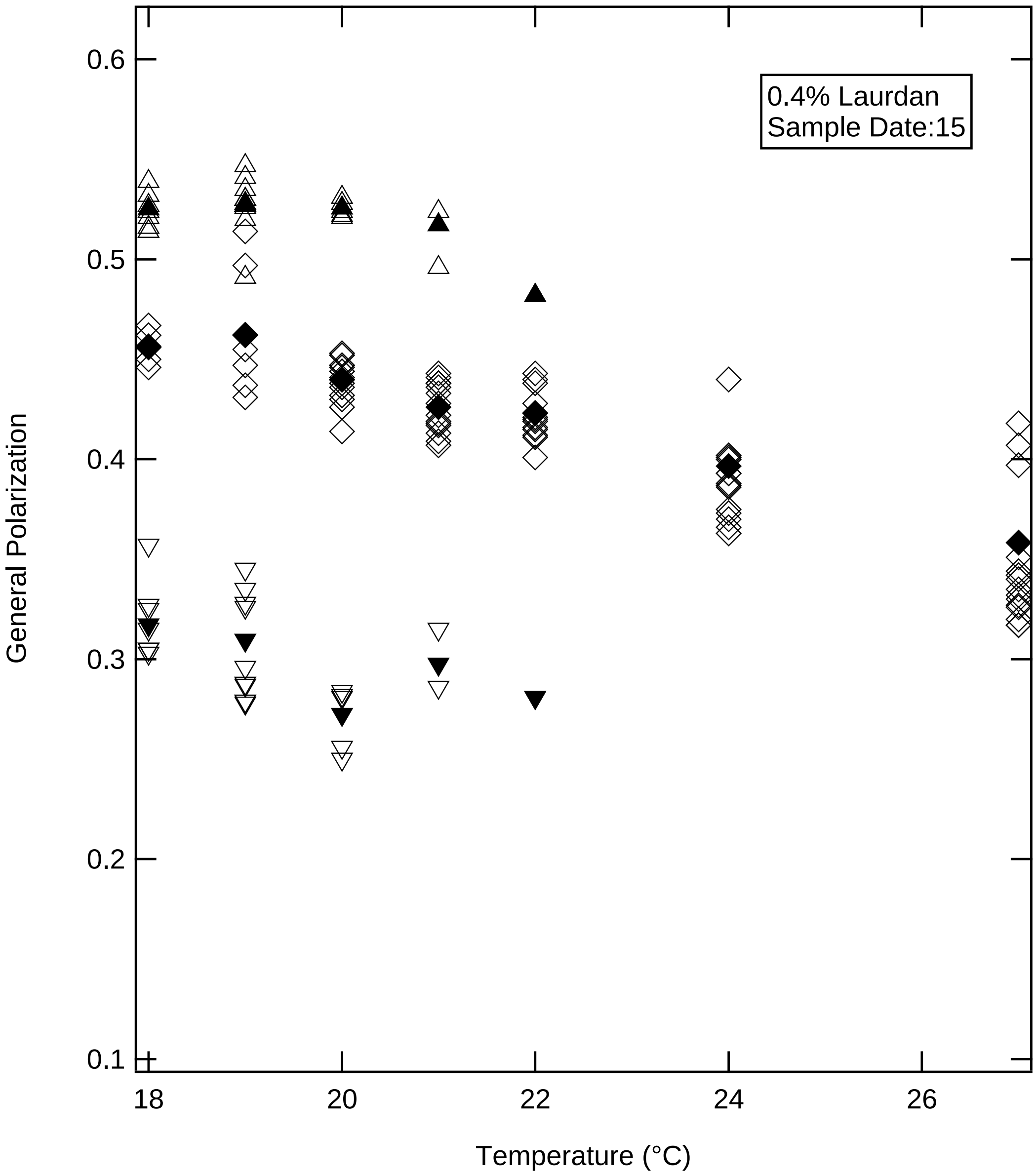

Figure 4.9: Temperature dependence of Laurdan GP at the equatorial plane of 35:35:30 DOPC/DPPC-D62/chol GUV doped with 0.4% Laurdan (sample 15). Each phase-separated vesicle is represented by two unfilled symbols: the GP value from the high-GP domain (△) and that from the low-GP domain (▽). Each homogeneous vesicle is represented by one unfilled symbol: the GP value from the whole vesicle(◇). The weighted mean GP are shown with filled symbols: high-GP domains (▲), low-GP domains (▼), and homogeneous vesicles (◆). Error bars have been left out for clarity.

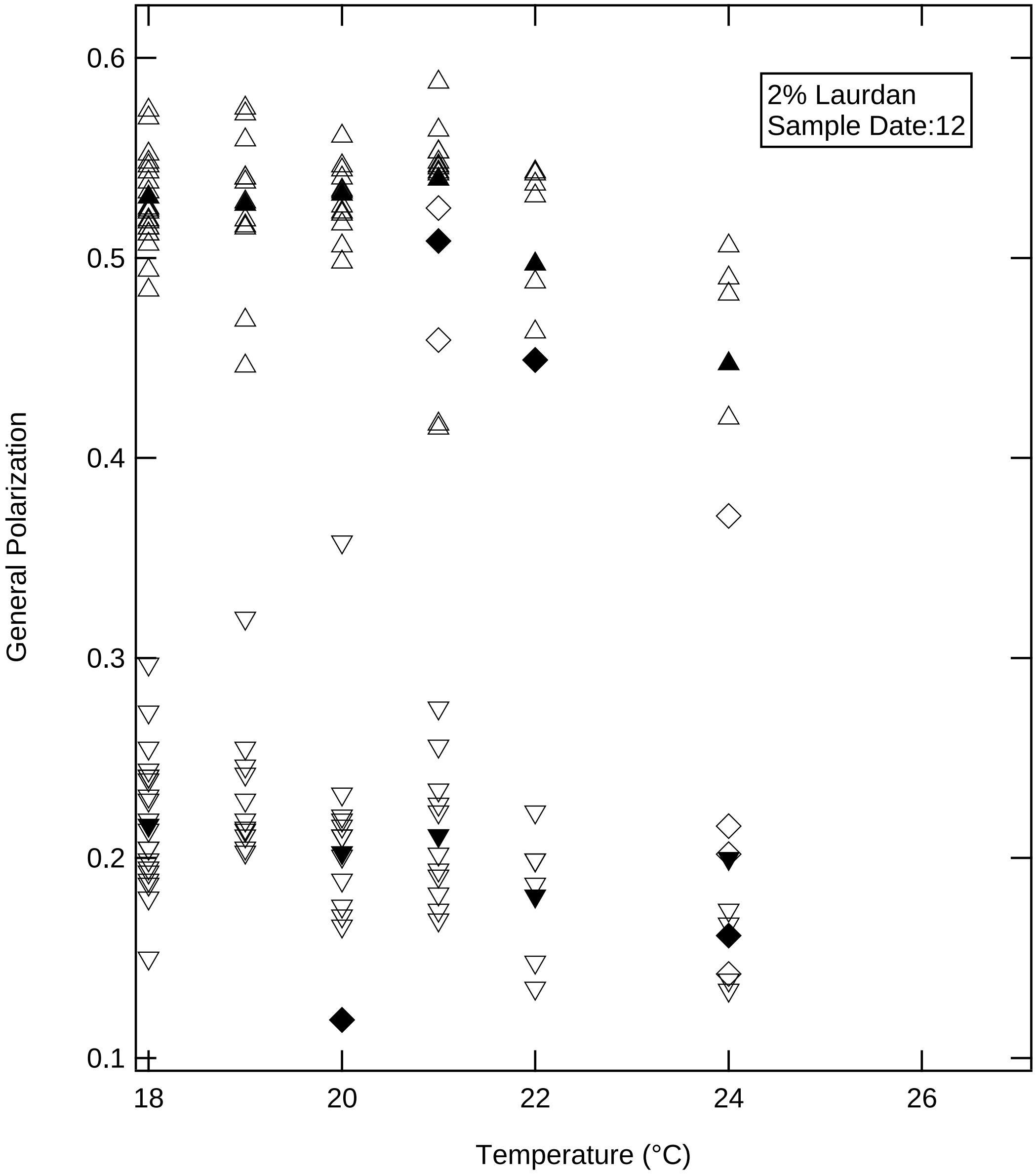

Figure 4.10: Temperature dependence of Laurdan GP at the equatorial plane of 35:35:30 DOPC/DPPC-D62/chol GUV doped with 2% Laurdan (sample 12). Each phase-separated vesicle is represented by two unfilled symbols: the GP value from the high-GP domain (△) and that from the low-GP domain (▽). Each homogeneous vesicle is represented by one unfilled symbol: the GP value from the whole vesicle(◇). The weighted mean GP are shown with filled symbols: high-GP domains (▲), low-GP domains (▼), and homogeneous vesicles (◆). Error bars have been left out for clarity.

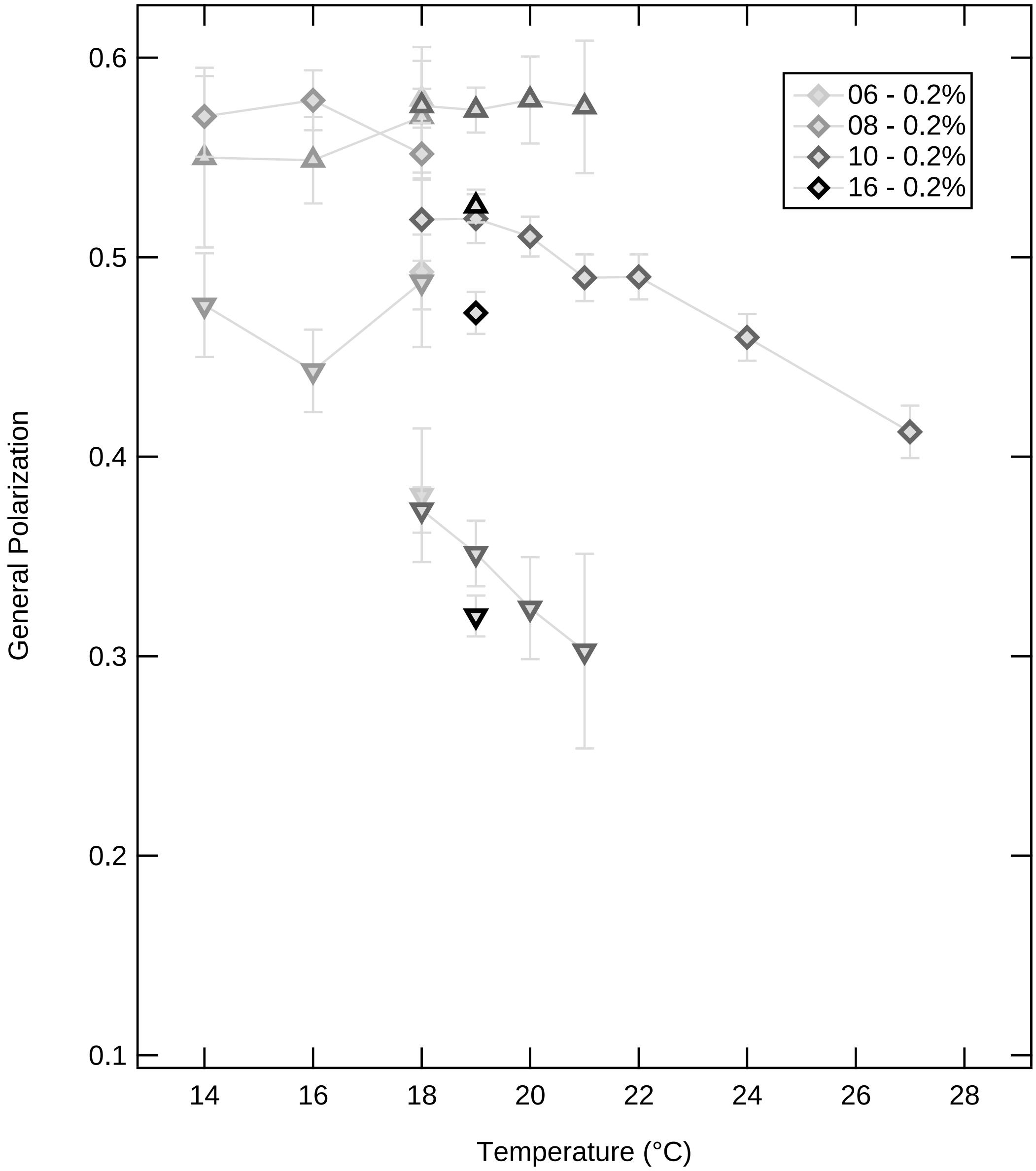

Figure 4.11: Temperature dependence of weighted population-averaged Laurdan GP for 0.2% Laurdan 35:35:30 DOPC/DPPC-D62/chol. The four different samples were made and imaged on different days. The samples are identified by the date the images were taken and by different symbol outline colours. Homogeneous vesicle (◇), high-GP domains (△), and low-GP domains (▽) share the same symbol shapes as Figs. 4.8-4.10. Lines are added between the data points to aid in tracking data points belonging to the same sample. Vertical error bars are the weighted standard deviations. Horizontal error bars (±0.5°C) have been left out for clarity.

than sample 10. There is only data for sample 16 at 19°C. The GP values of this sample are lower than those of sample 10, but the relative differences between high-GP domain, homogeneous, and low-GP domain values are similar: the difference between the high-GP domains and the homogeneous GP were 0.05, while the difference between the homogeneous GP and the low-GP domain was 0.17 for sample 10 and 0.15 for sample 16.

In general, the GP values of the high-GP domains are less sensitive to temperature compared with those of the low-GP domains or homogeneous vesicles. For both homogeneous vesicles and low-GP domains, GP decreases with increasing temperature, indicating that Laurdan gains access to more water at higher temperatures and the membrane is more disordered with increased thermal energy.

4.4 Typical measured values of GP

GP values can theoretically range from -1 (most fluid) to 1 (most ordered). These limiting values are experimentally obtainable in dodecane and methanol (GP $= 1.0$ for dodecane at 20°C and GP $= -1$ for methanol at 20°C) [109]. The 50 nm red-shift observed in the gel-to-liquid crystalline transitions in pure DPPC membrane (in Fig. 2.3) translates into GP roughly in the following way: at excitation $\lambda = 340$ nm, gel GP $= 0.64$ at 3.6°C, and liquid crystalline GP $= -0.12$ at 53.1°C [116, 118]. The main transition of DPPC occurs at 41°C. At 20°C, GP for the two PC used in this study has been measured by Parasassi et al. [119] using a fluorimeter DOPC is < -0.08 and for DPPC is 0.4 [119].

In Sec. 4.2, the GPs from steady-state fluorescence spectroscopy measurements on MLVs ranged from 0.03 to 0.6. Parasassi et al. [119] measured GP ≈ 0.6 for 35:35:30 DOPC/DPPC/chol MLV at 20°C. Zhou et al. [5] measured the GP of MLVs made with a slightly different composition (33:33:33 DOPC/DPPC/chol) vs. excitation wavelength at 37 and 50°C using a fluorimeter and found that the GP was mostly independent of the excitation wavelength between 350 and 415 nm. They measured GP $= 0.3$ at 37°C and 0.1 at 50°C. Figure 4.4 suggests that GPs might decrease linearly with increasing temperatures, but Parasassi et al. [119] showed that this is only true for a small temperature range. Based on the trends observed by Parasassi et al. [119], linear extrapolation of Zhou et al. [5]'s data should give an upper bound on GP expected. Linear extrapolation of Zhou et al. [5]'s measurements to ~ 24°C yields GP $= 0.5$. Our measured values are lower than reported by both of these papers (GP = 0.35 at 24°C). One source of difference between these experiments and those of this thesis is that DPPC-D62, and not DPPC, was used here.

In Sec. 4.3, most[6] of the population-averaged GP of low-GP domains range from 0.18 to 0.38, homogeneous vesicles range from 0.36 to 0.55, and high-GP domains range from 0.44 to 0.58. These values are consistent with the fluorimeter experiments. They are also consistent with our fluorimeter experiments in that these values are lower than those measured by Parasassi et al. [119] and Zhou et al. [5]. They are, however, comparable to those measured by others for $\mathbf{l_d}$+$\mathbf{l_o}$ coexistence and for the $\mathbf{l_d}$ phase (See Sec. 4.4.1). Highest high-GP domain from an individual vesicle is 0.60, and the lowest low-GP domain from an individual vesicle is 0.13. These values seem reasonable. In the literature, Zhou et al. [5] measured GP = 0.5 for 70:30 DPPC/chol MLV at 37°C, and GP = 0.15 at 50°C. In the same binary mixture, Harris et al. [118] measured GP = 0.8 at 25°C and ~ 0.6 at 50°C. Given DOPC, DPPC-D62, and chol, the highest GP possible would be ~ 0.8 (GP for 70:30 DPPC/chol), and the lowest possible would be ~ -0.08 (GP for pure DOPC) around 20°C. Differences between GPs of high-GP domain and homogeneous vesicle are ~ 0.05, and of homogeneous vesicles and low-GP domains is ~ 0.2 (Sec. 4.3). The difference in GP values for two liquid phases have been found to be between 0.2 and 0.3 in other mixtures [43, 112, 175].

Given what is known about DOPC/DPPC/chol mixtures in the literature (Sec. 5.1), we believe the high-GP domains should be associated with the $\mathbf{l_o}$ phase, and the low-GP domains should be associated with the $\mathbf{l_d}$ phase.

4.4.1 Measured GP in the literature

This section will give many examples of measured GP values in the literature. This section is intended to give the reader a feel for GP values.

Liquid phases of ternary mixtures

Kaiser et al. [113] measured the GP of POPC/eSm/chol LUV of various compositions using fluorescence spectroscopy: $\mathbf{l_o}$ (25:35:40) GP = 0.48, $\mathbf{l_d}$+$\mathbf{l_o}$ (45:30:25) GP = 0.42, $\mathbf{l_d}$+$\mathbf{l_o}$ (60:28:12) GP = 0.31, and $\mathbf{l_d}$ (70:25:5) GP = 0.11. These authors also showed using microscopy of 2:2:1 DOPC/sSm/chol GUVs[7] that GP = 0.91 ± 0.01 and 0.17 ± 0.08 for $\mathbf{l_o}$

---

[6] i.e., Ignoring outliers.

[7] These GUVs were dual labelled with 0.5% Laurdan, and 0.1% DiD or Rh-DOPE.

and $\mathbf{l_d}$ phase, respectively. This $\mathbf{l_o}$ GP value seems very high to be considered $\mathbf{l_o}$ since the theoretical maximum of GP is 1.

Liquid phases of binary mixtures and pure lipids

These authors also measured GP for some simpler membranes using fluorescence spectroscopy. They showed using spectroscopy GP $= 0.57 \pm 0.00$ for the $\mathbf{l_o}$ phase in 1:1 eSm/-chol, GP $= 0.42 \pm 0.00$ for the $\mathbf{l_d}$+$\mathbf{l_o}$ phase in 3:2 POPC/chol,[8] and GP $= -0.05 \pm 0.00$ for the $\mathbf{l_d}$ phase in POPC [113]. In plasma membrane studies, Gaus et al. [112] have identified a GP of 0.10-0.25 as $\mathbf{l_d}$ domains, and 0.35-0.55 as $\mathbf{l_o}$ domains.

Liquid crystalline and gel phase

The GPs listed above for membranes in the $\mathbf{l_d}$ and $\mathbf{l_o}$ phases can also be compared with those for membranes exhibiting $\mathbf{l_d}$-$\mathbf{s_o}$ phase coexistence. Most measurements of bulk GP have been done on $\mathbf{l_d}$ and $\mathbf{s_o}$. GP for the fluid phase was 0.05-0.25, and for the $\mathbf{s_o}$ phases was 0.25-0.55 [112]. Parasassi et al. [109] measured GP ≈ 0.6 for $\mathbf{s_o}$ and -0.2 for liquid crystalline for a number of pure lipid and binary mixtures (DPPC, 2:1 DPPS:DPPC, DPPG:DPPC 2:1, 2:1 DMPA:DMPC, 1:1 DPPG:DLPC, 1:1 DLPC:DPPC).

4.5 Dependence of phase behaviour on Laurdan concentration

What happens when Laurdan concentration is increased? In this section, micrographs for 35:35:30 DOPC/DPPC-D62/chol GUV with 0.2, 0.4, and 2% Laurdan are compared in three ways: GP, occurrence of phase separation in a population of vesicles, and average domain sizes in phase-separated vesicles.

Fig. 4.12 shows the temperature-dependence of GP for samples with 0.2-2% Laurdan. This figure differs from Fig. 4.11 in that 0.4 and 2% data are included. Symbol fill colour denotes probe concentration: higher probe concentrations are darker. The sample with the highest probe concentration, sample 12 (2%), had a number of elliptical vesicles at 24°C. This is correlated with the much lower homogeneous vesicle GP value at 24°C. The cause for

---

[8] It is controversial whether this composition would be considered $\mathbf{l_d}$+$\mathbf{l_o}$.

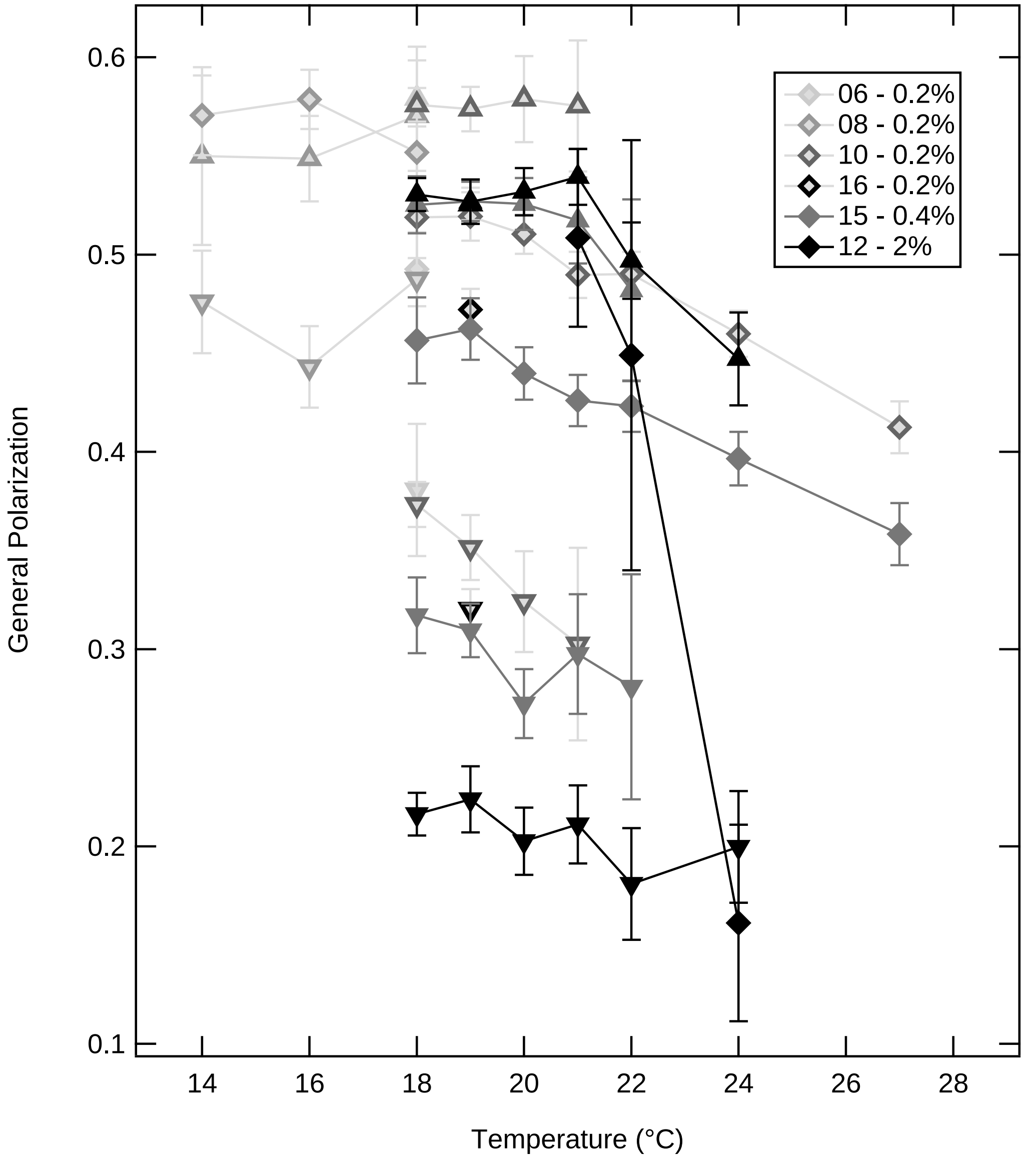

Figure 4.12: Temperature dependence of weighted population-averaged Laurdan GP for 0.2-2% Laurdan 35:35:30 DOPC/DPPC-D62/chol. The six different samples were made and imaged on different days. The samples are identified by the date the images were taken and by different symbol outline colours. Homogeneous vesicles (◇), high-GP domains (△), and low-GP domains (▽) share the same symbol shapes as Figs. 4.8 and 4.10. Lines are added between the data points to aid in tracking data points belonging to the same sample. Populations with only measurements from one vesicle are excluded (i.e., sample 12 20°C homogeneous vesicle). Vertical error bars are the weighted standard deviations. Horizontal error bars (±0.5°C) have been left out for clarity.

these ovular vesicles is unknown. Possible explanations include sample degradation and/or high probe concentration. Also, samples may degrade earlier because of the high probe concentrations. Aside from this oddity, the following can be said of all data presented: GPs of homogeneous vesicles and low-GP domains tend to decrease with increasing temperature; GP of the high-GP domains are constant at low temperatures and decrease near T_{mix}. These decreases are small compared to the changes observed in the homogeneous vesicles and the low-GP domains. The unchanging GP of the high-GP domain shows that the exposure of Laurdan to water is constant which suggests that the lipid composition of that domain is independent of temperature variations.

Fig. 4.13 shows the percent of observed vesicles that are phase separated as a function of temperature. There are two criteria for a vesicle to be considered phase separated: phase separation has to be discernible by micrograph visual inspection, and the difference in GP between the two domains must be at least 5%. Data from samples 10 (0.2%) and 15 (0.4%) are in excellent agreement. Phase separation is observed between 18 and 21-22°C; it is not found at 24 and 26°C. The T_{mix} of these two samples agrees to within 2°C of each other and is consistent with the T_{mix} observed from ^{2}H NMR data. Agreement between the two data sets is remarkable given that only 10-20 vesicles are imaged at each temperature for each sample. The data even overlap at 21°C. The number of phase-separated vesicles behaves as expected and decreases as the temperature increases.

Samples 06 (0.2%), 08 (0.2%), and 12 (2%) behave differently from the aforementioned two samples. The first two have the same probe concentration as sample 10, but the last one has 10 times more probe. Sample 08 is an odd one. There are very few phase-separated vesicles below 18°C in sample 08, but $> 50\%$ of the vesicles are phase separated at 18°C for four other samples. Also, the number of phase-separated vesicles in sample 08 does not decrease with increasing temperature. In contrast, the number of phase-separated vesicles decreased with increasing temperatures for all other samples with measurements at multiple temperatures. The data for sample 08 itself is self-consistent, however: percent phase separation is about the same at all three temperatures tested. It is not surprising that sample 12 behaves differently; 2% Laurdan is a rather high probe concentration. This is much higher than is typically used in fluorescence experiments and probably too high for the probe to be considered a trace component. All vesicles in sample 12 are phase separated at 18°C, and most vesicles remain phase separated at 19-24°C. Increasing temperature in

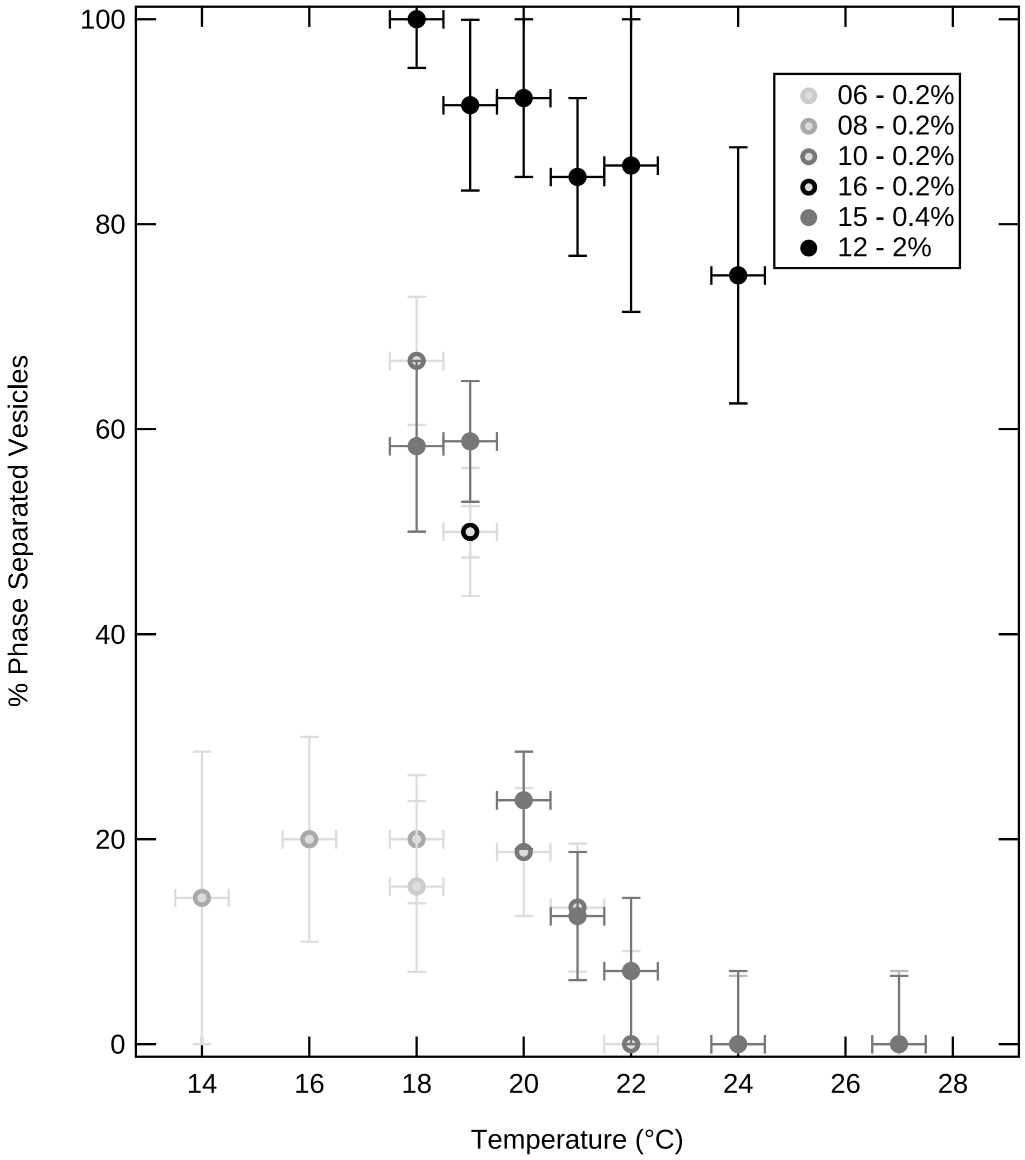

Figure 4.13: Percent of observed vesicles that appear phase separated in fluorescence micrographs. Data from samples 10 and 15 overlap at 21, 24, and 27°C. Data from samples 06 and 08 behaves differently than other 0.2% samples: there are few phase-separated vesicles at 14-18°C. Vertical error bars based on inverse number of vesicles observed.

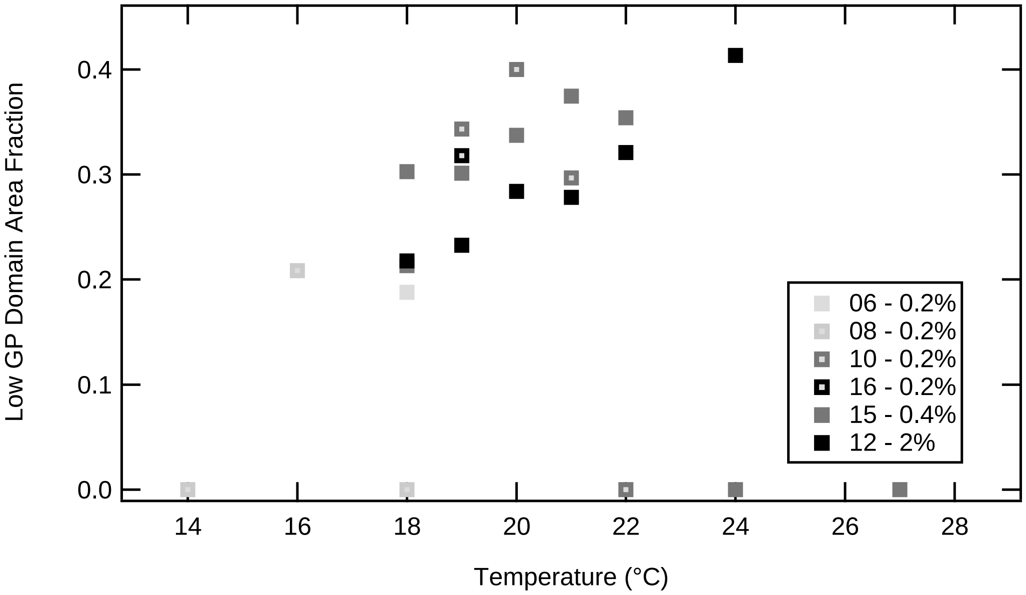

Figure 4.14: Fractional area of low-GP domains in GUV with Laurdan calculated from micrographs. The area of the low-GP regions is divided by the sum of the areas of the low- and high-GP regions. An area fraction of 0 signifies a homogeneous vesicle. Data from sample 08 behaves differently than other 0.2% samples: there are few phase-separated vesicles at 14-18°C.

this temperature range did not reduce the number of phase-separated vesicles observed in this sample by as much as sample 10 or 15.

Fig. 4.14 shows the fractional area of low-GP domains. The area of the low-GP ROI is divided by the sum of the areas of the low- and high-GP ROI. An area fraction of 1.0 denotes that all vesicles in the sample are in the homogeneous fluid phase. Differences between the various samples are less pronounced than in Figs. 4.12-4.13. The fractional area and its temperature trends are consistent in all phase-separated vesicles. The area fraction increases incrementally with temperature to a maximum of 0.4 at temperatures just below the phase transition and does not continue to increase. Above the transition, there are no domains. The low-GP domain does not increase continuously in size to cover the entire vesicle. This discontinuity cannot be caused by the microscope's resolution ($\sim$ 200-300 nm [30]) since domain area fraction of 20% is measurable at 16 and 18°C.

To summarize, Figs. 4.12-4.14 show that water penetration into the membrane increases with temperature for homogeneous vesicles and low-GP domains but not for high-GP domains. The percentage of phase-separated vesicles and the GP values are sensitive to slight compositional changes; the domain area fraction of phase-separated vesicles are not.

4.6 Chapter summary

Laurdan is sensitive to the polarity of its environment. Its fluorescence emission spectrum is red shifted when it is in a more disordered environment. Laurdan GP is used to characterize this shift: a lower GP means a more disordered membrane. GP can be measured using a fluorimeter or a microscope. Simple steady state bulk GP measurements on MLVs from a fluorimeter cannot be used to identify liquid-liquid phase coexistence unambiguously, but GP images from microscopy can.

Images of individual GUVs show that GUVs within a population can have different compositions, sizes, and shapes (data not shown). As a result, vesicles in a given sample can phase separate at different temperatures. It is important to keep this in mind when looking at population-averaged T_{mix}, low-GP domain area fraction, and GP values.

It is not possible to make measurements on probe-free membranes with fluorescence. There is a physical limitation to how little probe is used in fluorescence experiments. In this chapter, membranes with 0.2 and 0.4% Laurdan were shown to behave similarly. Previous work comparing 0.2% and higher concentrations of probe showed that probe effects may saturate (i.e., no difference in behaviour of membranes with 0.2 and 2% probe) [70]. Fluorescence alone cannot be used to illustrate probe effects. Combined with the ^{2}H NMR experiments of Ch. 3, however, it is clear that up to 0.4% Laurdan does not affect the membrane significantly.

In comparison, 2% Laurdan is a significant amount of probe, and it does causes a number of changes to the membrane: GPs are decreased, the differences in GP between the domains is higher, vesicles degrade faster, and vesicles are more phase separated. Interestingly, the low-GP domain area fraction is comparable to samples with 0.2 and 0.4% probe. In fact, domain area fraction in phase-separated vesicles is consistent in all samples tested.

Chapter 5

Discussion

In order to understand the effects of probes, we must first understand the membrane system we are using to study the probes. DOPC/DPPC/chol has been studied extensively, and a brief summary of the literature will be presented in Sec. 5.1. miscibility transition temperature (T_{mix}), domain composition and size can be inferred from the experiments of this thesis and will be compared with the literature in Secs. 5.2-5.4. Recently, lipid researchers have turned to looking at critical phenomena in lipid membranes; this will be touched upon in Sec. 5.5.

Next, the various aspects of our experiments must be considered within the context of the techniques used. deuterium nuclear magnetic resonance spectroscopy (^{2}H NMR) looks at the atomistic changes to the lipid chain, whereas fluorescence microscopy gives macroscopic information, such as size and shapes of vesicles, and of their phase separated domains. ^{2}H NMR is a bulk technique in that measurements are done on the sample as a whole, but fluorescence microscopy examines individual vesicles, allowing us to see that every vesicle is unique. ^{2}H NMR experiments are done on multilamellar vesicles (MLVs), and fluorescence-microscopy experiments are performed on giant unilamellar vesicles (GUVs). The differences between MLVs and GUVs were brought up in Sec. 1.3; the implications of this are discussed in Sec. 5.6. The use of high-intensity lasers in microscopy has been shown to introduce artifacts, which can affect how we interpret the images. This will be discussed in Sec. 5.8. Despite all these differences, we will attempt to correlate ^{2}H NMR order parameter and Laurdan general polarization (GP) in Sec. 5.7. Finally, we will return to discuss the implications of research on the effects of equipartitioning *vs.* non-equipartitioning probes on lipid membranes in Sec. 5.9.

5.1 Phase diagrams in the literature

Partial phase diagrams[1] for DOPC/DPPC/chol have been mapped out experimentally by three independent research groups using ^{2}H NMR and fluorescence [23, 25, 145]. Two of these have been overlaid in Fig. 5.1: that of Davis et al. [23] is shown with solid lines and that of Veatch et al. [25] with dotted lines. Ignoring the dotted lines for the moment, Fig. 5.1 shows the essential features of this phase diagram: a $\mathbf{l_d{+}l_o{+}s_o}$ three-phase region, a number of two-phase regions, and $\mathbf{l_d}$, $\mathbf{l_o}$, $\mathbf{s_o}$ phase one-phase regions. The phase diagram is inaccessible at high cholesterol concentrations since cholesterol crystallizes out as cholesterol monohydrate.

Davis and colleagues used ^{2}H NMR [23] and confocal fluorescence microscopy (CFM) [131] to study DOPC/DPPC-D62/chol. They performed their experiments from high to low temperatures. Phase diagrams at 18, 22 (Fig. 5.1), 24, 26, and 28°C were created using ^{2}H NMR [23, 131]. Davis et al. [23] reported the following for 35:35:30 DOPC/DPPC-D62/chol membranes. These membranes are in the $\mathbf{l_d{+}l_o{+}s_o}$ three phase coexistence region below ~10°C, and in the $\mathbf{l_d{+}l_o}$ phase region above 10°C. Significant line broadening occurs in ^{2}H NMR spectra at 26-35°C. Using the criteria in this thesis,[3] T_{mix} for Davis et al.'s 35:35:30 DOPC/DPPC-D62/chol MLV is 26 ± 1°C. This is approximately 4 degrees higher than the T_{mix} of the samples in this thesis (Sec. 5.2). In their CFM experiments, 0.1% Texas Red 1,2-dihexadecanoyl-sn-glycero-3-phosphoethanolamine, triethylammonium salt (TR-DPPE) was included in the membrane, and T_{mix} was defined as the temperature where fluctuations in fluorescence intensity over the surface of most of the vesicles in the sample were first detected (as temperature was lowered) [131]. Slightly above T_{mix}, most vesicles had homogeneous probe distribution except for a few small dark spots on some of the vesicles. For 35:35:30 DOPC/DPPC-D62/chol GUV, small domains were first detected at 32.2°C. The domains coalesced and reached their equilibrium distribution at 23.5°C. ^{2}H NMR line broadening was observed at slightly higher temperatures (26-35°C) than domain fluctuations in CFM (24-32°C).

---

[1] Readers unfamiliar with how to read ternary phase diagrams are referred to Appendix F.

[3] T_{mix} reported here for Davis et al. [23] are determined using the prominent methyl peaks in ^{2}H NMR spectra as in Sec. 3.2. In their paper, Davis et al. [23] defined T_{mix} using these broadened peaks between 26-35°C. This is different from the definition of T_{mix} used in this thesis. There is no standard definition of T_{mix} because T_{mix} determinations are complicated and technique dependent.

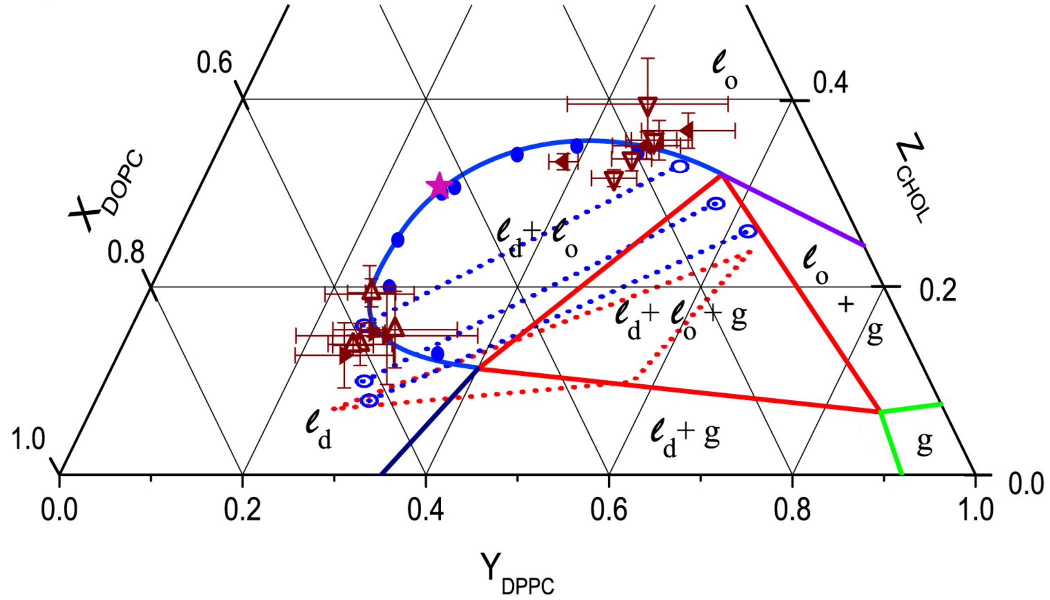

Figure 5.1: Overlay of two DOPC/DPPC-D62/chol phase diagrams mapped out using ^{2}H NMR by two independent research groups. Readers unfamiliar with how to read ternary phase diagrams are referred to Appendix F. The three-phase triangle at 20°C (red dotted lines), $\mathbf{l_d{+}l_o}$ tie-lines[2] and end-points at 22.5°C (blue dotted lines and blue open circles) are described in tables 1 and 2 in the supplementary information of Veatch et al. [25]. These features are superimposed on the 22°C phase diagram of Davis et al. [23, fig. 9b]. All one-, two- and three-phase region labels, solid lines, and filled-in symbols are from the Davis et al. phase diagram. The triangular symbols are $\mathbf{l_d{+}l_o}$ end-points determined from spectral subtraction and the magenta star is the estimated critical composition by Davis et al. The Davis et al. tie-lines (not shown) are almost parallel to the left edge of the three phase triangle. Adapted from [25] and [23], and reproduced from [165] by permission of The Royal Society of Chemistry.

Veatch and Keller also used nuclear magnetic resonance (NMR) and fluorescence microscopy to study DOPC/DPPC/chol [25, 61, 67]. In 2003, they looked at 3 different compositions (33:33:33, 50:25:25, 40:40:20) at 10-50°C using the probe TR-DPPE and epifluorescence microscopy [61]. Transitions were recorded as the temperature at which recognizable domains appeared and then disappeared as temperature was decreased and then increased. Scan rates of 0.2-0.5°C/min were used to minimize photo-oxidation. Veatch and Keller did not measure T_{mix} in equilibrium conditions, but they believe the T_{mix} measured should represent the upper and lower bounds of the true equilibrium T_{mix} [61].

In 2004, Veatch et al. studied three similar compositions (35:35:30, 47:23:30, 23:47:30) using ^{2}H NMR, ^{1}H-MAS NMR, and fluorescence microscopy [67]. Note that in contrast to our experiments, the ^{2}H NMR samples in [67] did not contain fluorophores, and the lipids used in fluorescence microscopy were not deuterium labelled. As with Davis' group, Veatch et al. defined T_{mix} slightly differently than we did: they defined two temperatures, T_{low} and T_{misc}. Below their T_{low}, Veatch et al. observed superposition of $\mathbf{l_d}$ and $\mathbf{l_o}$ ^{2}H NMR spectra; i.e., their T_{low} is T_{mix} in this thesis. Between T_{low} and their T_{misc}, the methylene resonances are poorly resolved; this is presumably the same temperature range where Davis et al. [23] observed line broadening.

The partial phase diagram in Fig. 5.1 shows that the two groups' findings are in broad agreement. Davis et al. [23] reported that the main differences between the two groups' phase diagrams lie above 30°C, which is beyond the temperature range tested in this thesis. In this thesis, the lipid composition of 35:35:30 DOPC/DPPC-D62/chol is exclusively used. This composition is near the $\mathbf{l_d}+\mathbf{l_o}$ coexistence phase boundary and is indeed near a line of critical points [177]. This phase diagram also shares the same basic features reported for several other different ternary mixtures made with a low melting temperature lipid, a high melting temperature lipid, and chol (DOPC/pSm/chol, POPC/PSm/chol, POPC/DPPC/-chol, and eggPC/bSm/chol) [61, 63].[4]

In addition to the phase diagrams of Veatch et al. and Davis et al., the research group of Nagle and Tristram-Nagle also studied fully hydrated 35:35:30 DOPC/DPPC/chol using WAXS and SAXS [47, 145]. Two peaks, corresponding to two lamellar *D* spacings were clearly resolvable in the second order reflection for $T \leq 20$°C. A single *D* spacing was observed for $T \geq 25$°C. To see two lamellar repeat spacings, not only do the *D* spacings have to

---

[4] Parts of the phase diagrams of the last three mixtures are contentious.

be different enough, the domains must also be aligned across the water layer in neighboring bilayers. Being able to measure two Ds is clear evidence for phase coexistence [47].[5] Their results confirm phase separation at $T \leq 20°C$, but they do not rule it out above 20°C. No data was taken between 20 and 25°C. The order parameters measured from X-ray experiments are higher than those measured by Veatch et al. [25] using ^{2}H NMR [47, fig. 6D]. In [145], they determined the angles of tie-lines in the phase diagram of DOPC/DPPC/chol at 15°C from x-ray lamellar D spacing. Fragments of these tie-lines are shown in Fig. 5.2. The angle of their tie-lines near 35:35:30 DOPC/DPPC/chol are similar to those of Veatch et al. [25], and their results will not be discussed separately from here on.

The above describes the efforts of numerous experimentalists to map the phase diagram of a single ternary mixture. In principle, lateral lipid heterogeneity is caused by differences in interaction free energies between different lipids, and it should be possible to calculate phase compositions and phase boundaries from first principles. These calculations are not simple. Very little theoretical work has been done on the phase behaviour of cholesterol and lipids [178]. Those that have been done are summarized in a review by Komura and Andelman [179]. Most models in the existing literature cannot produce a phase diagram that has liquid-liquid phase separation in the ternary mixture but no liquid-liquid phase separation in any of the three binary ones. The only exception is Radhakrishnan and McConnell [180]'s model involving condensed complexes. Their model fails to produce a gel phase in the appropriate compositions, however. Attempts to create a ternary lipid phase diagram using regular solution theory required an overly large attractive interaction between at least two of the components [178]. They also ignore the degrees of freedom possessed by the lipid tails. Atomistic calculations can in principle be used to include this, but they are computationally expensive. A model for determining the ternary phase diagram for DOPC/DPPC/chol was recently proposed by Wolff et al. [181].

5.2 T_{mix}

One simple way to characterize a ternary mixture is by its T_{mix}. The T_{mix} measured using ^{2}H NMR in this thesis, 22 ± 2°C (Fig. 3.20), is similar to those reported in the literature: 18 ± 2°C (Veatch et al. [25]), 20 ± 3°C (Mills et al. [47]), and 26 ± 1°C (Davis

---

[5] The reverse is not true: the absence of two D spacings does not imply absence of phase coexistence.

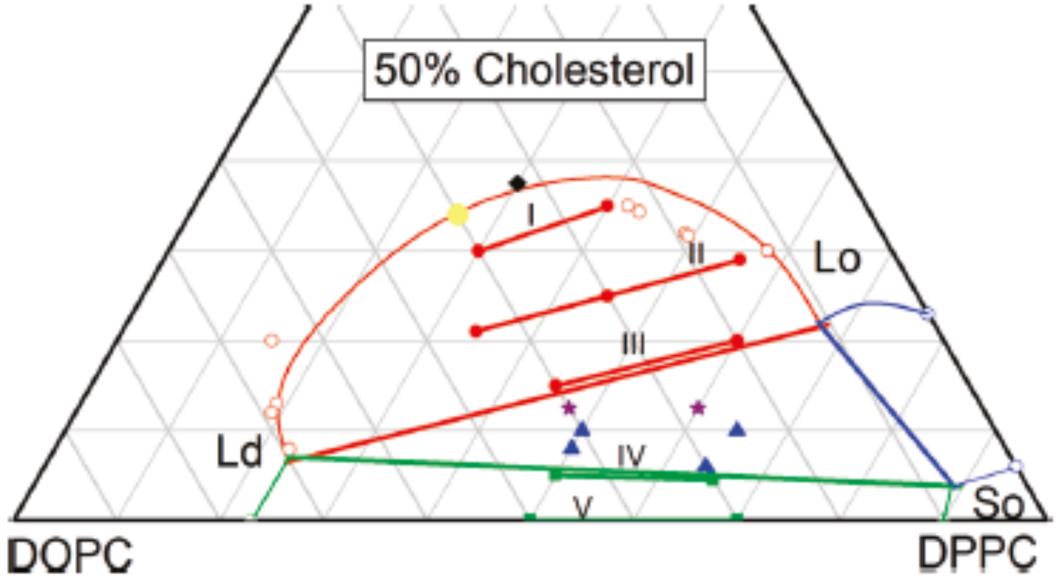

Figure 5.2: Overlay of the DOPC/DPPC-D62/chol phase diagrams at 15°C mapped out by Uppamoochikkal et al. [145] using x-ray and by Veatch et al. [25] using ^{2}H NMR at 15°C. The $\mathbf{l_d}$ + $\mathbf{s_o}$ two-phase region is enclosed by three straight green lines and contains Uppamoochikkal et al. [145]'s IV and V tie-line fragments; the two open green circles at zero chol show the coexistence compositions of Furuya and Mitsui [148]. The $\mathbf{l_d}+\mathbf{l_o}$ two-phase region is enclosed by one straight and one curved line, and it contains tie-line fragments I, II, and III from Uppamoochikkal et al. [145]; the open red circles show the coexistence compositions of Veatch et al. [25]. The $\mathbf{l_o}$ + $\mathbf{s_o}$ two-phase region is enclosed by two straight lines and one curved blue line; the open blue circles at 0% DOPC show the coexistence compositions of Vist and Davis [20]. The yellow point suggests the location of an upper critical point. Grid marks off increments of 0.1. Reprinted with permission from [145]. Copyright 2010 American Chemical Society.

et al. [23]). The T_{mix} reported by Mills et al. [47] is only two degrees lower than ours, i.e. within errors. The next section (Sec. 5.3) will demonstrate that the data from all four research groups are consistent.

5.3 Compositions of $\mathbf{l_d}$ and $\mathbf{l_o}$ phases

One of the main questions regarding phase coexistence is: what are the lipid compositions of the coexisting phases? By definition, below T_{mix}, the two phases have two different lipid compositions. In the absence of a theoretical framework, these compositions are independent of each other. For example, using the data of Davis et al. [23] at 22°C the $\mathbf{l_d}$ phase is 57:25:18 DOPC:DPPC-D62:chol, and the $\mathbf{l_o}$ phase is 24:40:36 DOPC/DPPC-D62/chol (Table 5.1).

Figure 5.3 compares the percent of the total DPPC-D62 in the $\mathbf{l_d}$ phase calculated using the ^{2}H NMR experiments of this thesis with the literature [23, 25, 61, 131]. In this thesis, the relative amounts of DPPC-D62 in the two phases (e.g., fraction of DPPC-D62 in $\mathbf{l_d}$ vs $\mathbf{l_o}$) were determined using ^{2}H NMR methyl peak area ratios in Sec. 3.6. The literature values were calculated using the the phase diagram, in conjunction with the lever rule and the left-hand side of Eq. (3.9). For example, using the data of Davis et al. [23] at 22°C, the ratio of $\mathbf{l_d}$ to $\mathbf{l_o}$ phase fraction in mixtures is 32:68 (Table 5.1). The left-hand side of Eq. (3.9) becomes $(32 \times 25)/(68 \times 40) = 0.29$. This means that 29% of the DPPC-D62 in the sample is in the $\mathbf{l_d}$ phase and 71% of it is in the $\mathbf{l_o}$ phase. Davis et al. [23] measured a lower fraction of DPPC-D62 in the $\mathbf{l_d}$ phase than we did (see Fig. 5.3), consistent with the higher T_{mix} they measure.

Table 5.1: All end-points for tie-lines crossing the composition of 35:35:30 DOPC/DPPC-D62/chol, as measured by the Davis et al. group [23, 28].

Temp	$\mathbf{l_d}$				$\mathbf{l_o}$			
°C	Composition			f_{ld}	Composition			f_{lo}
	DOPC	DPPC-D62	Chol		DOPC	DPPC-D62	Chol	
18	61	23	16	31	24	40	37	69
22	57	25	18	32	24	40	36	68
24	52	26	22	36	25	41	34	64
26	46	30	24	44	27	39	34	56
28	48	31	21	9	33	36	31	91

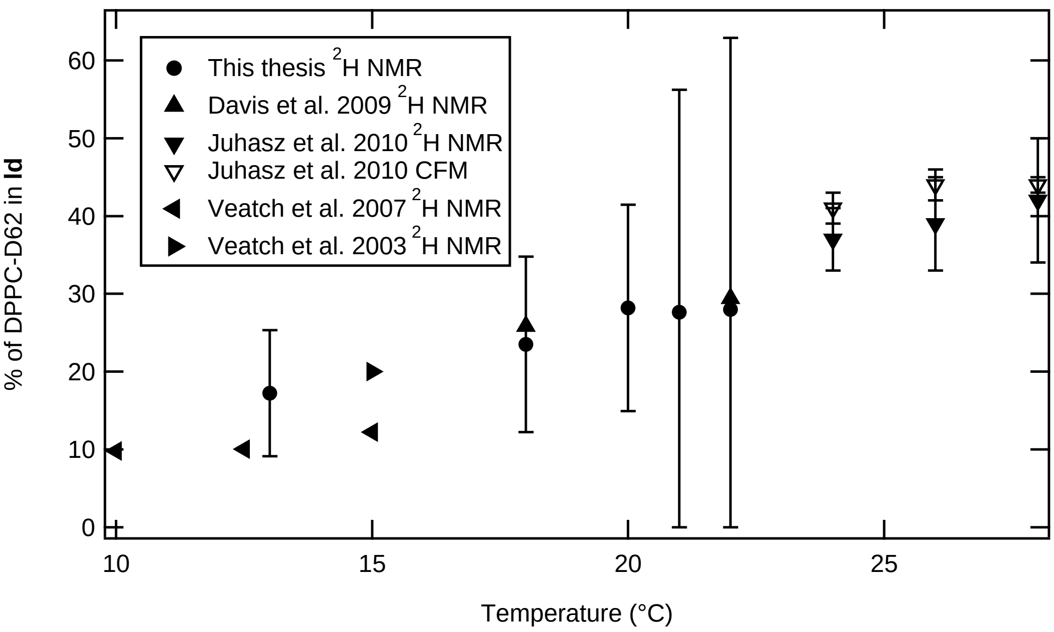

Figure 5.3: Percent of the total DPPC-D62 that is in the $\mathbf{l_d}$ phase in 35:35:30 DOPC/DPPC-D62/chol mixtures. Note that this is not the same as DPPC-D62 composition in the $\mathbf{l_d}$ phase.

The data of the four research groups are in broad agreement, even though the T_{mix} of the sample used in these methyl peak measurements (batch L2, $T_{mix} = 24.0 \pm 0.5$°C) is lower than the T_{mix} of Davis et al. [23] (26 ± 1°C), and higher than the T_{mix} of Veatch et al. [25] (18.2 ± 1.5°C). The three groups' data agree that below T_{mix}, DPPC-D62 in the $\mathbf{l_d}$ phase does not exceed ∼ 40% of the total DPPC-D62 content. Changes in the distribution of DPPC-D62 between the two phases are gradual as temperature is varied between 10°C and T_{mix}. The isothermal slices of thd Davis et al. [23] phase diagram have been combined in Fig. 5.4 to show that temperature dependent changes between 18 and 28°C to the $\mathbf{l_d}+\mathbf{l_o}$ phase boundary are more dramatic on the $\mathbf{l_d}$ side than the $\mathbf{l_o}$ side. Table 5.1 shows that in this temperature range, the $\mathbf{l_d}$ phase compositions change more than the $\mathbf{l_o}$ compositions: e.g., $\mathbf{l_d}$ composition changes upon heating from 18 to 28°C: % DOPC drops by 21% (e.g., 46 vs. 61), % DPPC-D62 increases by 35%, and % chol increases by 31%. In comparison, the $\mathbf{l_o}$ phase composition increase by 38% for DOPC, decrease by 10% for DPPC-D62, and decrease by 10% for chol. This is also seen in the more recent work Davis and Schmidt [177], where they studied a slightly different composition with less cholesterol (37.5:37.5:25 DOPC/DPPC-D62/chol), and found that chol concentration of the

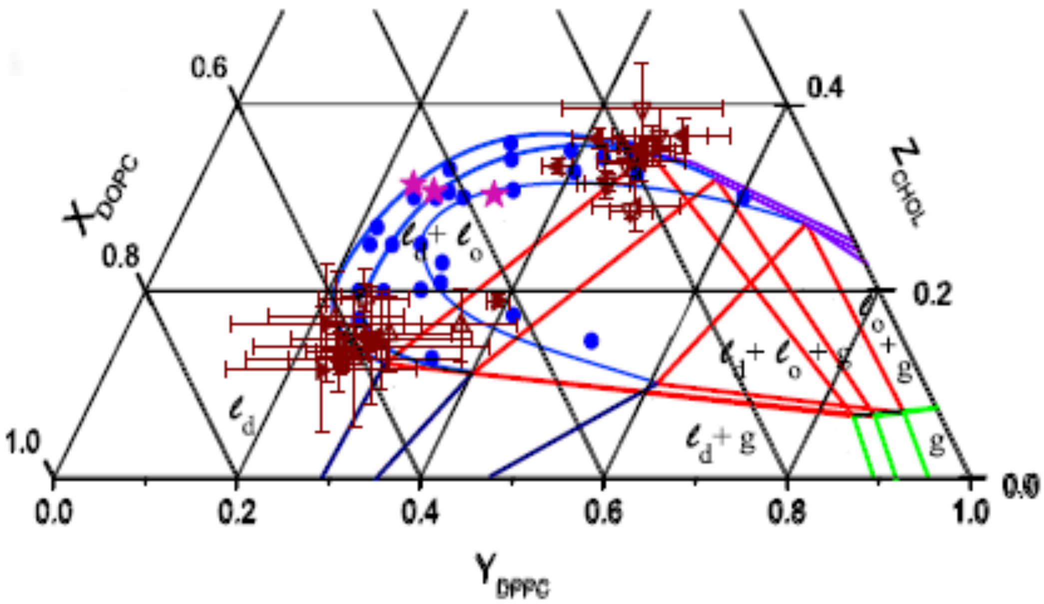

Figure 5.4: 35:35:30 DOPC/DPPC-D62/chol phase diagrams at 18, 22, and 24°C from Davis et al. [23] overlaid on top of each other. 18°C has the largest $\mathbf{l_d} + \mathbf{l_o} + \mathbf{s_o}$ three phase region (red triangle) and the largest $\mathbf{l_d}+\mathbf{l_o}$ two phase region (blue), the medium sized ones are at 22°C, and the smallest ones are at 24°C. The maroon triangular symbols are $\mathbf{l_d}+\mathbf{l_o}$ end-points determined from spectral subtraction and the magenta stars are estimated critical composition by Davis et al.. The Davis et al. tie-lines (not shown) are almost parallel to the left edge of the three phase triangle. Adapted from [23] with permission from Elsevier.

$\mathbf{l_d}$ phase decreased substantially, while the chol concentration of the $\mathbf{l_o}$ phase increased only somewhat as temperature was lowered.

The data from this project also shows greater changes in membrane composition in the $\mathbf{l_d}$ phase. Above T_{mix}, the fluid phase ^{2}H NMR DPPC-D62 methyl splitting decreases with increasing temperature; the increased thermal energy increases membrane fluidity. Below T_{mix}, the methyl splitting of the $\mathbf{l_o}$ phase also decreases with increasing temperature, but that of the $\mathbf{l_d}$ phase increases. The former is analogous with the fluid phase above T_{mix}. The latter – the increase in $\mathbf{l_d}$ methyl order – suggests that compositional changes are ordering the lipid chains, and opposing the disordering effects of increased thermal energy. This agrees with the notion that the composition of the $\mathbf{l_o}$ phase remains relatively constant with temperature. All samples in this thesis, regardless of probe content, exhibited these behaviours. This suggests that the trends are caused by the membranes themselves.

Fluorescence microscopy data from this thesis lends further support to the idea that the $\mathbf{l_o}$ composition remains constant. The high-GP domain GP, at low probe concentrations, is less correlated with temperature changes than the low-GP domain's GP (Fig. 4.12). The high-GP domains should be associated with the $\mathbf{l_o}$ domains, and the low-GP domains should be associated with the $\mathbf{l_d}$ domains (Sec. 4.4). Thus, the unchanging GP value of the high-GP domains supports the idea that the composition of the $\mathbf{l_o}$ phase varies with temperature less than the composition of the $\mathbf{l_d}$ phase.

5.4 Domain size

One of the contentious issues surrounding the existence of lipid rafts is their size. One of the advantages of microscopy is its ability to provide spatial information. The caveat is that if the domains are smaller than optical resolution ($\sim$ 200-300 nm), then they are not directly observable with standard microscopy techniques. Although ^{2}H NMR does not provide spatial information about domains, estimates can be made based on spectral appearance [67] (see below). The length scales probed by ^{2}H NMR could be shorter than those probed by microscopy. Juhasz et al. [131] showed that well within the two-phase coexistence region, relative domain area of equilibrated membranes measured by ^{2}H NMR and CFM are in quantitative agreement.

Figure 4.14 showed that the area fraction occupied by low-GP, $\mathbf{l_d}$, domains increases incrementally with temperature to a maximum of 0.4 at temperatures just below the phase transition and does not continue to increase. Veatch and Keller [61] also noted that 35:35:30 DOPC:DPPC:chol possess roughly equal area fractions of bright and dark phase as the membrane passes through the miscibility transitions. Davis and Schmidt [177] recently performed ^{2}H NMR measurements with very small temperature increments near and below the critical point for 35:35:30 DOPC/DPPC-D62/chol membranes. A number of parameters were found to obey the power laws of critical phenomena: the temperature-dependent changes in these parameters were the greatest near the critical point (see Sec. 5.5). Also, ^{2}H NMR line broadening was observed above T_{mix} by all three research groups that used ^{2}H NMR. Thus, the discontinuity in domain area fraction in GUVs (from $\sim 40\%$ just below T_{mix} to completely homogeneous at T_{mix}) is probably caused by our inability to measure something (e.g., with small enough temperature increments or with good enough spatial resolution), rather than an actual discontinuous change in domain area fraction.

Figure 3.19 showed the proportion of DPPC-D62 in the two phases found using ^{2}H NMR. In Fig. 5.5, the fraction of DPPC-D62 in the $\mathbf{l_d}$ phase measured using ^{2}H NMR is shown together with the fraction of low-GP domain area observed in fluorescence images (Fig. 4.14). The two techniques are in surprising agreement, given that the fluorescence microscopy experiments show domain area sizes for the entire phase, and not just for DPPC-D62, as in ^{2}H NMR.

Knowing the location and directions of the tie-lines in the phase diagram, we can determine the composition of each phase. Effective area per lipid molecule has been measured by Nagle and Tristram-Nagle [182]: 5.9-7.2 nm^2 for $\mathbf{l_d}$ DOPC, 5.7-6.8 nm^2 for $\mathbf{l_d}$ DPPC, and 296 nm^2 for cholesterol. Note that the area occupied by DPPC is dependent on cholesterol concentration. It should be possible to calculate absolute domain size if the total number of lipids in a vesicle is known. Unfortunately, the latter information is not measurable by ^{2}H NMR. Thus, a direct comparison between GUV and MLV domain sizes is not possible.

It is, however, possible to estimate domain size by considering the spectroscopic timescale of ^{2}H NMR and using the difference in quadrupolar splitting of the two phases [67]. In order for coexistence spectra to be superpositions of spectra of the lipid subpopulations, exchange of lipids between the populations must be slow (see Appendix H). The smallest resolvable ^{2}H NMR methyl splittings between the $\mathbf{l_d}$ and the $\mathbf{l_o}$ phase is 1.1 kHz in

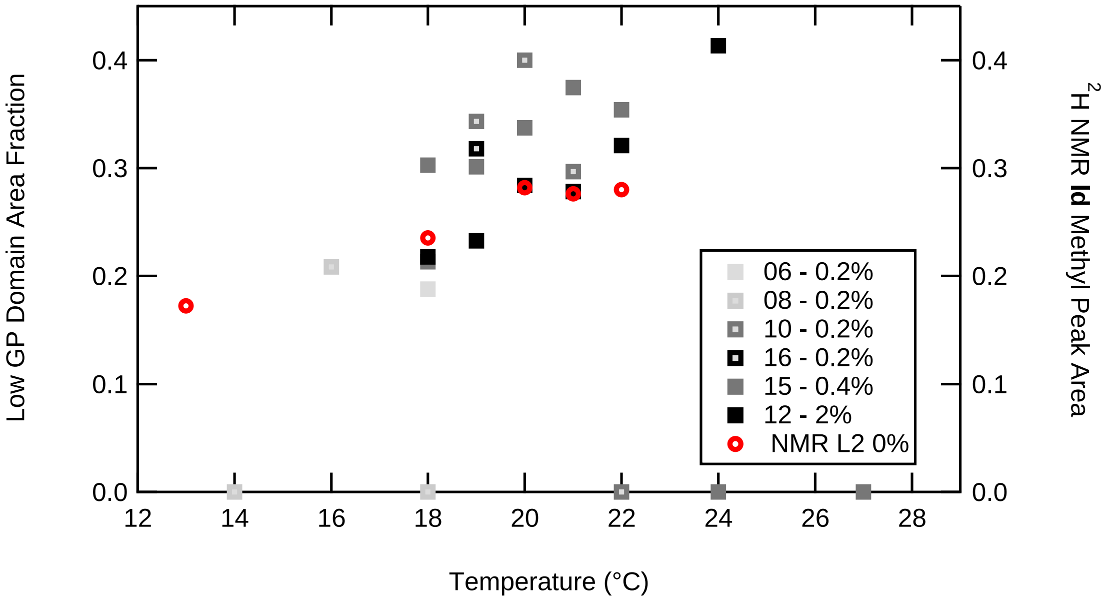

Figure 5.5: Liquid disordered ($\mathbf{l_d}$) fraction - fluorescence microscopy *vs.* ^{2}H NMR. (Left axis) Fractional area of low-GP domains in GUV with Laurdan calculated from micrographs from Fig. 4.14. (Right axis) ^{2}H NMR percent of DPPC-D62 methyl signal from the $\mathbf{l_d}$ phase in 35:35:30 DOPC/DPPC-D62/chol MLV from Fig. 3.19 (red).

our spectra. Since this smallest resolvable splitting is achievable near $T_{\rm mix}$, the two lipid environments are expected to be very similar. Under these circumstances, the lipids are expected to undergo Brownian diffusion [183]. For two-dimensional Brownian diffusion, the mean-square distance traveled by a lipid molecule in time interval τ is

$$\langle r^2 \rangle = 4D\tau \ , \tag{5.1}$$

where D is the diffusion coefficient. Diffusion coefficients of DPPC-D72, DPPC, and DOPC were measured to be 0.5-1.4$\times 10^{-12}$ m^2/s in 35:35:30 DOPC/DPPC/chol and in 35:35:30 DOPC/DPPC-D72/chol at 20-30°C [144]. Assuming that DPPC-D62 is similar to DPPC and DPPC-D72, this implies domain sizes have to be 30-120 nm in diameter in order for the lipids to travel to both types of environments. In fact, the condition for slow exchange (see Appendix H) requires that the domain sizes are much greater than 30-120 nm in diameter.

Given this lower bound for domain size, we expect that fluorescence microscopy and ^{2}H NMR methyl splittings should detect domains of similar sizes. As mentioned earlier, agreement in relative domain fraction between the two techniques was shown by Juhasz et al. [131]. In this thesis, fluorescence imaging was done at the equatorial plane. Vesicles were only imaged near $\mathrm{T_{mix}}$, and we expect $\mathbf{l_d}$ to $\mathbf{l_o}$ ratio to be close to unity [61]. With large domains, we can be sure that domains were not missed simply because they did not present themselves in equatorial plane images. As mentioned in Sec. 5.1, Veatch and Keller did not do their fluorescence microscopy experiments at equilibrium [61]. In equilibrated phase separated membranes, the two phases separate completely into two domains. Juhasz et al. [131] found that waiting for only 1 min, as was done in the fluorescence microscopy experiments of [61], is not long enough for equilibration. They found that 5 min is necessary for $\mathbf{l_d}$ and $\mathbf{l_o}$ domains to fully separate. Based on this criterion, equilibration conditions should have been met in both our ^{2}H NMR and our fluorescence microscopy experiments (20 min equilibration time). Thus, macroscopically phase-separated domains were expected in our experiments, and small domains (e.g., $\mathbf{l_o}$ domain only occupying 10% of the vesicle surface) were not expected.

5.5 Critical behaviour

Compositional variations are more noticeable near $\mathrm{T_{mix}}$. Even small changes in lipid composition can cause mixtures close to phase boundaries to move outside the two-phase coexistence region [47, 61]. There were signs of this in both the fluorescence and the ^{2}H NMR experiments of this thesis. In the Laurdan fluorescence microscopy experiments, the four 0.2% Laurdan samples showed diverse phase behaviour. Figure 4.13 also showed that vesicle populations tend to be heterogeneous: vesicles in a population do not all phase separate at the same temperature. Highly heterogeneous GUV preparations have also been reported by others [61, 87, 131]. This implies that the individual vesicles have different compositions [61]. In the ^{2}H NMR experiments, one of three probe-free samples had a $\mathrm{T_{mix}}$ that was 2 degrees higher. The methyls of that sample also experienced slightly different environments from those of the other two samples. These observations imply that the vesicles are sensitive to the details of the sample preparation protocol and that the chosen composition for our experiments is near a phase boundary, and is perhaps even near a critical point.

Davis and Schmidt [177] recently studied critical behaviour in DOPC/DPPC-D62/chol mixtures using ^{2}H NMR. In that study, they fitted the difference in ^{2}H NMR methyl

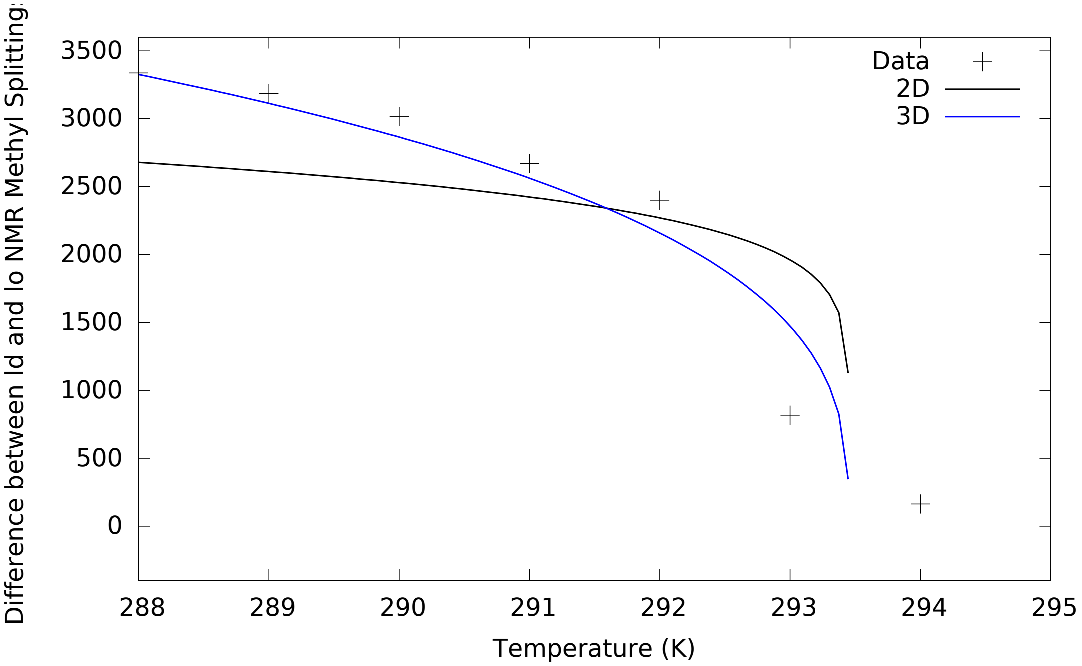

Figure 5.6: Difference between $\mathbf{l_d}$ and *sn*-1 $\mathbf{l_o}$ ^{2}H NMR methyl quadrupolar splittings of 35:35:30 DOPC/DPPC-D62/chol MLV. Two of the parameters in Eq. (5.2) were fixed: $T_c = 293.45$ K (20.3°C), $\beta_c = 0.125$ (2D)^6 and 0.3265 (3D). The fit returned values of 4400 ± 700 Hz (2D) and 12200 ± 700 Hz (3D) for $\Delta(\delta\nu)_0$.

quadrupolar splittings between the $\mathbf{l_o}$ and the $\mathbf{l_d}$ peaks $\Delta(\delta\nu)$ of 37.5:37.5:25 DOPC/DPPC-D62/chol MLV to

$$\Delta(\delta\nu) = \Delta(\delta\nu)_0 \left[\frac{(T_c - T)}{T_c}\right]^{\beta_c} \tag{5.2}$$

where $\Delta(\delta\nu)_0$ and β_c were the fitting parameters. They found that β_c was closer to the critical exponent of the 3D Ising model than that of the 2D Ising model. The Ising model is a simple theoretical model that displays phase-transition behaviour [184]. The model considers nearest-neighbour interactions. The Ising model has been used successfully to describe a large variety of physical systems, and the values of these critical exponents are very similar for a wide range of physical systems [185]. Although our data does not have the temperature resolution (0.05°C [186]) necessary for a study of the critical behaviour in 35:35:30 DOPC/DPPC-D62/chol membranes [177, 186], we plotted our data (Fig. 5.6) with Eq. (5.2) holding T_c and β_c constant to see if our data is consistent with the findings of Davis and Schmidt [177]. T_c was roughly equal to $\mathrm{T_{mix}}$ ($T_c = 293.45$ K), and the values of the 2D and 3D Ising model were used for β_c ($\beta_c = 0.125$ and 0.3265, respectively) [185]. The third parameter $(\delta\nu)_0$ was found by fitting Eq. (5.2) with Igor Pro: the fit returned values of 4400 ± 700 Hz and 12200 ± 700 Hz for $(\delta\nu)_0$. These values seem in agreement with expected quadrupolar splitting at $T_{\rm mix}$, given the data near $T_{\rm mix}$. Davis and Schmidt [177] showed that 35:35:30 DOPC/DPPC-D62/chol MLVs belonged to the 3D Ising universality class, and our data is consistent with this finding. Honerkamp-Smith et al. [186] showed that GUVs may belong to the 2D Ising universality class, but this is still debated [177, 187]. In the next section, possible differences between the two types of vesicles used this thesis, MLVs and GUVs, will be discussed.

5.6 MLV vs GUV

I used two techniques to study the membranes. Although efforts were made to make the two different types of experiments directly comparable (i.e., same equilibration time, the use of deuterated lipids and fluorophores in both types of experiments), the type of model membrane used had to be different: ^{2}H NMR required the use of MLVs and microscopy required the use of GUVs.

The difference in lamellarity is known to change basic thermodynamic properties of the vesicles [38]. Gel-to-liquid crystalline phase transitions occur in a narrower range of temperatures in MLV than in GUV [188], large unilamellar vesicle (LUV) [189], and small unilamellar vesicle (SUV) [189]. This is because of the high cooperative unit size (i.e., multiple bilayers) in MLV [67, 188]. This is consistent with our limited data that suggests MLVs belong to the 3D universality class (Sec. 5.5). In contrast, the work of [186] showed that GUVs belong to the 2D university class. Brumm et al. [189] also showed using DMPC/DSPC mixtures and pure lipids that vesicles of different types of sizes have different $T_{\rm m}$ distributions. Planar membranes had the highest $T_{\rm m}$ and SUV had the lowest because increased membrane curvature lowered the lateral pressure of the membrane. Curvature stress in GUV is expected to be negligible. Our ^{2}H NMR and fluorescence-microscopy experiments showed MLVs and GUVs have similar $T_{\rm mix}$. This implies that the slight osmotic stress imposed on the GUVs to make them spherical had no effect on $T_{\rm mix}$.

^{2}H NMR does not measure transition temperatures of individual MLVs; $T_{\rm mix}$ is measured for the sample as a whole. In GUV experiments, it is in principle possible to measure the $T_{\rm mix}$ of an individual vesicle. Even without such measurements, it is evident that the vesicle population observed was very heterogeneous. For a range of 4°C, both phase separated and homogeneous vesicles were observed. This has been noted by others as well [190]. We attempted to track individual GUV, but this was unsuccessful. The vesicles moved around the observation chamber too much, so that their identity cannot be verified between measurements. Also, photo-peroxidation would be a concern if repeated measurements were made on the same vesicle. Therefore, $\mathrm{T_{mix}}$ of individual vesicles was not determined. We are also unable to determine the width of the $\mathbf{l_d}+\mathbf{l_o}$ to homogeneous phase transition in GUVs since our experiments were done in a narrow range of temperatures.

5.7 Correlation between Laurdan GP and ^{2}H NMR order parameter

Laurdan's fluorescent moiety is situated near the phospholipids' glycerol backbones (Fig. 2.2), and hence GP measures the polarity in this region. The methylenes near the glycerol backbone have the largest ^{2}H NMR quadrupolar splittings. Using the very distinct ^{2}H NMR plateau edge quadrupolar splitting as a measure of the molecular order of the most-ordered $\mathbf{l_o}$ phase methylenes, we can correlate the ^{2}H NMR order parameter to Laurdan GP. Figure 5.7 shows pairs of Laurdan GP and ^{2}H NMR order parameter from samples with the same or very similar Laurdan concentrations, at the same temperature. Low-GP domain GPs were not used here since the plateau edge belongs to the $\mathbf{l_o}$, and not the $\mathbf{l_d}$ phase methylenes below $\mathrm{T_{mix}}$. In some ^{2}H NMR spectra the $\mathbf{l_d}$ "edge" splitting is also measurable, so this could be attempted in the future.

The Pearson's product-moment correlation coefficient (r) between GP and ^{2}H NMR order parameter (Scd^7) is defined as

$$r = \frac{\sum\limits_i (GP_i - GP_{\mathrm{mean}})(Scd_i - Scd_{\mathrm{mean}})}{\sqrt{\sum\limits_i (GP_i - GP_{\mathrm{mean}})^2}\sqrt{\sum\limits_i (Scd_i - Scd_{\mathrm{mean}})^2}} \,. \tag{5.3}$$

GP and ^{2}H NMR plateau methylene order parameter were found to be strongly correlated ($r = 0.9$). The maximum possible value for r is 1. Correlation was even stronger when the pairs are segregated by probe concentrations: the 2% Laurdan data were slightly less

---

[7] Scd is typeset differently than in Eq. (2.65) to avoid doubling up on subscripts.

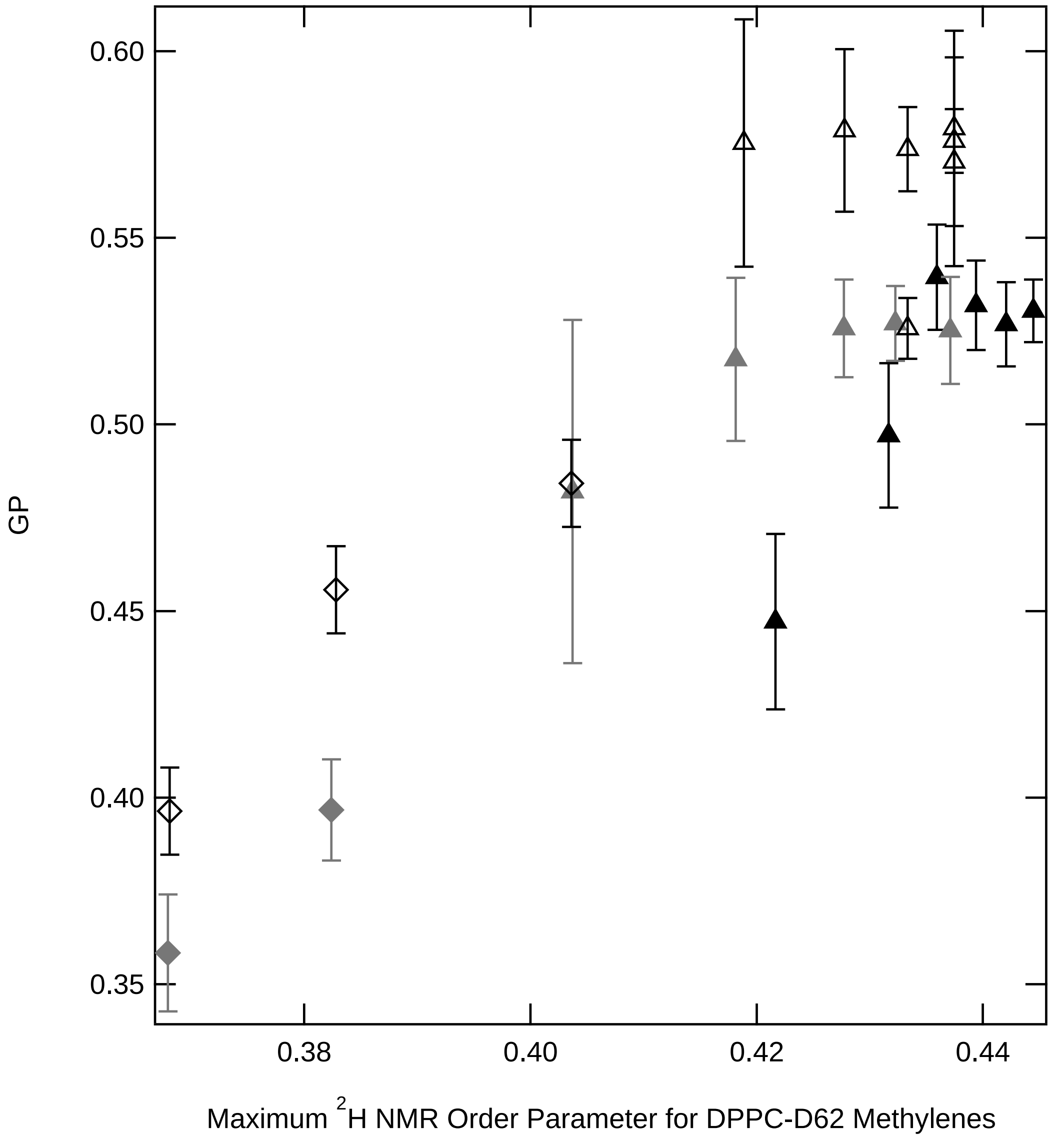

Figure 5.7: Scatter plot of population-average Laurdan GP from fluorescence microscopy and ^{2}H NMR plateau edge order parameters. The plateau edge doublets come from the most ordered methylenes of $\mathbf{l_o}$ phase DPPC-D62. Only GPs from the high-GP domains (△) and homogeneous vesicles (◇) were used. Each point comes from experiments that were done at the same temperature, and from samples with approximately the same probe concentration. Laurdan GP for GUVs with 0.2% Laurdan (unfilled symbols) were plotted against the ^{2}H NMR order parameter of MLVs with 0.3% Laurdan. Samples with 0.4% (gray) and 2% (black) Laurdan were available from both experiments. Horizontal errors are equal to the width of the symbol.

well correlated ($r = 0.9$) than the 0.2 and 0.4% Laurdan data ($r = 1$). When the pairs were separated based on the type of domain that the GP was obtained from (i.e., high-GP domain and homogeneous vesicles), the pairs from the $\mathbf{l_o}$ domains (△) were much less correlated ($r = 0.4$). The pairs from the homogeneous vesicles (◆) had a high correlation coefficient ($r = 0.9$), but this may be an artifact caused by the lack of data.

5.8 Photo-peroxidation

During microscopy experiments, high-intensity light was used to illuminate the vesicles. To minimize photo-damage and light induced phase separation, only 10-20 vesicles were imaged at each chosen temperature for each sample (Sec. 4.1.5). Given the small sample size, rare occurrences of a phase-separated vesicle may have been missed in our sampling, and the reported $\mathrm{T_{mix}}$ may be lower than the true $\mathrm{T_{mix}}$.

In the presence of photo-peroxidation, we might expect to see time-dependent changes during data collection. GP values from a given sample, measured at a given temperature, did not change with time; and neither did the number of phase-separated vesicles (data not shown). In addition, an experiment was done to ensure that the phase separation observed near $\mathrm{T_{mix}}$ was not caused by photo-peroxidation (sample 16, 0.2% Laurdan). This sample was not previously exposed to microscopy measurements prior to data collection at 19°C. The GP (Fig. 4.12), % phase-separated vesicles in the population (Fig. 4.13), and the low-GP domain area (Fig. 4.14) of this sample are in agreement with those measured in samples 10 (0.2% Laurdan) and 15 (0.4% Laurdan). For these other two samples, data collection started at 18°C. Photo-peroxidation was ruled out definitively for GUV measurements at and below 19°C. It is interesting to note that Zhao et al. [68] found that photo-peroxidation was not expedited at increased temperatures: light-induced domains appeared at similar rates at 10 and 23°C. If, despite our best efforts at avoiding photo-peroxidation, there was photo-induced phase separation, then the reported $\mathrm{T_{mix}}$ may be higher than the true $\mathrm{T_{mix}}$.

In the fluorescence-microscopy experiments, the 2% Laurdan sample was much more phase separated than samples with lower probe concentrations at all temperatures. Photo-induced phase separation can explain this using the same argument posed by Bouvrais et al. [72] to prove that lipid photo-peroxidation altered the bending elasticity of fluorescently labelled POPC membrane (Sec. 1.4.1). Using phase contrast and fluorescence microscopy, Bouvrais et al. [72] showed that the addition of 2% of six commonly used fluorescent dyes modulated membrane bending elasticity of POPC membranes. TR-DPPE, Rh-DPPE, Bodipy-PC, and NBD-PC induced the greatest changes, and the effects of Laurdan and DiIC18 were less prominent. They argued that the changes were induced by lipid peroxide formation with the following points:

1. Increased illumination power or increased exposure length increased the magnitude of the probe-induced modulations.
2. Variance of k_c was highest with the probes that altered k_c the most. These large variations were attributed to varying degrees of light exposure. Microscopists typically require at least a few seconds to find a candidate GUV, and to focus on the region of interest within the vesicle [33, 68]. This time can be quite variable depending on the quality and quantity of GUVs available, the specific desired feature that is sought, and the experience level of the microscopist. This amounts to variable light exposure time of the sample, which would result in a wide distribution of bending modulus for individual GUVs.
3. Decreasing dye concentration from 2% to 0.5% reduced the spread in k_c and minimized rigid-looking facets that only develop in Rh-DPPE labelled membranes after prolonged light exposure.

Analogous to Bouvrais et al.'s observations [72], our microscopy experiments showed increased phase separation and larger Laurdan GP variations in individual GUVs for 2% Laurdan than for 0.2 or 0.4% Laurdan (Figs. 4.8-4.10). Although our GUVs doped with 2% Laurdan behaved differently than those doped with 0.2 and 0.4% Laurdan, Bouvrais et al. [72] showed that bending elasticity was only slightly modified by 2% Laurdan. Our ^{2}H NMR experiments also showed that lipid chain order was only slightly modified by 2% Laurdan. Note that the latter may be attributed to the lack of light exposure in ^{2}H NMR experiments, whereas the former cannot.

5.9 Effects of probes on lipid membrane phase behaviour

There is significant evidence in the literature that shows trace amounts ($< 0.1\%$) of various $\mathbf{l_d}$-preferring probes altering T_{mix}. Juhasz et al. [28] performed CFM experiments on 35:35:30 DOPC:DPPC:chol GUV using six commonly used fluorescent probes at probe concentrations of $0.1 \pm 0.01\%$ and found that the different probes measured different $\mathrm{T_{mix}}$. The $\mathrm{T_{mix}}$ reported by Rh-DPPE deviated the most (2.5°C) from the $\mathrm{T_{mix}}$ reported by the other probes. Rh-DPPE has been reported to favour the $\mathbf{l_d}$ phase in various types of membranes (e.g., $k_p^{lo/ld} = 0.7 \pm 0.2$ in POPC/chol and 0.3 ± 0.1 in POPC/Sm/chol [53]) [28, 53, 78]. Our lab has also found that 0.05% of the $\mathbf{l_d}$-preferring probe DiIC12 increased $\mathrm{T_{mix}}$ by 3.5 ± 0.5°C in 35:35:30 DOPC/DPPC-D62/chol MLV [70], and 0.02% TR-DPPE ($k_p < 0.4$ [61]) induced phase separation in POPC/DPPC/brassicasterol membranes [129]. The amount of $\mathbf{l_d}$ probe needed to induce a change is minimal. In contrast, 0.03-0.6% weakly partitioning naphthopyrene also only slightly altered the membrane. ^{2}H NMR also showed that 0.1-2% equipartitioning probe Laurdan did not alter $\mathrm{T_{mix}}$. Evidence for the benign nature of equipartitioning probes is mounting. Previously, we also found that the nearly equipartitioning probe DiOC18 did not greatly disturb the lipids [70].

We previously suggested that probes alter the entire phase diagram, and not just the characteristic of a single phase [70]. Our data on naphthopyrene lends further support to this idea. Even though naphthopyrene preferentially partitions into the $\mathbf{l_o}$ phase, ^{2}H NMR detected changes to the $\mathbf{l_d}$ membrane order. Zhao et al. [68] found that naphthopyrene can give rise to light-induced phase separation. Our ^{2}H NMR results suggest that the effects of naphthopyrene are not only light-induced, but also intrinsic to the fluorophore since the samples are kept in the dark throughout a ^{2}H NMR experiment. In other words, any changes in the membrane observed in a ^{2}H NMR experiment can be directly attributed to the presence of probe. The effects that fluorescent probe have on membranes are magnified by light exposure.

Although naphthopyrene was considered a representative $\mathbf{l_o}$-preferring probe, it is important to remember that it only showed a modest preference for the $\mathbf{l_o}$ phase. ^{2}H NMR experiments found that 0.03-0.6% naphthopyrene only increased $\mathrm{T_{mix}}$ by 2 ± 1°C. In comparison, 0.5% DiIC12 raised $\mathrm{T_{mix}}$ by an impressive 6°C. The effects of naphthopyrene may be less pronounced because its partitioning is less complete than that of DiIC12.

5.10 Chapter summary

The properties of our 35:35:30 DOPC/DPPC-D62/chol membranes are in good agreement with the literature: T_{mix}, relative domain size, and DPPC-D62 compositions of the two phases were all comparable to published values. Analysis of ^{2}H NMR methyl splittings suggests that our MLVs likely belong to the 3D universality class, which is also in agreement with the literature. Below T_{mix}, ^{2}H NMR spectra were well-resolved, indicating that domains have to be $\gg$ 100 nm. Consistent with this estimate, and despite differences in model system used (MLV vs GUV), micron-scale phase separation was observed in GUVs using two-photon excitation microscopy below the ^{2}H NMR T_{mix} of $\sim$ 22°C. ^{2}H NMR also showed that DPPC-D62 was enriched in the $\mathbf{l_o}$ phase.

In this thesis, we performed two types of experiments on the membranes: fluorescence microscopy and ^{2}H NMR. Laurdan GP from individual vesicles measured using two-photon excitation microscopy correlated well to ^{2}H NMR methylene order parameters of DPPC-D62. This shows that GP reflects the lipid environment near the phospholipids' glycerol backbones.

This thesis was focused on studying the effect of trace amounts of two probes, Laurdan and naphthopyrene, using 35:35:30 DOPC/DPPC-D62/chol membranes. ^{2}H NMR and two-photon excitation microscopy showed that the equipartitioning probe Laurdan does not alter the melting behaviour of 35:35:30 DOPC/DPPC-D62/chol membranes. Our previous work showed that DiOC18, another nearly equipartitioning probe in 35:35:30 DOPC/DPPC-D62/chol membranes, has only small effect on T_{mix}, but disorder-preferring probe DiIC12 increases T_{mix} markedly [70]. Naphthopyrene (0.03-0.6%), a probe with modest preference for the $\mathbf{l_o}$ phase in DOPC/DPPC/chol, slightly altered the molecular order of lipids in the $\mathbf{l_d}$ phase. Surprisingly, no effects were observed in the $\mathbf{l_o}$ phase. The fact that naphthopyrene altered the molecular order of the $\mathbf{l_d}$ phase it partitions out of suggests that probes alter the entire phase diagram, and not just the characteristic of a single phase. ^{2}H NMR experiments were performed in the absence of light. Thus, changes observed by ^{2}H NMR shows that photo-peroxidation alone cannot explain naphthopyrene-induced changes in membranes.

At high (2%) Laurdan concentration, there were multiple signs of photo-peroxidation in fluorescence images: increased phase separation and increased variations in Laurdan GP of individual GUVs. In the absence of light (e.g., in ^{2}H NMR experiments), the inclusion of even 2% Laurdan did not perturb the membrane.

Chapter 6

Conclusions and future work

Fluorescence can provide dynamic and structural information about membranes. As with the use of any probe method, it is important to understand the perturbations caused by the probe on the system they are being used to study. Careful characterization of photophysical properties and membrane lateral organization of fluorescent probes is important for correct interpretation of the data from fluorescence experiments. The effects of probe addition can be found by comparing labelled and label-free results using non-perturbing methods (e.g., nuclear magnetic resonance (NMR) and X-ray) on lipid model systems.

This thesis used two techniques, fluorescence microscopy and deuterium nuclear magnetic resonance spectroscopy (^{2}H NMR). We have made an initial foray into determining the correlation between Laurdan general polarization (GP) and ^{2}H NMR maximum methylene order parameter, with promising results (Fig. 5.7). More work is needed to see how general this correlation is – after all, we looked at a single labelled lipid with ^{2}H NMR while Laurdan presumably reports the behaviour of the composite membrane. Laurdan is present in the liquid disordered and the liquid ordered phase. How does it interact with DOPC or cholesterol? These questions can be answered by incorporating deuterated DOPC instead of DPPC-D62, for example. It is also important to see if this correlation is affected by the type of lipid used (PC vs Sm).

While it is clear that lipid peroxide formation is a contributing factor to artifacts such as light-induced phase separation, the mechanism is not clear [68]. Are the free radicals acting through chemical reactions such as fragmentation of the lipids? The products of photoperoxidation in the presence of fluorescent probes, and the chemical interactions between these products and lipids need to be established. There is already a large body of research dedicated to studying lipid oxidation [e.g., 191, 192]. What is needed is specific studies on light-induced peroxidation of lipids in well-defined systems such as model membranes.

General effects caused by impurities on membranes also need to be better understood. Does the simple presence of probes alter the free energy landscape of lipid membranes? The ^{2}H NMR experiments of this thesis falls into this second category. While equipartitioning probes had minimal effects on miscibility transition temperature (T_{mix}), $\mathbf{l_d}$ or $\mathbf{l_o}$- "preferring" probes always increased T_{mix}. Our results support the idea that probe partitioning is at least one of the contributing factors to probe-induced membrane phase changes. Several computational groups have modeled inclusion of fluorescent probes into single-component lipid membranes [71, 193–196], but none have been done on binary or ternary membranes so far. An extension of the ternary model proposed by Wolff et al. [181] to include an impurity, either as the third component added to a binary system or as a fourth component modifying the ternary phase diagram, could illuminate the perturbation to the phase boundaries caused by a trace component. This can help us understand the counterintuitive reduction in T_{mix} caused by caveolin, for example.

Fluorescence is widely used in cell studies. The effects from the addition of fluorescent probes can impact our interpretation of these studies. In general, lipid probes show membrane-composition-dependent behaviour. It is important to study probes in a large variety of lipid mixtures in order to understand their interaction with the membrane. It is also important to characterize individual probes, since they are all unique. As demonstrated by Baumgart et al. [59] and Juhasz et al. [28], there are as many exceptions to the generalizations about probes as the number of generalizations themselves.

Membrane physical properties are most sensitive to compositional changes near phase boundaries and critical points. Zhao et al. [68] found light-induced domains were only present in mixtures close to the phase boundary. It is tempting to think that probe-induced artifacts can be avoided by staying away from such compositions, but there is mounting evidence illustrating the importance of studying membrane compositions near phase boundaries in biological membranes. Veatch et al. [44] found that giant plasma membrane vesicle (GPMV) isolated from rat basophil leukemia cells maintained proximity to miscibility critical points, and Gray et al. [197] found that liquid general anesthetics lower critical temperatures in these GPMV. In addition, a number of other studies illustrated the effects of trace biomolecules on membrane phase behaviour (Sec. 1.4.2). Clearly, critical points and phase boundaries are where the interesting things happen. In answer to the question posed in the title of this thesis, our experiments demonstrated that trace components can indeed affect global membrane properties. Our results suggest that one possible way trace biomolecules can perform their functions inside living systems is by modulating membrane phase behaviour.

Bibliography

[1] Brewer, J. W., 2013. Phospholipids: "greasing the wheels" of humoral immunity. *Biochim. Biophys. Acta* 1831:642–51.

[2] McLaughlin, S., J. Wang, A. Gambhir, and D. Murray, 2002. PIP(2) and proteins: interactions, organization, and information flow. *Annu. Rev. Biophys. Biomol. Struct.* 31:151–75.

[3] Sperelakis, N., 1997. Cell physiology source book. Academic Press, San Diego, 2nd ed. edition.

[4] Johnson, J. E., and R. B. Cornell, 1999. Amphitropic proteins: regulation by reversible membrane interactions (review). *Mol. Membr. Biol.* 16:217–35.

[5] Zhou, Y., S. J. Plowman, L. M. Lichtenberger, and J. F. Hancock, 2010. The anti-inflammatory drug indomethacin alters nanoclustering in synthetic and cell plasma membranes. *J. Biol. Chem.* 285:35188–35195.

[6] Simons, K., and E. Ikonen, 1997. Functional rafts in cell membranes. *Nature* 387:569–572.

[7] Lingwood, D., and K. Simons, 2009. Lipid rafts as a membrane-organizing principle. *Science* 327:46–50.

[8] Staneva, G., M. Seigneuret, K. Koumanov, G. Trugnan, and M. I. Angelova, 2005. Detergents induce raft-like domains budding and fission from giant unilamellar heterogeneous vesicles: a direct microscopy observation. *Chem. Phys. Lipids* 136:55–66.

[9] Fivaz, M., L. Abrami, and F. G. van der Goot, 1999. Landing on lipid rafts. *Trends Cell Biol.* 9:212–3.

[10] Almeida, P. F. F., A. Pokorny, and A. Hinderliter, 2005. Thermodynamics of membrane domains. *Biochim. Biophys. Acta - Biomembr.* 1720:1–13.

[11] Hanzal-Bayer, M. F., and J. F. Hancock, 2007. Lipid rafts and membrane traffic. *FEBS Lett.* 581:2098–2104.

[12] Sabra, M. C., K. Jørgensen, and O. G. Mouritsen, 2001. Effects of the insecticides malathion and deltamethrin on the phase behaviour of dimyristoylphosphatidylcholine multilamellar lipid bilayers. *In* T. Razumas, V and Lindman, B and Nylander, editor, Surf. Colloid Sci. Springer, volume 116 of *Prog. Colloid Polym. Sci.*, 1–8.

[13] Kirjavainen, M., J. Mönkkönen, M. Saukkosaari, R. Valjakka-Koskela, J. Kiesvaara, and a. Urtti, 1999. Phospholipids affect stratum corneum lipid bilayer fluidity and drug partitioning into the bilayers. *J. Control. Release* 58:207–14.

[14] Allen, T. M., and P. R. Cullis, 2013. Liposomal drug delivery systems: From concept to clinical applications. *Adv. Drug Deliv. Rev.* 65:36–48.

[15] Simons, K., and W. L. C. Vaz, 2004. Model systems, lipid rafts, and cell membranes. *Annu. Rev. Biophys. Biomol. Struct.* 33:269–95.

[16] Feigenson, G. W., 2006. Phase behavior of lipid mixtures. *Nat. Chem. Biol.* 2:560–563.

[17] Rubenstein, J. L., B. A. Smith, and H. M. McConnell, 1979. Lateral diffusion in binary mixtures of cholesterol and phosphatidylcholines. *Proc. Natl. Acad. Sci. U. S. A.* 76:15–18.

[18] Almeida, P. F., W. L. Vaz, and T. E. Thompson, 1992. Lateral diffusion in the liquid phases of dimyristoylphosphatidylcholine/cholesterol lipid bilayers: a free volume analysis. *Biochemistry* 31:6739–6747.

[19] Scherfeld, D., N. Kahya, and P. Schwille, 2003. Lipid dynamics and domain formation in model membranes composed of ternary mixtures of unsaturated and saturated phosphatidylcholines and cholesterol. *Biophys. J.* 85:3758–68.

[20] Vist, M. R., and J. H. Davis, 1990. Phase equilibria of cholesterol/dipalmitoylphosphatidylcholine mixtures: 2H nuclear magnetic resonance and differential scanning calorimetry. *Biochemistry* 29:451–464.

[21] Filippov, A., G. Orädd, and G. Lindblom, 2003. Influence of cholesterol and water content on phospholipid lateral diffusion in bilayers. *Langmuir* 19:6397–6400.

[22] Marsh, D., 2010. Liquid-ordered phases induced by cholesterol: a compendium of binary phase diagrams. *Biochim. Biophys. Acta* 1798:688–99.

[23] Davis, J. H., J. J. Clair, and J. Juhasz, 2009. Phase equilibria in DOPC/DPPC-d62/cholesterol mixtures. *Biophys. J.* 96:521–539.

[24] Leung, S. S. W., J. V. Busto, A. Keyvanloo, F. M. Goñi, and J. Thewalt, 2012. Insights into sphingolipid miscibility: separate observation of sphingomyelin and ceramide N-acyl chain melting. *Biophys. J.* 103:2465–2474.

[25] Veatch, S. L., O. Soubias, S. L. Keller, and K. Gawrisch, 2007. Critical fluctuations in domain-forming lipid mixtures. *Proc. Natl. Acad. Sci. U. S. A.* 104:17650–17655.

[26] Buboltz, J. T., C. Bwalya, K. Williams, and M. Schutzer, 2007. High-resolution mapping of phase behavior in a ternary lipid mixture: do lipid-raft phase boundaries depend on the sample preparation procedure? *Langmuir* 23:11968–71.

[27] Goñi, F. M., A. Alonso, L. A. Bagatolli, R. E. Brown, D. Marsh, M. Prieto, and J. L. Thewalt, 2008. Phase diagrams of lipid mixtures relevant to the study of membrane rafts. *Biochim. Biophys. Acta - Mol. Cell Biol. Lipids* 1781:665–684.

[28] Juhasz, J., J. H. Davis, and F. J. Sharom, 2010. Fluorescent probe partitioning in giant unilamellar vesicles of 'lipid raft' mixtures. *Biochem. J.* 430:415–423.

[29] van Swaay, D., and A. DeMello, 2013. Microfluidic methods for forming liposomes. *Lab Chip* 13:752–67.

[30] Bagatolli, L. A., 2006. To see or not to see: Lateral organization of biological membranes and fluorescence microscopy. *Biochim. Biophys. Acta* 1758:1541–56.

[31] Bagatolli, L. A., 2009. Membranes and fluorescence microscopy. Reviews in Fluorescence. Springer New York, New York, NY.

[32] Zhou, Y., C. K. Berry, P. a. Storer, and R. M. Raphael, 2007. Peroxidation of polyunsaturated phosphatidyl-choline lipids during electroformation. *Biomaterials* 28:1298–306.

[33] Morales-Penningston, N. F., J. Wu, E. R. Farkas, S. L. Goh, T. M. Konyakhina, J. Y. Zheng, W. W. Webb, and G. W. Feigenson, 2010. GUV preparation and imaging: Minimizing artifacts. *Biochim. Biophys. Acta - Biomembr.* 1798:1324–1332.

[34] Gruner, S. M., R. P. Lenk, a. S. Janoff, and M. J. Ostro, 1985. Novel multilayered lipid vesicles: comparison of physical characteristics of multilamellar liposomes and stable plurilamellar vesicles. *Biochemistry* 24:2833–2842.

[35] D, M. T., Tilcock C P, W. K, and P. R. Cullis, 1988. Spontaneous vesiculation of large multilamellar vesicles composed of saturated phosphatidylcholine and phosphatidylglycerol mixtures. *Biochemistry* 27:8724–8730.

[36] Brandl, M., M. Drechsler, D. Bachmann, and K. H. Bauer, 1997. Morphology of semisolid aqueous phosphatidylcholine dispersions, a freeze fracture electron microscopy study. *Chem. Phys. Lipids* 87:65–72.

[37] Detoni, C. B., E. C. M. Cabral-Albuquerque, S. V. a. Hohlemweger, C. Sampaio, T. F. Barros, and E. S. Velozo, 2009. Essential oil from Zanthoxylum tingoassuiba loaded into multilamellar liposomes useful as antimicrobial agents. *J. Microencapsul.* 26:684–691.

[38] Ahl, P. L., and W. R. Perkins, 2003. Interdigitation-fusion liposomes. *Methods Enzymol.* 367:80–98.

[39] Veatch, S., 2004. Liquid immiscibility in model bilayer lipid membranes. Ph.D. thesis, University of Washington.

[40] Baumgart, T., A. T. Hammond, P. Sengupta, S. T. Hess, D. a. Holowka, B. a. Baird, and W. W. Webb, 2007. Large-scale fluid/fluid phase separation of proteins and lipids in giant plasma membrane vesicles. *Proc. Natl. Acad. Sci. U. S. A.* 104:3165–3170.

[41] Fadeel, B., and D. Xue, 2010. The ins and outs of phospholipid asymmetry in the plasma membrane: roles in health and disease. *Crit. Rev. Biochem. Mol. Biol.* 44:264–277.

[42] Veatch, S. L., and S. L. Keller, 2002. Organization in lipid membranes containing cholesterol. *Phys. Rev. Lett.* 89:268101.

[43] Dietrich, C., L. A. Bagatolli, Z. N. Volovyk, N. L. Thompson, M. Levi, K. Jacobson, and E. Gratton, 2001. Lipid rafts reconstituted in model membranes. *Biophys. J.* 80:1417–1428.

[44] Veatch, S. L., P. Cicuta, P. Sengupta, A. Honerkamp-Smith, D. Holowka, and B. Baird, 2008. Critical fluctuations in plasma membrane vesicles. *ACS Chem. Biol.* 3:287–293.

[45] Reinl, H., T. Brumm, and T. Bayerl, 1992. the physical properties of the liquid-ordered phase with temperature in binary mixtures of DPPC with cholesterol: A 2H-NMR, FT-IR, DSC, and neutron scattering study. *Biophys. J.* 61:1025–1035.

[46] Nicolini, C., J. Kraineva, M. Khurana, N. Periasamy, S. S. Funari, and R. Winter, 2006. Temperature and pressure effects on structural and conformational properties of POPC/SM/cholesterol model raft mixtures–a FT-IR, SAXS, DSC, PPC and Laurdan fluorescence spectroscopy study. *Biochim. Biophys. Acta* 1758:248–58.

[47] Mills, T. T., S. Tristram-Nagle, F. a. Heberle, N. F. Morales, J. Zhao, J. Wu, G. E. S. Toombes, J. F. Nagle, and G. W. Feigenson, 2008. Liquid-liquid domains in bilayers detected by wide angle X-ray scattering. *Biophys. J.* 95:682–90.

[48] Seelig, J., 1977. Deuterium magnetic resonance - Theory and application to lipid-membranes. *Q. Rev. Biophys.* 10:353–418.

[49] Sankaram, M. B., and T. E. Thompson, 1990. Interaction of cholesterol with various glycerophospholipids and sphingomyelin.

[50] Chiantia, S., N. Kahya, J. Ries, and P. Schwille, 2006. Effects of ceramide on liquid-ordered domains investigated by simultaneous AFM and FCS. *Biophys. J.* 90:4500–4508.

[51] Evans, E. a., 1983. Bending elastic modulus of red blood cell membrane derived from buckling instability in micropipet aspiration tests. *Biophys. J.* 43:27–30.

[52] de Almeida, R. F. M., J. Borst, A. Fedorov, M. Prieto, and A. J. W. G. Visser, 2007. Complexity of lipid domains and rafts in giant unilamellar vesicles revealed by combining imaging and microscopic and macroscopic time-resolved fluorescence. *Biophys. J.* 93:539–53.

[53] Castro, B. M., R. F. M. de Almeida, A. Fedorov, and M. Prieto, 2012. The photophysics of a Rhodamine head labeled phospholipid in the identification and characterization of membrane lipid phases. *Chem. Phys. Lipids* 165:311–319.

[54] Gennis, R. B., 1989. Biomembranes: molecular structure and function. Springer-Verlag, New York, NY.

[55] Leidy, C., W. F. Wolkers, K. Jørgensen, O. G. Mouritsen, and J. H. Crowe, 2001. Lateral organization and domain formation in a two-component lipid membrane system. *Biophys. J.* 80:1819–1828.

[56] Marguet, D., P.-F. Lenne, H. Rigneault, and H.-T. He, 2006. Dynamics in the plasma membrane: how to combine fluidity and order. *EMBO J.* 25:3446–57.

[57] Munro, S., 2003. Lipid Rafts: Elusive or Illusive? *Cell* 115:377–388.

[58] Simons, K., and M. J. Gerl, 2010. Revitalizing membrane rafts: new tools and insights. *Nat. Rev. Mol. Cell Biol.* 11:688–699.

[59] Baumgart, T., G. Hunt, E. R. Farkas, W. W. Webb, and G. W. Feigenson, 2007. Fluorescence probe partitioning between Lo/Ld phases in lipid membranes. *Biochim. Biophys. Acta - Biomembr.* 1768:2182–2194.

[60] McConnell, H. M., 1990. Harmonic shape transitions in lipid monolayer domains. *J. Phys. Chem.* 94:4728–4731.

[61] Veatch, S. L., and S. L. Keller, 2003. Separation of liquid phases in giant vesicles of ternary mixtures of phospholipids and cholesterol. *Biophys. J.* 85:3074–3083.

[62] Aussenac, F., M. Laguerre, J. M. Schmitter, and E. J. Dufourc, 2003. Detailed structure and dynamics of bicelle phospholipids using selectively deuterated and perdeuterated labels. 2H NMR and molecular mechanics study. *Langmuir* 19:10468–10479.

[63] Veatch, S. L., and S. L. Keller, 2005. Seeing spots: complex phase behavior in simple membranes. *Biochim. Biophys. Acta* 1746:172–185.

[64] Snyder, R. B., and C. A. Eckert, 1973. Effect of third component on liquid-liquid critical point. *J. Chem. Eng. Data* 18:282–285.

[65] Rice, O. K., 1976. The effect of an impurity on the critical point of a binary liquid system as a surface phenomenon. *J. Chem. Phys.* 64:4362.

[66] Mondal, T. K., and E. S. R. Gopal, 1991. Perturbation of critical solution temperatures by impurity doping. *J. Therm. Anal.* 37:2613–2619.

[67] Veatch, S. L., I. V. Polozov, K. Gawrisch, and S. L. Keller, 2004. Liquid domains in vesicles investigated by NMR and fluorescence microscopy. *Biophys. J.* 86:2910–2922.

[68] Zhao, J., J. Wu, H. Shao, F. Kong, N. Jain, G. Hunt, and G. Feigenson, 2007. Phase studies of model biomembranes: Macroscopic coexistence of Lα + Lβ, with light-induced coexistence of Lα + Lo Phases. *Biochim. Biophys. Acta - Biomembr.* 1768:2777–2786.

[69] Veatch, S. L. Personal Communication.

[70] Veatch, S. L., S. S. W. Leung, R. E. W. Hancock, and J. L. Thewalt, 2007. Fluorescent probes alter miscibility phase boundaries in ternary vesicles. *J. Phys. Chem. B* 111:502–504.

[71] Skaug, M. J., M. L. Longo, and R. Faller, 2011. The impact of texas red on lipid bilayer properties. *J. Phys. Chem. B* 115:8500–8505.

[72] Bouvrais, H., T. Pott, L. A. Bagatolli, J. H. Ipsen, and P. Méléard, 2010. Impact of membrane-anchored fluorescent probes on the mechanical properties of lipid bilayers. *Biochim. Biophys. Acta* 1798:1333–1337.

[73] Vaz, W., and E. Melo, 2001. Fluorescence spectroscopic studies on phase heterogeneity in lipid bilayer membranes. *J. Fluoresc.* 11:255–271.

[74] Zhou, Y., J. F. Hancock, and L. M. Lichtenberger, 2010. The nonsteroidal anti-inflammatory drug indomethacin induces heterogeneity in lipid membranes: Potential implication for its diverse biological action. *PLoS One* 5:1–8.

[75] Ariola, F. S., Z. Li, C. Cornejo, R. Bittman, and A. A. Heikal, 2009. Membrane fluidity and lipid order in ternary giant unilamellar vesicles using a new bodipy-cholesterol derivative. *Biophys. J.* 96:2696–708.

[76] Bagatolli, L. A., T. Parasassi, and E. Gratton, 2000. Giant phospholipid vesicles: comparison among the whole lipid sample characteristics using different preparation methods - A two photon fluorescence microscopy study. *Chem. Phys. Lipids* 105:135–147.

[77] Bagatolli, L. A., and E. Gratton, 2001. Direct observation of lipid domains in free-standing bilayers using two-photon excitation fluorescence microscopy. *J. Fluoresc.* 11:141–160.

[78] Baumgart, T., S. T. Hess, and W. W. Webb, 2003. Imaging coexisting fluid domains in biomembrane models coupling curvature and line tension. *Nature* 425:821–824.

[79] Coste, V., N. Puff, D. Lockau, P. J. Quinn, and M. I. Angelova, 2006. Raft-like domain formation in large unilamellar vesicles probed by the fluorescent phospholipid analogue, C12NBD-PC. *Biochim. Biophys. Acta* 1758:460–467.

[80] Lin, S., and W. S. Struve, 1991. Time-resolved fluorescence of nitrobenzoxadiazole-aminohexanoic acid: effect of intermolecular hydrogen-bonding on non-radiative decay. *Photochem. Photobiol.* 54:361–365.

[81] Kucherak, O. a., S. Oncul, Z. Darwich, D. a. Yushchenko, Y. Arntz, P. Didier, Y. Mély, and A. S. Klymchenko, 2010. Switchable nile red-based probe for cholesterol and lipid order at the outer leaflet of biomembranes. *J. Am. Chem. Soc.* 132:4907–4916.

[82] Coban, O., M. Burger, M. Laliberte, A. Ianoul, and L. J. Johnston, 2007. Ganglioside partitioning and aggregation in phase-separated monolayers characterized by bodipy GM1 monomer/dimer emission. *Langmuir* 23:6704–11.

[83] Girotti, A. W., 1990. Photodynamic lipid peroxidation in biological systems. *Photochem. Photobiol.* 51:497–509.

[84] Ayuyan, A. G., and F. S. Cohen, 2006. Lipid peroxides promote large rafts: effects of excitation of probes in fluorescence microscopy and electrochemical reactions during vesicle formation. *Biophys. J.* 91:2172–2183.

[85] Liu, A. P., and D. a. Fletcher, 2006. Actin polymerization serves as a membrane domain switch in model lipid bilayers. *Biophys. J.* 91:4064–70.

[86] Horton, M. R., J. Rädler, and A. P. Gast, 2006. Phase behavior and the partitioning of caveolin-1 scaffolding domain peptides in model lipid bilayers. *J. Colloid Interface Sci.* 304:67–76.

[87] Hammond, A. T., F. A. Heberle, T. Baumgart, D. Holowka, B. Baird, and G. W. Feigenson, 2005. Crosslinking a lipid raft component triggers liquid ordered-liquid disordered phase separation in model plasma membranes. *Proc. Natl. Acad. Sci. U. S. A.* 102:6320–6325.

[88] Van Heyningen, S., 1982. Cholera toxin. *Biosci. Rep.* 2:135–146.

[89] Chaudhuri, K., and S. N. Chatterjee, 2009. Bacterial toxins: A brief overview. *In* Cholera Toxins, Springer-Verlag Berlin Heidelberg, i, 5–11.

[90] Putzel, G. G., and M. Schick, 2009. Theory of raft formation by the cross-linking of saturated or unsaturated lipids in model lipid bilayers. *Biophys. J.* 96:4935–40.

[91] Filippov, A., B. Munavirov, G. Gröbner, and M. Rudakova, 2012. Lateral diffusion in equimolar mixtures of natural sphingomyelins with dioleoylphosphatidylcholine. *Magn. Reson. Imaging* 30:413–421.

[92] Shipley, G. G., L. S. Avecilla, and D. M. Small, 1974. Phase behavior and structure of aqueous dispersions of sphingomyelin. *J. Lipid Res.* 15:124–31.

[93] Róg, T., and M. Pasenkiewicz-Gierula, 2006. Cholesterol-sphingomyelin interactions: a molecular dynamics simulation study. *Biophys. J.* 91:3756–67.

[94] Sugár, I. P., T. E. Thompson, and R. L. Biltonen, 1999. Monte Carlo simulation of two-component bilayers: DMPC/DSPC mixtures. *Biophys. J.* 76:2099–2110.

[95] Lemmich, J., K. Mortensen, J. H. Ipsen, T. Hønger, R. Bauer, and O. G. Mouritsen, 1997. The effect of cholesterol in small amounts on lipid-bilayer softness in the region of the main phase transition. *Eur. Biophys. J.* 25:293–304.

[96] Fernandez-Puente, L., I. Bivas, M. D. Mitov, and P. Méléard, 2007. Temperature and Chain Length Effects on Bending Elasticity of Phosphatidylcholine Bilayers.

[97] Lakowicz, J. R., 2006. Principles of fluorescence spectroscopy. Springer, 3rd edition.

[98] Sanchez, S., M. Tricerri, and G. Gunther, 2007. Laurdan generalized polarization: from cuvette to microscope. *Mod. Res.* 1007–1014.

[99] Bagatolli, L. A., 2013. LAURDAN Fluorescence Properties in Membranes : A Journey from the Fluorometer to the Microscope. *Springer Ser. Fluoresc.* 13:3–35.

[100] Sinha, M., S. Mishra, and P. G. Joshi, 2003. Liquid-ordered microdomains in lipid rafts and plasma membrane of U-87 MG cells: a time-resolved fluorescence study. *Eur. Biophys. J.* 32:381–91.

[101] Maier, O., V. Oberle, and D. Hoekstra, 2002. Fluorescent lipid probes: some properties and applications (a review). *Chem. Phys. Lipids* 116:3–18.

[102] Bagatolli, L. A., and E. Gratton, 1999. Two-photon fluorescence microscopy observation of shape changes at the phase transition in phospholipid giant unilamellar vesicles. *Biophys. J.* 77:2090–101.

[103] Patterson, G. H., and D. W. Piston, 2000. Photobleaching in two-photon excitation microscopy. *Biophys. J.* 78:2159–62.

[104] Ustione, A., and D. Piston, 2011. A simple introduction to multiphoton microscopy. *J. Microsc.* 243:221–226.

[105] Göppert-Mayer, M., 1931. Uber Elementarakte mit zwei Quantensprungen. *Ann. Phys.* 401:273–294.

[106] Laud, B. B., 2011. Lasers and non-linear optics. New Age International, Daryaganj, IND.

[107] Xu, C., and W. W. Webb, 1996. Measurement of two-photon excitation cross sections of molecular fluorophores with data from 690 to 1050 nm. *J. Opt. Soc. Am. B* 13:481.

[108] Bort, G., T. Gallavardin, D. Ogden, and P. I. Dalko, 2013. From one-photon to two-photon probes: "caged" compounds, actuators, and photoswitches. *Angew. Chem. Int. Ed. Engl.* 52:4526–37.

[109] Parasassi, T., G. De Stasio, G. Ravagnan, R. M. Rusch, and E. Gratton, 1991. Quantitation of lipid phases in phospholipid vesicles by the generalized polarization of Laurdan fluorescence. *Biophys. J.* 60:179–89.

[110] Antollini, S. S., and F. J. Barrantes, 1998. Disclosure of discrete sites for phospholipid and sterols at the protein-lipid interface in native acetylcholine receptor-rich membrane. *Biochemistry* 37:16653–16662.

[111] Kim, H. M., H.-J. Choo, S.-Y. Jung, Y.-G. Ko, W.-H. Park, S.-J. Jeon, C. H. Kim, T. Joo, and B. R. Cho, 2007. A two-photon fluorescent probe for lipid raft imaging: C-laurdan. *Chembiochem* 8:553–9.

[112] Gaus, K., T. Zech, and T. Harder, 2006. Visualizing membrane microdomains by Laurdan 2-photon microscopy. *Mol. Membr. Biol.* 23:41–8.

[113] Kaiser, H.-J., D. Lingwood, I. Levental, J. L. Sampaio, L. Kalvodova, L. Rajendran, and K. Simons, 2009. Order of lipid phases in model and plasma membranes. *Proc. Natl. Acad. Sci. U. S. A.* 106:16645–50.

[114] Parasassi, T., E. K. Krasnowska, L. A. Bagatolli, and E. Gratton, 1998. LAURDAN and PRODAN as polarity-sensitive fluorescent membrane probes. *J. Fluoresc.* 8:365–373.

[115] Mukherjee, S., and A. Chattopadhyay, 2005. Monitoring the organization and dynamics of bovine hippocampal membranes utilizing Laurdan generalized polarization. *Biochim. Biophys. Acta - Biomembr.* 1714:43–55.

[116] Parasassi, T., G. De Stasio, A. D'Ubaldo, and E. Gratton, 1990. Phase fluctuation in phospholipid membranes revealed by Laurdan fluorescence. *Biophys. J.* 57:1179–1186.

[117] Parasassi, T., A. M. Giusti, E. Gratton, E. Monaco, M. Raimondi, G. Ravagnan, and O. Sapora, 1994. Evidence for an increase in water concentration in bilayers after oxidative damage of phospholipids induced by ionizing radiation. *Int. J. Radiat. Biol.* 65:329–334.

[118] Harris, F. M., K. B. Best, and J. D. Bell, 2002. Use of laurdan fluorescence intensity and polarization to distinguish between changes in membrane fluidity and phospholipid order. *Biochim. Biophys. Acta* 1565:123–8.

[119] Parasassi, T., E. Gratton, W. M. Yu, P. Wilson, and M. Levi, 1997. Two-photon fluorescence microscopy of Laurdan generalized polarization domains in model and natural membranes. *Biophys. J.* 72:2413–2429.

[120] Bagatolli, L. A., 2003. Direct observation of lipid domains in free standing bilayers: From simple to complex lipid mixtures. *Chem. Phys. Lipids* 122:137–145.

[121] Juhasz, J., J. H. Davis, and F. J. Sharom, 2012. Fluorescent probe partitioning in GUVs of binary phospholipid mixtures: implications for interpreting phase behavior. *Biochim. Biophys. Acta* 1818:19–26.

[122] Chong, P. L.-G., and M. Olsher, 2007. Fluorometric assay for detection of sterol oxidation in liposomal membranes. *Methods Mol. Biol.* 400:145–158.

[123] McIntosh, A. L., B. P. Atshaves, H. Huang, A. M. Gallegos, A. B. Kier, and F. Schroeder, 2008. Fluorescence techniques using dehydroergosterol to study cholesterol trafficking. *Lipids* 43:1185–1208.

[124] Sengupta, P., A. Hammond, D. Holowka, and B. Baird, 2008. Structural determinants for partitioning of lipids and proteins between coexisting fluid phases in giant plasma membrane vesicles. *Biochim. Biophys. Acta - Biomembr.* 1778:20–32.

[125] Xu, X., R. Bittman, G. Duportail, D. Heissler, C. Vilcheze, and E. London, 2001. Effect of the structure of natural sterols and sphingolipids on the formation of ordered sphingolipid/sterol domains (rafts). Comparison of cholesterol to plant, fungal, and disease-associated sterols and comparison of sphingomyelin, cerebrosides, and cer. *J. Biol. Chem.* 276:33540–33546.

[126] Margineanu, A., J.-i. Hotta, R. a. L. Vallée, M. Van der Auweraer, M. Ameloot, A. Stefan, D. Beljonne, Y. Engelborghs, A. Herrmann, K. Müllen, F. C. De Schryver, and J. Hofkens, 2007. Visualization of membrane rafts using a perylene monoimide derivative and fluorescence lifetime imaging. *Biophys. J.* 93:2877–2891.

[127] Wüstner, D., 2007. Fluorescent sterols as tools in membrane biophysics and cell biology. *Chem. Phys. Lipids* 146:1–25.

[128] Garvik, O., P. Benediktson, A. C. Simonsen, J. H. Ipsen, and D. Wüstner, 2009. The fluorescent cholesterol analog dehydroergosterol induces liquid-ordered domains in model membranes. *Chem. Phys. Lipids* 159:114–118.

[129] Shaghaghi, M., 2014. H-NMR Study of Model Membranes : Investigating the Effect of Sterol Structure on the Chain Ordering and Phase Behavior of Lipid Mixtures. Ph.D. thesis, Simon Fraser University.

[130] Levental, I., F. J. Byfield, P. Chowdhury, F. Gai, T. Baumgart, and P. a. Janmey, 2009. Cholesterol-dependent phase separation in cell-derived giant plasma-membrane vesicles. *Biochem. J.* 424:163–7.

[131] Juhasz, J., F. J. Sharom, and J. H. Davis, 2009. Quantitative characterization of coexisting phases in DOPC/DPPC/cholesterol mixtures: comparing confocal fluorescence microscopy and deuterium nuclear magnetic resonance. *Biochim. Biophys. Acta* 1788:2541–2552.

[132] Cape, J. L., P.-A. Monnard, and J. M. Boncella, 2011. Prebiotically relevant mixed fatty acid vesicles support anionic solute encapsulation and photochemically catalyzed trans-membrane charge transport. *Chem. Sci.* 2:661.

[133] Feigenson, G. W. Personal Communication .

[134] Leung, S. S. W., 2007. Study of sphingomyelin and ceramide model embrane phase behavior using deuterium nuclear magnetic resonance spectroscopy. Master's thesis, Simon Fraser University.

[135] Seelig, J., and A. Seelig, 1980. Lipid conformation in model membranes and biological membranes. *Q. Rev. Biophys.* 13:19–61.

[136] Stockton, G. W., and I. C. Smith, 1976. A deuterium nuclear magnetic resonance study of the condensing effect of cholesterol on egg phosphatidylcholine bilayer membranes. I. Perdeuterated fatty acid probes. *Chem. Phys. Lipids* 17:251–263.

[137] Bloom, M., E. Evans, and O. G. Mouritsen, 1991. Physical properties of the fluid lipid-bilayer component of cell membranes: a perspective. *Q. Rev. Biophys.* 24:293–397.

[138] Davis, J., K. Jeffrey, M. Bloom, M. Valic, and T. Higgs, 1976. Quadrupolar echo deuteron magnetic resonance spectroscopy in ordered hydrocarbon chains. *Chem. Phys. Lett.* 42:390–394.

[139] Davis, J. H., 1983. The description of membrane lipid conformation, order and dynamics by 2H-NMR. *Biochim. Biophys. Acta* 737:117–171.

[140] Dico, A. S., J. Hancock, M. R. Morrow, J. Stewart, S. Harris, and K. M. W. Keough, 1997. Pulmonary surfactant protein SP-B interacts similarly with dipalmitoylphosphatidylglycerol and dipalmitoylphosphatidylcholine in phosphatidylcholine/phosphatidylglycerol mixtures. *Biochemistry* 36:4172–4177.

[141] Palacios, L. E., and T. Wang, 2005. Egg-yolk lipid fractionation and lecithin characterization. *JAOCS, J. Am. Oil Chem. Soc.* 82:571–578.

[142] Solomon, I., 1958. Multiple echoes in solids. *Phys. Rev.* 110:61–65.

[143] Thewalt, J. L., 1986. Deuterium NMR studies of model membranes containing 1-alkanol anesthetics or alpha-tocopherol. Ph.D. thesis, Simon Fraser University.

[144] Orädd, G., P. W. Westerman, and G. Lindblom, 2005. Lateral diffusion coefficients of separate lipid species in a ternary raft-forming bilayer: a Pfg-NMR multinuclear study. *Biophys. J.* 89:315–320.

[145] Uppamoochikkal, P., S. Tristram-Nagle, and J. F. Nagle, 2010. Orientation of tie-lines in the phase diagram of DOPC/DPPC/cholesterol model biomembranes. *Langmuir* 26:17363–8.

[146] De Joannis, J., P. S. Coppock, F. Yin, M. Mori, A. Zamorano, and J. T. Kindt, 2011. Atomistic simulation of cholesterol effects on miscibility of saturated and unsaturated phospholipids: Implications for liquid-ordered/liquid-disordered phase coexistence. *J. Am. Chem. Soc.* 133:3625–3634.

[147] Lentz, B. R., Y. Barenholz, and T. E. Thompson, 1976. Fluorescence depolarization studies of phase transitions and fluidity in phospholipid bilayers. 2. Two-component phosphatidylcholine liposomes. *Biochemistry* 15:4529–4537.

[148] Furuya, K., and T. Mitsui, 1979. Phase Transitions in Bilayer Membranes of Dioleoyl-Phosphatidylcholine/Dipalmitoyl-Phosphatidylcholine.

[149] Elliott, R., K. Katsov, M. Schick, and I. Szleifer, 2005. Phase separation of saturated and mono-unsaturated lipids as determined from a microscopic model. *J. Chem. Phys.* 122:44904.

[150] Lentz, B. R., D. A. Barrow, and M. Hoechli, 1980. Cholesterol-phosphatidylcholine interactions in multilamellar vesicles. *Biochemistry* 19:1943–54.

[151] Ipsen, J. H., G. Karlström, O. G. Mouritsen, H. Wennerström, and M. J. Zuckermann, 1987. Phase equilibria in the phosphatidylcholine-cholesterol system. *Biochim. Biophys. Acta* 905:162–72.

[152] Ipsen, J. H., O. G. Mouritsen, and M. Bloom, 1990. Relationships between lipid membrane area, hydrophobic thickness, and acyl-chain orientational order. The effects of cholesterol. *Biophys. J.* 57:405–12.

[153] McMullen, T. P., and R. N. McElhaney, 1995. New aspects of the interaction of cholesterol with dipalmitoylphosphatidylcholine bilayers as revealed by high-sensitivity differential scanning calorimetry. *Biochim. Biophys. Acta* 1234:90–98.

[154] Smondyrev, a. M., and M. L. Berkowitz, 1999. Structure of dipalmitoylphosphatidylcholine/cholesterol bilayer at low and high cholesterol concentrations: molecular dynamics simulation. *Biophys. J.* 77:2075–89.

[155] Chiu, S. W., E. Jakobsson, R. J. Mashl, and H. L. Scott, 2002. Cholesterol-induced modifications in lipid bilayers: a simulation study. *Biophys. J.* 83:1842–1853.

[156] Veatch, S. L., K. Gawrisch, and S. L. Keller, 2006. Closed-loop miscibility gap and quantitative tie-lines in ternary membranes containing diphytanoyl PC. *Biophys. J.* 90:4428–4436.

[157] Maulik, P. R., and G. G. Shipley, 1996. N-Palmitoyl Sphingomyelin Bilayers : Structure and Interactions with Cholesterol. *Biochemistry* 2960:8025–8034.

[158] Higgins, M. J., M. Polcik, T. Fukuma, J. E. Sader, Y. Nakayama, and S. P. Jarvis, 2006. Structured water layers adjacent to biological membranes. *Biophys. J.* 91:2532–42.

[159] Davis, J. H., 1979. Deuterium magnetic resonance study of the gel and liquid crystalline phases of dipalmitoyl phosphatidylcholine. *Biophys. J.* 27:339–358.

[160] Bloom, M., J. H. Davis, and A. L. Mackay, 1981. Direct determination of the oriented sample nmr spectrum from the powder spectrum for systems with local axial symmetry. *Chem. Phys. Lett.* 80:198–202.

[161] Lu, D., I. Vavasour, and M. R. Morrow, 1995. Smoothed acyl chain orientational order parameter profiles in dimyristoylphosphatidylcholine-distearoylphosphatidylcholine mixtures: a 2H-NMR study. *Biophys. J.* 68:574–583.

[162] Mehnert, T., K. Jacob, R. Bittman, and K. Beyer, 2006. Structure and lipid interaction of N-palmitoylsphingomyelin in bilayer membranes as revealed by 2H-NMR spectroscopy. *Biophys. J.* 90:939–946.

[163] Bartels, T., R. S. Lankalapalli, R. Bittman, K. Beyer, and M. F. Brown, 2008. Raft-like mixtures of sphingomyelin and cholesterol investigated by solid-state 2H NMR spectroscopy. *J. Am. Chem. Soc.* 130:14521–14532.

[164] Bunge, A., P. Muller, M. Stockl, A. Herrmann, D. Huster, P. Müller, and M. Stöckl, 2008. Characterization of the ternary mixture of sphingomyelin, POPC, and cholesterol: support for an inhomogeneous lipid distribution at high temperatures. *Biophys. J.* 94:2680–2690.

[165] Leung, S. S. W., and J. Thewalt, 2014. Deuterium NMR of mixed lipid membranes. *In* F. Separovic, and A. Naito, editors, Adv. Biol. Solid-State NMR, Royal Society of Chemistry, chapter 10.

[166] Manley, S., and V. D. Gordon, 2008. Making giant unilamellar vesicles via hydration of a lipid film. *Curr. Protoc. Cell Biol.* Chapter 24:Unit 24.3.

[167] Mathivet, L., S. Cribier, and P. F. Devaux, 1996. Shape change and physical properties of giant phospholipid vesicles prepared in the presence of an AC electric field. *Biophys. J.* 70:1112–21.

[168] Krasnowska, E. K., L. A. Bagatolli, E. Gratton, and T. Parasassi, 2001. Surface properties of cholesterol-containing membranes detected by Prodan fluorescence. *Biochim. Biophys. Acta* 1511:330–40.

[169] Veatch, S. L., 2007. Electro-formation and fluorescence microscopy of giant vesicles with coexisting liquid phases. *In* T. J. McIntosh, editor, Methods Mol. Biol., Humana Press Inc., Totowa, NJ, volume 398, chapter 6, 59–72.

[170] Bagatolli, L. A., and D. Needham, 2014. Quantitative optical microscopy and micromanipulation studies on the lipid bilayer membranes of giant unilamellar vesicles. *Chem. Phys. Lipids* 181:99–120.

[171] Nagle, J., and D. Wilkinson, 1978. Lecithin bilayers: Density measurements and molecular interactions. *Biophys. J.* 23:159–175.

[172] Brewer, J. Personal Communication.

[173] Leirer, C. T., B. Wunderlich, A. Wixforth, and M. F. Schneider, 2009. Thermodynamic relaxation drives expulsion in giant unilamellar vesicles. *Phys. Biol.* 6:016011.

[174] Bagatolli, L. A. Personal Communication .

[175] Gaus, K., E. Gratton, E. P. W. Kable, A. S. Jones, I. Gelissen, L. Kritharides, and W. Jessup, 2003. Visualizing lipid structure and raft domains in living cells with two-photon microscopy. *Proc. Natl. Acad. Sci. U. S. A.* 100:15554–9.

[176] Parasassi, T., and E. Gratton, 1995. Membrane lipid domains and dynamics as detected by Laurdan fluorescence. *J. Fluoresc.* 5:59–69.

[177] Davis, J. H., and M. L. Schmidt, 2014. Critical behaviour in DOPC/DPPC/cholesterol mixtures: Static 2H NMR line shapes near the critical point. *Biophys. J.* 106:1970–1978.

[178] Putzel, G. G., and M. Schick, 2008. Phenomenological model and phase behavior of saturated and unsaturated lipids and cholesterol. *Biophys. J.* 95:4756–4762.

[179] Komura, S., and D. Andelman, 2014. Physical aspects of heterogeneities in multi-component lipid membranes. *Adv. Colloid Interface Sci.* 208:34–46.

[180] Radhakrishnan, A., and H. McConnell, 2005. Condensed complexes in vesicles containing cholesterol and phospholipids. *Proc. Natl. Acad. Sci. U. S. A.* 102:12662–12666.

[181] Wolff, J., C. M. Marques, and F. Thalmann, 2011. Thermodynamic Approach to Phase Coexistence in Ternary Phospholipi-Cholesterol Mixtures. *Phys. Rev. Lett.* 128104:1–4.

[182] Nagle, J. F., and S. Tristram-Nagle, 2000. Lipid bilayer structure. *Curr. Opin. Struct. Biol.* 10:474–480.

[183] Heimburg, T., 2007. Thermal biophysics of membranes. Wiley-VCH Verlag, Weinheim.

[184] Plischke, M., and B. Bergersen, 1994. Equilibrium statistical physics. World Scientific, Singapore, 2nd edition.

[185] Pelissetto, A., and E. Vicari, 2002. Critical phenomena and renormalization-group theory. *Phys. Rep.* 368:549–727.

[186] Honerkamp-Smith, A. R., P. Cicuta, M. D. Collins, S. L. Veatch, M. den Nijs, M. Schick, and S. L. Keller, 2008. Line tensions, correlation lengths, and critical exponents in lipid membranes near critical points. *Biophys. J.* 95:236–246.

[187] Davis, J. Personal Communication.

[188] Bagatolli, L. A., T. Parasassi, G. D. Fidelio, and E. Gratton, 1999. A model for the interaction of 6-Lauroyl-2-(N,N-dimethylamino)naphthalene with lipid environments: Implications for spectral properties. *Photochem. Photobiol.* 70:557–564.

[189] Brumm, T., K. Jørgensen, O. G. Mouritsen, and T. M. Bayerl, 1996. The effect of increasing membrane curvature on the phase transition and mixing behavior of a dimyristoyl-sn-glycero-3-phosphatidylcholine/ distearoyl-sn-glycero-3-phosphatidylcholine lipid mixture as studied by Fourier transform infrared spectroscopy and . *Biophys. J.* 70:1373–9.

[190] Veatch, S. L., and S. L. Keller, 2005. Miscibility phase diagrams of giant vesicles containing sphingomyelin. *Phys. Rev. Lett.* 94:3–6.

[191] Girotti, A. W., 2001. Photosensitized oxidation of membrane lipids: Reaction pathways, cytotoxic effects, and cytoprotective mechanisms. *J. Photochem. Photobiol. B Biol.* 63:103–113.

[192] Jurkiewicz, P., A. Olzyska, L. Cwiklik, E. Conte, P. Jungwirth, F. M. Megli, and M. Hof, 2012. Biophysics of lipid bilayers containing oxidatively modified phospholipids: Insights from fluorescence and EPR experiments and from MD simulations.

[193] Cwiklik, L., A. J. A. Aquino, M. Vazdar, P. Jurkiewicz, J. Pittner, M. Hof, and H. Lischka, 2011. Absorption and fluorescence of PRODAN in phospholipid bilayers: a combined quantum mechanics and classical molecular dynamics study. *J. Phys. Chem. A* 115:11428–37.

[194] Parisio, G., A. Marini, A. Biancardi, A. Ferrarini, and B. Mennucci, 2011. Polarity-sensitive fluorescent probes in lipid bilayers: bridging spectroscopic behavior and microenvironment properties. *J. Phys. Chem. B* 115:9980–9.

[195] Jurkiewicz, P., L. Cwiklik, P. Jungwirth, and M. Hof, 2012. Lipid hydration and mobility: An interplay between fluorescence solvent relaxation experiments and molecular dynamics simulations. *Biochimie* 94:26–32.

[196] Ackerman, D. G., F. a. Heberle, and G. W. Feigenson, 2013. Limited perturbation of a DPPC bilayer by fluorescent lipid probes: A molecular dynamics study. *J. Phys. Chem. B* 117:4844–4852.

[197] Gray, E., J. Karslake, B. B. Machta, and S. L. Veatch, 2013. Liquid general anesthetics lower critical temperatures in plasma membrane vesicles. *Biophys. J.* 105:2751–2759.

[198] Atkins, P. W., 2006. Atkins' Physical Chemistry. Oxford University Press, Oxford, New York, 8th ed. edition.

[199] Vanounou, S., D. Pines, E. Pines, A. H. Parola, and I. Fishov, 2002. Coexistence of domains with distinct order and polarity in fluid bacterial membranes. *Photochem. Photobiol.* 76:1–11.

[200] Levental, I., M. Grzybek, and K. Simons, 2011. Raft domains of variable properties and compositions in plasma membrane vesicles. *Proc. Natl. Acad. Sci. U. S. A.* 108:11411–11416.

[201] Diamandis, E. P., and T. K. Christopoulos, 1991. The biotin-(strept)avidin system: Principles and applications in biotechnology. *Clin. Chem.* 37:625–636.

[202] Laitinen, O. H., V. P. Hytönen, H. R. Nordlund, and M. S. Kulomaa, 2006. Genetically engineered avidins and streptavidins. *Cell. Mol. Life Sci.* 63:2992–3017.

[203] Slichter, C. P., 2004. Principles of Magnetic Resonance Imaging. Springer-Verlag Berlin Heidelberg, 3 edition.

Appendix A

Gibbs phase rule

Here I repeat a derivation of Gibbs phase rule which is used to determine the number of phases that can coexist for a mixture of C components [see 198, chap. 6]. The mole fractions, x_i of such a mixture must sum to 1:

$$x_1 + x_2 + ... + x_C = 1. \tag{A.1}$$

Therefore, to specify the composition of a phase, only the mole fraction for $C-1$ components is required. At equilibrium, the chemical potential of component J in each of a set of coexisting phases $(\alpha, \beta, \gamma, \delta, ...)$ must be equal:

$$\mu_J(\alpha, p, T) = \mu_J(\beta, p, T) = \mu_J(\gamma, p, T) = \mu_J(\delta, p, T) = ... \tag{A.2}$$

where p is the pressure, and T is the temperature. For P phases in equilibrium, there are $P-1$ such equations. Since there are C components, there are $C(P-1)$ equations. For P phases, the total number of composition variables is $P(C-1)$ since the compositions of coexisting phases are different, and the total number of intensive variables is therefore $P(C-1)+2$ with the inclusion of pressure and temperature. It follows that the number of degrees of freedom is

$$F = P(C-1) + 2 - C(P-1) = C - P + 2, \tag{A.3}$$

which is the Gibbs phase rule. Accordingly, with F=2 for temperature and pressure, ternary membranes (C=3) can have up to three phases in coexistence (P=3) in a given region of the phase diagram. This assumes that the phase diagram does not depend on the amount of water present, i.e. water is “in excess”.

Appendix B

Detailed methods: electroformation practical matters

B.1 Cleaning

The “standard” cleaning procedure Kirstin Wagner, post-doc who was working with Luis Bagatolli, taught me in 2010 is as follows:

1. 10% Decon, sonicate for 96 min, 60°C water bath
2. Rinse with MilliQ water
3. 95% Ethanol, sonicate for 96 min, 60°C water bath
4. Rinse with ethanol and then MilliQ water
5. Repeat

A look at the electroformation wires using the confocal microscope prior to lipid deposition showed that the above standard protocol was inadequate. Fluorescent dyes were left on the wires. Even dyes from many experiments prior were found. Stronger cleaning solutions were seek and this is a compilation of what was found.

Alcoholic potassium/base bath:

1. 12 g potassium hydrooxide + 100 mL ethanol
2. Sonicate for 300 min, 60°C water bath.
3. Will turn yellow if the chambers are dirty.

Basic piranha solution:
(The acidic piranha solution is much more dangerous.)

1. 4:1:1 or 5:1:1 MilliQ water:ammonium hydrooxide:peroxide

2. Keep peroxide solution in cold room
3. Add ammonium hydrooxide to water and peroxide to the mixture after.
4. Heat to 80°C. Adam Cohen Simonsen said use for 30 min, but I found even used for 1 hour, the electroformation chambers are not clean.
5. (I was using 110°C on the hot plate, which might not be 80°C in the solution.)
6. Keep a lid on, but with space for gases to escape.
7. Perform in fumehood. Temperatures in fumehoods tend to be colder, shield from draft, if necessary, to maintain temperature.

Electrolysis:

1. 1M NaCl, sine wave, 7 V, 1 Hz, 60 seconds.
2. Repeat 5 times.
3. Do not do it for more than 60 seconds. If doing it for longer, the solution will turn black. I am not sure where the black is from.
4. Rinse well after, or the salts will dry onto the wire, and look fluorescent under the microscope.
5. I do two electrolysis with MilliQ water after, to make sure that there are no salts left. (Typically, the first one will still bubble, but the second one won't.)

These solutions have not been systematically tested, but experience shows that none of these will clean the wires in one shot. Repeated cleaning and verification under the microscope is necessary. Under the confocal microscope, it can be seen that dye and lipids get stuck where the platinum wire inserts into the Teflon even after repeated cleaning (Fig. B.1). It is difficult for even the strongest solutions to get in. Only time and further cleaning can get clean those nooks and crannies since scrubbing in such tight spaces is not possible.

Figure B.1: Tough spot to clean

An alternative to checking the wires under the microscope, is to use alcoholic potassium. Alcoholic potassium turns yellow if the items are dirty. When cleaning multiple items at a time, it is possible that only one item requires further cleaning. The alcoholic potassium bath method is also more time consuming than using the microscope. It is better to identify dirty chamber(s) with the microscope, and isolate them for further cleaning, so that experiments can proceed with the clean ones.

B.2 Lipid deposition

When Kirstin Wagner showed me how to deposit the lipids on to the electroformation wires, it reminded me of putting lipids on thin layer chromatography (Appendix D) plates. The smallest possible drop ($< 0.5\mu$L) of lipid solution are deposited on the wire using a electronic Hamilton syringe. One waits for that drop to dry, before applying the next drop. I was able to get quite a homogeneous coat of lipids on the wire using this technique. Homogeneity was inferred from the even distribution of vesicles formed on the wires. Note that evenly distributed, densely populated wires can make it difficult to observe the vesicles while they remained on the wire.

Luis Bagatolli showed me a different technique in 2012 in which he does not wait for the lipids to dry completely. Rather, he paints along the wire with the syringe tip before the lipid solution is dry. This seemed to give quite a homogeneous coat when done correctly. I did not master this technique.

B.3 Gluing together electroformation chamber

The electroformation/observation chambers are assembled after cleaning and prior to use each time. Figure 4.1 (top) shows the electroformation chamber before assembly, and the bottom of the figure shows post-assembly. Epoxy is used to glue the cover slip onto the Teflon that constitutes as the side-walls of the chamber. The epoxy glue needs to cure in the oven. Epoxy comes in various grades. Make sure to read instruction for the particular epoxy being used. Note carefully the temperature and duration required for curing. Note that heating and cooling of different materials, such as glass and Teflon, can cause them to expand and contract differently resulting in the parts separating or breaking after curing.

Appendix C

Histogram mean vs peak position

Some homogeneous vesicles have asymmetric peaks in their histograms in which the mean does not equal the peak position. Spot check confirmed that the difference between the mean and the peak position are within 0.5%. Possible explanations include nanodomains smaller than optical resolution, nanodomains with GP similar to that of the majority phase, and scattered light.

Peak position at the maximum intensity was determined for three samples manually: 13, 08, and 10. The data from Figs. 4.11 and 4.9 are reproduced here overlaid with these peak position GPs (Figs. C.1 and C.2). The GP obtained using the two different analysis methods are comparable. The peak position GP is typically higher than the mean GP, but the same temperature dependency can be seen in both. The same can be seen in Fig. C.2 for the 0.4% Laurdan sample (sample 15).

Data from sample 13 was not amenable to the automated analysis algorithm and was thus not included in the main text of the thesis. This sample contains data at lower temperature than presented in Fig. 4.11 (i.e., 10°C). Figure C.1 shows that GP at 10°C (0.57) is slightly higher than the homogeneous vesicle GPs at temperatures higher than 14°C and seems to follow the same trend. It is also similar to the GP of the high-GP domains at those higher temperatures. The level of water penetration into homogeneous membrane at 10°C suggests that these membranes are in the $\mathbf{l_o}$ phase.

In principle, one should be able to fit a curve to the histogram and get the peak position. Vanounou et al. [199] fit their GP histograms to three Gaussians without any physical explanations. My data also appeared to fit relatively well to three peaks. Naively, for a membrane exhibiting two different domains - and hence has two different environment for Laurdan to intercalate into, one might expect that the histogram can be fitted to two Gaussians, since the distribution will be bimodal. My data did not fit well to two peaks in most cases. The data shown in this thesis was not fitted.

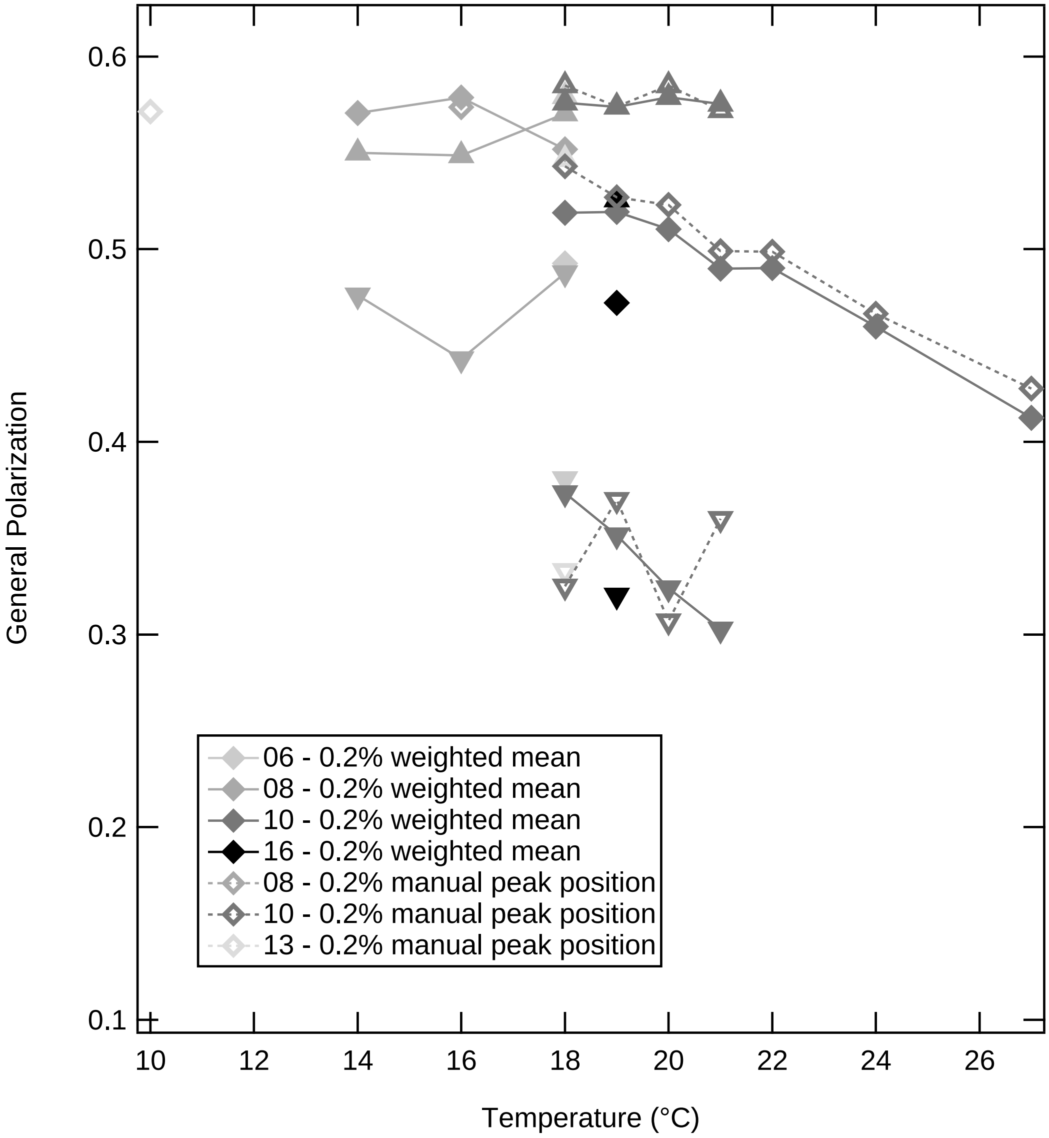

Figure C.1: Population average GP of 0.2% Laurdan 35:35:30 DOPC/DPPC-D62/chol GUV from different samples. The different samples were made and imaged on different days; they are identified by the date the images were taken and by different symbol colour. High-GP domains (▲), low-GP domains (▼), and homogeneous vesicle (◆) share the same symbol shapes as Figs. 4.8 and 4.9. Lines are added between the data points to aid in tracking which ones belonged to the same sample batch. The mean of the GP distribution is shown with filled symbols. GP of the peak position is shown with unfilled symbols.

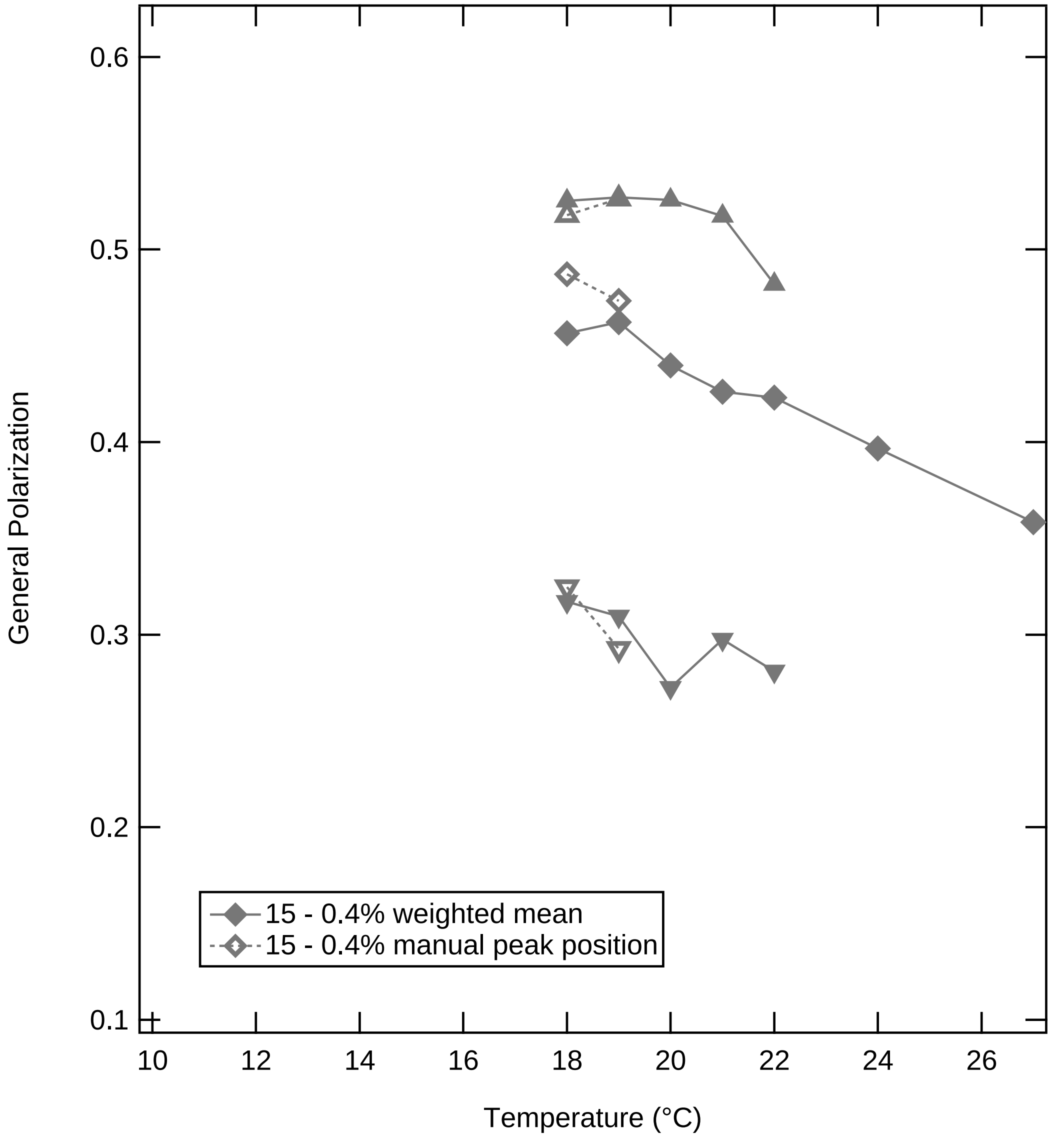

Figure C.2: Population average GP of 0.4% Laurdan 35:35:30 DOPC/DPPC-D62/chol GUV from different samples. The different sample samples were made and imaged on different days. The samples are identified by the date the images were taken and by different symbol colour. High-GP domains (▲), low-GP domains (▼), and homogeneous vesicle (◆) share the same symbol shapes as Figs. 4.8 and 4.9. Lines are added between the data points to aid in tracking which ones belonged to the same sample batch. The mean of the GP distribution is shown with filled symbols. GP of the peak position is shown with unfilled symbols.

Appendix D

Thin layer chromatography

This section is modified from my MSc thesis [134]. Thin layer chromatography (TLC) is like a small scale column. Lipids are loaded onto silica TLC plates and the solvent runs up a TLC plate via capillary action. Depending on the solvent and the lipid, different lipids move up the plate at different rates. As in column chromatography, like species dissolve like species. Because of this, TLC can also be used for testing solvent systems for column chromatography. The TLC plate is then developed using iodine vapors to visualize the presence of lipids. Iodine reacts with double bonds in lipids and turns the lipid a yellow or brown color. TLC is also useful for checking the presence of extraneous lipids and thus has been used for checking the purity of recovered products from the separation.

Appendix E

Protocol for phosphorus assay

Phosphorus assay is used for determining phospholipid content. It is also known as the Bartlett Assay. The principle behind this assay is based on the colorimetric determination of inorganic phosphate. The lipids are digested by the perchoric acid so that the inorganic phosphate becomes accessible. The inorganic phosphate is converted to phospho-molybdic acid by the addition of ammonium molybdate, which is reduced to a blue colored complex by 4-amino-2-naphthyl-4-sulfonic acid during heating. I received this protocol from a student named Maria at the Centre for Membrane Biophysics at the University of Southern Denmark. I unfortunately did not get her last name. This protocol is very similar to the protocol on Avanti Polar Lipids Inc. website, except the volumes used are much smaller.

1. Preparation of standard Na_2HPO_4 2mM
   Standard Na_2HPO_4 2 mM is diluted 1:4:
   i.e. 200 μl: 50μl Na_2HPO_4 2mM + 150 μl H_2O = 0.5 mM Na_2HPO_4

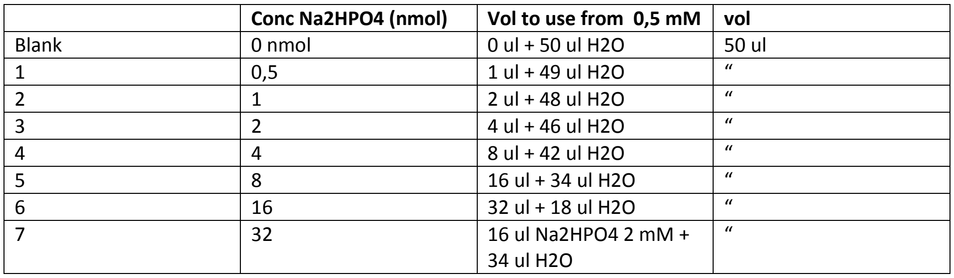

	Conc Na2HPO4 (nmol)	**Vol to use from 0,5 mM**	**vol**
Blank	0 nmol	0 ul + 50 ul H2O	50 ul
1	0,5	1 ul + 49 ul H2O	“
2	1	2 ul + 48 ul H2O	“
3	2	4 ul + 46 ul H2O	“
4	4	8 ul + 42 ul H2O	“
5	8	16 ul + 34 ul H2O	“
6	16	32 ul + 18 ul H2O	“
7	32	16 ul Na2HPO4 2 mM + 34 ul H2O	“

2. Preparation of control POPC 10 mg/ml
   - Dilute POPC 10 mg/ml: 1:10 (4 μl POPC + 36 μl H_2O)
   - 10 nmol POPC: 7.50 μl (1:10) POPC + 42.50 μl H_2O
   - 5 nmol POPC: 3.75 μl (1:10) POPC + 46.25 μl H_2O

3. Preparation of sample
   - Dilute samples to concentrations in range
   - Undiluted use 15 μl from the isolated and lipid extracted sample put 15 μl in 3 glass vials and let the methanol/chloroform evaporate. After that put 50 μl H_2O in every vial

- Always perform experiment in triplicates
- Add 50 μl perchloric acid in all vials (standard, control and sample)
- >200 degrees sand for half an hour
- >10 min. cool
- Reaction: 200 μl 1% ammoniummolybdat to each vial and afterwards 200 μl 4% ascorbic acid to each (color)
- Vortex
- Incubate 1 hour at 37°C
- ELISA plate 200 μl in each well
- Read 820nm/700nm

4% ascorbic acid: 0.4 g ascorbic acid + 10 ml H_2O (freshly made)
1% ammoniummolybdate tetrahydrate: 1 g + 100 ml H_2O

Appendix F

Gibbs triangle

According to Gibbs phase rule, in a given region of the phase diagram, ternary mixtures can have up to three phases in coexistence (Appendix A). The phase behaviours of these mixtures can be summarized onto a Gibbs triangle phase diagram that represents isothermal-isobaric conditions (Fig. F.1). For a lipids-themed introduction to Gibbs triangles, see Veatch and Keller [63]. A brief description adapted from Leung and Thewalt [165] is included here.

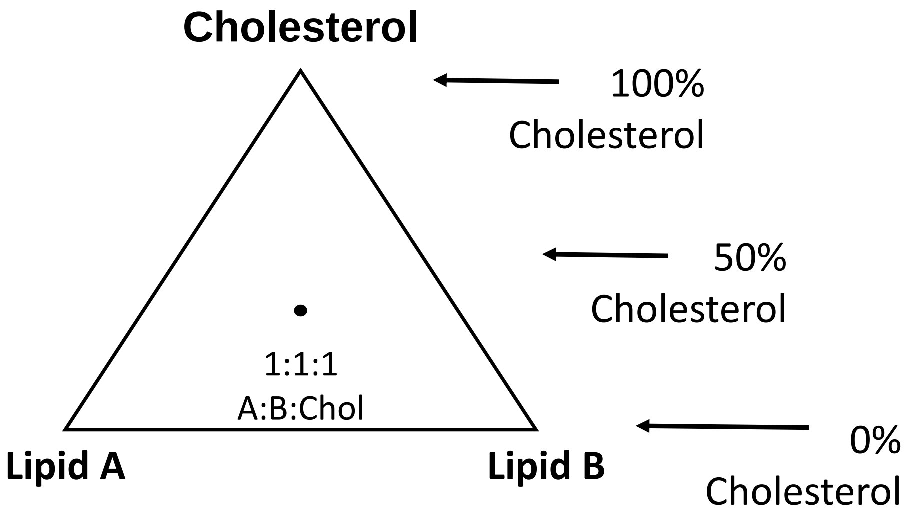

Figure F.1: How to read a Gibbs triangle

Each point within the triangle corresponds to a particular ternary lipid composition. The three vertices represent the three pure single-component systems. Each side corresponds to a binary mixture of the two components at the vertices it connects. Ternary mixtures lie inside the triangle, and their concentrations can be linearly interpolated.

On a Gibbs triangle, single phase regions as well as two- and three- phase coexistence regions are separated by phase boundaries. In a two-phase coexistence region, the compositions of the individual phases denote the phase boundaries. These compositions are known as the end-points, and these end-points are connected by tie-lines. Mixtures on the tie-lines separate into the phases with these end-point compositions. The lever rule states that the relative proportions of the two phases are proportional to the composition's distance from the end-points. A mixture that is closer to one of the end-points has more of that phase. As a result, ^{2}H NMR spectra from these compositions are a weighted sum of the spectra of the end-point phases. Tie-lines merge into single points at critical points. At critical points, very little energy is required to maintain phase coexistence.

Three-phase coexistence regions are triangular. Each vertex represents the composition of a single phase. Points within the three-phase triangle correspond to a membrane containing some proportion of each of the three phases. Model plasma membrane ternary mixtures studied at room temperature often have a region at low cholesterol concentrations where liquid ordered ($\mathbf{l_o}$), liquid disordered ($\mathbf{l_d}$) and solid ordered ($\mathbf{s_o}$) phases coexist.

Appendix G

Anchoring GUV using biotin-DPPE

In the literature, biotin and avidin are sometimes used to anchor giant unilamellar vesicle (GUV) for microscopy [166, 200]. Biotin and avidin bind very tightly (dissociation constant $K_d \approx 10^{-15}$ M [201]), and with high specificity. One avidin can bind up to four biotins. Biotin and avidin binding is widely used in molecular science [201, 202]. The use of biotin-avidin in GUV anchoring application is illustrated in Fig. G.1. Biotinylated-DPPE (Biotin-DPPE) is added to the GUV, and biotin is also used to coat the bottom of the observation chamber. Through interactions between biotin and avidin, the GUVs will attach to the bottom of the observation chamber, and be immobilized. Regular PE lipids form non-lamellar phases by promoting negative membrane curvature, but N-Rhodamine-PE, N-NBD-PE, Dansyl-PE, which has PE attached covalently to the amine group of the fluorophore, are known to not induce non-lamellar phase formation [references within 101].

^{2}H NMR experiments showed that the addition of 0.1% Biotin-DPPE does not alter T_{mix} of 35:35:30 DOPC/DPPC-D62/chol (Fig. G.2). Fluorescence-microscopy experiments presented in this thesis did not involve biotin and avidin.

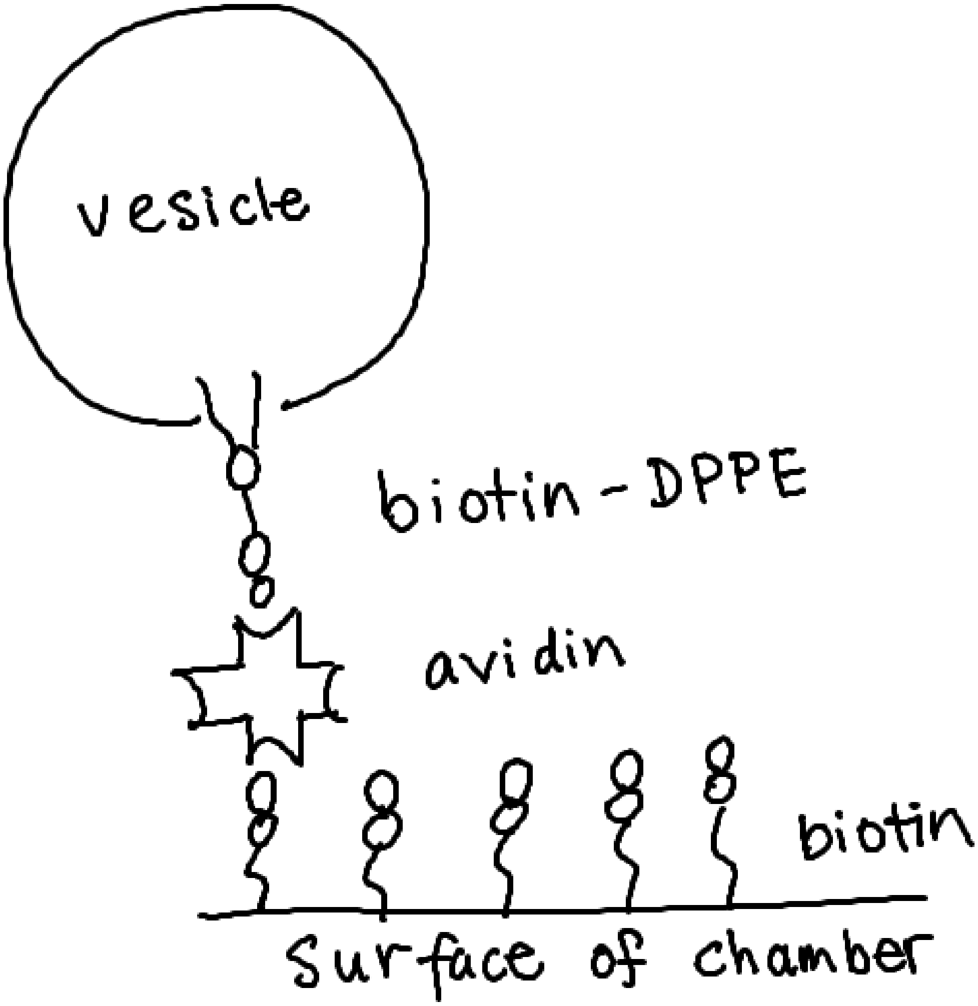

Figure G.1: Cartoon depicting how to anchor GUV with biotin-DPPE.

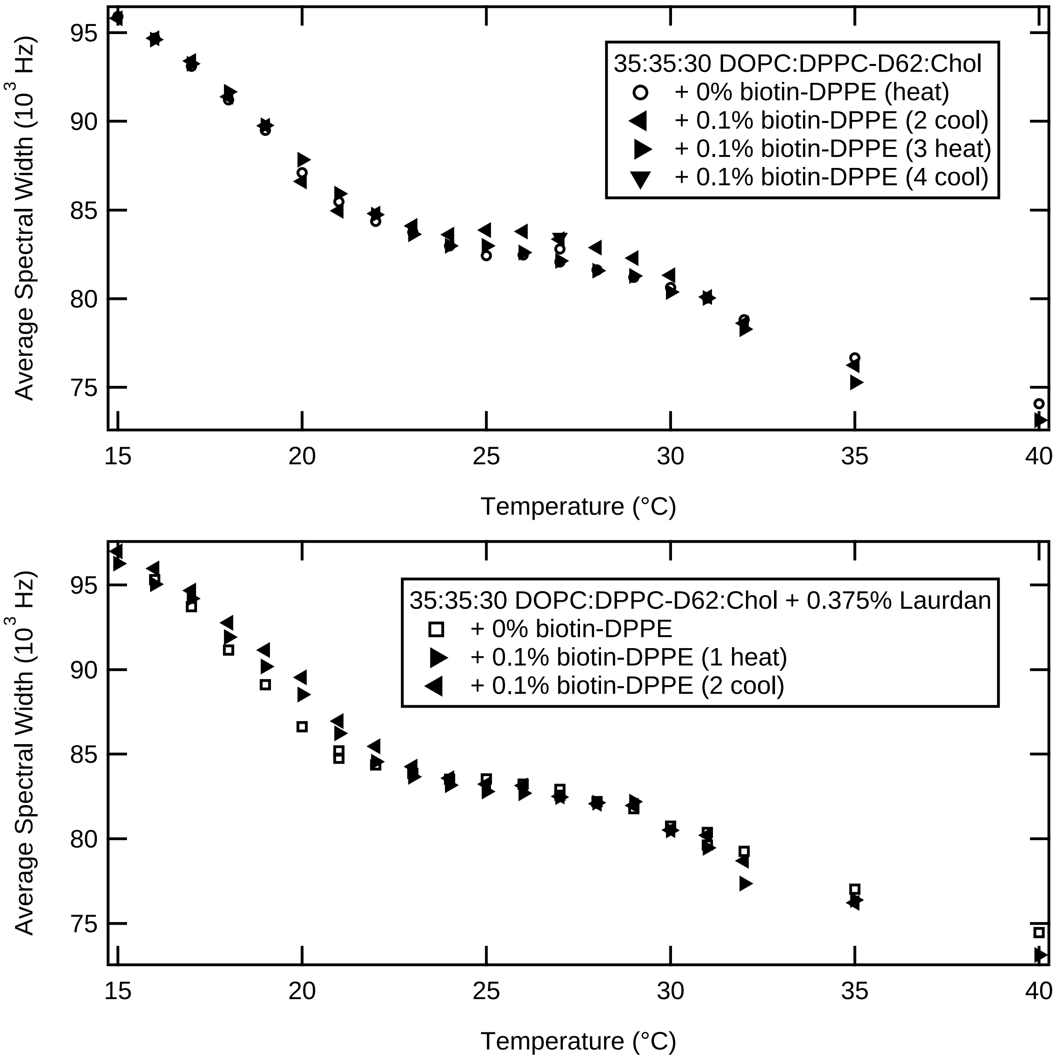

Figure G.2: Effect of adding trace amount of biotin-DPPE on M_1. ^{2}H NMR average spectral width temperature dependence for biotin-DPPE incorporated 35:35:30 DOPC/DPPC/chol membranes with (bottom) and without (top) 0.375% Laurdan. Heating and cooling cycles show no observable hysteresis. 0% biotin-DPPE M_1 from 15 to 20°C appears to be lower because of thermocouple misplacement.

Appendix H

Exchange-broadening of NMR line widths

Diffusion allows a nucleus to move from one local environment, characterized by a particular resonant frequency, to another environment. Following the treatment by Slichter [203], consider a simple case where there are two different environments, with two different resonant frequencies, separated by $\Delta\omega$. Let τ be the time describing how often on average the exchange between the two environments occurs. The exchange time-scale is $\tau_{ex} = \Delta\nu/(2\pi)$. If there is little exchange of the spins between the two environments (long τ, $\tau\Delta\omega \gg 1$), then there would be two peaks in an NMR spectrum. If exchange between them is sufficiently fast ($\tau\Delta\omega \ll 1$) that the spins experience a time-averaged environment (motional narrowing), then one resonance is observed. At intermediate exchange rates ($\tau\Delta\omega \approx 1$), two peaks are observed. The separation frequency is less than it is for in the low exchange case, and they are broadened.